



HAL
open science

X-ray diffraction and imaging with a coherent beam: application to X-Ray optical elements and crystal exhibiting phase inhomogeneities

Fabio Masiello

► **To cite this version:**

Fabio Masiello. X-ray diffraction and imaging with a coherent beam: application to X-Ray optical elements and crystal exhibiting phase inhomogeneities. Condensed Matter [cond-mat]. Université de Grenoble; Università di Torino (Turin, Italie), 2011. English. NNT: 2011GRENY020 . tel-00609216

HAL Id: tel-00609216

<https://theses.hal.science/tel-00609216>

Submitted on 18 Jul 2011

HAL is a multi-disciplinary open access archive for the deposit and dissemination of scientific research documents, whether they are published or not. The documents may come from teaching and research institutions in France or abroad, or from public or private research centers.

L'archive ouverte pluridisciplinaire **HAL**, est destinée au dépôt et à la diffusion de documents scientifiques de niveau recherche, publiés ou non, émanant des établissements d'enseignement et de recherche français ou étrangers, des laboratoires publics ou privés.

THÈSE

Pour obtenir le grade de

DOCTEUR DE L'UNIVERSITÉ DE GRENOBLE

Spécialité : **Physique de la matière condensée et du rayonnement**

Arrêté ministériel : 7 août 2006

Présentée par

Fabio MASIELLO

Thèse dirigée par **Jürgen HÄRTWIG** et
codirigée par **Carlo LAMBERTI**

préparée au sein du **European Synchrotron Radiation Facility**
dans l'**École Doctorale de Physique**

Diffraction et imagerie aux rayons X en utilisant un faisceau cohérent: applications aux optiques rayons X et aux cristaux comportant des hétérogénéités de phase.

Thèse soutenue publiquement le **13 mai 2011**
devant le jury composé de :

Dr. José BARUCHEL

Chercheur ESRF, Président

Pr. Brian TANNER

Professeur à l'Université de Durham – UK, Rapporteur

Pr. Simon CONNELL

Professeur à l'Université de Johannesburg – ZA, Membre

Dr. Pierre BASTIE

Chercheur ILL, Membre

Pr. Carlo LAMBERTI

Professeur à l'Université de Torino – I, Membre

Dr. Jürgen HÄRTWIG

Chercheur ESRF, Membre



To my Bibi...

Acknowledgements

Here I am, finally writing the acknowledgments of my thesis. The first person I am deeply indebted to is my theses (both MSc and PhD) supervisor, Jürgen Härtwig. The fact that, even during the more stressful period, you have been able to sustain me with the right words and a smile is priceless! It has been a real pleasure to work with you during almost five years and to travel in four different continents together. Danke schön Herr Härtwig.

Thanks to Prof. Simon Connell, with whom, after creating a nice professional relationship, I am also managing to create a great familiar one. What I found impressive about Simon is the fact that, whatever you chat with him about (could be nuclear physics, diamond synthesis, the rules of rugby, how to prepare a perfect braai or fixing a broken car) he is always able to engross you in an amazing way. I feel very lucky that I will be able to continue to listen to you for many years to come! But one thing is sure, I will never ever think that rugby is more fun to watch than soccer

Another person at the ESRF which I have rarely seen not smiling is José Baruchel. Thank you very much José for many things: for allowing me to come to the ESRF as a Master student, for finding some time in your very busy schedule to discuss the results of our experiments on the ferroelectric crystals, for accepting to be the president of this jury and especially for the nice words you had for me during our last meeting in your office and that I will never forget.

The other part of the joint collaboration between my university in Turin and the ESRF, which allowed me to come to Grenoble as a Master student, is due to Prof. Raffaello Garfagnini. Thank you very much for allowing me to start this adventure in Grenoble, which changed the rest of my life so deeply.

The other Professor at Turin University which I am indebted to is Prof. Carlo Lamberti. Unfortunately we didn't succeed in spending a lot of time together, but every time we met you have been able to, in a balanced way, compliment me for the results achieved and motivated me for the future challenges.

I would like to thank Prof. Brian Tanner and Prof. Tilo Baumbach for accepting the task of reviewing my thesis. Thanks also to Pierre Bastie for accepting to be part of the thesis jury on such short notice.

A special thanks goes to Tamzin Lafford. As I have told you Tamzin, you have been a kind of Marry Poppins for me. You arrived with many new ideas which improved considerably the working conditions at the beamline. Moreover, your dedication in helping me with essentially all my tasks has been fundamental for the final achievement of my thesis, not to mention your help in correcting the manuscript. But even more than this, how can I thank you for the patience which you showed listening to all the rehearsals of my presentations, the wonderful advice you gave me for my job interviews and, icing on the cake, your great muffins and delicious cakes you brought us for our delight? Well, I try with this THANK YOU TAMZIN

Another very important person has been Claudio Ferrero. The amount of nights we spent together, working on convolution and deconvolution code has been enormous. But during all this time, you always have managed to nicely switch between work and pleasant discussions about many different subjects. Thanks Claudio, even though I will never be able to talk or understand the dialect from my home town, il piemontese.

This five years spent in Grenoble would not have been the same without wonderful friends and colleagues, which I will briefly list here: Hedi, Harry, Rafael, Aymeric, Peter, Michael, David, Sebastien, Xavier, Federico, Genziana, Pierre-Jean, Valentina, Iulia, Min, Camille, Ali, Eliza,

Grazie ai miei genitori, che con il loro supporto morale ed economico mi hanno permesso di arrivare fino a qua ed alle mie sorelle, per essere sempre disponibili ad ascoltarmi ogniqualvolta ho avuto bisogno di qualcuno a cui parlare.

And last, but not least, to my wonderful wife Bibi, to whom this thesis is dedicated. You have been there for me during the hardest period of my thesis, the writing-up. Unfortunately, I will not be there for you in the same hard period, and of that I am deeply sorry; but I hope time will show us that the decision I took was the good one. To conclude with a happy thought, I remember that in my Master thesis acknowledgements, I wrote that I found my diamond in South Africa. Well, I am happy to say that this diamond will now be with me forever and, with God's will, it will allow us to generate even more little diamonds in the future

Contents

1	Introduction	1
2	Theoretical basis	5
2.1	Synchrotron radiation	5
2.1.1	Short historical overview on synchrotron radiation	5
2.1.2	Synchrotron radiation properties	8
2.2	X-ray diffraction	12
2.2.1	Kinematical theory of X-ray diffraction	12
2.2.2	Dynamical theory of X-ray diffraction by a perfect crystal	13
2.2.2.1	Bragg and Laue cases	19
2.2.2.2	Asymmetric reflections	22
2.2.2.3	Reflectivity curves in Bragg case	24
2.3	Coherence	28
3	Experimental techniques	31
3.1	High Resolution X-ray Diffractometry	31
3.1.1	Introduction	31
3.1.2	Determination of apparatus function.	33
3.1.2.1	Model and fit approach	35
3.1.2.2	Direct deconvolution methods	39
3.1.2.3	Comparison of the results obtained.	39
3.2	X-ray topography	42
3.3	X-ray surface sensitive techniques.	51
3.3.1	X-Ray Reflectivity (XRR)	52
3.3.2	Grazing Incidence Diffraction (GID) in non-coplanar geometry. .	55

CONTENTS

4	Characterization of single crystal diamonds	57
4.1	Diamond	57
4.1.1	Properties	57
4.1.2	Synthesis of diamonds	58
4.2	Characterization of synthetic diamonds. Experimental results.	66
4.2.1	High Resolution X-ray Diffractometry	66
4.2.2	X-ray Topography	67
4.2.2.1	White Beam Topography (WBT)	68
4.2.2.2	Double crystal Topography	71
4.2.2.3	Quantitative analysis of the effective misorientation in a high quality type IIa diamond	81
4.2.3	Coherence measurements	94
4.2.4	Surface sensitive techniques.	100
4.2.4.1	Optical surface profile and AFM results	103
4.2.4.2	Sample preparation	105
4.2.5	Grazing Incidence Diffraction	106
4.2.6	X-ray Reflectivity	108
5	Improvements to polishing of silicon crystals and beryllium windows	111
5.1	Improvements and quantification of silicon crystals processing at the ESRF Crystal Laboratory	111
5.1.1	First test - Localization of the main problem.	112
5.1.2	Second test - Calibration of the optical polishing.	116
5.1.3	Third test - Optimization of the MCP.	119
5.2	Coherence measurements of the polished samples	120
5.2.1	Talbot effect measurements	121
5.2.2	Coherence measurements using bi-lens-based interferometer	124
5.3	Improvements on the polishing of beryllium windows	128
6	X-ray coherence exploited in imaging of ferroelectric domains	133
6.1	Ferroelectricity	133
6.2	Ferroelectric crystals used for non-linear optics applications.	135
6.3	Visualization of ferroelectric domains using X-ray	139
6.4	Coherence preserving furnace	140

6.5	Visualization of inverted domains in KTA and Rb:KTP crystals.	144
6.6	Ferroelectric domain behaviour with temperature in Rb:KTP	146
6.7	Conclusions	152
7	Further diamond related studies	153
7.1	Bending diamonds by femtosecond laser ablation	153
7.2	X-ray topography of diamond using forbidden reflections: which defects do we really see?	155
7.3	Crystal growth and perfection of large octahedral synthetic diamonds .	157
8	Conclusions	159
	References	165
A	Apparatus function determination - Direct deconvolution methods	III
A.1	Burger - Van Cittert	III
A.2	Richardson - Lucy	VI

CONTENTS

Chapter 1

Introduction

The exceptional properties of synchrotron light sources have been and increasingly are exploited in very different disciplines, from archaeology to chemistry, from material science to biology, from medicine to physics. Among these properties it is important to mention the high brilliance, continuum spectrum, high degree of polarization, time structure, small source size and divergence of the beam, the last resulting in a high transversal coherence of the produced radiation.

This high transversal coherence of the synchrotron sources has permitted the development of new techniques [1], e.g. phase contrast imaging [2, 3], X-ray photon correlation spectroscopy [4, 5] and coherent X-ray diffraction imaging (CXDI) [6, 7].

The importance of X-ray coherence is striking if considering that the words coherence or coherent appear approximately 200 times in the so-called “ESRF Science and Technology Programme - 2008 - 2017”¹, where the future challenges and necessary upgrades of the ESRF are presented.

Therefore, it is of primary importance for many applications that the optical elements preserve this property, disturbing as little as possible the wavefront. At the same time it is fundamental to have methods able to characterize the coherence of the radiation. Many different methods to characterize the coherence of hard X-rays have been investigated and they make use of, *e.g.* a wedge-shaped silicon crystal and measuring the visibility of the Pendellösung fringes, [8], a Fresnel biprism composed of two diamonds [9], a round fiber or slits [10], a system of double slits [11], a double pinhole [12] or a

¹available at <http://www.esrf.eu/AboutUs/Upgrade/documentation/purple-book/>

1. INTRODUCTION

Material	Be	C*	Si	Ge
Atomic Number	4	6	14	32
Absorption coefficient μ at 8 KeV [cm^{-1}]	1.8	7.5	141	402
Conductivity, κ at 297 K [$\text{W cm}^{-1} \text{K}^{-1}$]	1.93	23	1.5	0.64
Expansion Coefficient, α at 297 K [10^{-6}K^{-1}]	7.7	1.1	2.4	5.6
Figure of merit, $\frac{\kappa}{\mu\alpha}$ at 297 K [KW]	140	2780	4.4	2.8

Table 1.1: Figures of merit for different material for X-ray optics [17]

double-grating interferometer [13]. We have been using two other methods, one based on the partial Talbot effect, [14] and another based on a system of bi-lenses [15].

With the new fourth generation sources, *e.g.* the X-ray free-electron lasers (XFEL), the coherence of the beam will be pushed even further since the radiation produced will be transversally almost fully coherent, reaching a degree of transverse coherence of 95%, [16]. At the same time, the heat-load on the optical elements will also increase considerably, especially for machines such as the European XFEL. Different solutions are proposed to overcome the heat-load problem at the E-XFEL. One is to use mirror optics which will allow to de-focus the beam and to have an enlarged footprint on the monochromator, therefore reducing the heat load. Another solution, in the case when beam expansion is not possible or not desirable, is to use diamond crystals.

In fact, among all the outstanding properties that diamond exhibits, three in particular make this material ideal for use as optical elements in light sources such as synchrotrons and X-ray free-electron lasers (XFEL):

- thermal conductivity at room temperature ($23 \text{ Wcm}^{-1}\text{K}^{-1}$);
- low expansion coefficient at room temperature $1.1 \times 10^{-6} \text{ K}^{-1}$;
- low linear absorption coefficient for X-rays (7.5 cm^{-1} at 8 keV);

The combination of these three properties is summarized in a figure of merit, obtained dividing the conductivity by the absorption and expansion coefficients. In tab.1.1 are compared the thermal properties of the most used materials for X-ray optical elements, showing that diamond is by orders of magnitudes the best material.

There are three principal issues that could impede the success of diamond as X-ray optical elements: the crystal perfection, the size and the processing technologies. Natural

diamonds are not suitable for two reasons: they possess a higher number of defects and greater strain due to the complicated growth process inside the Earth; and the cost is also prohibitive, since they are mostly used in jewellery. In contrast, synthetic diamonds seem to have the necessary characteristics.

Recently, two more possible applications of diamond crystals have been reported. The first is to use diamonds as element in an X-ray free-electron laser oscillators (XFEL) [18], by using high X-ray reflectivity of diamonds. The second is to use a diamond crystal between two undulators for generating highly monochromatic X-rays through the so-called self-seeding effect, [19].

My thesis work will consist essentially of three parts:

- characterization of high quality crystals foreseen as X-ray optical elements, in particular those made out of diamond;
- study of the temperature dependent behavior of the domain in periodically poled ferroelectrics crystals, which are possible only thanks to the coherence of the beam
- diamond related results, obtained in the framework of external collaborations

More specifically, in chapter 2, I will introduce the necessary theoretical basis of synchrotron radiation generation, some notions of the kinematical and dynamical theories of X-ray diffraction and an introduction to the formalism describing coherence.

The experimental techniques used will be presented in chapter 3: high resolution X-ray diffraction, X-ray diffraction topography, grazing incidence diffraction and X-ray reflectivity.

In chapter 4, I will show the results obtained with diamond crystals of different crystalline quality using the characterization techniques presented.

Chapter 5 will be dedicated to the results obtained from polishing tests of high quality silicon crystals and beryllium windows.

In chapter 6 I will present an example of applications that make use of the transversal coherence of a synchrotron beam: the investigation by coherent X-ray section topography of ferroelectric domain behaviour as a function of temperature in periodically-poled Rb:KTP.

1. INTRODUCTION

Chapter 7 will be a short introduction to studies which are not directly related with the main topic of my thesis but that have in common diamond as the material and X-ray topography as the characterization technique used.

Finally, in chapter 8 I will draw conclusions and comment on the outlook for the future.

Chapter 2

Theoretical basis

In this chapter, I introduce the theoretical basis necessary to understand the experimental techniques used and the data obtained in the rest of the thesis. Firstly, some of the properties of synchrotron radiation are presented, together with a historical overview. Afterwards, the fundamentals of kinematical and dynamical theories of X-rays diffraction are summarized. Finally, the necessary formalism to describe the phenomenon of coherence is introduced.

2.1 Synchrotron radiation

2.1.1 Short historical overview on synchrotron radiation

Synchrotron radiation is an electromagnetic wave generated by the acceleration of relativistic charged particles (moving at relativistic velocity) on curved trajectories in magnetic fields. An historical review of synchrotron radiation is available in [20]. I present here the more important events.

In 1898, Alfred Liénard published a paper in '*L'Éclairage Électrique*' entitled '*Champ électrique et magnétique produit par une charge électrique concentrée en un point et animée d'un mouvement quelconque*' where he derived, directly from Maxwell's equations, the so-called Liénard-Wiechert potentials. By using this potential, Liénard was able to calculate the energy lost by electrons moving in a circular trajectory in a homogeneous magnetic field. This theory can be considered the basis of synchrotron radiation, which was experimentally discovered about 50 years later.

2. THEORETICAL BASIS

The first observation, fig.2.1, of radiation emitted by relativistic charged particles, took place on the 24th April 1947, at the General Electric Research Laboratory, where a 70 MeV electron synchrotron was in use [21]; the radiation was thus called synchrotron radiation. The bright spot visible in the picture (visible thanks to a transparent vacuum chamber and a mirror) was bluish-white when the energy of the electrons was 70 MeV, and changed to yellow at 40 MeV, red and weaker at 30 MeV and disappeared below 20 MeV. This phenomenon is related to the fact that the critical energy of the radiation is proportional to the energy of the electron beam.

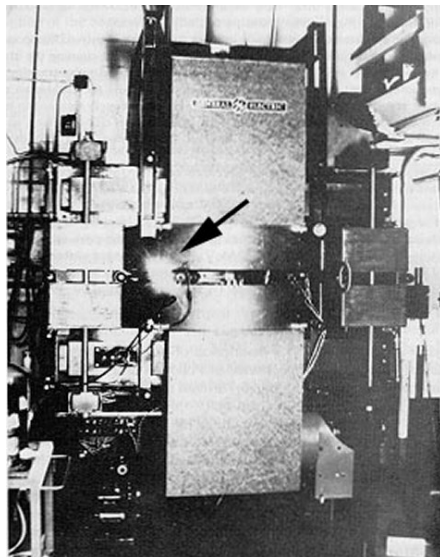


Figure 2.1: The General Electric 70 MeV synchrotron; the synchrotron radiation light is indicated by the arrow.

Initially, this radiation, produced by the bending magnets (magnetic dipoles), was a nuisance for high energy physicists, because it limits the maximum energy achievable by the accelerated particles, especially for light particles such as electrons and positrons. In fact, the first synchrotrons were designed exclusively for particle physics. Starting from the 1970's, a parasitic use of the synchrotron radiation began; those were the so-called *first generation sources*, e.g. SURF - USA, Frascati - Italy, INS - Japan, DESY - Germany, ACO - France.

The first storage ring designed for using synchrotron radiation, *second generation source*, was the Synchrotron Radiation Source in Daresbury - UK, followed by oth-

ers (NSLS - USA, Photon Factory - Japan, BESSY - Germany, LURE - France).

The next step, that brought the synchrotron community towards the *third generation* machine, was the idea of adding, in the straight sections of the ring, so-called Insertion Devices (ID). Inside the insertion devices, the electrons (or positrons) follow a periodic undulating trajectory in the magnetic field produced by a number of permanent magnets with alternating pole directions. This results in emitted beams much more intense than that from a single magnetic dipole. The European Synchrotron Radiation Facility, France, with its 6.04 GeV storage ring, was the first third-generation high energy synchrotron in the world (1994), quickly followed by the 7 GeV Advanced Photon Source, USA in 1996, the 8 GeV Spring8 in Japan in 1997 and only recently (2009) by Petra III, Germany with an energy of 6 GeV. These synchrotrons are, up to now, the four high energy synchrotron radiation sources in the world.

The next step is the *fourth generation sources*: these are light sources which exceed the performance of third generation synchrotrons by at least one order of magnitude in an important parameter such as brightness, coherence or pulse duration [22]. There are three general categories [23]:

Storage Ring Based [24], where very low emittance is achieved in a much bigger circumference and by increasing considerably the number of bending magnets [25]. The newest PETRA III synchrotron sits between the old third generation sources and the new fourth generation.

Energy Recovery Linac ERL which is also based on obtaining an electron beam with a very small emittance. This is achieved by having the electrons circulating only once into a transport loop where the different undulators for the production of X-rays are installed. In order to accelerate the electrons, a linear accelerator is used. The main problem with this scheme is the large amount of energy needed to accelerate the electrons, that are then damped after one circuit of the ring. This difficulty has been overcome by the concept of energy recovery. After one circuit, the electrons enter the linac again, but this time out of phase with the RF cavities. In this way the electrons are decelerated by the linac and they return most of their energy to the cavities themselves [26]. At the moment there are two main projects to build ERL for light sources: one is at Cornell University, USA

2. THEORETICAL BASIS

and the other is at the High Energy Accelerator Research Organization KEK, Japan.

X-ray Free Electron Laser XFEL which can be considered in a simplistic way as a very long undulator, [27]. The photons produced inside this undulator will interact with the electrons themselves. This organizes the electrons inside the bunches into microbunches, that are periodically separated by a period length equal to the undulator fundamental harmonic. The bunched electrons produce coherent radiation. This effect is called Self-Amplified Spontaneous-Emission and is at the basis of X-ray lasing. The first such machine, the Linear Coherent Light Source, (LCLS), was inaugurated in 2009 in Stanford, USA, using part of the already existing linear accelerator. The next will be the Spring-8 Compact SASE Source, Japan in 2011, followed by the European-XFEL, Germany in 2015.

2.1.2 Synchrotron radiation properties

Some of the main properties of synchrotron radiation at a third generation light source are briefly described here. First of all, three quantities that are important for characterizing and comparing different synchrotron sources are introduced: flux, brightness and brilliance, [28].

Flux is defined as the number of photons per second in 0.1% of the spectral bandwidth. The brightness is the flux over the emission angle. The brilliance is the brightness divided by the source area. As a formula:

$$\text{brilliance} = \frac{\# \text{ photons}}{[\text{s}] [\text{mrad}^2] [\text{mm}^2] [0.1\% \text{ bandwidth}]} \quad (2.1)$$

In order to have a very high brilliance, it is therefore important to have a very high flux, very well collimated, coming from a small source. All these properties are achieved at third generation synchrotrons.

The high flux derives directly from the total power radiated by an accelerated relativistic particle on a circular path:

$$P = \frac{2}{3} \frac{e^2 c}{R^2} \beta^4 \gamma^4 \quad (2.2)$$

where R is the radius of the circular path, e the charge of the electron, c the speed of light, β is the ratio between the speed of the particle and the speed of light and γ is the

2.1 Synchrotron radiation

Lorentz factor. It increases for high speed particles (therefore, high energy synchrotron) and for small radii of curvature. Remembering that $\gamma = \frac{E}{m_0 c^2}$, it is possible to see that the emitted power strongly decreases with the mass of the particle. This is the reason why only electrons and positrons are used in synchrotron light sources.

The high collimation of the photon beam is the result of the Lorentz transformation of the power emitted by accelerated relativistic particles. In the frame of the moving electron, the power distribution is the same as the pattern of an oscillating electric dipole. In the laboratory frame, the intensity distribution is transformed into a forward-peaked distribution, with semi-opening angle $\approx \frac{1}{\gamma}$, fig.2.2.

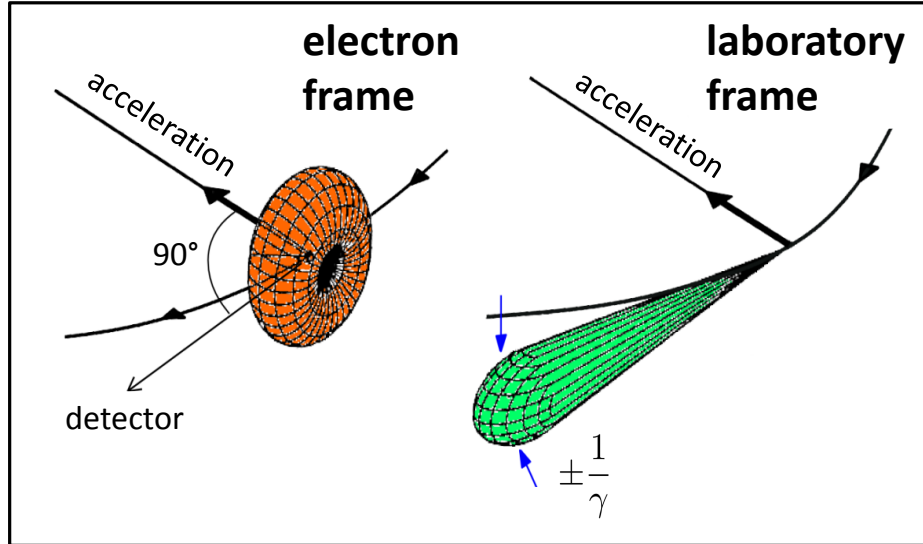


Figure 2.2: The effect of relativity on the angular distribution of the emitted beam.

The source size of the photon beam is given by the convolution of the sizes ($\sigma_{x,y}$) and divergences ($\sigma'_{x,y}$) of the electron beam with the intrinsic radiation characteristics of a single particle. The emittance (defined as the product of size and divergence of the electron beam) is therefore an important parameter. In a synchrotron, the horizontal emittance is larger than the vertical emittance. This is due to larger betatron oscillations in the plane of the ring. These oscillations are caused by the fact that the electrons, by emitting photons, lose a part of their energy, therefore changing the orbit radius. The energy lost by the electrons is recovered in the Radio Frequency (RF)

2. THEORETICAL BASIS

cavities. The vertical emittance is produced by the small inaccuracy in the magnetic fields or alignment of the magnetic quadrupoles.

The emittance of a beam is proportional to the square of the energy of the stored electrons and to the third power of the bending angle (in the approximation of small bending angles), [29]. This has important consequences, *e.g.* for the new light source Petra III. The storage ring used is bigger than any existing one, with a circumference of 2304m. Therefore the bending angles are much smaller and consequently the emittance is smaller, ≈ 1 [nm rad] compared to the 3 – 3.9 [nm rad] values for Spring8 and the ESRF.

Moreover, the small source size and the possibility of having long source-to-sample distances play a major role also in another important property of third generation synchrotrons: *i.e.* the high degree of transversal coherence. This point will be discussed later in the chapter, 2.3.

As previously mentioned, the main characteristic of third generation synchrotron is the presence of insertion devices in the straight sections. This results in an increase in the brilliance of the radiation produced compared to that from a bending magnet.

The idea of using insertion devices in order to increase the brightness comes from theoretical work by Ginzburg in 1947, [30] and Motz in 1951, [31]. In 1953 Motz and co-workers verified this idea experimentally, building an undulator that produced radiation with a wavelength varying from millimeters to hundreds of nm using a linear accelerator at Stanford University. The idea was to make the electron oscillate rapidly in the orbit plane using an array of permanent magnets. This device was inserted in the straight section of the Chasman-Green cell and for that reason they are called Insertion Devices (ID).

Two different types of ID are used: wigglers and undulators. In a wiggler, the amplitude of the oscillations is rather large and the cones of the emitted radiation do not superpose. Therefore, the intensities of the radiation fields are added incoherently. This results in an increased photon flux by a factor $2N$, where N is the number of magnetic dipoles. If the oscillations are small enough, then it is possible to add the radiation fields emitted by the electron coherently: this is the case for an undulator. To define what is meant by “small enough”, a dimensionless parameter is used:

$$K = \frac{eB_0\lambda_u}{2\pi mc}$$

2.1 Synchrotron radiation

where λ_u is the spatial period of the oscillations and B_0 is the maximum magnetic field. For a wiggler $K \gg 1$, whilst $K \approx 1$ for an undulator.

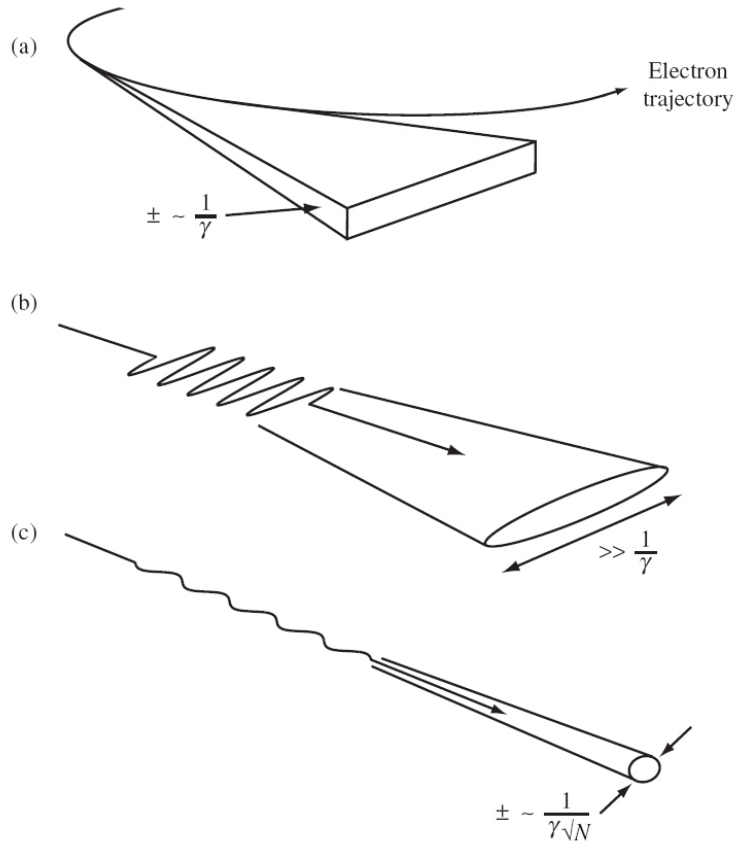


Figure 2.3: The different types of radiation in synchrotron facilities: a) bending magnet; b) wiggler; c) undulator

The radiation emitted by an undulator is more collimated in the horizontal direction, with an aperture that is $1/(\gamma\sqrt{N})$, fig.2.3. Another important undulator characteristic is the fact that the interference produced by adding coherently the electromagnetic fields gives a “quasi-monochromatic” wave (also called *pink beam*) and the presence of higher harmonics. This is just the opposite of what happens with a wiggler, where the incoherent sum gives a broad spectrum or white beam. There is no sharp border between these two devices. Depending on parameters there is a continuous transition between those limiting cases.

The very high brilliance is one of the main properties of synchrotron radiation. Just as

2. THEORETICAL BASIS

a term of comparison, the brilliance of an X-ray tube is about 10 orders of magnitude smaller than the brilliance for an undulator at the ESRF. Other important properties of the radiation produced at third generation sources are the high degree of polarization (σ -polarized in the plane of the orbit, slightly elliptical out of it), and the pulsed structure, allowing *e.g.* stroboscopic studies of acoustic vibrations in LiNbO₃ piezoelectric crystals, [32].

2.2 X-ray diffraction

The first X-ray diffraction experiment was performed in 1912 by Friedrich, Knipping and Laue [33]. The idea that the X-ray would be diffracted by a crystal came to Laue during a meeting he had with Ewald [34], whose thesis subject was “To find the optical properties of an anisotropic arrangement of isotropic resonators”. During this meeting von Laue asked Ewald: “what is the distance between such resonators”. Ewald’s answer was: “about one thousandth of the wavelength of light”. From previous work done by Sommerfeld, the wavelength of the radiation was also supposed to be of that order of magnitude and Laue immediately realized that, if crystals were made of a periodic array of atoms, they should diffract ¹.

Two main theories exist in order to explain the diffraction of the X-ray by a crystal: the kinematical and the dynamical theories of X-ray diffraction.

2.2.1 Kinematical theory of X-ray diffraction

The basis of the kinematical theory was given in the first paper written after the discovery of diffraction, [33]. It states that the amplitude diffracted by the crystal is simply the sum of the amplitudes of the waves diffracted by each atom, considering the phase shifts due to the different optical paths but neglecting the interaction of the incident wave with the crystal itself and is equivalent to the first Born approximation in scattering theory. This means that the amplitude of the incident wave is constant inside the crystal, which is a clear violation of the conservation of energy. Therefore

¹the history of Laue’s discovery of X-ray diffraction by crystals is available from the International Union of Crystallography website, at the following address www.iucr.org/__data/assets/pdf_file/0010/721/chap4.pdf

the kinematical theory is valid only as an approximation; the relevant approximations will be shown later.

Following Authier and Malgrange [35], we describe a crystal as a three dimensional, infinite, periodical array of electron densities $\rho_0(\mathbf{r})$ multiplied by a shape function $y(\mathbf{r})$, that takes into account the finite size of the crystal ($y(\mathbf{r}) = 1$ inside and 0 outside the crystal). The amplitude of the diffracted wave is:

$$A(\Delta\mathbf{K}) = \int_{-\infty}^{\infty} \rho_0(\mathbf{r})y(\mathbf{r})e^{-2\pi i\Delta\mathbf{K}\cdot\mathbf{r}} d\tau \quad (2.3)$$

where $\Delta\mathbf{K}$ is the diffraction vector defined as the difference between the incoming and diffracted wavevectors ¹, $\Delta\mathbf{K} = \mathbf{K}_h - \mathbf{K}_o$. The integration is over all space and $d\tau$ is a volume element. The amplitude $A(\Delta\mathbf{K})$ can be considered as the Fourier transform of the electron density distribution. By defining the structure factor as:

$$F_{\mathbf{h}} = \int_{-\infty}^{\infty} \rho_0(\mathbf{r})e^{2\pi i\mathbf{h}\cdot\mathbf{r}} d\tau \quad (2.4)$$

with \mathbf{h} being the reciprocal lattice vector, we can rewrite the amplitude as:

$$A(\Delta\mathbf{K}) = \frac{1}{V} \sum_{\mathbf{h}} F_{\mathbf{h}} Y(\Delta\mathbf{K} - \mathbf{h}) \quad (2.5)$$

where V is the volume of the unit cell, $Y(\Delta\mathbf{K} - \mathbf{h})$ is the Fourier transform of the shape of the crystal and the summation is over all the reciprocal lattice vectors \mathbf{h} . It is important to notice that $Y(\Delta\mathbf{K} - \mathbf{h})$ is proportional to the volume of the crystal itself, *i.e.* for larger and larger crystals the diffracted amplitude will diverge. This is, of course, not possible since it violates the conservation of energy. The kinematical theory is therefore only a first order approximation, valid for *thin crystals*. In order to define what is thin, it is necessary to introduce a more general theory, *i.e. the dynamical diffraction theory*.

2.2.2 Dynamical theory of X-ray diffraction by a perfect crystal

The main purpose of this section it is not to give a full description of dynamical theory; many excellent books, *e.g.* [36, 37], and papers, *e.g.* [38], are already available on the matter. The idea is simply to introduce a few concepts that will be used in the rest of

¹I follow the crystallographic definition of wavevector $k = \frac{1}{\lambda}$, omitting the factor 2π

2. THEORETICAL BASIS

the thesis. There are three different classical approaches to the dynamical diffraction theory for perfect crystals (not taking into consideration the more general quantum field theoretical approach). The first is the one proposed by C. G. Darwin [39]. His theory assumes that at every lattice plane, two waves are generated: a partially transmitted wave S and a partially reflected wave T , similarly to the optics of classical light at plane interfaces. It is possible to express this by writing the following recurrent formulae [37]

$$S_n = iqT_n + (1 - iq_0)e^{-i\phi}S_{n+1} \quad (2.6a)$$

$$T_{n+1}e^{i\phi} = (1 - iq_0)T_n - i\bar{q}e^{-i\phi}S_{n+1} \quad (2.6b)$$

where:

$$q = \frac{Nd_{hkl}\lambda r_e |F_{hkl}|}{\sin \theta_B}$$

$$\phi = \frac{d_{hkl}}{\lambda}$$

with N is the number of scattering unit per unit volume, d_{hkl} is the interplanar spacing of the lattice plane with Miller index hkl , λ the wavelength, r_e the classical electron radius, F_{hkl} the structure factor, θ_B is the Bragg angle; q_0 and \bar{q} follow the same expression as q but replacing F_{hkl} with F_{000} and $F_{\bar{h}\bar{h}\bar{h}}$, respectively.

The second theory was proposed by P.P. Ewald [40]. In his theory, Ewald, had a microscopic approach: he supposed that the crystalline lattice is formed of a three-dimensional array of electric dipoles. When excited by an external electromagnetic field, each dipole radiates a spherical wave. These spherical waves radiated by each dipole will also excite the other dipoles, producing what Ewald called a *wavelet*. He then used Hertz vector potentials to describe the electromagnetic field inside the crystal. I will not enter into details of this formulation.

The third and most commonly used formulation was made by M. von Laue [41]. Laue used a macroscopic approach based on Maxwell's equations in a medium with a periodic dielectric constant. This is the theory followed by Batterman and Cole [38] and part of the formulation I will use follows from this paper. Ewald's and Laue's theories have been proved to be equivalent if the same physical model is chosen for the electromagnetic resonators, *i.e.* point dipoles or atoms [42].

The problem, as stated by Laue, is to solve Maxwell's equations in a medium with a periodic dielectric constant. The dielectric susceptibility in such a medium is defined as

$$\chi(\mathbf{r}) = 1 - \frac{r_e \lambda^2}{\pi V} \sum_{\mathbf{h}} F_{\mathbf{h}} e^{-2\pi i \mathbf{h} \cdot \mathbf{r}}. \quad (2.8)$$

$F_{\mathbf{h}}$ are the complex and wavelength dependent structure factors, defined as:

$$F_{\mathbf{h}} = \sum_n (f + \Delta f' + i \Delta f'')_n e^{2\pi i \mathbf{h} \cdot \mathbf{r}_n} \quad (2.9)$$

where f is the atomic scattering factor, $\Delta f'$ and $\Delta f''$ are the Hönl corrections to the atomic scattering factor and are necessary to include the effects of anomalous dispersion, \mathbf{r}_n is the position of atom n and the summation is over all atoms in the unit cell.

In order to solve Maxwell's equations, we use as *Ansatz* for the electric and magnetic fields a sum of triply periodic plane waves (Bloch waves):

$$\mathbf{A} = e^{2\pi i \mathbf{k}_0 \cdot \mathbf{r}} \sum_{\mathbf{h}} \mathbf{A}_{\mathbf{h}} e^{2\pi i \mathbf{h} \cdot \mathbf{r}} \equiv \sum_{\mathbf{h}} \mathbf{A}_{\mathbf{h}} e^{2\pi i \mathbf{k}_{\mathbf{h}} \cdot \mathbf{r}} \quad (2.10)$$

where \mathbf{A} can be one of the four fields (E, D, B or H). The two definitions are equivalent if we consider that $\mathbf{k}_{\mathbf{h}} = \mathbf{k}_0 + \mathbf{h}$, but they give two explicit views:

- sum of plane waves with periodically modulated amplitude
- wavefield of infinite plane waves with different wavevectors $\mathbf{k}_{\mathbf{h}}$

By solving Maxwell's equation with this Ansatz, we obtain for the electric field \mathbf{E}

$$\frac{K^2 \mathbf{E}_m - \mathbf{k}_m^2 \mathbf{E}_{m[\perp \mathbf{k}_m]}}{K^2} + \sum_n P^{mn} \chi_{m-n} \mathbf{E}_n = 0 \quad (2.11)$$

that is a homogeneous system of equations of infinite order. The m and n are two reciprocal lattice points, \mathbf{k}_m are the wavevectors in the crystal, K is the wavevector in the vacuum, $\mathbf{E}_{m[\perp \mathbf{k}_m]}$ is the component of \mathbf{E}_m perpendicular to \mathbf{k}_m and P^{mn} is the amplitude polarization factor defined as the scalar product of the polarization unit vector e_m and e_n .

The system of infinite equations has non-trivial solutions if and only if the determinant is equal to zero. It is possible to make some qualitative considerations in order to reduce the number of equations to a finite number:

2. THEORETICAL BASIS

- the second part of the system of equations is approximately constant (due to the conservation of energy)
- $\mathbf{E}_{m[\perp \mathbf{k}_m]}$ is, to a good approximation, equal to \mathbf{E}_m
- if $K^2 \approx k_m^2$ then this implies that \mathbf{E}_m is large

With these simple considerations, it appears clear that only waves with wavevectors (reciprocal space points) that end close to the Ewald sphere are strong waves.

In the case of X-rays with not too high energies and/or not for crystals with large cell parameters like protein crystals, the radius of the sphere is quite small and by consequence often only two lattice points are close to the Ewald sphere. In this case, the system of equations becomes of order two, and the indices m and n take the value o (for the direct beam direction) and h (for the diffracted beam)

$$\begin{cases} [K^2(1 + \chi_o) - k_o^2]E_o + K^2 P^{oh} \chi_{\bar{h}} E_h = 0 \\ K^2 P^{oh} \chi_h E_o + [K^2(1 + \chi_o) - k_h^2]E_h = 0 \end{cases} \quad (2.12)$$

where P^{oh} is the polarization factor and is equal to 1 for electric vectors perpendicular to the plane of incidence (σ polarization) and $\cos 2\theta_B$ for electric vectors parallel to the plane of incidence (π polarization). Imposing the condition that the determinant needs to be equal to zero to obtain non-trivial solutions, we obtain the *dispersion relation*

$$(k^2 - k_o^2)(k^2 - k_h^2) = K^4 (P^{oh})^2 \chi_h \chi_{\bar{h}} \quad (2.13)$$

where $k = K^2(1 + \chi_0)$ is the average wavevector in the material. The solution of 2.13 is a complex surface in reciprocal space. A section of the real part of this complex surface is shown in fig.2.4, plotted in red. The points o and h are reciprocal lattice points, and the vector \mathbf{h} is the reciprocal lattice vector. In all the dispersion surface drawings I will consider only the σ polarization, being the synchrotron radiation σ polarized in the plane of the orbit.

The considerations so far apply to an infinitely extended crystal. For a finite crystal we have to apply boundary conditions for the wavevectors and for the amplitudes. For the wavevectors, the continuity of the tangential components is required; the boundary condition for the amplitudes will be discussed later on, sec.2.2.2.3.

The continuity of the tangential components of the wavevectors can be graphically represented by plotting on the dispersion surface fig.2.4 the vector normal to the surface of the crystal n_e passing through the excitation point M, which is the common extremity of the incident and diffracted wavevectors in vacuum. This vector intersects the dispersion surface at four points, called *tiepoints* which are indicated by A_1 to A_4 in fig.2.4. The intersections of the circles with radius K (wavevector in the vacuum) and k (average wavevector in the medium) are called Laue (La) and Lorentz (Lo) points respectively.

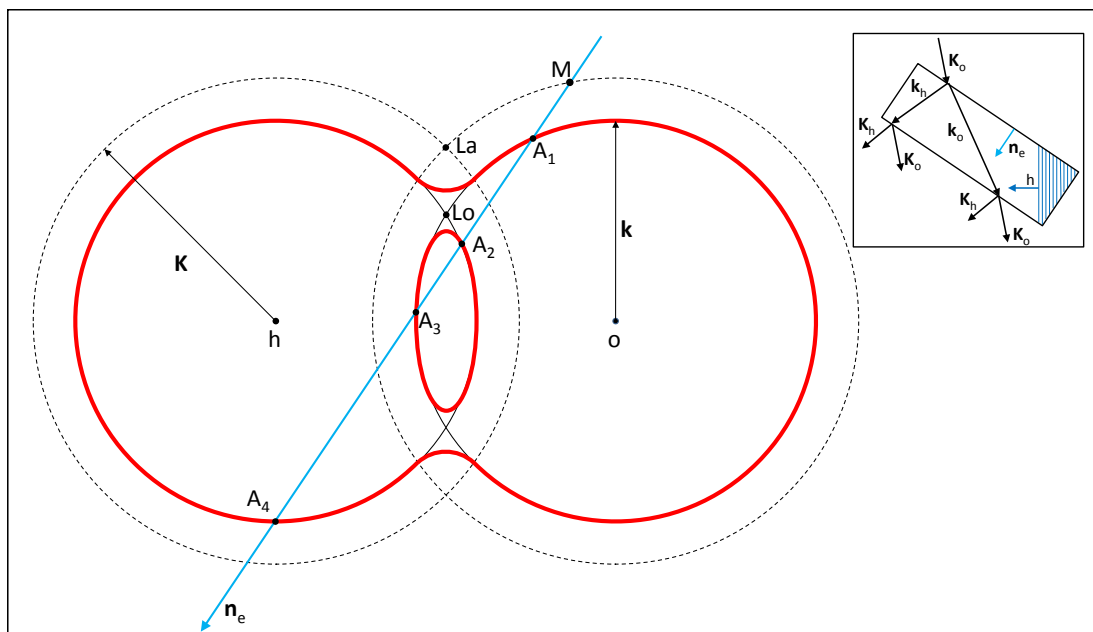


Figure 2.4: Section of the real part of three dimensional complex dispersion surface for the two beam case and one polarisation. M is the excitation point, A_1 to A_4 are the tiepoints. In the inset: direct space representation.

The only wavefields that may be strong are the whose tie points are close to the Lorentz point. It is possible to make an approximation, *i.e.* to ignore all the terms above the second order in 2.13. These approximations are valid except for “extreme diffraction conditions” (grazing incidence, grazing exit diffraction, or Bragg angle close to 90°). With this approximation, the dispersion relation can be written as

$$\xi_o \xi_h = \frac{1}{4} K^2 (P^{oh})^2 \chi_h \chi_{\bar{h}} \quad (2.14)$$

2. THEORETICAL BASIS

where ξ_o and ξ_h are $(k - k_o)$ and $(k - k_h)$, respectively. This is a second order equation, and, in terms of the dispersion surface plotted in fig.2.4, is equivalent to considering only the tiepoints A_1 and A_2 , *i.e.* the solutions close to the Laue and Lorentz points. Fig.2.5, shows a close-up of this region. Due to the fact that the radius of the circles (spheres) is large compared to the difference between the wavevectors in vacuum and the average wave vectors in the material, it is possible to approximate them with straight lines (planes), indicated with T_h and T_o for the sphere of radius k . We can see that, in the two-beam case, each tiepoint corresponds to a wavefield, composed of two plane waves, one with wave vectors directed towards h and the other towards o . The dispersion surface consists of two branches: the one closer to the Laue point (the crossing point of the two spheres of radius the wavevector in the vacuum K) is often called the α branch, while the other, further from the Laue point is called the β branch.

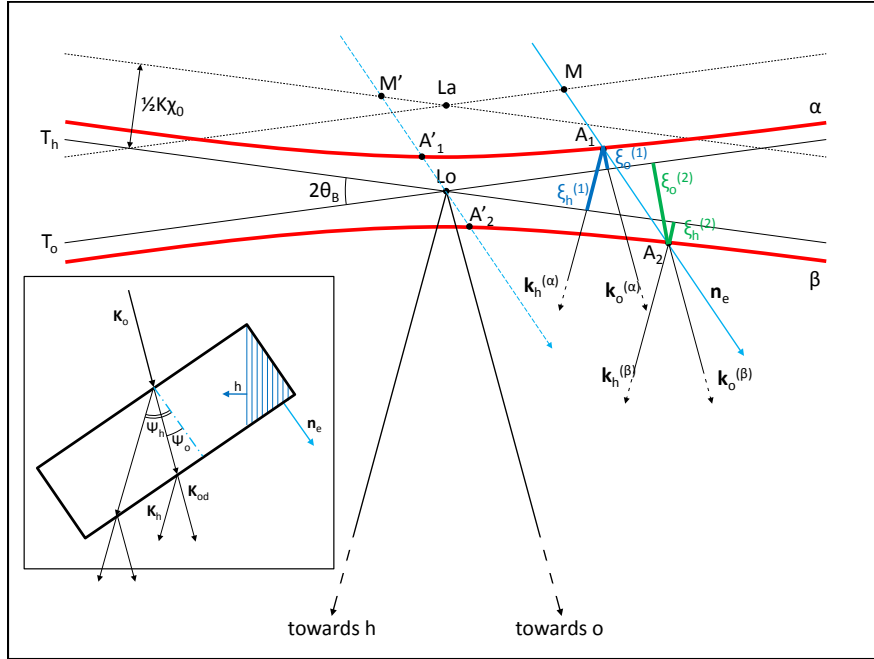


Figure 2.5: Zoom of the region around the Laue and Lorentz point, Laue case

These wavefields are coherent because they were all produced by one incoming plane wave. They will interfere inside the crystal producing two different interference effects. The first one is produced by wavevectors that have the same tiepoints but different directions. This interference will produce a standing wave field whose periodicity is

the lattice plane distance, when the Bragg condition within the crystal is fulfilled. Depending on the branch of the tiepoint, the maxima of the standing wave field are either between or on the lattice planes. This leads to large differences in the photoelectric absorption and results in the so-called *anomalous absorption*, discovered by Borrmann in 1941 [43] (therefore it is also called *Borrmann effect*) and explained by Laue in 1949, [44] and by the same Borrmann in 1950, [45].

The second interference effect is produced by wavefields with the same direction but different tiepoint. Since the relative length differences between the wavevectors are small ($\approx |\chi_o|K \approx 10^{-5}10^4\mu\text{m}^{-1}$), the beating frequency Λ of the interference field is of the order of tens of μm . This effect is called *Pendellösung effect*. The maximum value of Λ corresponds to the case that the surface normal passes through the Lorentz point, shown in fig.2.5 with the dashed arrow passing through M' (since in this case the length differences will be the smallest). This value is called *Pendellösung distance* Λ_0 and is defined as

$$\Lambda_0 = \frac{\lambda\sqrt{\gamma_o|\gamma_h|}}{P\sqrt{\chi_h\chi_{\bar{h}}}} \quad (2.15)$$

γ_h and γ_o are the cosines of the angles Ψ_h and Ψ_o (see the inset in fig.2.5) defined between the normal to the surface and the diffracted and incident wavevectors respectively. It is possible to show that γ_h and γ_o are equal to

$$\gamma_o = \sin(\alpha + \vartheta_B) \quad \gamma_h = \sin(\alpha - \vartheta_B) \quad (2.16)$$

where α is the angle between the diffracting lattice planes and the surface of the crystal and is called *asymmetric angle*. It is equal to zero for symmetric Bragg case and 90° for the symmetric Laue case.

The Pendellösung distance Λ_0 is also used to distinguish the range of applicability of the kinematical theory of diffraction by introducing the parameter $A = \pi t/\Lambda_0$, where t is the thickness of the crystal. The approximations used in the kinematical theory hold in the case $A \ll 1$, *i.e.* thin crystal.

2.2.2.1 Bragg and Laue cases

In the coplanar diffraction one distinguishes between two main scattering geometries:

2. THEORETICAL BASIS

the Bragg case (or reflection geometry), where the diffracted beam exits from the entrance surface;

the Laue case (or transmission geometry), where the diffracted beam is directed towards the inside of the crystal and it exits from the opposite surface.

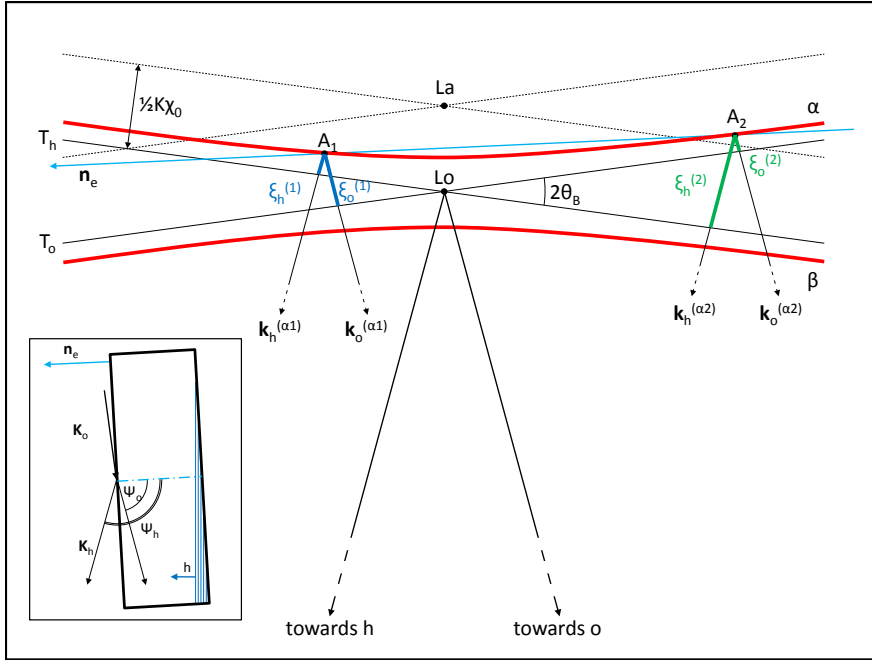


Figure 2.6: of the region around the Laue (La) and Lorentz (Lo) points, Bragg case.

By comparing fig.2.5 and fig.2.6 it is evident that one of the main difference between the two geometries is that, in the Bragg case, only wavefields with tiepoints on the same branch of the dispersion surface are excited at a particular angular position, while in the Laue case the excited wavefields have their tie-points on both dispersion surfaces. One of the consequences of this is that, for the Bragg case, there is a range of excitation points such that there is no intersection of the normal to the surface with any of the real part of the dispersion surfaces. This implies an imaginary solution resulting in an *interference total reflection range*. The width of the total reflection range is

$$w_h = \frac{2|P|\sqrt{\chi_h\chi_h}}{\sin 2\theta_B} \sqrt{\frac{|\gamma_h|}{\gamma_o}} \quad (2.17)$$

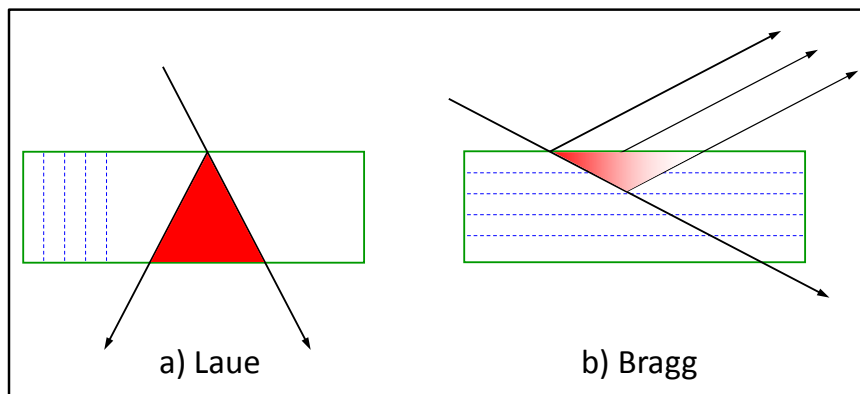


Figure 2.7: Areas of influence in the Laue and Bragg geometries, symmetrical cases.

and its real part is often called the *Darwin width*. Another consequence of the different geometries is the different *area of influence* [46], see fig.2.7. An X-ray beam from a point (or line) source impinges on the crystal. The intensity which is diffracted outside the crystal is influenced by every point inside the area shown in red. In the Laue case, this is the whole Borrmann triangle. In the Bragg case the situation is slightly more complicated; the area is in good approximation determined by the penetration depth (in the direction perpendicular to the surface) and by the width of the first maximum of the influence function of diffraction (in the parallel direction).

The penetration depth is the depth at which the intensity inside the crystal falls to $1/e$ of the incoming intensity. In Bragg diffraction, this is a function of $\Delta\theta$ (the difference between the angle of incidence and the Bragg angle) and is plotted in fig.2.8 for a Si 111 symmetric reflection, $E= 14.413$ keV. For angles far away from the interference total reflection range, the penetration depth tends asymptotically towards t_{abs}

$$t_{\text{abs}} = \frac{2}{\mu_0 \left(\frac{1}{\gamma_0} + \frac{1}{\gamma_h} \right)} \quad (2.18)$$

which is controlled only by the linear absorption coefficient μ_0 and by the geometry. In the region of interference total reflection, the absorption is dominated by extinction. In the middle of this region, it assumes the smallest value, and is equal to

$$t_{\text{ext}} = \frac{\Re\Lambda_0}{2\pi} \quad (2.19)$$

2. THEORETICAL BASIS

where Λ_0 is the Pendellösung length defined in 2.15 (in the Bragg case it is also called *extinction distance*).

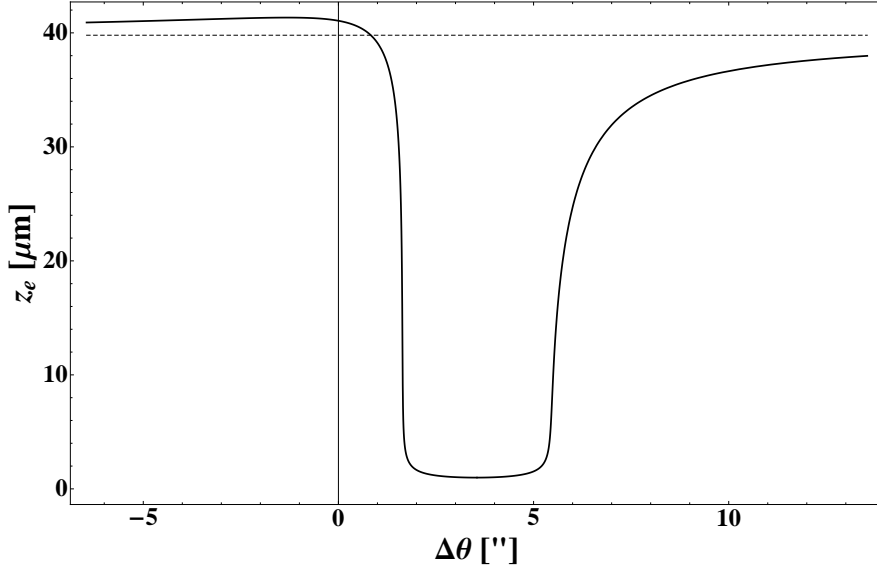


Figure 2.8: Penetration depth z_e in a Si111 crystal at 14.413 keV in a symmetric reflection geometry. The dashed horizontal line shows the penetration depth due to absorption, the vertical one the position of the kinematic Bragg angle. In the Bragg range the penetration depth is dominated by extinction.

As a result of anomalous transmission, the curve is asymmetric. The absorption is larger in the higher angle region than in the lower angle region. Even though the experiments carried out by Borrmann were in transmission geometry the physics behind them is the same in the reflection case. The lower angle side of the curve is produced by wavefields that belong to the α branch of the dispersion surface, whilst the higher angle side are created by the β branch and which undergo anomalous absorption.

2.2.2.2 Asymmetric reflections

From formula 2.17, it is possible to see that one of the possible ways to act on the width of the reflection is to change the ratio between the direction cosines. The asymmetry factor b is defined as as

$$b = \frac{\gamma_h}{\gamma_o} \quad (2.20)$$

By comparing the insets in fig.2.5 and fig.2.6 it is possible to see that γ_o is always positive whereas γ_h is positive in the Laue case but is negative in the Bragg case. In the case of the symmetric reflections, the value of b is either $+1$ or -1 . Consider now an asymmetric Bragg case in grazing incidence, *i.e.* the angle between the incoming beam and the surface is smaller than the angle between the diffracted beam and the surface (the inverse result would be obtained for a grazing exit case).

The dispersion surface for such a geometry is shown in fig.2.9. In the case of a divergent monochromatic wave with divergence w_o , the diffracted wave will have a divergence of w_h . The relationship between the two divergences will simply be:

$$w_h = b w_o \tag{2.21}$$

The Liouville theorem tells us that phase space is conserved. Therefore, if we consider the incoming beam to have a finite size L_o , then the size of the diffracted beam must be such that $w_o L_o = w_h L_h$ which implies that $L_h = \frac{L_o}{b}$

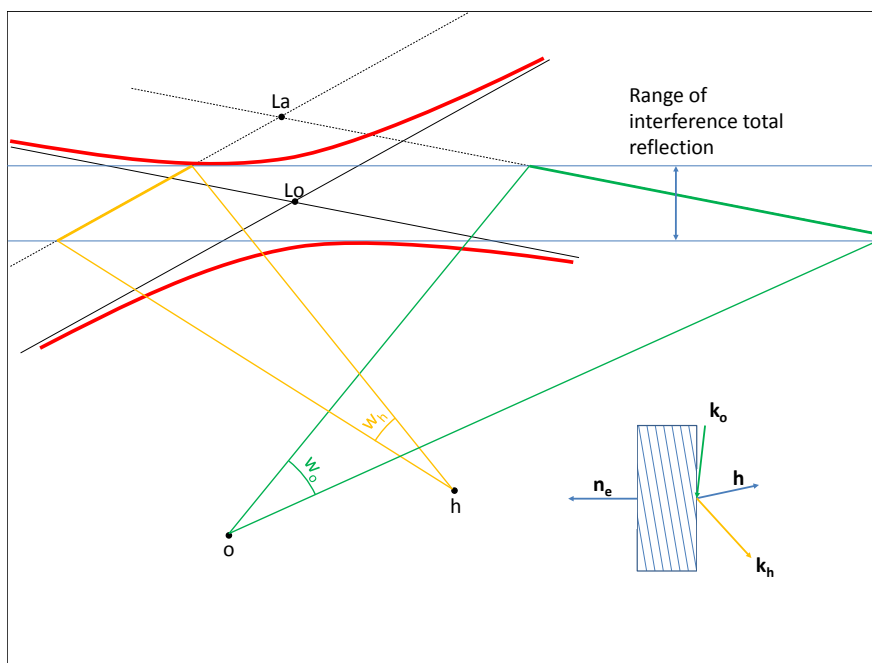


Figure 2.9: Section of the real part of a three dimensional complex dispersion surface for the two beam case, asymmetric reflection. In the bottom right, a sketch of an asymmetric reflection in real space.

2. THEORETICAL BASIS

This property of asymmetric reflections is very important and will be used in the rest of the thesis, *e.g.* to reduce the angular instrumental function at ID18, 3.1 or to obtain X-ray topographs in the quasi-plane wave approximation 4.2.2. Nevertheless, equation 2.21 is an approximation valid only for monochromatic waves. In the real case of polychromatic radiation there is an additional term to be considered. $\Delta\theta_{\text{out}}$ is defined as the divergence of the diffracted beam and $\Delta\theta_{\text{in}}$ as the divergence of the incoming beam. The relation between the two is given by the following formula:

$$\Delta\theta_{\text{out}} \approx \frac{\gamma_o}{\gamma_h} \Delta\theta_{\text{in}} + \frac{\Delta\lambda}{\lambda} \frac{(1 - \gamma_h^2)^{\frac{1}{2}} - (1 - \gamma_o^2)^{\frac{1}{2}}}{\gamma_h} \quad (2.22)$$

From this formula and from the definition of the direction cosines 2.16 it is possible to see that, in the case of polychromatic radiation, there is always an increase of the divergence due to the contribution of the second term in the equation, except in the symmetric Bragg case where this term is zero.

This also has an important consequence for coherence-preservation optics. With only one crystal, the only way not to increase the divergence of the beam, and therefore not to diminish the coherence of it, is by using symmetric Bragg reflections. With any other geometry, it is necessary to use more than one crystal in a non-dispersive configuration in order not to spoil the coherence of the beam.

Concerning the penetration depth in the case of asymmetric reflections, there will be two different asymptotes for the lower and higher angle sides of fig.2.8. For example, for grazing incidence geometry, the penetration depth will be smaller at lower incidence angles and greater at higher incident angles, and vice-versa for grazing exit.

2.2.2.3 Reflectivity curves in Bragg case

The boundary conditions for the wavevectors allow fixing the possible wavefields excited by the incoming beam. By introducing the boundary conditions for the electric fields it is possible to determine the absolute values of the intensities of the diffracted and transmitted waves, and not only their ratios. The reflectivity curve of a crystal is defined as the ratio between the incident and the diffracted beam intensities. We will discuss only the Bragg case, since this is the geometry we used in the High Resolution Diffraction (see 4.2.1). For a plane and parallel crystal plate the boundary conditions at the two surfaces are the continuity of the tangential component of the electric field. Since the

index of refraction is very close to 1, it is possible to approximate the continuity of the tangential component with the continuity of the electric field vector itself. By imposing these boundary conditions it is possible to obtain the formula for the reflectivity curve, which is presented in the Zachariasen [36] (see also [47] for the complete derivation in the Laue case), but also in a slightly more compact form in [48]:

$$R_h(\Delta\theta) = \frac{|b|P^2|\chi_h|^2(\sin^2(av) + \sinh^2(aw))}{Q + U \sinh^2(aw) - V \sin^2(av) + \frac{1}{2}\sqrt{U^2 - |q|^2} \sinh |2aw| + \frac{1}{2}\sqrt{V^2 - |q|^2} \sin |2av|} \quad (2.23)$$

with

$$z = \frac{1-b}{2}\chi_0 + b \sin(2\theta_B)\Delta\theta \quad q = b\chi_h\chi_{\bar{h}} \quad v + iw = \sqrt{q + z^2}$$

$$a = \pi k_0 \frac{t_0}{\gamma_0} \quad Q = |q + z^2| \quad U = Q + |z|^2 \quad V = Q - |z|^2$$

where t_0 is the crystal thickness.

This formula is valid for any thickness of the sample. It is possible to obtain a simplified formulation by considering a semi-infinite crystal. By following [38, 49], we introduce the normalized angular coordinate η :

$$\eta = \frac{-b\Delta\theta \sin(2\theta_B) - \frac{1}{2}\chi_0(1-b)}{|P^{oh}|\sqrt{|b|}\sqrt{\chi_h\chi_{\bar{h}}}} \quad (2.24)$$

The term normalized angular coordinate come from the fact that, for these coordinates, the region of interference total reflection goes from -1 to +1.

$\Delta\theta_0$ is the complex refraction correction. This is the difference between the Bragg angle calculated with the kinematical theory and the middle of the reflection range and is defined by

$$\Delta\theta_0 = -\frac{\chi_0(1-b)}{2 \sin(2\theta_B)} \quad (2.25)$$

Only in the Laue symmetric case ($b=1$) the refraction correction is zero.

In a semi-infinite crystal the wavefields which propagate inside the crystal are absorbed before reaching the exit surface. In this approximation it is possible to neglect one wavefield and to obtain a simplified formula for the reflectivity curve

$$R_h = |b| \left| \frac{\chi_h}{\chi_{\bar{h}}} \right| \left| \eta \pm \sqrt{(\eta^2 - 1)} \right|^2 \quad (2.26)$$

2. THEORETICAL BASIS

where the signs are chosen in such a way that $R_h \rightarrow 0$ for $\eta \rightarrow \infty$. With this formulation it is very easy to understand what is happening to the reflectivity as a function of the normalized angular coordinate: for $|\eta| < 1$ the reflectivity curve, in the case of zero absorption, is exactly equal to one whilst $|\eta| > 1$ it decays to zero (for $|\eta| \gg 1$ it decays as $\frac{1}{\eta^2}$).

In fig.2.10 are presented examples of reflectivity curves for semi-infinite crystals in the case of zero absorption and in a “real” case, that is the 111 reflection of silicon at 14.413 keV.

Fig.2.11 shows a comparison between the reflectivity curves obtained using the general formula 2.24 and the approximated one for semi-infinite crystals, 2.26.

It is possible to see that increasing the thickness results in two effects: an increase in the period of the oscillations and a decrease of their amplitudes. In this particular case, for thicknesses larger than $500\mu m$, the calculations obtained using the two formulations are almost equivalent, with discrepancies that are of the order of 3×10^{-4} . Therefore, in the case of “thick” samples, *i.e.* the silicon crystals described in this thesis, the simpler formulation has been preferred whilst for the low absorbing diamonds the more general formulation has been used.

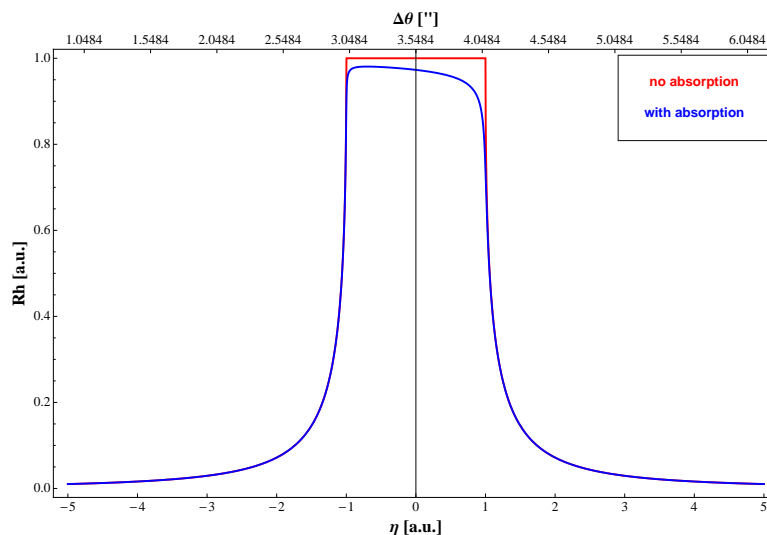


Figure 2.10: Comparison between reflectivity curves with and without absorption. The case with absorption is a Si 111 reflection at 14.413 keV. The x-scale on the bottom is the normalized coordinate range η whilst the one on the top is the angular deviation from the Bragg angle, $\Delta\theta$.

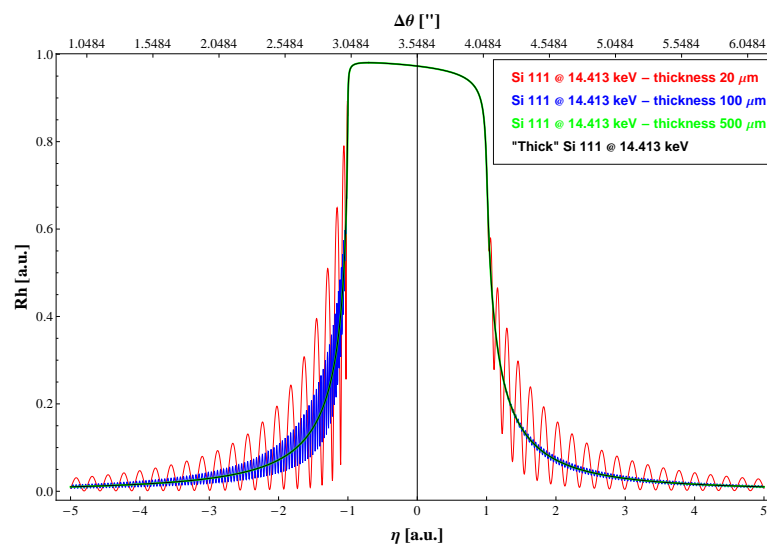


Figure 2.11: Reflectivity curves of various thicknesses calculated using equation 2.24 (red, blue, green) compared to the one for semi-infinite crystals, 2.26 (black).

2. THEORETICAL BASIS

2.3 Coherence

The notion of coherence is widespread in many areas of physics, from optics to quantum mechanics, from neutron to X-ray scattering [50]. I will briefly introduce here the main concepts of coherence of light. A light source is said to be coherent if it has the possibility of forming interference fringes. This is possible if the phase difference of the electromagnetic field between all pairs of points inside a region is constant with time. In the case of *perfectly coherent* light, this region extends to the entire space. For *partially coherent* light, it has finite size. It is common to define two different coherence lengths that determine this region: the *longitudinal* and *transverse coherence lengths*, fig.2.12.

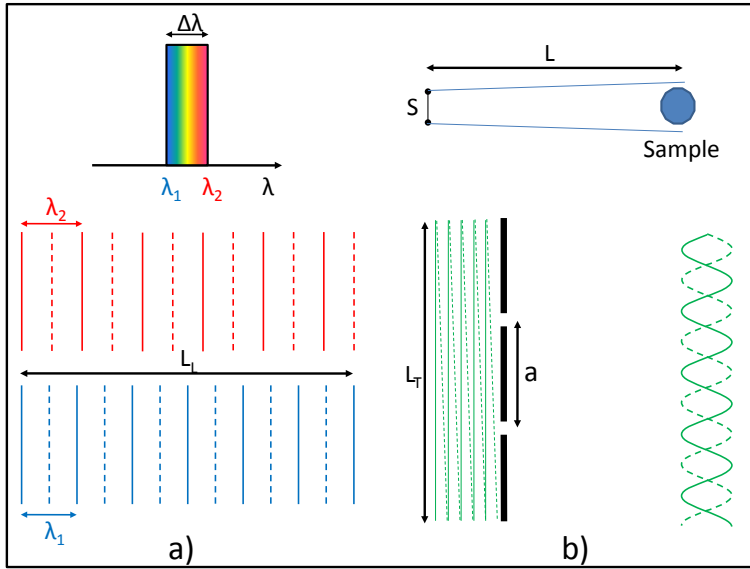


Figure 2.12: a) the longitudinal coherence, related to the bandwidth of the source; b) the transverse coherence, related to the angular source size of the source.

The longitudinal coherence length (also called temporal coherence length) is related to the non-monochromaticity of the source. Every source produces wave trains whose length is finite. This is equivalent (via Fourier transform) to saying that every source produces radiation which has a certain spectral bandwidth. The longitudinal coherence is defined as:

$$l_l = \frac{\lambda^2}{\Delta\lambda} \quad (2.27)$$

It is possible to measure the longitudinal coherence length by using, for example, a Michelson interferometer. If the optical path length between the two rays is equal to or larger than the transverse coherence length, no interference is recorded.

The transverse coherence length (also called spatial coherence length) is related to the fact that the source size has a finite extension in space. The transverse coherence length is defined as:

$$l_t = \frac{\lambda L}{S} \quad (2.28)$$

where L is the distance from the source and S is the source size. The effect of an extended source size is that, in a Young's double slit experiment, if the distance between the slits is equal to or larger than the longitudinal coherence length, no interference is recorded.

The coherence of light can also be treated, in a more general way, as the study of the randomness of the light through a more statistical approach. See [51] for a more complete description. It is possible to define the *mutual coherence function* as:

$$\Gamma_{12}(\tau) = \langle V_1(t + \tau)V_2^*(t) \rangle \quad (2.29)$$

where V_1 and V_2 represent the electromagnetic field at positions P_1 and P_2 , respectively, and τ is the time delay at which the correlation between the fields is calculated. If the two points coincide we obtain $\Gamma_{11}(\tau)$, that is the self-correlation function; if the delay τ is set to zero, $\Gamma_{11}(0)$ is simply the intensity I_0 . The normalized version of the mutual coherence function is the *complex degree of coherence*, which is defined as:

$$\gamma_{12}(\tau) = \frac{\Gamma_{12}(\tau)}{\sqrt{I_1 I_2}} \quad (2.30)$$

The quantity $\gamma_{12}(\tau)$ has values between zero and one. If it is equal to zero (or one), the radiation is *incoherent* (or *coherent*). For all other values, the radiation is *partially coherent*. If we assume the light to be quasi-monochromatic, *i.e.* the spectral bandwidth is small compared to the frequency of the radiation, we find that the visibility of the fringes is proportional to the complex degree of coherence. In the case $I_1 = I_2$, the visibility is equal to the complex degree of coherence. This is an important conclusion, which is used to determine the degree of spatial coherence of an X-ray beam after an optical element, by using either the Talbot effect [14] or an interferometer based on refractive bi-lenses [15].

2. THEORETICAL BASIS

The wavefront can be perturbed by imperfections in the optical elements. For example, low quality beryllium windows [52] create speckles that deteriorate the wavefront [53]. Wang *et al.* [54] simulated the effect of roughness in beryllium window and measured a decrease of the spatial coherence for rms values above $0.15\ \mu\text{m}$. The requirements on the roughness become more stringent in the case of a mirror; due to the grazing angle of incidence, the maximum acceptable roughness is of the order of $0.15\ \text{\AA}$.

In the case of monochromator crystals, vibrations can cause an increase of the virtual source size. As an example, this has been measured by Diaz *et al.* [13] using a double-grating interferometer and comparing a channel-cut monochromator with a double crystal monochromator. The results showed that vibrations of the double crystal monochromator results in an increased effective source size.

In our analysis we decided to work with a simpler approach to coherence in diffraction, and we always separate the transverse and longitudinal coherence lengths. A more complete approach on the preservation of the coherence in diffraction was done by Yamazaki and Ishikawa [55]. It requires solving the linear time-dependent Takagi-Taupin equations the result obtained is that the temporal coherence and the spatial coherence of the beam mix in X-ray diffraction and that the coherence is modified in the direction of the diffraction vector.

Chapter 3

Experimental techniques

In this chapter I will present the X-ray experimental techniques used to characterize the different samples, basing myself especially on books written by the following authors: Bowen and Tanner [56], Authier, [37], Als-Nielsen and McMorrow [57], Daillant and Gibaud [58] and Holý, Pietsch and Baumbach [59]. Each technique has different characteristics, such as sensitivity to bulk and/or near-surface defects, local or integrated information, strain sensitivity etc. Therefore, the combined use of complementary techniques is very useful and results in a deeper understanding of the crystal quality.

3.1 High Resolution X-ray Diffractometry

3.1.1 Introduction

High Resolution X-ray Diffractometry (HRXRD) includes the measurement of *rocking curves* of a sample, *i.e.* the ratio of the diffracted and the incident intensities as a function of the angular deviation of the sample from the Bragg angle. The term high resolution is referred to the condition of having a small resolution area in the reciprocal space, *i.e.* a small divergence of the beam and a small spectral width. HRXRD is one of the standard methods of characterizing the quality of crystals. It is widely applied, for example, to the study of epitaxial structures of compound semiconductors, where performances of the devices are strongly correlated with the quality of the epilayers, *e.g.* GaAs and AlAs/GaAs on silicon [60] or $\text{Al}_x\text{Ga}_{1-x}\text{N}/\text{AlN}/\text{GaN}$ [61]. It has been demonstrated that in the case of large mismatch between the different layers it is possible to resolve the presence of a single buried monolayer [62].

3. EXPERIMENTAL TECHNIQUES

In our case, we used HRXRD to characterize the quality of crystals foreseen for use as X-ray optical elements. We assume that the presence of defects in the crystals (or on their surfaces) gives rise to a broadening of the rocking curve. This broadening may be well below an arc second. We had two different situations. In the first we wanted to study the quality of the surface of silicon crystals after different surface treatments whilst in the second we were interested in the contributions to the rocking curve from bulk and surface defects in synthetic diamonds.

In the first case, we used an X-ray tube with a simple double crystal configuration using an asymmetrically cut silicon monochromator (to obtain a good collimation) was enough to obtain the desired resolution. The obtained results will be shown in chapter 5.

For the second condition, due to the impossibility of having a perfect reference diamond crystal to be used as monochromator, an extraordinary effort was made to reduce the instrumental function as much as possible, both in angular and in wavelength spread. This has been achieved by using the Inelastic Scattering beamline ID18, 3.1. The energy of the X-ray beam was 14.413 keV, which corresponds to the ^{57}Fe nuclear resonance transition.

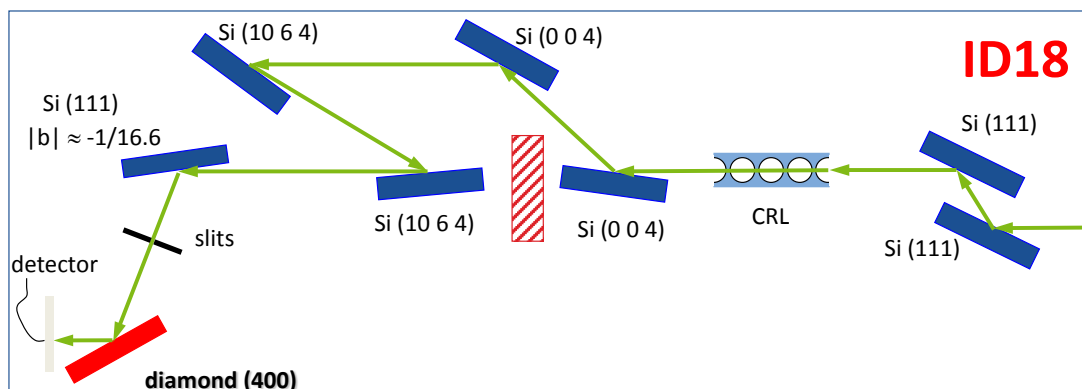


Figure 3.1: ID18 experimental configuration used for High Resolution X-ray Diffractometry.

We assume the experimental rocking curve of a high quality single crystal to be the result of the convolution of three curves, see fig.3.2: the *reflectivity curve* defined in 2.2.2.3, the *instrumental broadening/apparatus function*, which takes into account all contributions from the optical elements that condition the beam impinging on the

sample and the *broadening due to defects*, which is the effect produced by the presence of bulk and surface defects. Thanks to the very high monochromaticity of the beam delivered at ID18 ($\frac{\Delta\lambda}{\lambda} \approx 10^{-7}$), we can concentrate only on the angular convolutions, ignoring the wavelength spread.

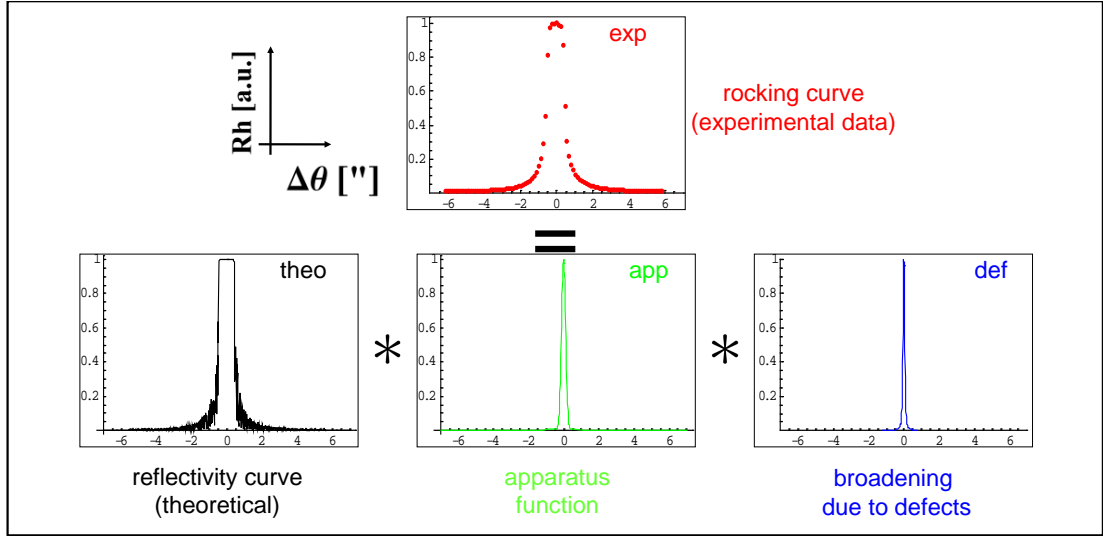


Figure 3.2: Pictorial example of a rocking curve assumed to be the convolution of three distinct curves: the reflectivity curve, apparatus function and a function describing in an integral way the broadening due to defects. Experimental data were obtained on a high quality IIa HPHT crystal, 400 reflection, E=14.413 keV.

Therefore, in order to be able to isolate the function describing the broadening due to defects, it is necessary to determine the apparatus function with high precision.

3.1.2 Determination of apparatus function.

It is possible to describe the effect of the instrumental broadening with a convolution integral:

$$e(t) = \int_{-\infty}^{\infty} f(\tau)i(t - \tau)d\tau \stackrel{\text{def}}{=} (f * i)(t) \quad (3.1)$$

The function $f(t)$ represents the theoretical function one is attempting to measure; the function $e(t)$ is the measured curve, that is a weighted average by the function $i(t)$ of the true curve $f(t)$. The instrumental broadening can be either calculated or measured experimentally. We decided to follow both methods and to compare the

3. EXPERIMENTAL TECHNIQUES

results obtained. The calculation of the instrumental broadening has been made by using a program written by Franco Cembali, an external collaborator. This program calculates the instrumental broadening by taking into account all the optical elements present at the beamline (slits, monochromators, Compound Refractive Lenses - CRL). In fig.3.3 the calculations of the angular instrumental function after each crystal are plotted.

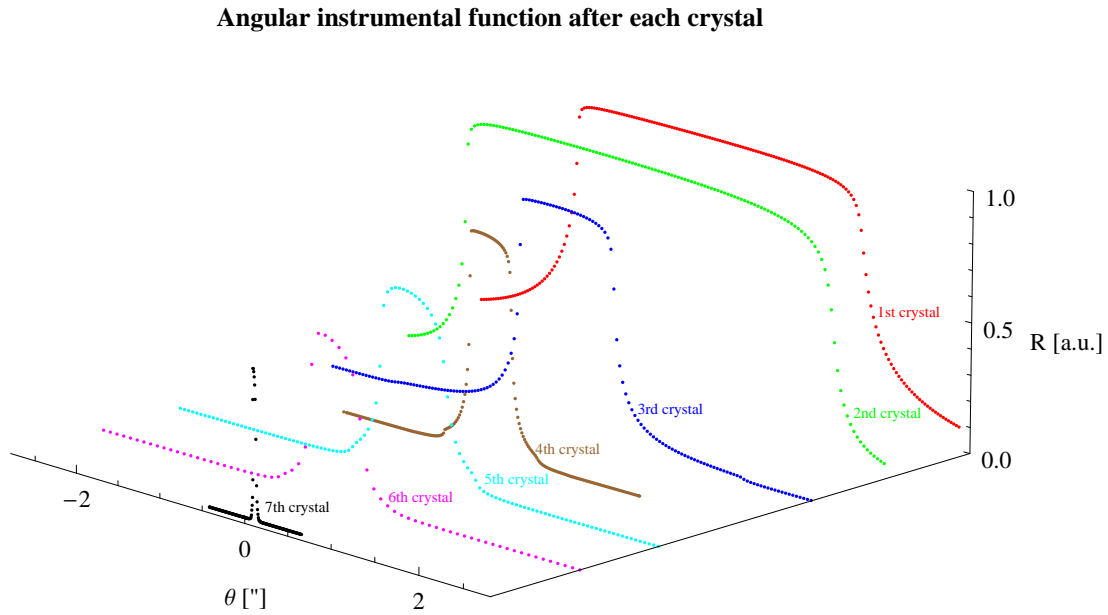


Figure 3.3: The angular instrumentation function calculated after each crystal of the configuration shown in 3.1.

The curve obtained (corresponding to the curve after the 7th crystal in figure 3.3) has a FWHM of 0.037 arc seconds. It is important to highlight the fact that this estimation is done without taking into consideration any imperfection in the system. It is therefore to be considered as a theoretical lower limit of the real instrumental function.

In order to measure experimentally the apparatus function it would be necessary to sample the incoming beam with a δ -shaped curve, obtaining in response the instrumental function itself, as it is possible to see from 3.1 and from fig.3.2. This is of course impossible, but it is possible to approach the situation. Firstly, one has to use a crystal (analyser) the perfection of which is such that we can ignore the broadening due to defects. Secondly, by measuring the incoming beam with different reflections with de-

creasing Darwin widths of that “perfect” sample, in our case of silicon, it is possible to approach step by step a δ function. The analysis for this experimental determination of the instrumental function has been developed in two independent ways: in the first, the instrumental broadening has been modelled by a curve with free parameters and fitted; in the second, direct deconvolution algorithms have been used. One of the most serious problems in both methods has been simply the fact that the instrumental broadening by the optical system installed at the beamline ID18 is indeed very small, thanks to its high beam collimation and energy resolution. To extract tiny broadenings from a series of measured rocking curves is quite a complicated task.

3.1.2.1 Model and fit approach

The instrumental function has been described by the sum of a Gaussian and a Lorentzian function (similar to a pseudo Voigt, often used in the description of the diffraction peak shape, for example by Ida *et al.* [63]):

$$\text{app}(\Delta\theta) = A_L \frac{2}{\pi} \frac{\omega^2}{4\Delta\theta^2 + \omega^2} + A_G \frac{1}{\sqrt{2\pi}\sigma} e^{-\frac{\Delta\theta^2}{2\sigma^2}} \quad (3.2)$$

where A_L and ω are the area and the FWHM of the Lorentzian, respectively, and A_G , σ are the area and standard deviation, respectively, of the Gaussian.

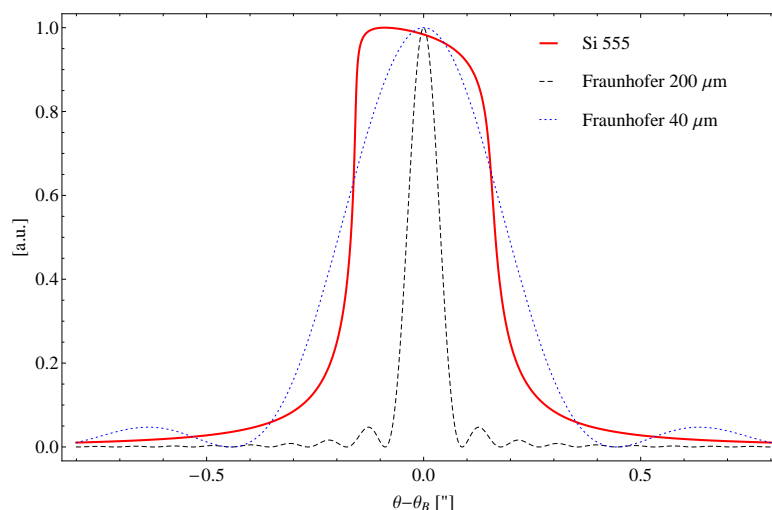


Figure 3.4: Comparison of the Si 555 reflectivity curve, $E=14.413$ keV, with the Fraunhofer diffraction from rectangular slits opened respectively $200 \mu\text{m}$ and $40 \mu\text{m}$.

3. EXPERIMENTAL TECHNIQUES

The code was written in Mathematica [64] and uses the Global Optimization 6.0 package (Loehle Enterprises, Naperville, IL, USA) to minimize the difference between experimental data and the convolution of the instrumental function with the theoretical reflectivity. Due to the large number of convolution integrals required in this procedure, the code is quite slow and has problems in dealing with curves with more than ≈ 250 points. The first result we obtained during the analysis of the data was the dependence of the apparatus function on the size of the vertical slits. The Fraunhofer diffraction from the slits becomes important in such a high resolution experiment of sub-arcseconds distortions, fig.3.4.

The first attempt to solve this problem was to include the Fraunhofer diffraction from the slits as an additional broadening of the theoretical reflectivity curve. The results were not satisfactory, above all for slits opened less than 100 μm . We supposed that other effects (such as diffuse scattering, small angle scattering or not ideal shape profile of the slits) dominate for narrow apertures. Since these effects are more complicated to simulate, we decided to include the diffraction from the slits into the apparatus function. So we worked with three different apparatus functions for the three slits size used: 700 μm , 200 μm and 40 μm .

Another problem was that different sets of parameters may give similar goodnesses of fit. An example of this is visible in fig.3.5; three fitting functions, shown in fig.3.5.b) (together with the respective parameters), fit equally well the experimental data collected, fig.3.5.a) (the inset shows a zoom in the region indicated). This problem was solved by comparing the results obtained for the different fit parameters with a broader scan (in this case ± 25 arc seconds), fig.3.5.c),d) and e) which could not be analyzed directly due to the limit on the maximum number of points the fitting code accepts. In this particular case, the best solution is the one shown in fig.3.5.e), corresponding to the blue fit parameters.

Finally, a series of instrumental broadening functions was obtained for the different reflections used, namely 111, 333, 444 and 555 symmetric Bragg reflections. By extrapolating the results obtained towards a “zero-width curve”, *e.g.* for the 200 μm slits size 3.6, we obtained the final three instrumental broadening functions for the different vertical slits sizes used during the experiment, shown in fig.3.7.

3.1 High Resolution X-ray Diffraction

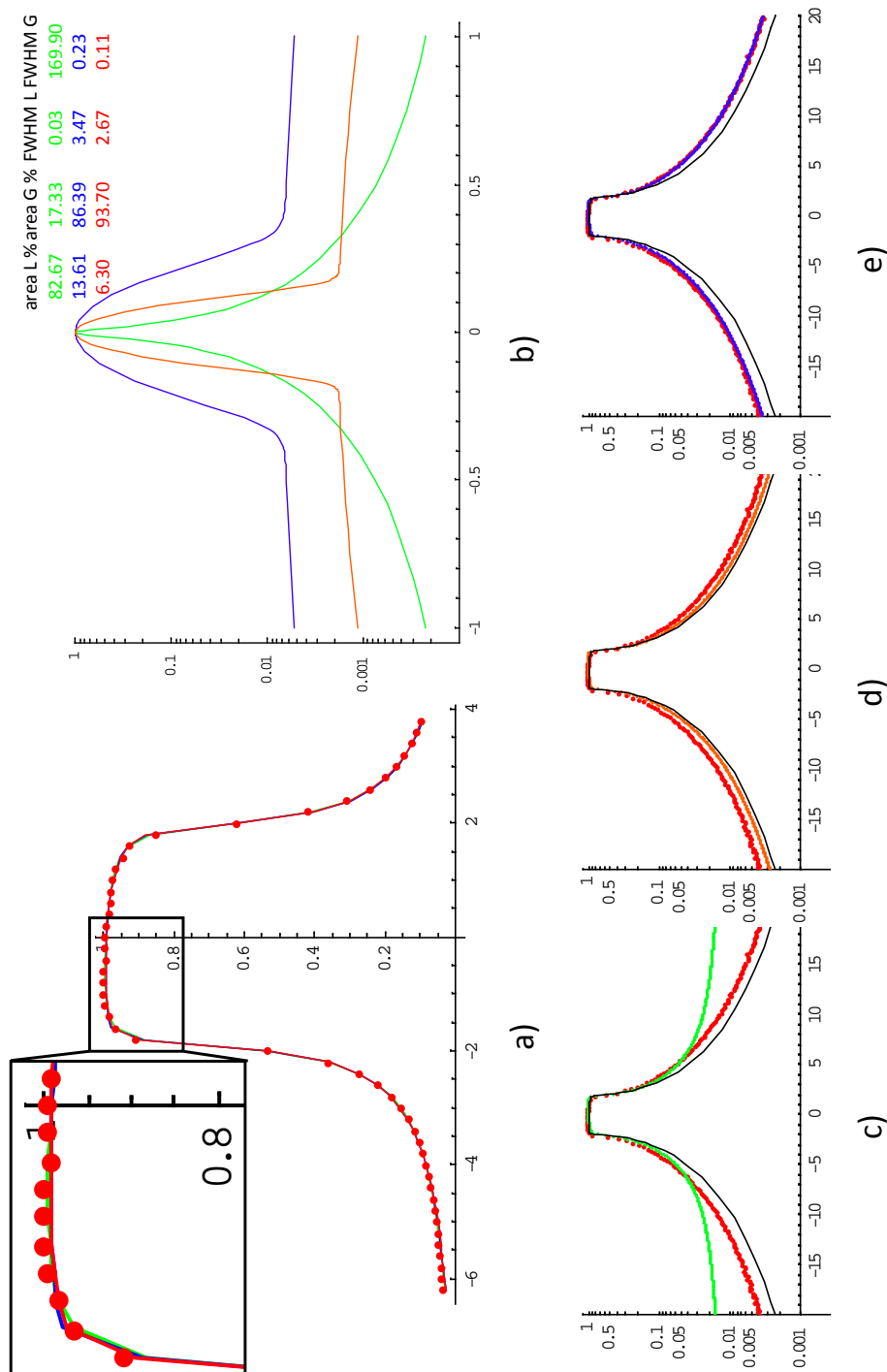


Figure 3.5: a) comparison between the experimental data (Si 111 reflection) with the results obtained from the convolution of the reflectivity curve with three different apparatus functions obtained using the fitting method. In the inset, zoom of the region indicated with a black rectangle, showing that the three solutions are equally good. b) the three apparatus functions, plotted on a log scale, together with the fit parameters of each one c),d),e) comparison between the experimental data collected on a broader range (± 25 arc seconds) with the three functions shown in b). The best results is obtained with the blue curve, as shown in e).

3. EXPERIMENTAL TECHNIQUES

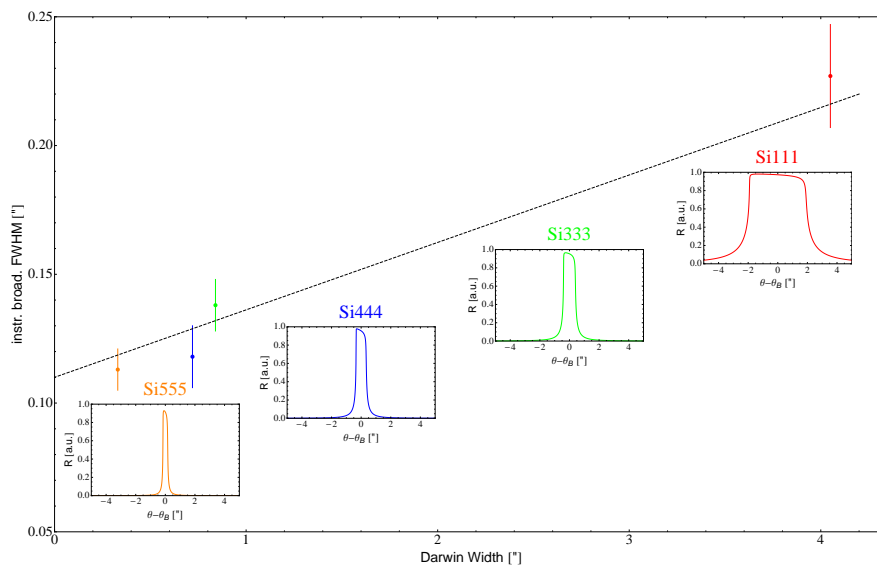
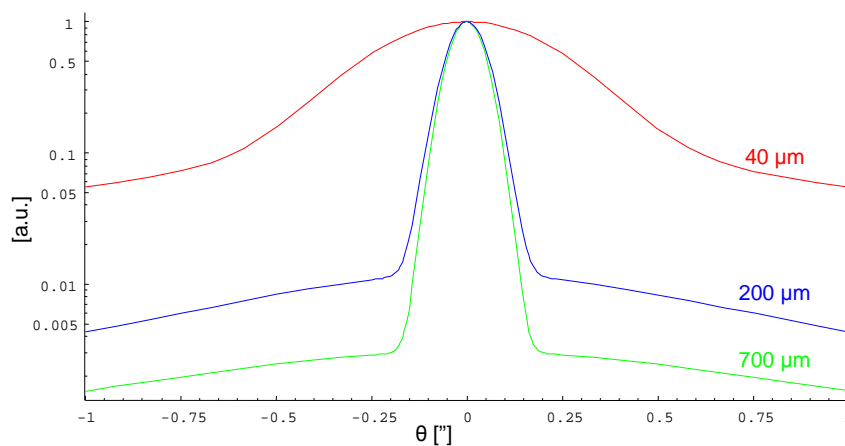


Figure 3.6: Extrapolation of the instrumental broadening towards a “zero width” curve, slits size 200 μm . The points represent the values of the FWHMs for the instrumental broadening corresponding to the different reflections (111, 333, 444 and 555).



	A_L	ω	A_G	σ	FWHM	FW20%M	FW2%M
700 μm	0.006	2	0.07	0.045	0.11	0.16	0.26
200 μm	0.008	1.5	0.035	0.05	0.12	0.18	0.31
40 μm	0.045	2.6	0.06	0.23	0.58	0.93	4.23

Figure 3.7: Plot of the final apparatus functions obtained for the three different vertical slits sizes, together with the fit parameters and the full widths at different heights (50%, 20%, 2%).

3.1.2.2 Direct deconvolution methods

A problem with every deconvolution algorithm is that, in general, equation 3.1 need not have any solution at all [65]. In fact, the presence of statistical noise in the experimental data makes the equation irreversible, and the deconvolution becomes an ill-posed problem. To overcome this problem approximations are always necessary. I wrote a code using Mathematica that uses two different algorithms: the Burger-Van Cittert algorithm, [66] and the Richardson-Lucy algorithm, [67, 68], in order to deconvolve the instrumental broadening. The theory of the two methods, together with some results and limitations, are presented in Appendix A.

3.1.2.3 Comparison of the results obtained.

In fig.3.8 the results obtained with all the different methods and for a slits size of 200 μm are presented. This is also the slits size that gave the best results when analyzing the

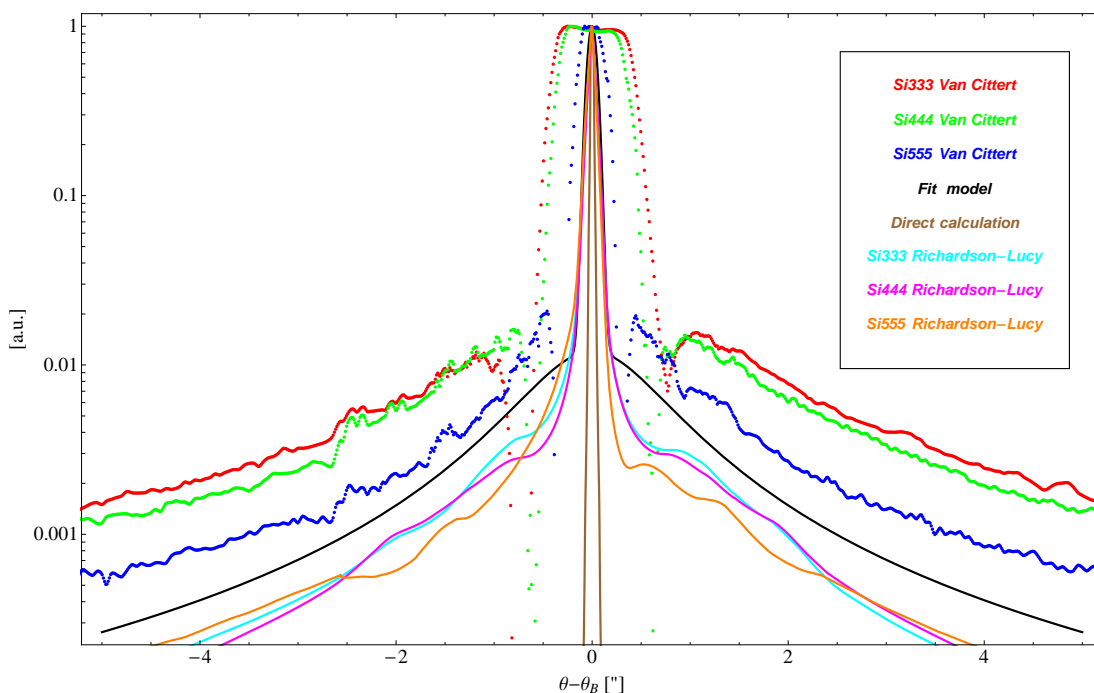


Figure 3.8: Comparison of the instrumental broadening functions obtained with the different methods.

diamond crystal. The reason for this is simply because for the wider slits the footprint

3. EXPERIMENTAL TECHNIQUES

on the sample was ≈ 1.5 mm for the 400 reflection and ≈ 3.4 mm for the 111 reflection, therefore measuring at the same time the high and low quality regions of the crystal. For the narrower slits, the Fraunhofer diffraction from the slits covers the “broadening due to defects” effects we are interested in measuring.

As discussed previously, the direct calculation of the instrumental broadening is the narrowest curve, giving a theoretical lower limits in the case no imperfections are present in the system. The results obtained with the Van Cittert deconvolution algorithm depend strongly on the different theoretical reflections, *i.e.* a much wider curve is obtained when deconvolving the Si 333 rocking curve respect to the one obtained from the Si 555. This effect is not present in the results obtained using the Richardson-Lucy algorithm, where the apparatus functions obtained are not influenced by the width of the reflectivity curve. Finally, the results obtained with the model-and-fit approach compare well with the direct deconvolution result, and therefore are the ones used for the rest of the analysis.

Recently we performed a last experiment in order to obtain an even more accurate estimation of the apparatus function. This was done by using a different energy (23.880 keV, corresponding to the nuclear resonance of ^{119}Sn) in order to be able to excite even higher order reflection, 777, 888 and 999 together with the quasi-forbidden 222 reflection. The idea behind the experiment was the same of the previous one, *i.e.* approaching a δ -shaped function in order to be able to record only the instrumental broadening function. The FWHM for the allowed reflections, 777, 888 and 999 are respectively 0.063”, 0.062” and 0.033” whilst for the 222 forbidden reflection I obtained a value of 0.025” by using the experimentally determined structure factor by Alkire *et al.* [69] of 1.456. Fig.3.9 shows the comparison of the experimental data obtained with the different reflections together with the apparatus function obtained for a slits size of 200 μm . This graph demonstrates that, even though the theoretical curves are narrower and narrower, the experimental rocking curve is almost constant, *i.e.* we are directly measuring the apparatus function. Moreover the agreement between the experimental data and the apparatus function determined previously is very good, considering that the experimental conditions for the two cases were not the same.

To conclude, we are confident that the apparatus function determination is accurate and will allow a correct estimation of the the broadening due to defects for the diamond samples.

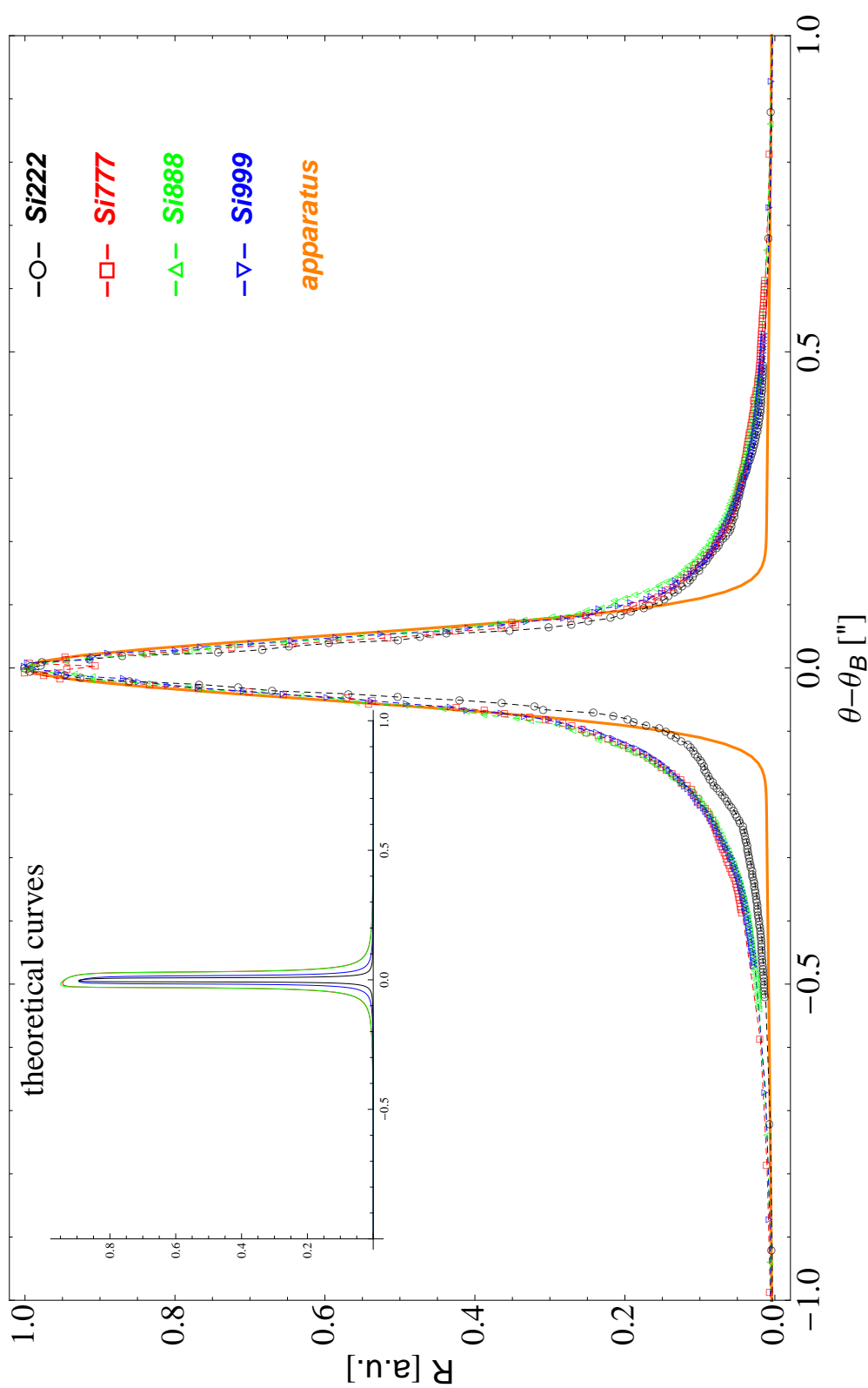


Figure 3.9: Comparison of the rocking curves obtained with high order reflections (777, 888 and 999) and with the 222 forbidden reflection together with the apparatus function estimated from the previous experiment.

3. EXPERIMENTAL TECHNIQUES

3.2 X-ray topography

X-ray topography is an imaging technique based on diffraction and described by the dynamical diffraction theory. It is used in the characterization of crystal defects and macroscopic deformations. The first topographic experiments were made in reflection geometry by Berg in 1931 [70] and Barrett in 1945 [71] and in transmission geometry by Ramachandran in 1944, [72], (who also was the first to use the name topography for this technique). Bond and Andrus [73] were the first to use a double crystal configuration followed by Lang [74], when for the first time individual dislocations became visible in X-ray topographs. It must be remarked that the name is somewhat misleading, because it suggests this technique to be surface sensitive (the Greek origin of the name is in fact topo-, “place”, and graphia, “writing”, and is often used to represent surfaces shapes and features), whereas it is often used to probe the bulk of a crystal. In fact, it is the topography of the crystal lattice planes that is examined. An alternative name for the technique is X-ray diffraction imaging.

A spatially extended X-ray beam, impinging on the crystal is diffracted and the diffracted beam/beams is/are recorded on a two dimensional detector (e.g. a photographic film or a CCD camera) giving a 2D image/images of the crystal.

Different X-ray topography techniques have been developed. It is possible to classify them depending on three basic elements [75]: 1) the source geometry and characteristics, together with the eventual optical elements (slits, other crystals, etc...); 2) the sample properties and geometry, *e.g.* transmission or reflection; 3) the detector, together with possible optical elements. We can define:

Limited beam techniques: the size of the incoming beam is reduced in order to avoid the overlap of too many Borrmann triangles (see 2.7) generated at the entrance surface of the crystal. As a rule of thumb the beam needs to be much narrower than the base of the Borrmann triangle, *e.g.* in the symmetrical Laue case, is equal to $2t \sin(\theta_B)$, where t is the thickness of the crystal. Typical values of 10 to 20 μm are used. The beam can be limited either in one or two directions, obtaining respectively *section* and *pin-hole* topographs. An advantage of these techniques is, in the case of section topography, the possibility of spatially separating on the detector intensities arising from different depths in the crystal. Moreover, a section topograph of a low absorbing perfect crystal will show Kato

fringes, [76] produced by the interference between the wavefields created from the two different branches of the dispersion surface. This is a manifestation of the Pendellösung effect explained in section 2.2.2 in the case of incoming spherical waves. The fringes are very sensitive to lattice distortion, as shown *e.g.* by Patel [77] in the study of oxygen precipitation in silicon. In the framework of this thesis, section topography was the technique used for the visualization of ferroelectric domains in chapter 6.

Extended beam techniques: the size of the incoming beam is larger than in the limited beam techniques. At a synchrotron the distance from the source to sample can be large, the size of the beam (especially at wiggler or bending magnet beamlines) can go up to few cm, *e.g.* at ID19 or BM05. In the laboratory, the size of the beam is small; one way to obviate this problem has been found by Lang, [78]. A narrow beam (typically of the order of 100-250 μm) impinges on the sample, which can translate synchronously with the detector. In this way, the image of the entire crystal can be recorded. This method is called *Lang or traverse topography*. The characterization of high quality crystals was done using extended beam techniques at different beamlines, (see chapters 4.2.2 and 5).

Integrated wave techniques the angular source size is larger than the width of the reflectivity curve of the crystal, defined in 2.17 and/or the energy bandwidth of the incident beam is larger than the Darwin width defined in energy scale, $w_h^\lambda = \lambda w_h \cot \theta_B$. Concerning the angular source size, in a laboratory source it is in general bigger than the angular acceptance of the crystal; at a synchrotron beamline, it could be smaller than the crystal acceptance *e.g.* at ID19 the divergence of the beam is ≈ 0.05 arc seconds. Regarding monochromaticity, in both laboratory and synchrotron configurations, it is possible to be in integrated wave conditions. Examples of integrated wave techniques are Lang topography, white beam topography, and in some cases, monochromatic beam topography.

Monochromatic plane wave techniques: contrary to integrated wave conditions, the angular source size and the energy bandwidth are smaller than the reflectivity curve width in angular and energy space respectively. Special effort is needed to obtain these conditions, but the strain sensitivity achieved is much higher

3. EXPERIMENTAL TECHNIQUES

compared to integrated wave techniques. Moreover, the quantitative analysis of monochromatic plane wave topographs is easier than for the integrated wave techniques.

After defining the different types of techniques, the sources of inhomogeneities in the images is now discussed. Defects inside the crystal produce long range strain fields which distort the perfect lattice structure. This leads to local differences in the diffracted intensity and consequently to “contrast” in the image at the detector. Following Baruchel and Härtwig [79] it is possible to distinguish three types of contrast:

Structure factor contrast due to differences in the phase or modulus of the structure factor. This contrast is fundamental to the visualization of ferroelectric domains in chapter 6;

Orientation contrast arises when different parts of the crystal are misoriented with respect to one another. If the misorientation in a given part is larger than the beam angular source size (or the equivalent wavelength spread is larger than the bandwidth of the incident beam), then the misoriented part will not satisfy the Bragg condition and will not diffract, and a loss of intensity is registered by the detector (fig.3.10a). If the wavelength spread of the incident beam is sufficiently large (*e.g.* white beam), then all misoriented parts will diffract, because there will always be a wavelength to fulfil the Bragg condition in the misoriented part. Consequently, differently oriented parts of the crystal will diffract in different directions. Thus, the images of these different crystal regions (*e.g.* different grains) may separate or overlap, if the sample to detector distance is large enough, leading to local losses or gains of intensity (fig.3.10b). This type of contrast can occur also around lattice defects like dislocations, as shown by Dudley *et al.* [80].

Extinction contrast is produced by the local variations of the scattering power, *e.g.* around a defect. In order to interpret this contrast it is necessary to use the dynamical diffraction theory for deformed crystal. The parameter that describes the effect of the distortion of the lattice on diffraction is the *effective misorientation* $\delta\theta$:

$$\delta\theta(\vec{r}) = \theta(\vec{r}) - \vartheta_B^{perfect} = -\frac{\lambda}{\sin 2\vartheta_B} \frac{\partial(\vec{h} \cdot \vec{u}(\vec{r}))}{\partial s_h} \quad (3.3)$$

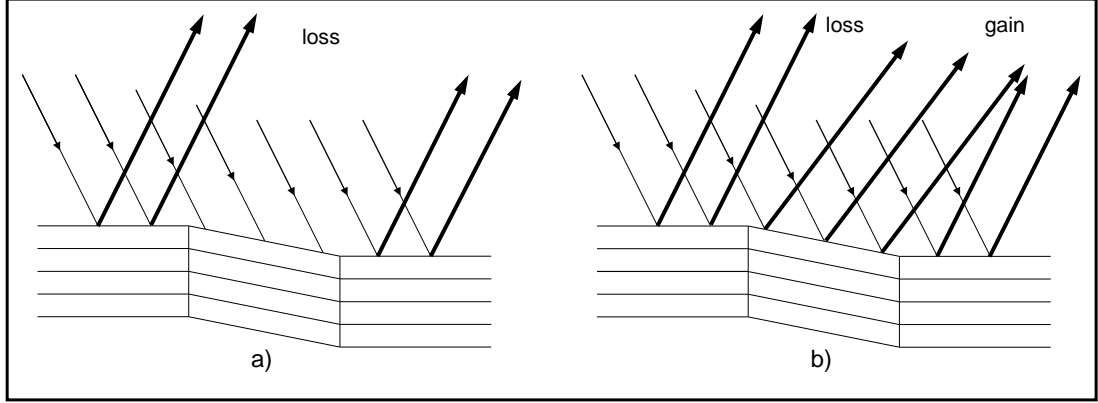


Figure 3.10: Misorientation contrast. a) the misorientation in the middle part is larger than beam divergence and/or equivalent wavelength spread b) the misorientation is smaller than beam divergence and/or equivalent wavelength spread

where \vec{h} is the undistorted reciprocal lattice vector, $\vec{u}(\vec{r})$ is the displacement field vector and $\partial/\partial s_h$ is the differentiation along the diffracted beam direction. It is the angular departure of the locally deformed part of the crystal from the Bragg angle of the reference perfect lattice. It is also possible to rewrite the effective misorientation as a function of the local variation in lattice parameter $\Delta d/d$ and of the rotation of the lattice planes $\Delta\varphi$ as:

$$\delta\theta = \frac{\Delta d}{d} \tan \vartheta_B + (n_t \cdot n_g) \Delta\varphi \quad (3.4)$$

where n_t and n_g are the unit vectors normal to the incidence plane and parallel to the defect misorientation axis, respectively. This equation permits the derivation of a powerful tool for characterizing defects, the *contrast extinction rule*. A defect whose displacement vector field is perpendicular to the diffraction vector gives no contrast on the image. It is possible to define three different types of images produced by the extinction contrast in the case of integrated wave (see fig.3.11):

- the *direct image*, consisting of additional intensity that originates from regions with an effective misorientation larger than the Darwin width of the perfect crystal, 2.17. It is visible under the conditions of integrated wave (or section topography) and low absorption ($\mu_0 t \lesssim 2$). It arises from the kinematical diffraction of the X-rays that are outside the wavelength range

3. EXPERIMENTAL TECHNIQUES

($\Delta\lambda/\lambda = \cot \theta_B w_h$) participating in the dynamical diffraction in the perfect crystal.

- the *dynamical image*, consisting of dips in the intensity. This is due to the disruption of the transmission created by the defect (it can be imaged as a shadow produced by the defect). This contrast is the predominant in case of high absorption ($\mu_0 t \gtrsim 6$), since the direct image is completely absorbed.
- the *intermediate image*, produced by the interference between the wavefields existing in the crystal and a new wavefield created by interbranch scattering in the region of the defect itself. This interference produces an oscillatory contrast. This contrast is visible only in the case of low and intermediate absorption ($\mu_0 t \lesssim 6$).

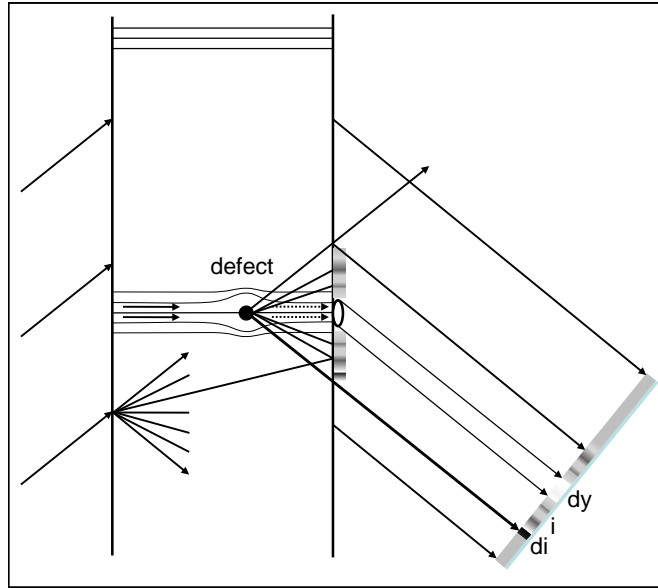


Figure 3.11: Extinction contrast: formation of the three types of image around a defect: (di) direct, (i) intermediate and (dy) dynamical images.

All the topography experiments in this thesis were carried out at synchrotron radiation sources. The properties of synchrotron radiation, such as high intensity, continuous spectrum, narrow angular collimation and small source size, opened new possibilities compared to conventional sources, see Tanner and Bowen [81] for a review. These include:

- shorter exposure time, allowing real time experiments, [82], [83],[84] and [85].
- the possibility of having larger sample-to-film distances whilst maintaining micrometer image resolution, allowing room for bulky apparatus such as cryostats [86],[87] and furnaces [88]. Moreover, the possibility of changing the sample-to-film distance gives the possibility of studying focusing/defocusing effects for dislocations [89], dynamic deformation such as vibrations [90] and static deformation, *e.g.* created in a bonded wafer [91]. I have also used this possibility to determine the bending radius of diamonds bent by femtosecond laser ablation [92].¹
- the very simple possibility of collecting more than one topograph at the same time in a short time, allowing *e.g.* the determination of the type of dislocations present in a crystal and the associated Burgers vector from one single exposure [93].

Two techniques using a wide and homogeneous beam are often employed for synchrotron X-ray topography: white beam topography (single crystal) and monochromatic beam topography (double crystal), 3.12.

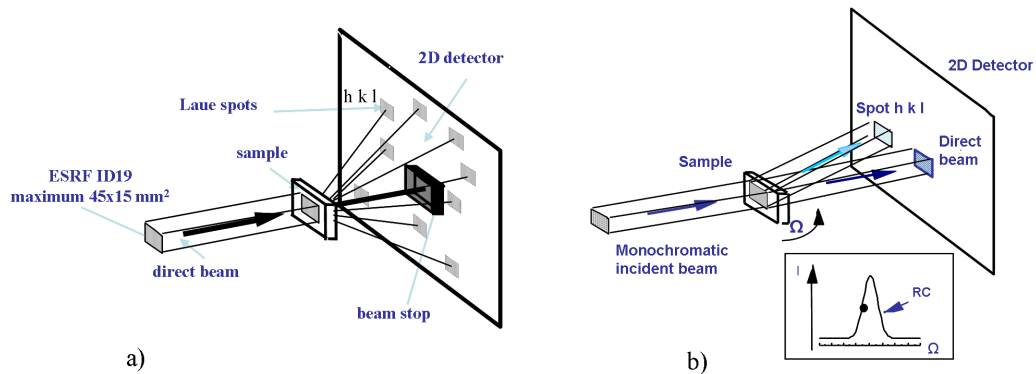


Figure 3.12: Schema of the two techniques used: a) white beam topography, b) monochromatic beam topography

White beam topography is the easiest to set up. In principle, little orientation of the sample is necessary. Using the continuous spectrum coming from a bending magnet or

¹this publication together with others that arise during my work at the ESRF but that are not part of the main subject of the thesis will be presented in chapter 7.

3. EXPERIMENTAL TECHNIQUES

a wiggler, different lattice planes diffract at their corresponding Bragg angles, selecting different energies from the incident beam. The first white beam topography at a synchrotron was done at by Tuomi *et al.* in 1974 [93]. Numerous diffraction spots, also called Laue spots, are recorded by the detector. Each one is a topograph corresponding to a different diffraction vector. Due to the large energy bandwidth, this technique is sensitive to variations of lattice plane orientation but not to changes of d-spacing. Parts of the crystal with different d-spacings will diffract with a different wavelength but in the same direction and with the same intensity onto the detector. Moreover, all parts of the crystal diffract, including strongly misoriented regions. Some drawbacks include the heat load in case of highly absorbing material, leading to deformations and sometimes even the destruction of the sample (a possible solution is the use of a chopper or to some extent filters to remove the softer X-rays, [94]) and the limited sensitivity for weak distortions (the sensitivity to effective misorientation in this technique is in the order of $10^{-3} - 10^{-6}$ radians).

Using in addition a monochromator crystal (or a system of several crystals) that diffracts the radiation coming from the source in a narrow energy band, it is possible to obtain higher strain sensitivity, *e.g.* by working on the flanks of steep rocking curves. This technique is called double crystal or monochromatic beam topography. In order to avoid artefacts on the topographs that are not due to the sample, the monochromator crystals must be of very high quality. It is possible to distinguish two different configurations for monochromatic beam topography: the *non-dispersive* (+n,-n) and the *dispersive* (+n, ±m) configurations, where n and m represent two different reflections and the signs are defined according the DuMond notation [95].

The difference between the two arrangements (in the synchrotron case) is shown in fig.3.13. The source produces a divergent and polychromatic beam which impinges on the crystal at a range of angles (*e.g.* ≈ 0.3 μ rad at BM05). For each angle there is a wavelength satisfying the Bragg condition. All the different wavelengths that are diffracted by the first crystal impinge on the second crystal at different angles. If the second crystal is of the same material as the first, set in a way that the same reflection is excited and with antiparallel diffraction vectors, then all the wavelengths diffracted by the first crystal are diffracted by the second, and the arrangement is said to be *non-dispersive* (fig.3.13a). All other configurations are *dispersive*, *i.e.* the two crystals are made of different materials and/or different reflections are used or from the same

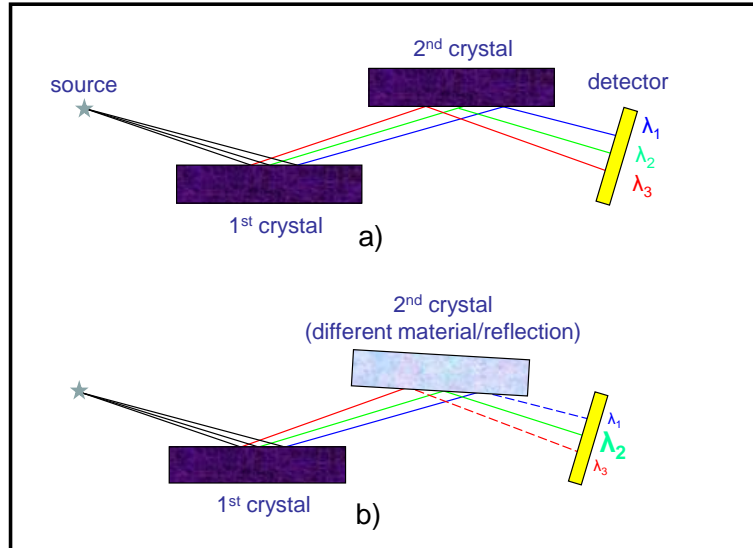


Figure 3.13: Example of two different configurations: a) non-dispersive (+n,-n), b) dispersive (+n,-m).

material and same reflection but with no antiparallel diffraction vectors (fig.3.13b). As a result, only radiation inside a narrow local band fulfils the Bragg condition at the second crystal and, consequently, only a narrow image appears on the film and one of the advantages of X-ray topography using a synchrotron source is lost.

The main advantage of non-dispersive schemes is that the rocking curve obtained is narrower and has steeper flanks compared to the dispersive curve. Recording topographs on the flanks of the rocking curve allows high strain sensitivity since, in this region, a small change in the effective misorientation gives rise to large changes in the recorded intensity. The main drawback is that very few kinds of crystal are available with sufficiently high quality, and this restricts the use of this technique to a limited number of substances. In the case of synchrotron sources, there are suitable solutions. The limited narrow local band on the second crystal that fulfils the Bragg condition may be extended by rocking the crystal and integrating the topograph on the detector. The penalty for the larger reflecting crystal area is the reduced strain sensitivity, as for the integrated wave techniques introduced before.

Another possibility is to correct for dispersion by bending the monochromator. For an experimentally-defined bending radius, the dispersive configuration becomes non-

3. EXPERIMENTAL TECHNIQUES

dispersive. In this way, high strain sensitivity is achieved for unmatched sample and monochromator materials. This technique is also called curved collimator topography, introduced at laboratory source [96, 97] and later adapted to synchrotron radiation [98] with the construction of an instrument. This instrument was recently relocated from ID19 to BM05. In this occasion a large part of the electronics and the mechanics was improved/changed and I have been strongly involved (together with D. Van Brussel and P. Van Vaerenbergh) in the reinstallation and the commissioning of the instrument.

It is also possible to use a perfect crystal as the first crystal, choosing a set of planes whose d-spacing is close to that of the reflecting planes in the sample and obtaining a quasi-non-dispersive setup. Moreover, by using an asymmetric reflection, it is possible to obtain the low divergence required for quasi-plane wave topography, [99, 100]. Another possibility is to use multiple crystal system in order to obtain a highly monochromatic beam, therefore limiting the possible dispersion [101].

The advantages of the dispersive and non-dispersive double crystal techniques with respect to white beam topography are: a higher strain sensitivity can be achieved (in the range of about $10^{-4} - 10^{-7}$ for the dispersive configuration, up to about 10^{-8} or even better for the non-dispersive), the lower heat load and the fact that images are easy to simulate. Drawbacks are the more demanding requirements of the experiment (*e.g.* sample orientation is necessary, sensitivity to mechanical and temperature drifts) and the fact that only one diffraction can be recorded at one time.

A powerful extension of double crystal topography is a technique called Rocking Curve Imaging. Here, the crystal is rotated step by step over the entire rocking curve, and at each step an image is recorded. In this way, a series of topographs is obtained with each image belonging to a different working point (angular position) on the rocking curve. The strain fields are therefore mapped in a more complete way.

Moreover, by using CCD cameras as detectors and PC-based analysis, it becomes easy to analyze the image series pixel by pixel and to extract local parameters such as the local rocking curve maxima (which reflect the local Bragg angles), the rocking curve widths or their integral reflectivities, [102]. Taking those series for different sample positions (rotating around the normal of the reflecting lattice planes) it is possible to separate the lattice parameter and the lattice inclination contributions to the effective misorientation.

3.3 X-ray surface sensitive techniques.

Two techniques have been used in order to characterize the surface roughness and crystalline quality of the sub-surface layer of high quality diamond crystals: X-ray Reflectivity (XRR) and Grazing Incidence Diffraction (GID). Both techniques take advantage of the fact that the index of refraction of X-rays in matter is less than one and may be written in the form:

$$n = 1 - \delta - i\beta \quad (3.5)$$

with:

$$\delta = \frac{2\pi\rho_e r_e}{k^2} \quad \beta = \frac{\mu_0}{2k} \quad (3.6)$$

where k is the wavevector, ρ is the electron density of the material and μ_0 is the linear absorption coefficient. For X-rays, δ and β are of the order of 10^{-6} and 10^{-9} , respectively. The fact that the refractive index is less than 1 implies that there exists a critical angle α_c below which X-rays undergo *external total reflection*. The value of the critical angle is obtained by using the Snell-Descartes law. In X-ray optics, the convention for the beam angles is to measure them between the beams and the surface, while in geometrical optics it is between the beams and the normal to the surface,3.14. This implies that the sine functions in the Snell-Descartes law are converted into cosines, giving:

$$n_1 \cos \alpha_i = n_2 \cos \alpha_t \quad (3.7)$$

where $\alpha_{i,t}$ are respectively the incident and transmitted angles and $n_{1,2}$ are the indices of refraction of the different media. Total reflection occurs when α_t is equal to zero. By substituting the refractive indices for air (to a good approximation, $n_{\text{air}} = 1$) and for the medium from 3.5, neglecting the absorption and using the Maclaurin expansion of the cosines, it is possible to obtain the critical angle α_c :

$$\alpha_c \approx \sqrt{2\delta} \quad (3.8)$$

Typical values for α_c are of the order of milliradians, *i.e.* *grazing incidence*. The penetration depth Λ as a function of the angle of incidence α_i (for the specular condition,

3. EXPERIMENTAL TECHNIQUES

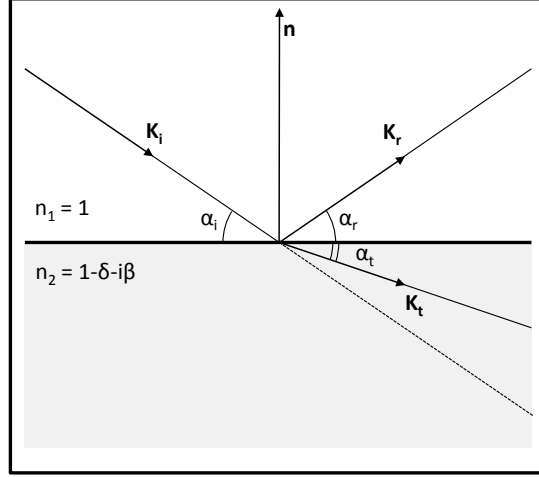


Figure 3.14: Scheme of the incoming, reflected and transmitted beam together with the beam angles at the boundary between vacuum and a material with index of refraction smaller than 1.

$\alpha_i = \alpha_f$) can be written [103]:

$$\Lambda(\alpha_i) = \frac{\lambda}{4\sqrt{2}\pi\sqrt{(\alpha_c^2 - \alpha_i^2) + \sqrt{(\alpha_i^2 - \alpha_c^2)^2 + (2\beta)^2}}} \quad (3.9)$$

Fig.3.15 is a plot of the penetration depth of 7 keV X-rays in diamond.

For angles below α_c , an evanescent wave is produced inside the sample fig.3.16. This wave propagates parallel to the surface, and is exponentially damped in the perpendicular direction. The minimum depth of this wave is $\approx \lambda/4\pi\alpha_c$, therefore it depends only on the material and wavelength used. It is of the order 3 nm for diamond at 7 keV X-ray energy. Around the critical angle, the penetration depth increases abruptly and above the critical angle it follows the Beer-Lambert law. This phenomenon enables studies of the quality of the crystal at different penetration depths.

3.3.1 X-Ray Reflectivity (XRR)

XRR is insensitive to the degree of long-range order of the material investigated (*e.g.* crystalline, amorphous). It is sensitive to changes in the local electron density (including surface and interface roughness) and not to strain fields, which are exploited in X-ray topography. XRR was pioneered by Kiessig [104] and developed by Parrat [105].

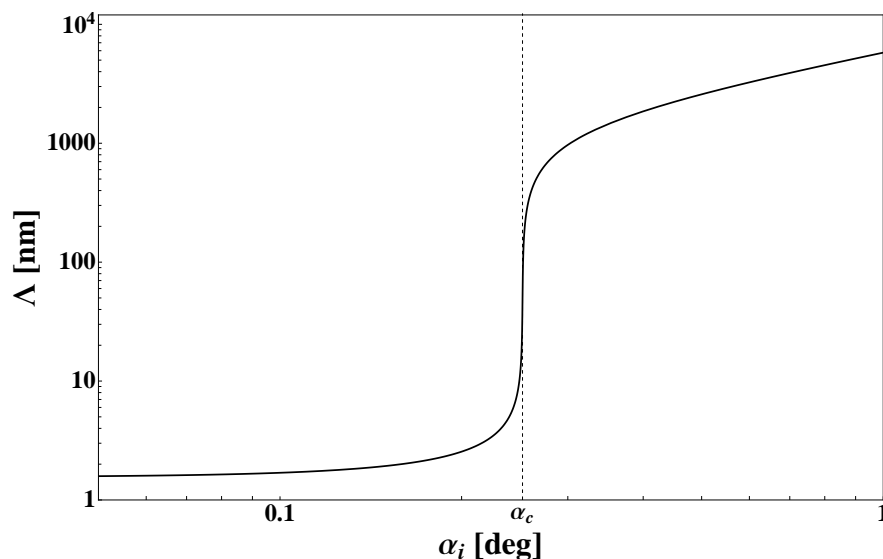


Figure 3.15: Penetration depth in diamond as a function of the incident grazing angle, $E = 7$ keV

In the case of a perfectly smooth, infinite surface with an infinitely thick bulk and zero absorption coefficient, the reflectivity is one below the critical angle and decays proportional to $q^{-4} = \frac{\sin(\alpha_i)^{-4}}{4\pi\lambda}$ for larger angles. If the sample is rough, the decay is stronger. A first theoretical model to take into account the roughness has been developed by Nevot and Croce, [106], assuming the roughness to have a Gaussian distribution. A second model based on the distorted wave Born approximation (DWBA) has been formulated by Sinha [107].

Moreover, if the sample is made of layers of different electron densities, interference fringes (called Kiessig fringes) are obtained in the reflectivity curve above the critical angle. These fringes are more pronounced if the difference in electron density between the layers is large. The distance between fringes is inversely proportional to the thickness of the layer. These effects are used to build multilayer monochromators, where many layers of materials of alternating high and low electron densities are stacked on each other, giving high intensity peaks at larger angles compared to typical critical angles. These peaks have a broader bandwidth than that obtained using crystal monochromators ($\frac{\Delta\lambda}{\lambda} \approx 10^{-1}-10^{-3}$ compared to $\frac{\Delta\lambda}{\lambda} \approx 10^{-4}-10^{-5}$), see fig.3.17, allowing a higher photon intensity at the price of a lower energy resolution. Geometrical

3. EXPERIMENTAL TECHNIQUES

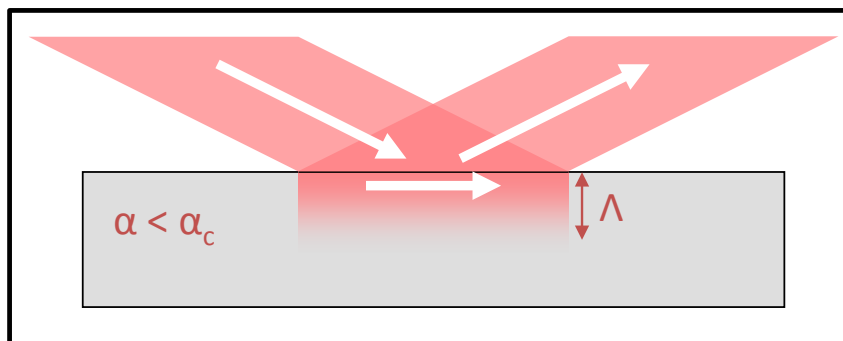


Figure 3.16: The evanescent wave created in total reflection, and its penetration depth Λ

and resolution function factors such as sample dimensions and beam divergence play a major role, especially in the region of total reflection, and in order to obtain a good agreement with the data they need to be taken into account [108].

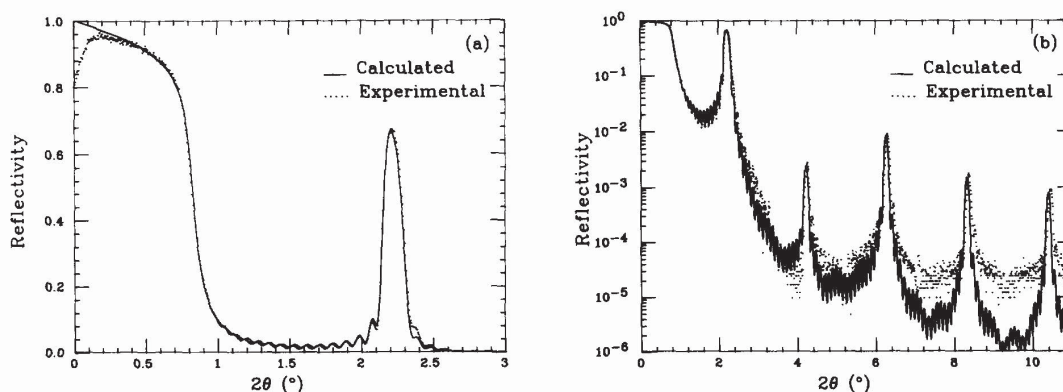


Figure 3.17: Reflectivity curve of tungsten-carbon multilayer for Cu Ka X-rays, (a) linear scale and (b) logarithmic scale. From [109]

In our experiment on the study of diamond surfaces after polishing, three kinds of XRR scans were performed:

specular scans - the detector angle is swept at twice the rate of the sample angle whilst maintaining the condition $\omega = 0.5 * 2\theta$ (called $\omega - 2\theta$ scans). In this type of scan, the scattering vector q is perpendicular to the surface of the sample, and only the electron density differences in this direction are probed;

off-specular scans - longitudinal diffuse - the detector is again moved at twice the angular speed of the sample ($\omega - 2\theta$), but the sample is initially positioned with an offset θ_{off} compared to the specular scan. It is possible to subtract the average of two longitudinal diffuse scans collected at $\Delta\theta \pm \theta_{\text{off}}$ from the data obtained in a specular scan, obtaining the so-called *true specular*.

transverse diffuse scans - in this case the detector is kept at a fixed position whilst the sample is rocked. These scans allow the scattering vector parallel to the surface to be probed in order to determine in-plane correlation of the roughness. Moreover, transverse diffuse scans allow the separation of roughness and composition grading which is impossible in specular reflectivity. Characteristic peaks are present on both sides of the specular peak, called Yoneda peaks [110]. They appear when either the incoming or the exit beam angles with respect to the sample surface are equal to the critical angle.

3.3.2 Grazing Incidence Diffraction (GID) in non-coplanar geometry.

GID combines the surface and the depth-controlled sensitivity of X-ray at grazing incidence together with Bragg diffraction from planes approximately perpendicular to the sample surface. The technique was introduced by Marra *et al.* [111] and used in a depth-controlled study by Dosch *et al.* [103]. The geometry used is shown in fig.3.18. The incidence and exit beams are kept at a small angle around the critical angle of total reflection. Lattice planes perpendicular to the crystal surface are used for Bragg diffraction (non-coplanar diffraction geometry). Exploiting such a geometry gives access to the momentum transfer almost parallel to the crystal surface, therefore probing the crystalline structure close to the surface, *e.g.* possible mosaicity near the surface, or sub-surface distortion due to the crystal processing. This can complement the measurements of the strain components perpendicular to the crystal surface measured by high-resolution diffraction.

The angle between the incident beam and the surface of the crystal is kept constant during a scan; this implies that the penetration depth is also constant. By correctly implementing the rotations of the sample (around the surface normal) and of the detector, it is possible to collect transverse and radial scans of the reciprocal lattice point corresponding to the diffracting lattice planes. By repeating this at different incident

3. EXPERIMENTAL TECHNIQUES

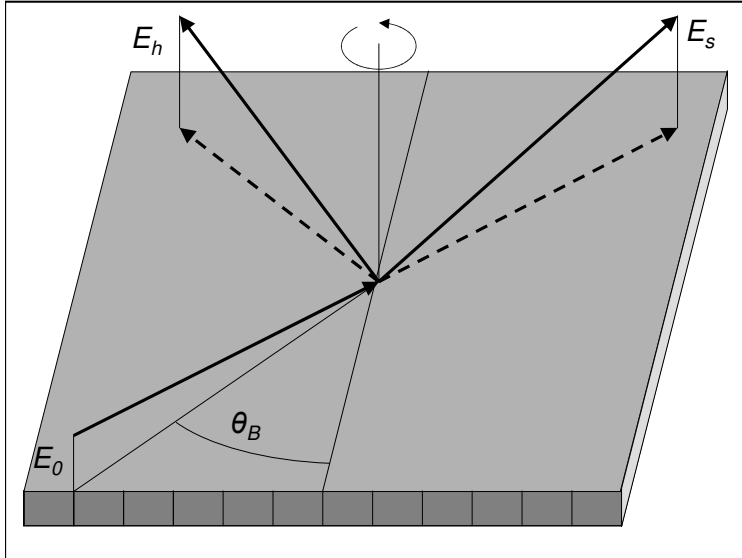


Figure 3.18: Grazing incidence diffraction, E_0 , E_s , and E_h are the incident, specular and diffracted waves respectively, and θ_B is the Bragg angle, from [112].

angles, it is possible to study the crystalline structure at different depths and, *e.g.* obtain a quantitative measure of the thickness of the region which is distorted due to polishing.

Chapter 4

Characterization of single crystal diamonds

In this chapter, I will first present the characteristics that make diamond an interesting material for 3rd and 4th generation synchrotron sources. Afterwards, I will show some of the results obtained from the characterization of single crystal diamonds, mostly using X-ray related techniques but also, in some cases, compared with alternative techniques such as Atomic Force Microscopy (AFM) and optical profilometer. Some of the results presented here have been published in different papers, [113, 114, 115], of which I am co-author.

4.1 Diamond

4.1.1 Properties

Diamond is one of the allotropes of carbon, some of the others being *e.g.* graphite, graphene and fullerene. At room temperature, diamond is metastable; the thermodynamically stable form is graphite. At high temperature and ambient pressure is possible to graphitize diamonds, from 600 °C to 800 °C in the presence of oxygen or a metallic catalyst [116], and from 950 °C or higher in vacuum [117]. The diamond crystal is formed by carbon atoms bounded by four equidistant nearest neighbours in a tetrahedral symmetry due to the sp^3 orbital. In comparison, in graphite, the bonding between carbon atoms is sp^2 , resulting in layers of graphite weakly bonded by van der Waals forces. The diamond unit cell consists of two interpenetrating face-centered

4. CHARACTERIZATION OF SINGLE CRYSTAL DIAMONDS

cubic lattices, one at $(0,0,0)$ and the second shifted at $(\frac{1}{4},\frac{1}{4},\frac{1}{4})$. The lattice parameter at room temperature is between (0.356683 ± 0.00001) nm and (0.356725 ± 0.00003) nm [118]. Two different crystallographic forms of diamond exist: the cubic and the hexagonal (also known as lonsdaleite). The difference between these two forms is the result of a different sequence of atomic layers. If the sequence is ABABAB, *i.e.* the third layer exactly superposes the first, then the crystal has hexagonal structure. With a sequence of ABCABC, *i.e.* the fourth layer superposes the first, then the crystal has cubic structure, fig.4.1.

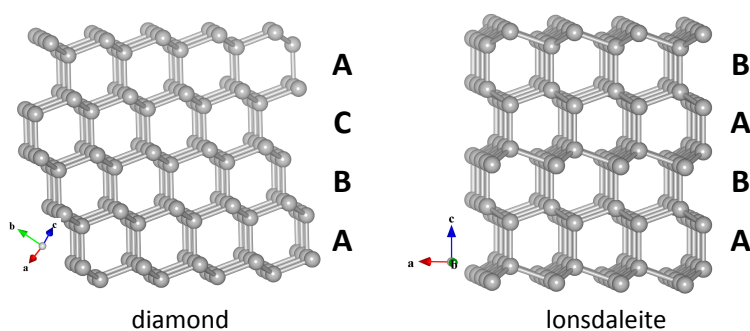


Figure 4.1: Differences between diamond (cubic) and lonsdaleite (hexagonal). The pictures of the two structures were generated using the software *Vesta*,[119]

Diamond has the highest hardness of all natural materials (only man-made aggregated diamond nanorods [120] and ultrahard fullerite [121] are harder than diamond). This explains the origin of the name, *adamas* (Greek) that means the “untameable” or the “unconquerable”.

4.1.2 Synthesis of diamonds

The first commercially successful synthetic diamond was synthesised in Stockholm, Sweden, in 1953 using High Pressure and High Temperature (HPHT). The discovery was kept secret [122]. One year later, there were two reported syntheses of diamond at the General Electric Research Laboratory: one by H.M. Strong and the second by H.T. Hall. The results were quickly published in *Nature* [123] and the method of growing man-made diamond was patented. Those first diamonds were tiny (1×0.3 mm) and hardly reproducible. After further experiments, it became clear that to synthesize

diamond, a metal “solvent/catalyst” bath was necessary. In 1971, R.H Wentorf Jr. showed the possibility of growing bigger diamonds using the so called “thermal gradient method” [124]. This method is best done in a large volume belt press system and will be described in more detail in the next section. With the HPHT method, single crystal diamonds with more than 1 cm maximum dimension can be grown and routinely 5-7 mm diamonds with low nitrogen content are grown by companies such as Element Six (formerly De Beers Industrial Diamond) and Sumitomo Electric Industries. An alternative method, the “pressure gradient” method, makes use of a different type of high pressure system, called split-sphere BARS press (from the Russian acronym of press-free high-pressure setup “split sphere”) to grow large size single crystal, see *e.g.* [125].

Another technique used to grow synthetic diamond is Chemical Vapour Deposition (CVD) [126], [127]. It is the most widely used technique for depositing many materials in the semiconductor industry, including a wide range of dielectrics and many metals and metal alloys. The technique generally involves the growth of a solid material from the gas phase using a reactive gas mixture, which supplies the necessary active species (carbon from methane in the case of diamond) onto a controlled surface (or substrate). The substrate does not have to be diamond but in order to grow single crystal CVD diamond (instead of polycrystalline diamond) it is necessary to use a diamond substrate with high quality surface finish. Numerous different methods have been developed; the main difference consists in which technique is used to activate the gas-phase carbon-containing precursor molecules (*e.g.* hot filament, DC-plasma, RF-plasma, microwave-plasma, electron cyclotron resonance-microwave plasma). The main advantages of CVD techniques are the low pressure necessary (consequently a lower cost in terms of equipment); the possibility of growing large diamonds; and the possibility of growing diamond on different substrates. Unfortunately, until now, the quality of the bulk material does not meet the requirements for use as X-ray optical elements, even though recently great improvements have been made by using high quality Ila HPHT single crystals as seeds, [128]. In the next section, the HPHT method will be described. Up to now, this method facilitates synthesis of diamonds with the highest structural quality.

4. CHARACTERIZATION OF SINGLE CRYSTAL DIAMONDS

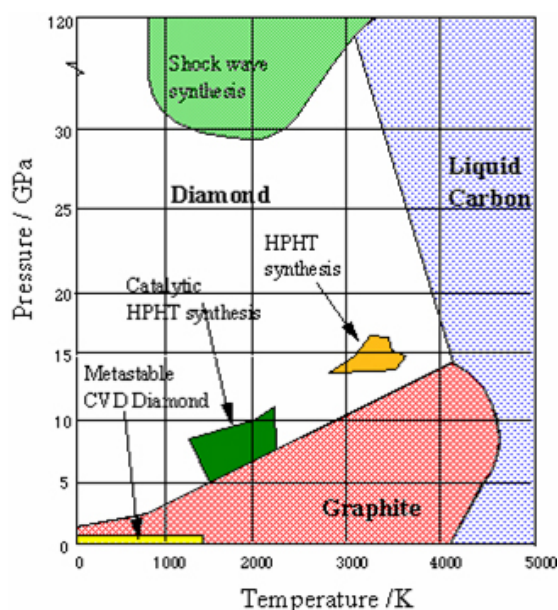


Figure 4.2: The P,T phase diagram of carbon, from Bundy [129].

High-Pressure High-Temperature synthesis of diamond

Fig.4.2 shows the phase diagram for elemental carbon, from Bundy [129]. Four regions are recognizable:

- the CVD method at low pressure;
- shock wave synthesis, where very high pressure and temperature are achieved by detonation;
- HPHT direct conversion;
- HPHT catalytic synthesis.

Shock wave synthesis produces very small diamonds (of the order of a few μm), not suitable for application as optical elements. Direct conversion of graphite to carbon faces a high kinetic barrier, so that it takes place at pressures above 13 GPa and temperatures around 3000 K [130, 131] but these conditions are difficult and expensive to achieve. In order to overcome the kinetic barrier, a metal solvent-catalyst bath is used. This allows conversion at lower temperature and pressure, typically around 1550

to 1600 K and 5 to 6 GPa [132]. This is the method used to grow high quality synthetic diamonds and attention will now be focused on this specific technique.

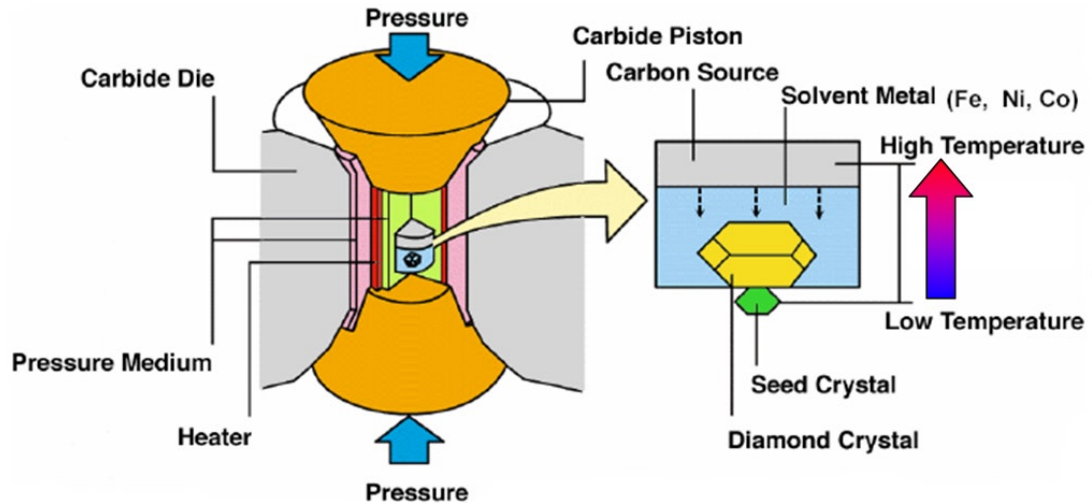


Figure 4.3: Scheme of a HPHT system for growing diamonds, from Sumiya *et al.* [133]

Fig.4.3 shows a schematic diagram of a press used to grow synthetic diamonds (details differ between manufacturers and, being a commercial procedure, it is covered by intellectual patents and kept confidential). The essential parts for the growth are [134]:

- carbon source: could be graphite but higher quality crystals are obtained using a fine diamond powder as the carbon source;
- a growth medium of metal solvent-catalyst. As mentioned before, the liquid metal solvent is necessary to enable the process to proceed at lower pressure and temperature. Alloys of metals such as Fe-Ni, Mn-Ni and Co-Fe are generally used;
- a diamond seed: as usual in crystal growth, it is necessary to use a very high quality seed crystal in order to grow high quality diamond. The seed must also be embedded to avoid it floating away, and it must be in contact with the bottom of the metal bath.

All the components are placed inside a heater and the heater is filled with a pressure medium, *e.g.* NaCl. The cell as formed is compressed in a high pressure vessel. A thermal gradient (20 to 50 K) is produced inside the heater between the carbon source

4. CHARACTERIZATION OF SINGLE CRYSTAL DIAMONDS

and the seed (*e.g.* in a simple cylindrical heater the temperature is higher in the middle and it decreases along the axis of the cylinder). The driving force for the reconstitution of diamond is provided by the difference in solubility of carbon in the metal bath at different temperatures (as usual in crystal growth from solution). The carbon source is kept at a higher temperature, so that diamond dissolves in the bath whilst the seed is kept at a lower temperature. This generates a supersaturation of the carbon that deposits on the diamond seed homoepitaxially, fig.4.4.

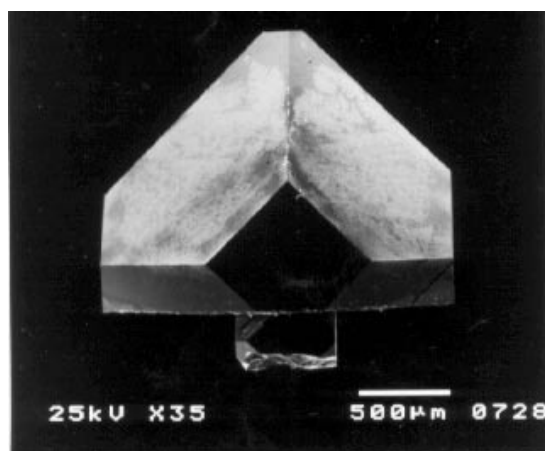


Figure 4.4: A Scanning Electron Micrograph (SEM) of a synthetic diamond, from Kanda [135]; the diamond seed is clearly visible on the bottom part of the stone.

The growth parameters (pressure, temperature gradient) must be extremely stable. Fluctuations may produce growth defects that may not be tolerable for a crystal foreseen for X-ray optics applications. The growth rate of the diamond is also related to the temperature gradient: larger gradients give rise to higher growth rates, but metallic inclusions are easily incorporated in the diamond, destroying the quality of the crystal. A compromise between high quality and feasible growth time has to be found. Typical growth rates for a good crystal are around 2 to 5 mg/h and typical growth times are of the order of 200 to 500 hours, [134].

Defects in diamonds

During the growth process, numerous crystallographic defects may be formed inside the crystal, destroying the necessary perfection. These defects could be zero-, one-, two-

or three-dimensional, respectively atomic impurities, dislocations, stacking faults and inclusions. Among a large variety of possible atomic impurities in diamond, the most common are nitrogen and boron. A classification of natural diamonds has been made and it applies perfectly also to synthetic crystals, [118].

- Type Ia: high concentration of nitrogen, from 10 up to 3000 ppm, in aggregated form; two subcategories are the IaA with nitrogen clusters made by neighbouring pairs of substitutional atoms and the IaB, believed to be four substitutional nitrogen atoms neighbouring a vacancy. These kinds of impurities do not absorb visible light, so they are typically transparent under optical illumination. Almost 98% of natural diamonds are type Ia.
- Type Ib: 25 to 800 ppm nitrogen atoms, in single substitutional form; these impurities absorb radiation in the UV region, with a tail also in the violet-blue, giving the characteristic yellow-brown colour. They are quite rare in nature but are the most common synthetic diamonds produced because of the higher growth rate.
- Type IIa: very low concentration of nitrogen, normally less than 10 ppm; they are optically transparent and very rare in nature albeit some of the finest historical stones, such as the Cullinan and Koh-i-Noor, are type IIa.
- Type IIb: in this case the classification is not due to the nitrogen but to the boron impurities, up to 50 ppm; this kind of impurity gives absorption in the red/IR region, giving to the stone a characteristic blue colour. They are very rare in nature but it has been discovered that they show interesting semiconducting properties

The concentration of N impurities in synthetic diamond strongly depends on the crystallographic orientation of the growth sector, [136]. For example, growth in the $\langle 111 \rangle$ direction contains more N than growth in the $\langle 100 \rangle$ direction, and much more than in the $\langle 110 \rangle$, fig.4.5. At the boundaries between these growth sectors, the lattice is slightly deformed due to the difference in the diamond lattice parameter, which for single substitutional nitrogen (also called C or P1 defect) is [114]

$$\frac{\Delta a_0}{a_0} = (0.12 \pm 0.03) \times C_N \quad (4.1)$$

4. CHARACTERIZATION OF SINGLE CRYSTAL DIAMONDS

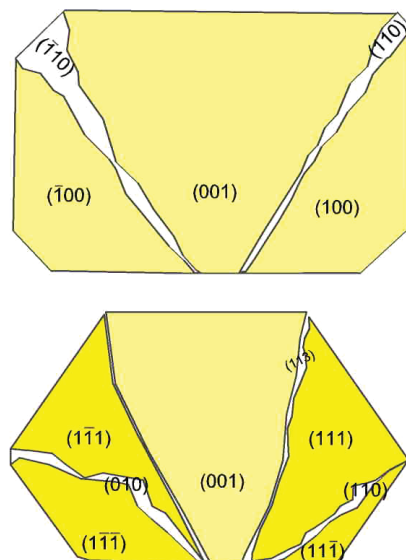


Figure 4.5: Concentration-dependence of nitrogen in the different growth sector. The colour density indicates the N concentration; N concentration in $\langle 111 \rangle > \langle 100 \rangle > \langle 113 \rangle > \langle 110 \rangle$, from [114].

where C_N is the concentration of nitrogen impurities expressed as an atomic fraction. Due to the lower nitrogen content, type IIa diamonds are less affected by this kind of deformation. Consequently, it is accepted that for the highly demanding application of X-ray optical elements, type IIa crystals of very high quality are the preferred material. To produce type IIa diamond, it is necessary to add to the metal solvent/catalyst elements with high affinity for N, such as Ti, Zr and Al. These elements are called “nitrogen getters” and forming nitrides such as TiN and ZrN in the solvent catalyst, they lower the concentration of nitrogen impurities inside the diamond.

Fig.4.6 shows a comparison between type Ib and type IIa diamond specimens. It is possible to observe in the optical image the pale yellow colour of the Ib and the transparency of the type IIa. This effect is due to the nitrogen impurity, which is a deep donor and absorbs blue light and so it makes the diamond appear yellow. Also clearly visible are the different growth sectors with different nitrogen concentrations (as illustrated in fig.4.5). These are also clearly visible in the UV image: the nitrogen, excited by the UV light, emits in the green-yellow region, except for the 110 sector, where the concentration is much lower. The different growth sectors are also visible in

the IIa diamond, under UV light. The last images are X-ray topographs, showing the much lower quality of type Ib with respect to type IIa.

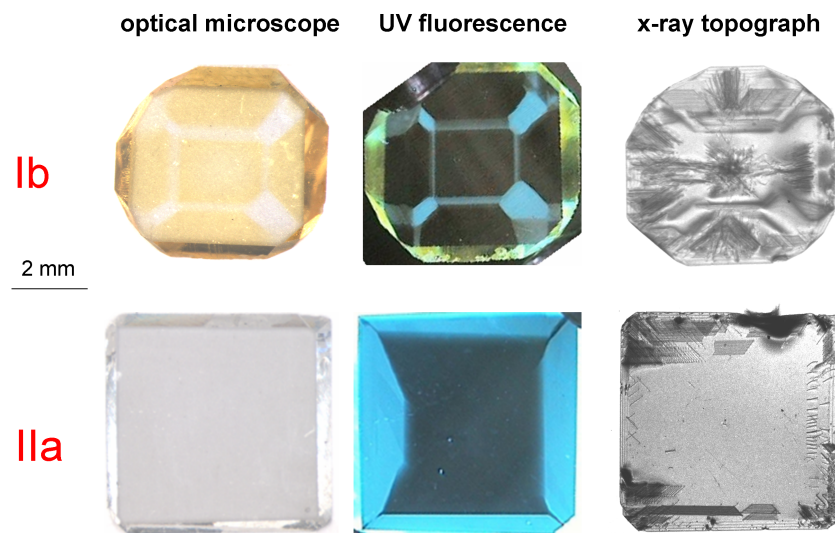


Figure 4.6: Comparison between type Ib and type IIa synthetic diamonds.

Dislocations are linear defects. There are two basic types of dislocations: edge dislocations and screw dislocations. A combination of edge and screw dislocations is called a mixed dislocation.

- Edge dislocations may be thought of as the result of adding a half-plane of atoms mid way through the crystal.
- Screw dislocations can be thought of as the result of cutting through the crystal and slipping one half with respect to the other by a lattice vector parallel to the edge of the cut.

It is possible to define a vector, called the Burgers vector, which represents the magnitude and direction of the lattice distortion arising from a dislocation. The Burgers vector and the dislocation line are parallel for a screw dislocation and perpendicular for an edge dislocation. In a mixed dislocation, the angle will be between 0° and 90° . Stacking faults are planar defects and are regions within the crystal where the regular stacking sequence has been interrupted. Two types of stacking fault are possible in fcc

4. CHARACTERIZATION OF SINGLE CRYSTAL DIAMONDS

crystals: intrinsic stacking faults (ABC**A**BABC instead of ABCABCABC), which can be pictured as vacancy agglomeration and extrinsic stacking faults (ABC**A**BACAB), which can be thought as a layer of interstitial atoms added to the sequence. Inclusions are normally due to metal from the solvent catalyst bath that remains trapped inside the crystal during the growth process. The size of the inclusions can vary from 1 μm to 1 mm and their shape is normally plate or rod-like, with rounded corners. The strain in the crystal due to this kind of defect may be very large, so that inclusions must be completely avoided for a diamond to be used as an X-ray optical element. A greater concentration of defects is present near the seed (*e.g.* dislocations, stacking faults) [125] and [137]. The dislocations radiate outwards from the seed, following roughly the growth direction of the respective growth sector. Therefore the upper part of the crystal possesses quite a wide central zone almost defect-free. Moreover, as is usual in crystal growth, crystals with a lower density of defects may be grown using a defect-free diamond as the seed [138].

4.2 Characterization of synthetic diamonds. Experimental results.

In chapter 3 I have introduced the different methods used to characterize synthetic diamonds, here I will present a selection of the results obtained.

4.2.1 High Resolution X-ray Diffractometry

After the determination of the experimental apparatus function discussed in 3.1 it is now possible to estimate the rocking curve broadening for different diamond samples due to the presence of defects. This has been done by using a similar procedure (model and fit) presented for the determination of the apparatus function, equation 3.2.

Table 4.1 shows an overview of different typical diamond plates, selected from all the samples analyzed. In order to quantify the broadening of the rocking curve, we decided to extract the full width at different peak heights, namely 50%, 20% and 2% of the maximum intensity. This allows one to study also the influence of defects on the wings of the rocking curve. For comparison, the Darwin widths of the intrinsic reflectivity curves of diamond for the different reflections, sample thicknesses and the energy used (14.413 keV) are given together with the white beam topographs.

4.2 Characterization of synthetic diamonds. Experimental results.

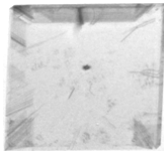
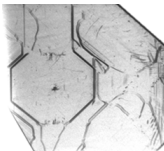
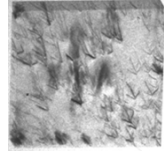
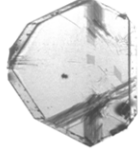
Diamond	1. (100) IIa	2. (100) Ib	3. (100) CVD	4. (111) IIa
WBT				
w_h	1.056''	1.129''	1.000''	2.954''
$\Delta\text{FW}50\%M$	0.04'' \pm 0.06''	0.86'' \pm 0.06''	0.37'' \pm 0.06''	0.43'' \pm 0.06''
$\Delta\text{FW}20\%M$	0.08'' \pm 0.09''	1.71'' \pm 0.09''	0.74'' \pm 0.09''	0.68'' \pm 0.09''
$\Delta\text{FW}2\%M$	0.28'' \pm 0.15''	3.25'' \pm 0.15''	2.61'' \pm 0.15''	11.9'' \pm 0.15''

Table 4.1: Widths of the broadening due to defects curve at different heights of the peaks for different types of diamonds, together with the Darwin widths w_h . The errors are estimated from the values obtained for the apparatus function at the same height.

The results obtained show a negligible broadening for sample 1, IIa HPHT diamond, 100 oriented in a region close to the centre of the plate. For the Ib sample and the CVD diamond the situation is worse, with a greater broadening recorded at all levels. For sample 4, a type IIa HPHT plate 111 oriented, the results are different. The bulk quality seems good (the theoretical rocking curve is broader for the 111 reflections than for the 400, therefore the increase of 0.43 arcseconds is relatively smaller), but the full width at 2% of the maximum is very large. We think this is related to a much worse quality of the surface of the plate, since the 111 surface is the most difficult to polish. The surface quality of the crystal has been characterized also using X-ray techniques, and the results are presented in section 4.2.4.

4.2.2 X-ray Topography

In our case, a better adapted method to control the quality of the different diamond crystals is X-ray topography, introduced in section 3.2, since it allows us to obtain local information about the defect distribution in the crystal.

All the results presented here have been collected at two beamlines at the ESRF: BM05 and ID19. It is impossible to present all the topographic results obtained during my PhD, since a lot of them have been assessment of a industrially sensitive nature of

4. CHARACTERIZATION OF SINGLE CRYSTAL DIAMONDS

purchased high quality IIa diamonds. I will concentrate on a selection of interesting cases, showing the differences between crystals of different quality but also between the results obtained using different strain sensitive techniques.

The X-ray topographs were recorded either on photographic films or using a CCD camera. For the films, we typically used Kodak Industrex SR45 films or AGFA Structurix D3, with a grain size of approximately 3 μm . For the CCDs we used either the FReLoN camera (developed at the ESRF, [139]) or a PCO.2000 camera ¹. The reason of having two different cameras is simply the fact that the FReLoN camera is too heavy to be mounted on some of the existing diffractometers. In both cases, the X-rays are first converted to optical light by scintillator crystals, then, by using a set of lenses, the image is focused on the CCD chip. It is therefore possible by changing the optics to change the spatial resolution of the image (*e.g.* with the PCO, two sets of optics produce an estimated pixel size of 3 μm and 10 μm). All the different optics have been conceived and developed in the Detector Group of the ESRF.

The main advantage of films over CCD cameras is the combination of a large field of view (*e.g.* 13 \times 18 cm in our case) with a high spatial resolution (1 to 3 μm in our case), allowing, for example, the collection of the different Laue spots in a white beam experiment. Nevertheless, when the field of view required is not large, the CCD cameras allow Rocking Curve Imaging, *i.e.* a combination of High Resolution Diffractometry and Topography. An additional advantage of CCD cameras over photographic films is the fact that the signal recorded is proportional to the X-ray intensity whilst for the films, an additional digitalisation step of the transmitted light is required and this is an additional source of error in the cases when a quantitative analysis is performed.

4.2.2.1 White Beam Topography (WBT)

Fig.4.7 shows an example of a transmission WBT of a high quality type IIa diamond. The different inhomogeneities in the images are related to defects such as dislocations, stacking faults and inclusions but also, in the case of the equal thickness fringes, simply related to the fact that the edge are bevelled and confirm the high local crystal quality (interferences are not perturbed).

Fig.4.8 shows a zoom of fig.4.7, where a clearly visible set of dislocations is present. The conditions for the formation of the three types of extinction images (direct, dynamical

¹see <http://www.pco.de/sensitive-cameras/pco2000/> for details about this camera

4.2 Characterization of synthetic diamonds. Experimental results.

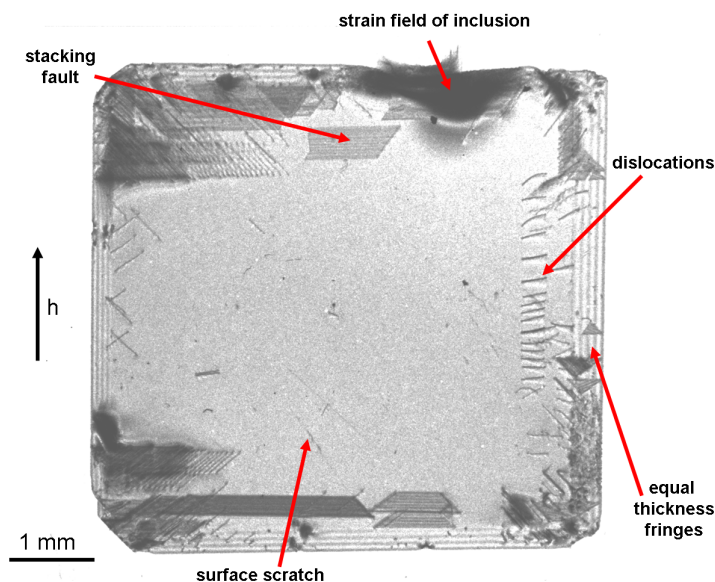


Figure 4.7: Example of a white beam topograph of a IIa type diamond, $\bar{2}20$ reflection

and intermediate) are fulfilled. On one end of the dislocation image (in this case left side of the picture), the direct and dynamical images converge while on the other end they diverge. This implies that the dislocation is a threading dislocation, passing through the crystal plate and crossing the two surfaces at two points: the point on the exit surface of the X-ray (*i.e.* towards the detector) correspond to the point where the direct and dynamical image are joined together. Furthermore, by using topographs with different diffraction vectors it is possible to determine the orientation of the Burgers vector associated to a dislocation by using the contrast extinction rule introduced on page 45. In this particular case, the dislocations that are clearly visible on this topograph are completely invisible on the spot diffracted perpendicularly (*i.e.* the 220 reflection). The Burgers vector of these dislocations is therefore parallel to the $[\bar{1}10]$ direction.

It is also possible to obtain an estimation of the strain produced by the inclusion present in fig.4.7. By measuring the distance between the core of the inclusion (assuming it to be in the middle of the strain field) and to the outermost deformed part of the image, d , it is possible, by simple geometrical calculation, to derive the distortion created by the inclusion. Using the sample to film distance L and the distance from the beam-stop

4. CHARACTERIZATION OF SINGLE CRYSTAL DIAMONDS

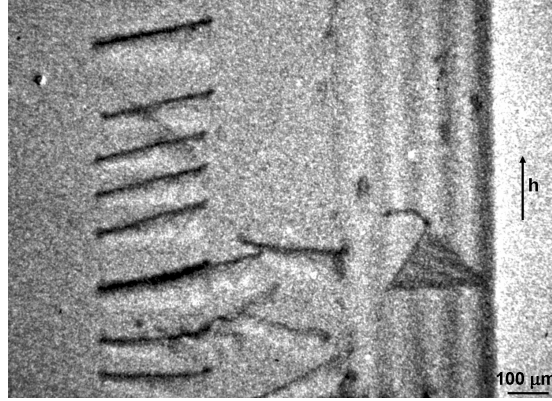


Figure 4.8: Zoom of the topograph showed in fig.4.7. It is possible to see a set of dislocations in the left part (the black line is the direct image, the brighter shadow is the dynamical image), a stacking fault (the triangular shape on the right part of the image) and the equal thickness fringes on the right.

shadow to the topograph D it is possible to calculate the misorientation angle $\delta\vartheta$ as

$$\delta\vartheta \approx \arcsin \frac{d}{\sqrt{L^2 + D^2}}$$

In the case of the inclusion shown in fig.4.7, we have $d = 0.9$ mm, $L = 23$ cm and $D = 8.2$ cm, resulting in a misorientation of $\delta\vartheta \approx 3 \times 10^{-3}$ rad. This is just a rough estimation, but it shows that it is possible to make quick estimations of relatively strong misorientation from white beam topographs.

A series of WBT topographs for different types (CVD, HPHT Ib and IIa) of diamonds is shown in tab.4.1. It gives a clear indication of the low quality of the CVD and Ib samples compared to the IIa ones.

In figure 4.9 the X-ray topographs together with UV fluorescence maps of high quality IIa diamond plate are compared. The schematic drawing above the topographs shows the different positions at which top and bottom plates are extracted. It is clear from these images that the quality of the plates increases significantly the farther from the seed the plate is extracted. From the UV fluorescence maps it is possible to see the different growth sectors; most of the dislocations and stacking faults grow in the 111 or 113 sectors (see fig 4.5), leaving the 100 direction almost free of defects. The basic phenomenon leading to the UV maps is that of broad blue band emission from donor-acceptor recombination for close pairs, as modified by the different relative

4.2 Characterization of synthetic diamonds. Experimental results.

concentrations of the boron acceptor and nitrogen donor within the different growth sectors, [114, 140]. Due to the fact the nitrogen concentration is small (normally less than 20 ppb), the d-spacing difference in the different growth sectors produces growth sector boundaries which deformations are below the strain sensitivity of white beam topography and therefore are not visible.

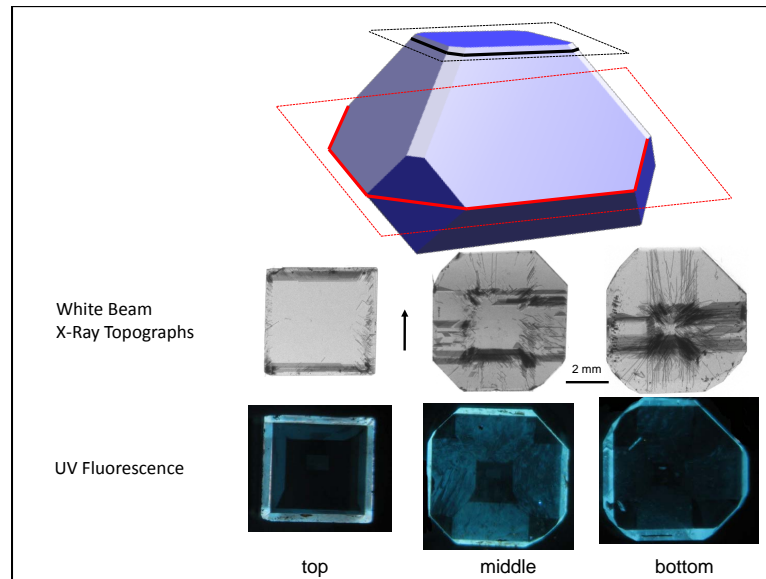


Figure 4.9: White beam -220 topographs and UV fluorescence maps of different IIa plates cut from the same stone at different distances from the seed, as shown schematically for the top and bottom plates in the top drawing. In the fluorescence maps, the different growth sectors are clearly visible. The arrow indicates the projection of the diffraction vector on the film for the different topographs.

In the case where the plate is cut in a different crystallographic direction, *e.g.* 110, the region closer to the seed is clearly distinguishable from the opposite side, see fig.4.10; the seed was clearly on the bottom part of the topograph while the 100-cubic growth sector, defect free, is at the top.

4.2.2.2 Double crystal Topography

The main drawbacks for the white beam are the high background, the limited sensitivity to weak distortion and the sensitivity only to lattice inclination. This problems can be overcome by using a reference crystal (or a set of crystals) before the sample.

4. CHARACTERIZATION OF SINGLE CRYSTAL DIAMONDS

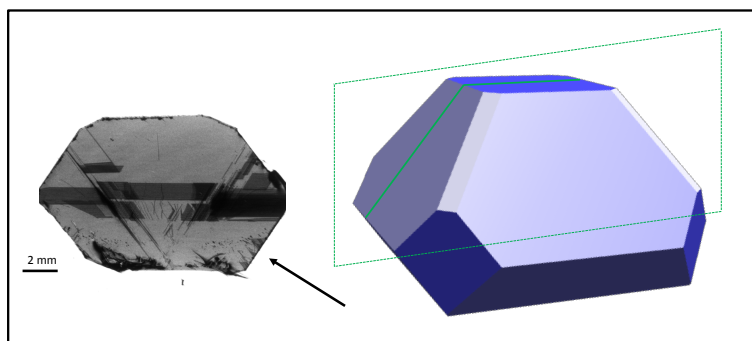


Figure 4.10: White beam 111 topograph, projection of the diffraction vector shown with an arrow, of a IIa high quality diamond crystal, together with a diagram showing approximately where the plate was extracted. From the defects, it is possible to determine that the seed was in the lower part of the plate.

As shown in fig.3.13, there are two arrangements possible for the double crystal topography, the dispersive ($+n, \pm m$) and the non-dispersive ($+n, -n$).

X-ray topography in the dispersive configuration. Fig.4.11 is an example of topographs collected in a dispersive configuration, *i.e.* using a double silicon 111 monochromator and a diamond sample, 220 Laue reflection, at ID19, beam energy $E=20$ keV, shown together with a white beam topograph. The sample is a type Ib diamond, grown with the split-sphere (BARS) method by colleagues in Novosibirsk. The angular step size between images is $2.7''$.

Due to the angular divergence and energy spread of the incident beam, different regions of the sample diffract at slightly different angular positions with slightly different wavelength. The rocking curve is broad, with shallow flanks implying relatively low strain sensitivity. In this sample growth sector boundaries are clearly visible, in the form of strong double line contrast on the left part of the image (visible in the white beam topograph). They are caused by the differences in nitrogen concentration between different growth sectors and the relative dilatation of the lattice following equation 4.1. The double contrast can be understood by assuming that at the boundaries between the two regions the lattice planes are distorted. After cutting out a crystal plate from the crystal, the internal stresses relax, leaving the surface stress free. This leads to a rather complicated strain field with two strongly strained regions close to the outcrops

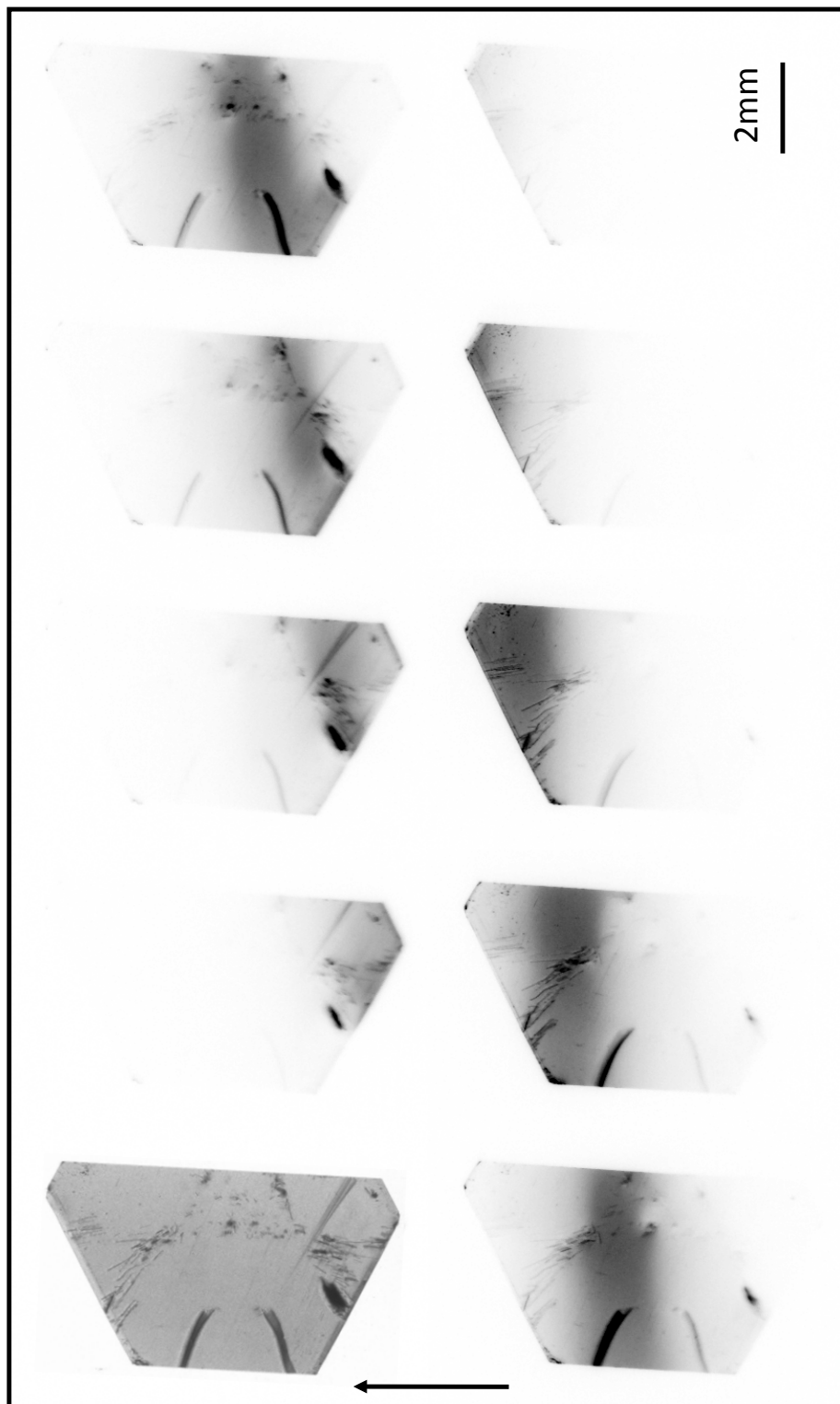


Figure 4.11: Series of 220 Laue topographs in a dispersive arrangement taken at ID19 using the beam from a double Si 111 monochromator, $E = 20$ keV. The step size between each image is 2.7°. The top left image is a white beam topograph of the same crystal. The arrows show the projection of the diffraction vector.

4. CHARACTERIZATION OF SINGLE CRYSTAL DIAMONDS

of the growth sector boundary through the surfaces, as shown in fig.4.12, from [141], and which are responsible for the double contrast.

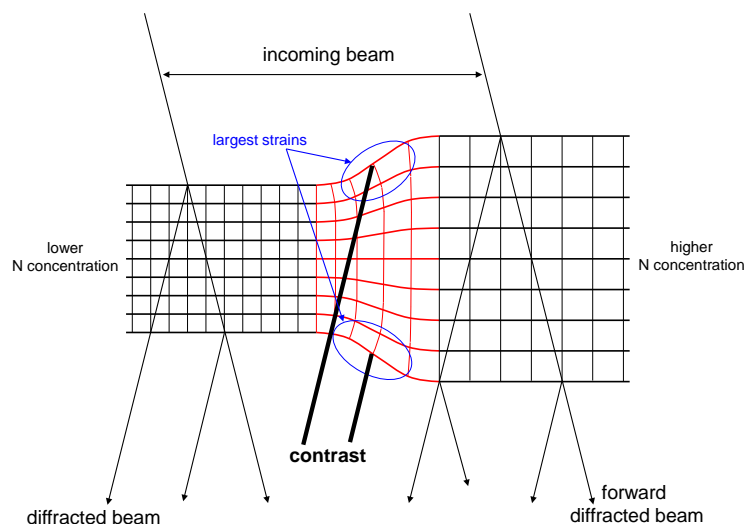


Figure 4.12: Scheme of the boundary between two different growth sectors with different N concentrations, showing the source of the double contrast in fig.4.11.

X-ray topography in the non-dispersive configuration. In the ideal configuration, the crystal conditioner is a perfect crystal of the same material and diffracts from the same atomic planes as the sample. Unfortunately this is not always possible. The problem of having a flawed reference crystal is that, since the distance from the source is very large, every defect on the first crystal is imaged together with the defects from the second. Fig.4.13 shows two white beam topographs (220 type reflections) of two 111 oriented type IIa HPHT diamond crystals. These two crystals have been used for a mechanical feasibility test of a double diamond high-heat load monochromator, [115]. Since it was only a feasibility test, the quality of the two crystals was not very high. In fact, in both plates are present a high number of defects, mostly stacking faults and dislocation bundles. We note the very strong deformation present in the second crystal (vertical double line with interference fringes on both sides), that is similar to micropipes which are normally found in SiC. We suppose it is a superdislocation with a large Burgers vector but, as distinct from a micropipe, without being hollow.

4.2 Characterization of synthetic diamonds. Experimental results.

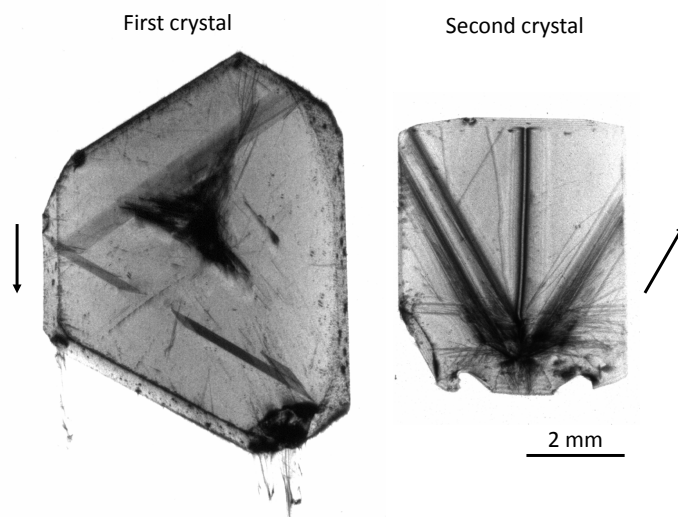


Figure 4.13: White beam topography in transmission geometry of two diamond plates, 111 oriented. The reflections used were of the $\{220\}$ family, and the projection of the diffraction vectors are indicated by the arrows. Both plates present a large number of defects, which are clearly visible in the double crystal topographs shown in fig.4.14

Fig.4.14 shows a series of topographs collected by rocking the second crystal, after the first crystal was set to diffract the monochromatic beam ($E= 10.5$ keV) produced by a double Si 111 crystal monochromator at ID06. The angular step between images was 0.36° . The reflections used were the 333 for both crystals. Each image obtained is an overlap of defective regions in both crystals.

In order to overcome the problem of dispersion in double crystal topography when a good reference crystal of the same material is not available, there are different solutions. One is to obtain a beam with high monochromaticity and small divergence using multiple crystal systems, [101, 142]. We concentrated on two other possible solutions: to use a perfect crystal and to slightly bend it in order to correct for dispersion [96, 97, 98] or to use a set of planes in the beam conditioner whose d-spacing is not too different from that of the reflection in the sample [99]. I will now present some of the results obtained with the two methods. Fig.4.15 shows a series of reflection topographs of the same Ib diamond shown in fig.4.11, collected using a bendable monochromator. The reflections used were the 800 for the bent silicon and 444 for the diamond, and the energy was 20 keV. The angular step size between two images is 0.2° . The difference compared to the

4. CHARACTERIZATION OF SINGLE CRYSTAL DIAMONDS

previous dispersive setup is clear; it is now possible to clearly distinguish the different growth sectors that diffract at different angular positions of the sample. This is related to the different concentrations of nitrogen in the different growth sectors that expands the lattice as shown in equation 4.1. It is possible to estimate the difference in the lattice parameter between different growth sectors simply from the angular positions where the intensity in a given growth sector is maximum. For example, a difference of $0.8''$ is present between the fourth image in the first row and the third image in the second row. If we assume only differences in d-spacing between growth sectors and by using 3.4 we obtain an estimation of $\Delta d/d \approx 3.9 \times 10^{-6}$ between regions in the two growth sectors.

An example of topographs taken using a quasi non-dispersive configuration by combining the silicon asymmetric 331 of a 111 oriented plate reflection with a high quality type IIa diamond 220 symmetric Bragg reflection is shown in fig.4.16. The mismatch between the silicon lattice planes and the diamond lattice planes in this configuration is 1.22 %. The angle between 111 and 331 lattice planes is 22° resulting in an asymmetry factor b , for an energy of 13 keV, of $-1/79$. The divergence of the beam after the collimator is shrunk to $0.14''$ and is smaller than the angular the Darwin width of the diamond, $0.82''$.

The sample is a high quality IIa type HPHT diamond, 0.5 mm thick. The streaky artefacts that clearly appear only near the peak of the rocking curve (darker pictures) come from the direct beam and are phase contrast images probably related to a low quality beryllium window. Due to the high asymmetry of the first reflection, they appear as vertically elongated features. From this series of topographs it is also possible to notice the different penetration depth of the X-ray along the rocking curve, see fig.2.8. For the 220 reflection at 13 keV the extinction distance t_{ext} is $\approx 4 \mu\text{m}$ whilst the absorption depth t_{abs} is $\approx 1.2 \text{ mm}$, *i.e.* more than the sample thickness. The large absorption depth allows a perspective view of all the defects in the bulk. On the top of the rocking curve, *e.g.* the first topograph on the second row, only the surface layer is visible since the absorption is dominated by the extinction.

Finally, it is not possible to discern whether the inhomogeneity of the diffracted intensity for the topographs near the maximum of the rocking curve is due to the small dispersion or to the fact that the sample is slightly bent.



Figure 4.14: Series of topographs in a non-dispersive arrangement taken at ID06 using two diamond crystals, 111 oriented, 333 reflection, monochromatic beam of $E=15$ keV. The arrow shows the projection of the incident and diffracted wavevectors.

4. CHARACTERIZATION OF SINGLE CRYSTAL DIAMONDS

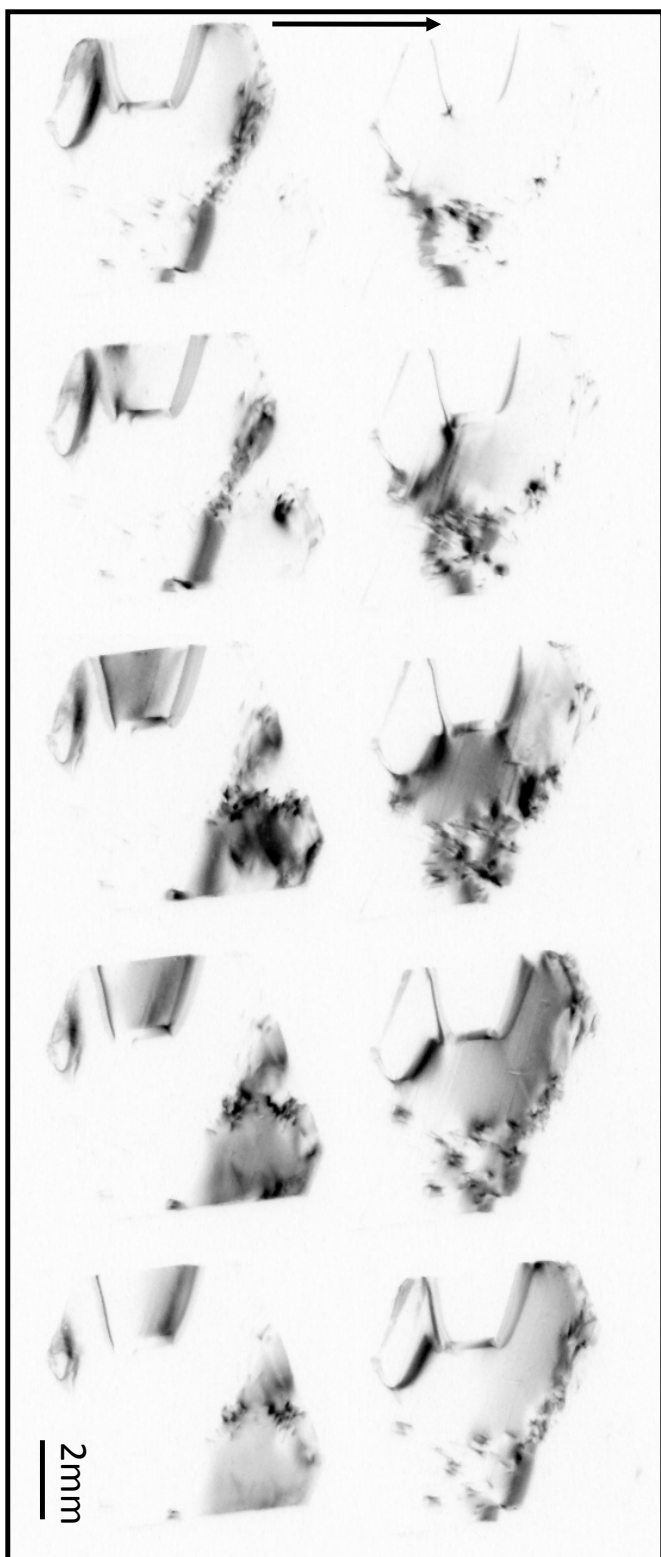


Figure 4.15: Part of a series of topographs in a non-dispersive arrangement taken at ID19 using the beam coming from a bendable. $E = 20$ keV, 800 reflection of the bendable silicon crystal, 444 reflection for the diamond, Bragg geometry. The diamond sample is the same as the one in fig.4.11. The step size between two images is 0.2° and the arrow shows the projection of the incident and diffracted wavevectors.

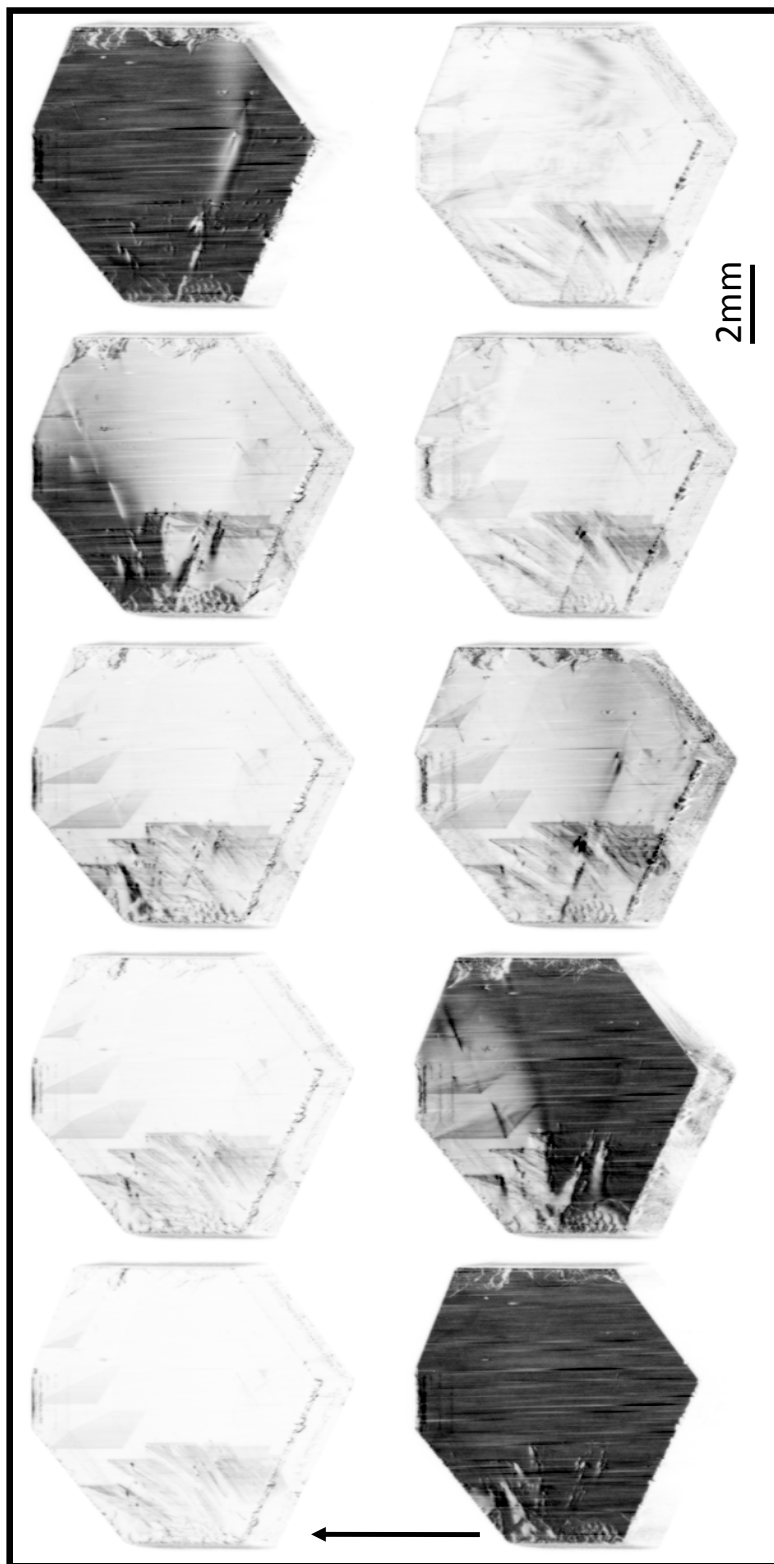


Figure 4.16: Series of topographs in a quasi non-dispersive arrangement taken at BM05 using the beam coming from an asymmetric reflection. $E=13$ keV, 531 reflection from the silicon collimator, 220 reflection for the diamond. The sample is a high quality IIa type HPHT diamond. The defects that clearly appear on the top of the rocking curve (darker pictures) are coming from the direct beam and are phase contrast images probably related to a low quality beryllium window. The projection of the incoming and diffracted wavevectors is represented by the arrow.

4. CHARACTERIZATION OF SINGLE CRYSTAL DIAMONDS

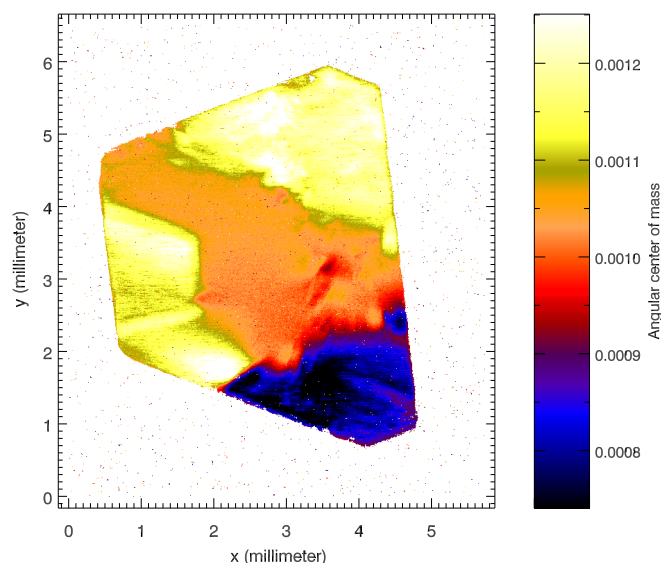


Figure 4.17: Map of the angular center of mass positions of the pixel by pixel rocking curve obtained using the diamond shown in fig.4.15 using the software *Visrock*.

By combining all the topographs collected at different angular positions it is possible to obtain a map of local rocking curves pixel by pixel. This method is called Rocking Curve Imaging RCI and has been developed by Lübbert and co-workers, [102]. One of the requirements for the RCI is that the topographs are collected with a CCD camera. In order to analyze the series of images I have used the program *Visrock*, developed by Lübbert and Baumbach, [143]¹ *Visrock* analyzes the series of images to obtain different maps related to the local rocking curve pixel by pixel, such as angular position of the maximum or FWHM of the rocking curve. It is possible to perform a refined estimation of the nitrogen content difference between the different growth sectors using a similar series of topographs as the one shown in fig.4.17 (with a smaller step size and an extended angular range), using the angular position of the centre of mass of each pixel. For example, the difference between the growth sectors shown in yellow in fig.4.17 and the large part of the diamond shown in orange is of $\approx 0.0002^\circ$. This can be transformed in a difference of d-spacing of $\approx 3.5 \times 10^{-6}$. This is similar to the value obtained by the previous estimation, but now it is obtained pixel by pixel. Moreover, this value

¹ *Visrock* is available from this link: <http://www.esrf.eu/computing/scientific/VISROCK/MAIN.htm>.

4.2 Characterization of synthetic diamonds. Experimental results.

is similar to what was found by Lang and co-workers, [144] on a type Ib sample. By using equation 4.1, we obtain a difference of concentration of (29 ± 7) ppm, which is a plausible value for Ib diamonds.

A second example of the potentiality of RCI is illustrated in fig.4.18, which shows an example of the results obtained with a similar series of topographs of the IIa diamond shown in fig.4.16 (with smaller step size and a broader scan). The rocking curve collected in one pixel belonging to the more perfect region, together with the integral rocking curve of the entire crystal, are compared with the theoretical reflectivity curve. For the single pixel rocking curve, there are very small deviations from the ideal reflectivity curve, which is a confirmation of the high quality of this diamond plate in this region.

4.2.2.3 Quantitative analysis of the effective misorientation in a high quality type IIa diamond

It is possible to determine the effective misorientation defined in 3.4 using X-ray topography. Nevertheless, it is important to mention that to “back calculate” the origin of the deformation from the topograph is an inverse problem and is not possible in a general way due to the missing information related to the phase, which is lost when recording the diffracted intensities, [145]. An exception is given if it is possible to apply the dynamical theory for perfect crystal to locally deformed crystals, [146]. This is an approximation that holds only if the effective misorientation is small inside the “area of influence” [46], which is represented with the red regions for the Bragg and Laue case in fig.2.7.

We used two different methods in order to determine the effective misorientation in this approximation:

- analyzing a topograph collected on the steepest part of the flank of the rocking curve, where the strain sensitivity is highest;
- collecting a series of topograph for several working points along the rocking curve and recording the angular positions of the maximum intensity in the different regions of the sample.

The first method was introduced by Bonse in 1958 [147]. If we assume that the changes in $\delta\theta$ in the region of interest are so small that the working point shifts in the linear

4. CHARACTERIZATION OF SINGLE CRYSTAL DIAMONDS

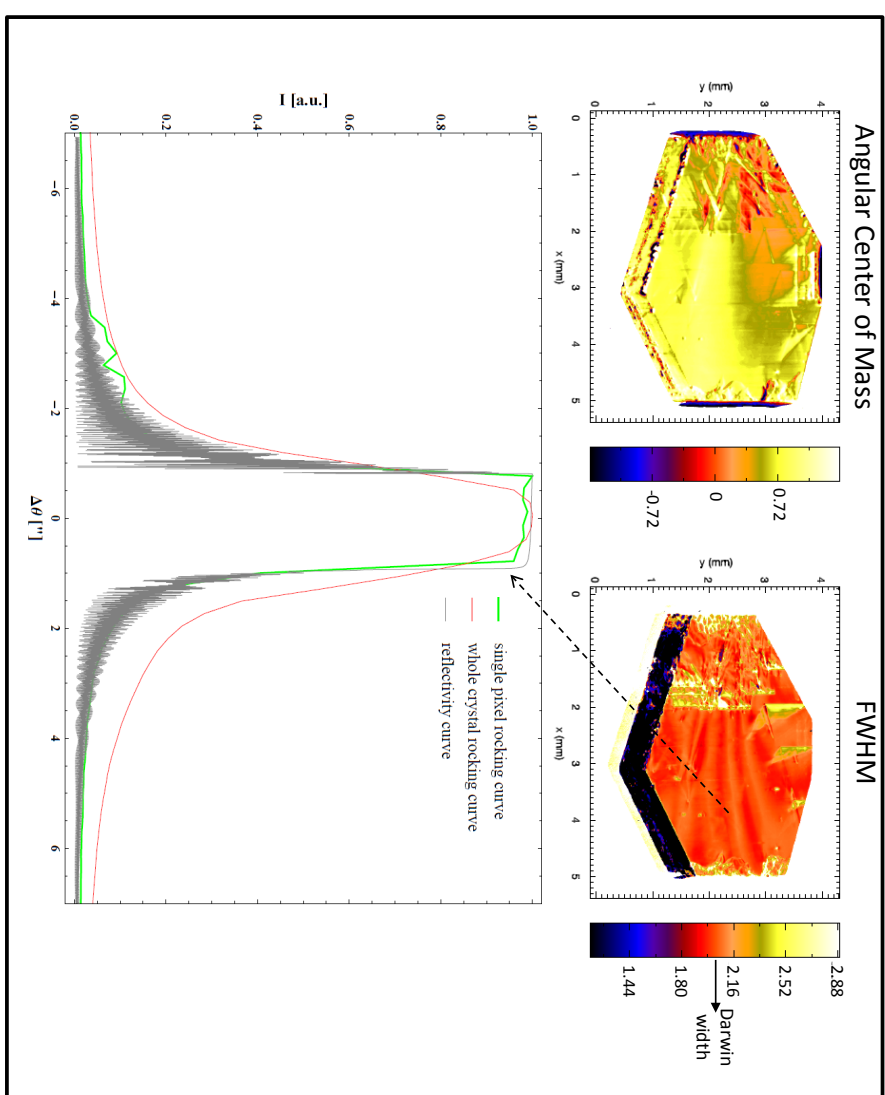


Figure 4.18: Top: Rocking Curve Imaging maps of the type IIa diamond shown in fig. 4.16; left: angular position of the center of mass, and right: value of the FWHM calculated pixel by pixel. Bottom: comparison between the rocking curve obtained from the pixel indicated with the arrow, the average rocking curve of the entire crystal and the theoretical reflectivity curve.

4.2 Characterization of synthetic diamonds. Experimental results.

part of the flank it is possible to directly relate the intensity variation on the topograph to the variation of the effective misorientation simply by

$$\frac{\delta I^x}{I_{\max}^x} = k \delta\vartheta \quad (4.2)$$

where δI^x is the relative change of intensity, I_{\max}^x is the X-ray intensity on the top of the rocking curve, k is the slope of the rocking curve normalized to one (the superscript x is to indicate X-ray). It is clear from equation 4.2 that for larger slopes the intensity variation corresponding to the same misorientation will be larger (or similarly, a same intensity variation will corresponds to smaller effective misorientation). One of the advantages of the bent monochromator is the possibility to change the strain sensitivity by changing the pair of reflections used for the monochromator and the sample. In order achieve this, a series of silicon bendable monochromators with different orientation are available.

Fig.4.19 shows three topographs of a high quality type IIa HPHT diamond, 100 oriented, see [113]. The left image is a white beam transmission topograph, reflection 220. There are clearly visible scratches on the bottom left part of the plate, the rest of the plate is almost defect-free, with mainly three isolated dislocations barely visible. The other two topographs are collected using the bendable monochromator, in Bragg geometry. The middle one was taken at 12 keV, using the 444-reflection for the monochromator (Darwin width $w_h = 1''$) and the diamond 115-reflection ($w_h = 1.02''$). The slope of the rocking curve, in the steepest point is about $1.2''^{-1}$. If we assume that it is possible to detect intensity variation of 1%, this implies a theoretical detection limit of $\approx 4 \times 10^{-8}$. In this topograph, the dislocations are now well visible, but the rest of the plate seems still homogenous. The right topograph was taken at 20 keV using Si-800 and C*-800 reflections (Darwin widths of $0.31''$ and $0.25''$ respectively). The slope on the flanks is about $4''^{-1}$, and the detection limit is $\approx 1.2 \times 10^{-8}$. With this enhanced strain sensitivity it is possible to see inhomogeneities in the region which before were homogenous; moreover, the image width of the single dislocations is now much larger, up ≈ 1 mm from the core of the dislocation.

The topographs can be collected with either CCD cameras or with films. In the latter case, an intermediate conversion is necessary in order to obtain the X-ray intensity that stroke the film. If the film is not overexposed, the darkening S is proportional to the X-ray intensity. During the digitalization, optical light is transmitted through

4. CHARACTERIZATION OF SINGLE CRYSTAL DIAMONDS

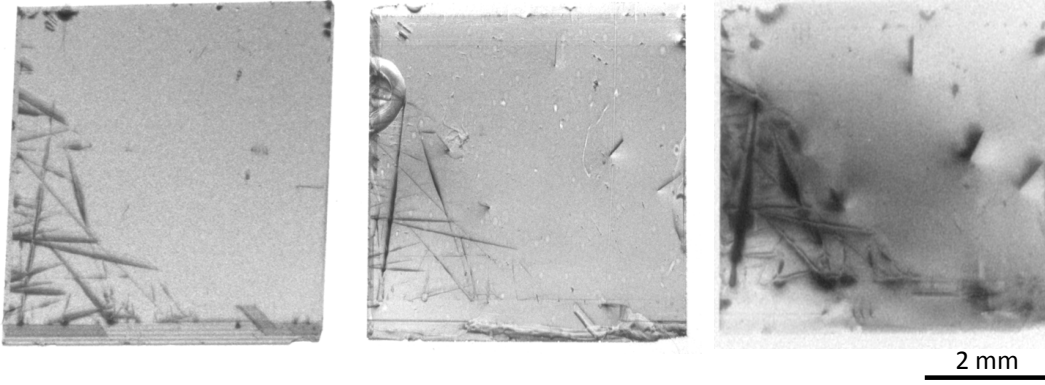


Figure 4.19: Left, white beam topographs in Laue geometry, 220 reflection, of a high quality type IIa diamond. Middle and right, double crystal topographs collected with the bendable monochromator diffractometer. The detection limits for the two topographs are of about $\approx 4 \times 10^{-8}$ for the middle one and $\approx 1.2 \times 10^{-8}$ for the right one.

the film and is recorded by a CCD camera. The visible light is absorbed by the film following the Beer-Lambert law of absorption, $S(x, y) = \log(I_0^L/I^L(x, y))$, where I_0^L is the intensity of light transmitted at a point of the film that is unexposed and $I^L(x, y)$ is the intensity at a point (x, y) of the image. These considerations will bring to the following

$$\frac{\delta I^x}{I_{\max}^x} = \frac{I^x - I_{\text{av}}^x}{I_{\max}^x} = \frac{\log \frac{I_0^L}{I^L} - \log \frac{I_0^L}{I_{\text{av}}^L}}{\log \frac{I_0^L}{I_{\max}^L}} = \frac{\log \frac{I_{\text{av}}^L}{I^L}}{\log D_R} \quad (4.3)$$

where the subscript av stands for the average intensity in the region we want to study (if possible - in a perfect reference region) and D_R is the dynamic range. This is defined as the ratio of the light intensities in an unexposed part of the film, I_0^L , and in the region we are interested, measured on the topograph collected on the top of the rocking curve, I_{\max}^L . The estimation of the dynamic range can be source of errors, *e.g.* if the angular step size used to collect the topographs is too large one could jump over the top of the rocking curve, resulting in a wrong I_{\max}^L . Finally, by joining equations 4.2 and 4.3 we obtain:

$$\delta\vartheta = \frac{\log \frac{I_{\text{av}}^L}{I^L}}{k \log D_R} \quad (4.4)$$

4.2 Characterization of synthetic diamonds. Experimental results.

It is now important to determine the value of k , which is the slope of the normalized rocking curve. As defined previously in section 3.1, the rocking curve is given by the convolution of the reflectivity curves of the two crystals, *i.e.* the bent silicon and the diamond crystal.

Uschmann and co-workers [148] have calculated the X-ray reflection properties of elastically bent crystals in Bragg geometry. They based their calculations on the Takagi-Taupin theory [149, 150] for deformed crystals. It is necessary to understand whether for our experimental conditions it is necessary to calculate the reflectivity curve for the bent crystal or if the perfect flat crystal one is a sufficient good approximation. This is possible by estimating the bending radius of the silicon crystal. After Chukhovskii *et al.* [151], the general equation for the non-dispersive setting for a polychromatic and divergent wave and two curved crystals is

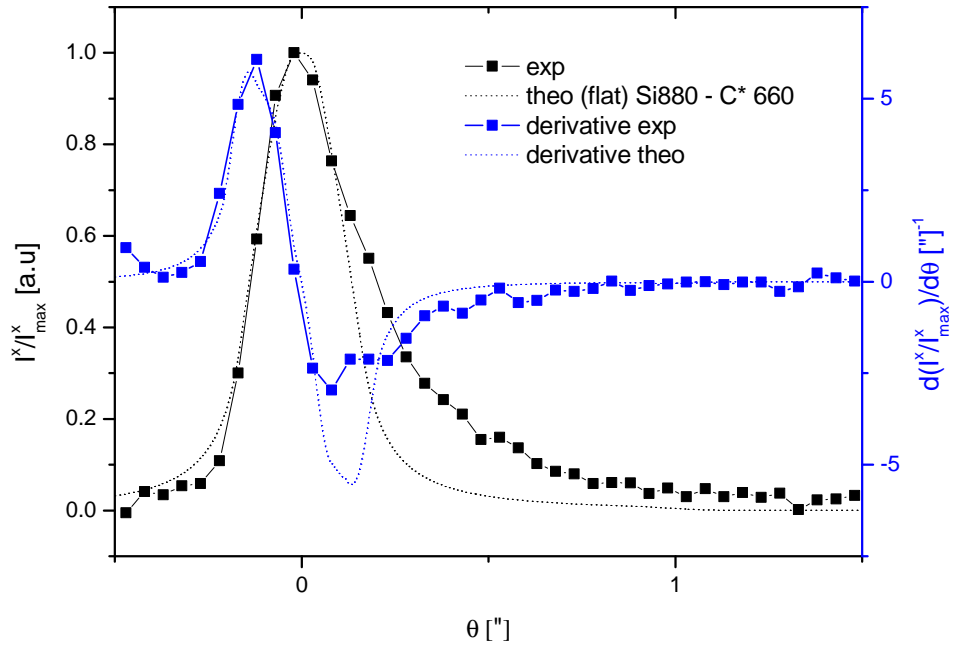


Figure 4.20: Comparison between the experimental and the theoretical rocking curves, together with their derivatives. The experimental rocking curve is different respect the theoretical one in the high angles side. The experimental data are obtained from a RCI series using a ROI of $\approx 0.5 \times 0.5 \text{ mm}^2$ in a region of the sample without defects.

4. CHARACTERIZATION OF SINGLE CRYSTAL DIAMONDS

$$\frac{\tan \theta_{B,2}}{\tan \theta_{B,1}} = \frac{\left(1 - \frac{L_{0,2}}{R_2 \sin \theta_{0,2}}\right) \left(1 + \frac{2L_{0,1}}{R_1 \sin \theta_{0,1}}\right)}{\left(1 + \frac{L_{0,1}}{R_1 \sin \theta_{0,1}}\right)} \quad (4.5)$$

where the index 1 and 2 represent the first and second crystal, R are the curvature radii (positive if the first crystal is convex and the second is concave), L_0 is the source to crystal distance, θ_B and θ_0 are respectively the Bragg and incident angles, allowing asymmetric reflections to be considered. In our case we assume the diamond crystal to be flat, *i.e.* R_2 is infinite. From 4.5 is possible to obtain the radius of curvature of the first crystal to obtain a non-dispersive setting

$$R_1 = \frac{L_{0,1}}{\sin \theta_{0,1}} \left(1 + \frac{1}{1 - \frac{\tan \theta_{B,2}}{\tan \theta_{B,1}}}\right)^{\ddagger} \quad (4.6)$$

If we substitute in the formula typical experimental values for the distances and the Bragg angles, we obtain a bending radius of the order of few kilometres at ID19 and some hundredths of meters at BM05. Therefore in the first approximation, we decided to use the reflectivity curve of the flat crystal to calculate the theoretical rocking curve, and to calculate the slope on the flanks.

Fig.4.20 shows a comparison between the theoretical calculation (Si880 and C* 660 reflections, $E=20$ keV) and the experimental data. The data have been obtained from a series of topographs collected with a PCO camera on a high quality type IIa diamond and integrating the intensity in a ROI of $\approx 0.5 \times 0.5$ mm², chosen in a part of the sample without defects. The agreement is quite good on the low angle side of the rocking curve but is worse on the high angle side. We attributed this difference to the fact that the first crystal is bent. In order to confirm this, we decided to calculate the rocking curve using the reflectivity curve of a bent silicon crystal.

The reflectivity curves of bent crystal were calculated by I. Uschmann. A comparison between the reflectivity curves of flat and cylindrically bent (radii of curvature of -208 m and -463 m) silicon crystals is shown in fig.4.21. Some oscillations due to the bending are present on the high angle side. Such oscillations in bent crystals have been measured for the first time by Uschmann and co-workers [152] on a quartz crystal.

[‡]in the Altin *et al.*, [98] a similar formula is obtained, but is present a typing error, $\theta_{B,1}$ and $\theta_{B,2}$ are inverted. Moreover, the convention for the sign is opposite.

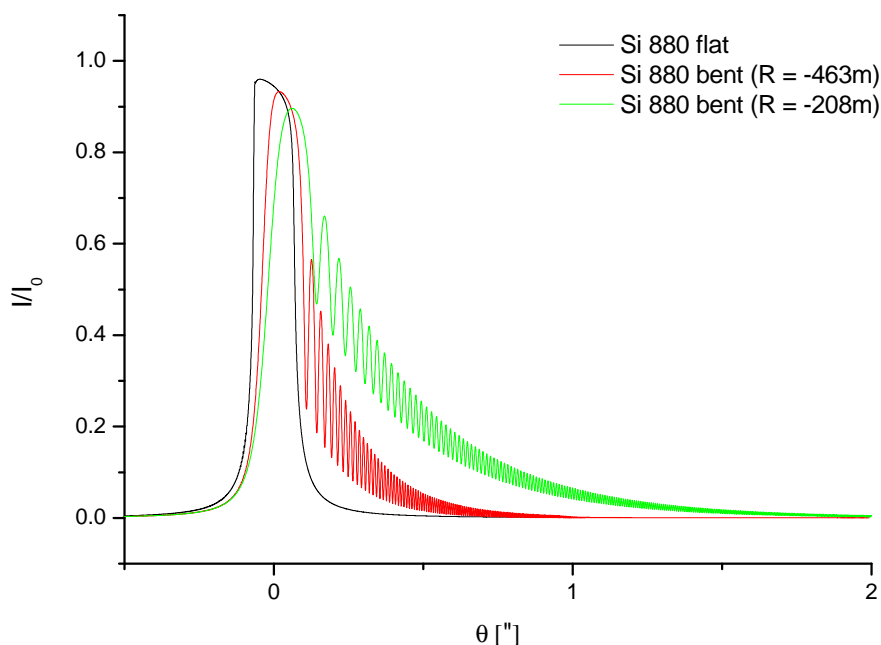


Figure 4.21: Comparison between the theoretical rocking curve for flat and bent silicon crystal for two different radii of curvature. 880 reflections, $E = 20$ keV, crystal thickness 2 mm.

Fig.4.22 shows the comparison between the same experimental data shown in fig.4.20 with the rocking curve calculated using the bent crystal reflectivity curve. The agreement between the theory and the experimental data is considerably improved, especially on the high angle side, and is a confirmation of the exactness of the theory used. Nevertheless, since the working point of the analysed topograph sits on the low angle side of the rocking curve, the error made by using the reflectivity curve of a flat crystal instead of a bent one is negligible.

Moreover for these experimental conditions (concave crystal, negative curvature), the high angle side of the rocking curve is less sensitive to deformations, since the slope is much smaller. This is clearly visible in fig.4.23; on the left is shown a topograph recorded on the low angle side of the rocking curve in fig.4.22 while on the right is the topograph recorded on the high angle side. For example, the width of the single

4. CHARACTERIZATION OF SINGLE CRYSTAL DIAMONDS

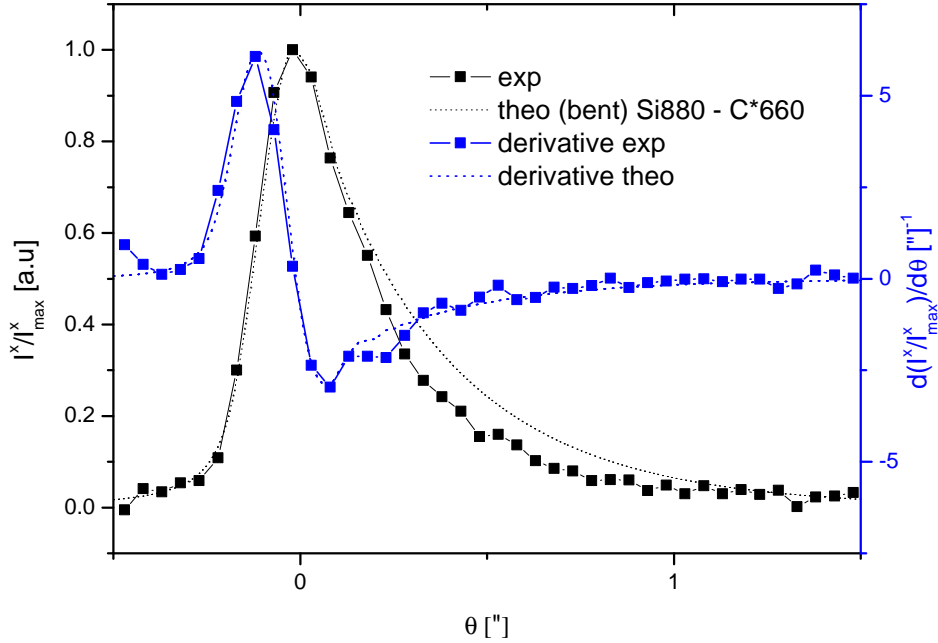


Figure 4.22: Comparison between the experimental and the theoretical rocking curves obtained using bent silicon reflectivity curve shown in fig.4.21, together with their derivatives. The agreement is improved on the high angle side respect fig.4.20.

dislocation is much larger on the left topograph than on the right one. In addition, whilst in the topograph taken on the lower strain sensitive condition the intensity is quite homogenous on most of the crystal plate, on the topograph taken on the high strain sensitive side the image is more inhomogenous.

In the second method, a series of topographs at different angular positions is recorded. The scan needs to be large enough in order to cover the entire rocking curve. By using the software *Visrock*, the angular position of the center of mass of the rocking curve of each pixel is obtained. This map represents directly the effective misorientations.

In both methods it is possible to separate the two components - $\Delta d/d$ and $\Delta\varphi$ - of 3.4 by collecting the topographs at two opposite azimuthal positions, *i.e.* by rotating about the surface normal of 180° between the two positions. This method was introduced by Bonse [153] in the study of natural quartz crystal, and has been used among others

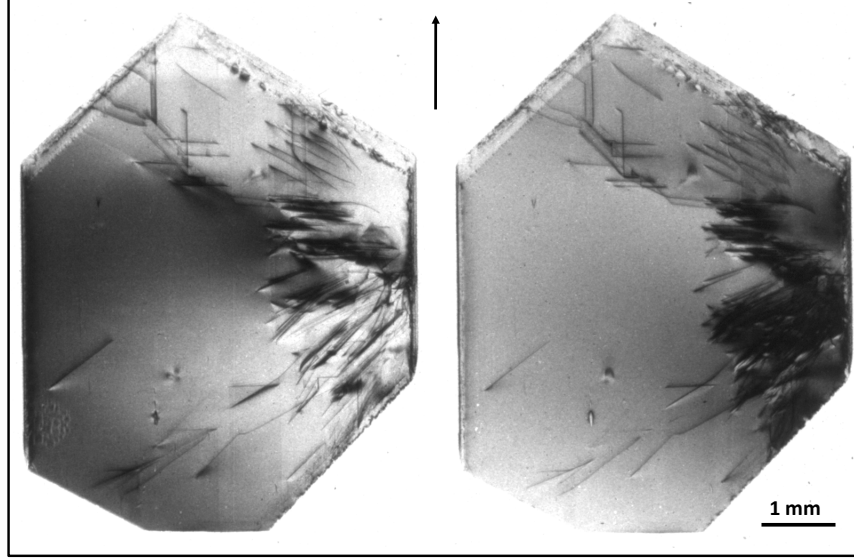


Figure 4.23: X-ray topographs in a non-dispersive setup collected with the bendable monochromator; left on the low angle side of the rocking curve, right on the high angle side. The difference in strain sensitivity, as estimated by the rocking curve in fig.4.22 is well visible, for example in the width of the single dislocation image on the left side of the plate. The arrow represent the projection of the incoming and diffracted wavevectors.

by Kikuta [154] on silicon crystals, by Yoshimura *et al.* [155] on synthetic quartz, by Lang *et al.* [144] on Ib diamond crystals and recently by Macrander *et al.* [156] also on Ib diamond crystals. The idea behind this method is that, when changing the azimuthal positions of the crystal by 180° , the regions where the effective misorientation is composed only of lattice spacing variation will present the same contrast, whilst for the tilted regions the contrast will be inverted.

By calling $\Theta_0(x, y)$ and $\Theta_{180}(x, y)$ the angular positions of the maximum for the pixel (x, y) and the azimuthal angles 0° and 180° respectively, we obtain that the d-spacing variation can be written as:

$$\frac{\Delta d}{d}(x, y) = \cot \vartheta_B \left(\frac{\Theta_0(x, y) + \Theta_{180}(x, y)}{2} \right) \quad (4.7)$$

whilst the angular tilt can be expressed as

$$\Delta \varphi(x, y) = \frac{\Theta_{180}(x, y) - \Theta_0(x, y)}{2} \quad (4.8)$$

4. CHARACTERIZATION OF SINGLE CRYSTAL DIAMONDS

It is possible now to compare the results obtained with the two methods on a high quality diamond sample. Fig.4.24 shows the quantitative misorientation map obtained from a topograph collected on the steepest part of the flank of the rocking curve, obtained using the 880 reflection of the silicon crystal and the 660 reflection of the diamond, at 20 keV. The slope used in the calculation was $5.8''^{-1}$, resulting in a theoretical detection limit of $\approx 0.810^{-8}$. The image was collected on a film due to the very low intensity of the reflection, and the dynamic range was estimated to be ≈ 24 . A CCD camera was also used to collect the series of topographs at different angular positions, but the pictures had a very small dynamic range (≈ 5) and noisy data. Therefore the results obtained are worse and will not be presented.

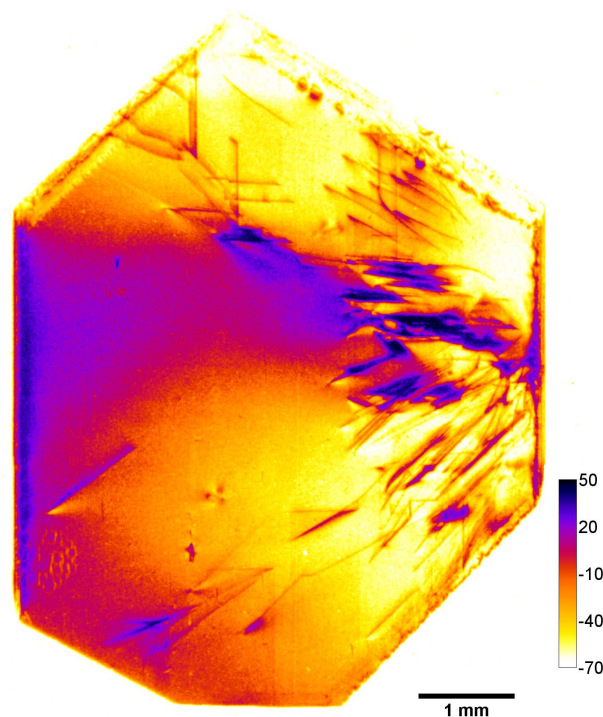


Figure 4.24: Effective misorientation map of a IIa diamond crystal, bent silicon 880, diamond 660 reflections, 20 keV. The values in the colour bar are expressed in 10^{-8} .

The effective misorientation is of the order of 4×10^{-8} for a region of interest of $0.5 \times 0.5 \text{ mm}^2$ and 1×10^{-7} in a region of $1 \times 1 \text{ mm}^2$. Fig.4.25 shows angular position maps of the center of mass of the pixel by pixel rocking curves. The reflections used were the 440 for both the silicon and the diamond crystal. The strain sensitivity in

4.2 Characterization of synthetic diamonds. Experimental results.

this case is smaller, with a slope of the rocking curve of $\approx 2''^{-1}$. At the same time, the intensity of the reflections is higher than in the high strain sensitive configuration discussed previously, and therefore it was possible to collect images with a good statistic using the CCD camera.

The maps of d-spacing variations and tilt are shown in fig.4.26. The values obtained for the d-spacing variation in a similar region of interest of $0.5 \times 0.5 \text{ mm}^2$ is about 8×10^{-8} ; in the same region the tilt variations are of the order of 4×10^{-8} .

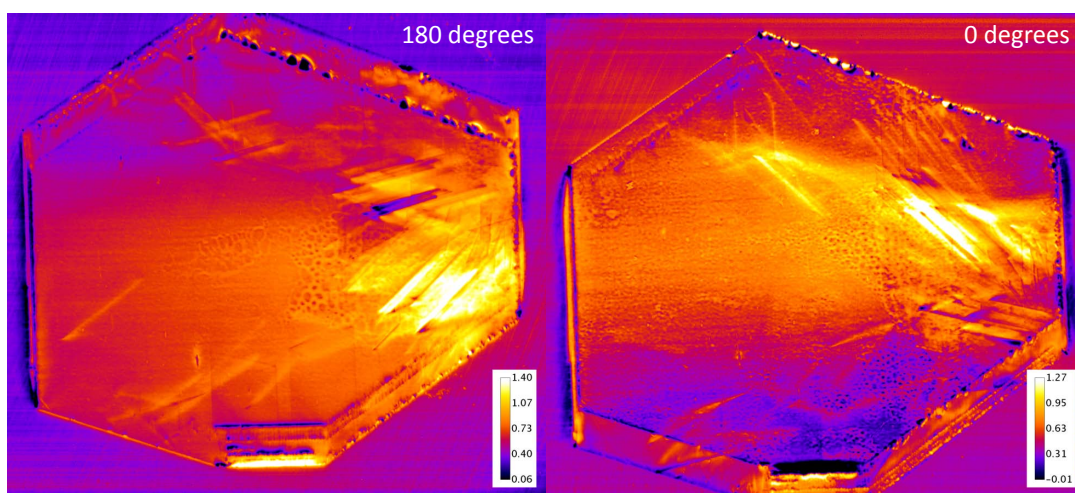


Figure 4.25: Maps of the angular position of the center of mass of the rocking curve pixel by pixel, obtained using *Visrock*. Si 440 and C* 440 reflection, $E = 20 \text{ keV}$. The color bar is expressed in arcseconds. The roundish structured features presented in the images are phase contrast artefacts present in the direct beam.

Therefore the values obtained with the two methods are in good agreement and are a proof of the validity of the method. It is therefore possible to select the method that better suits the experimental conditions. It is finally important to highlight the incredibly high quality of the diamonds studied. In regions of up to $1 \times 1 \text{ mm}^2$ the quality is comparable to the one obtained for silicon crystals, [157], and are therefore perfectly suited to be used as optical elements at the beamlines.

In fig.4.27 it is possible to see the improvements in the quality of the synthetic diamonds used as phase plates at the ESRF. On the top row, two Ib diamonds used in the past as phase plates, the left one at BM28 and the right one at ID24; on the bottom row, two of the recently purchased plates, now in use at the beamlines ID06 and ID20.

4. CHARACTERIZATION OF SINGLE CRYSTAL DIAMONDS

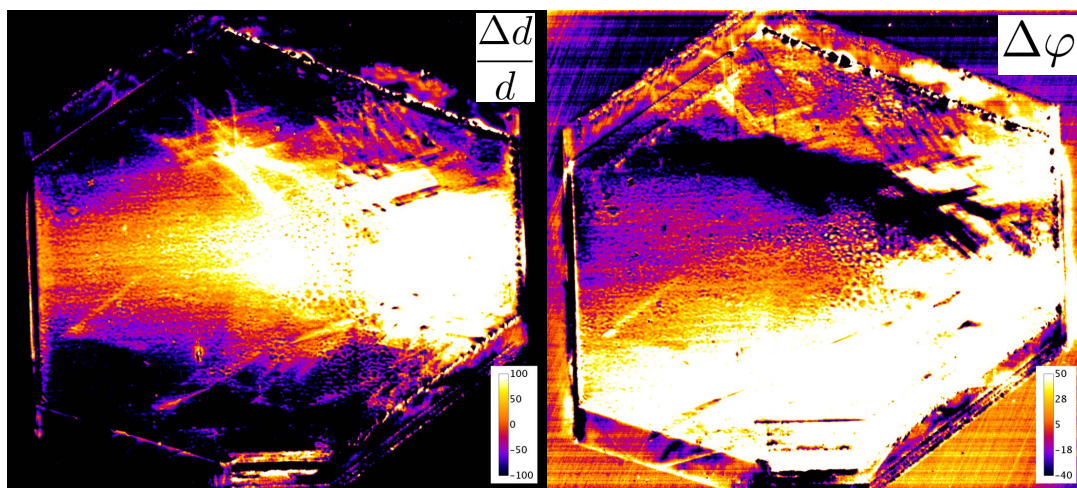


Figure 4.26: Separated maps of d-spacing variations and tilt. In order to visualize the high quality part of the crystal the contrast has been exaggerated. The values are expressed in 10^{-8} .

Recently we obtained a further demonstration that an improvement in the quality of the diamond used can make a large difference to the performance of a beamline. At ID14-2 they replaced an old type Ib 100 oriented diamond beam splitter which used the 111 asymmetric Laue reflection with a recently purchased type IIa 110 oriented one (111 symmetric Laue reflection). The flux measured with the new diamond was 1×10^{12} , ten times larger than the maximum flux obtained with the old one.

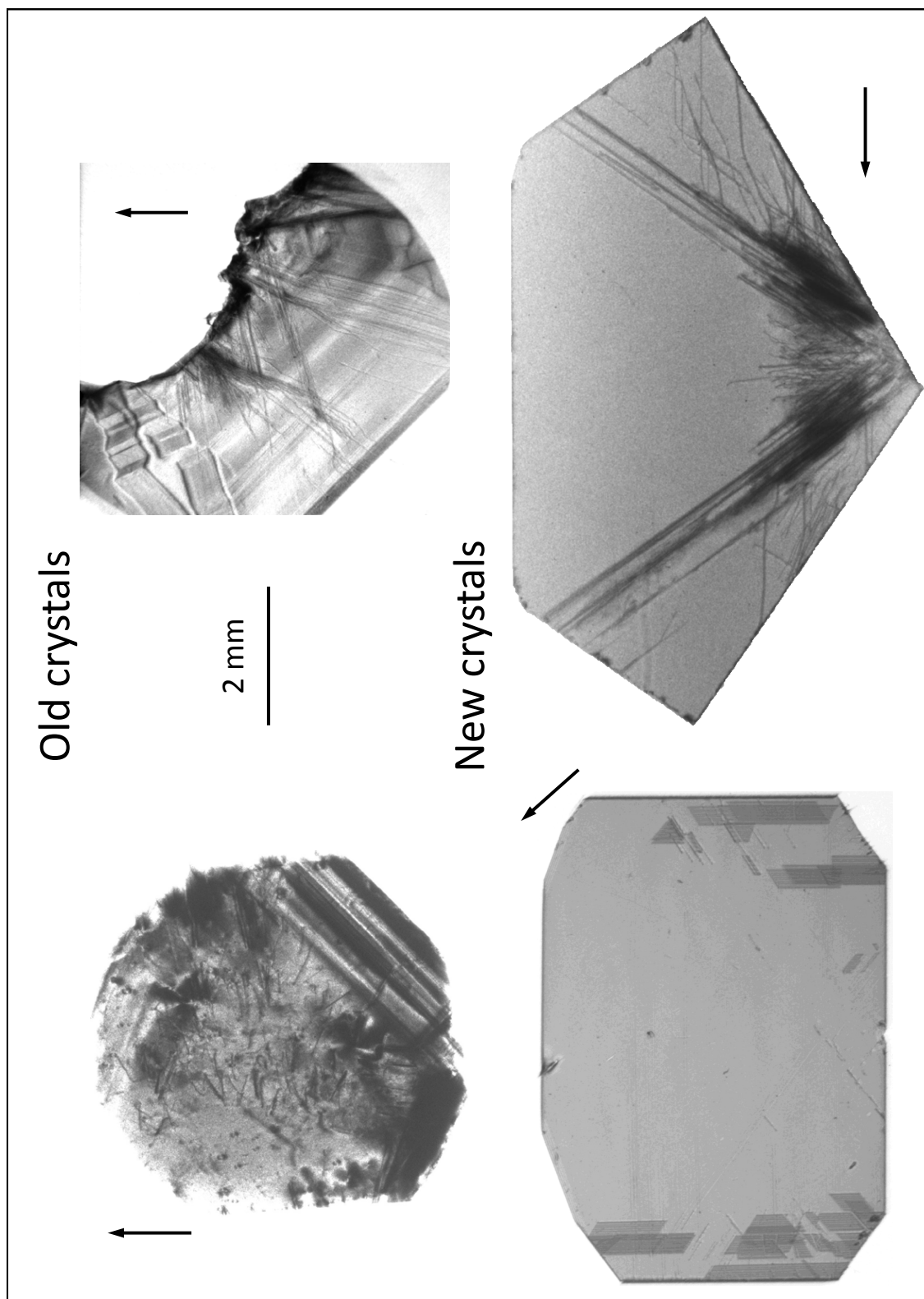


Figure 4.27: White beam topographs of synthetic diamond crystals used as phase plates. Top row, old plates. Bottom row, plates recently delivered by Element Six. The arrows represent the projection of the diffraction vector.

4. CHARACTERIZATION OF SINGLE CRYSTAL DIAMONDS

4.2.3 Coherence measurements

In 2.3 the theoretical basis of the coherence of electromagnetic waves is presented. In this section I will show the results obtained using the Talbot effect in the characterization of the wavefront deformations related to the use of diamonds, especially when used as diffracting elements but also in transmission, as filter or window. The Talbot effect is the self-imaging of periodic structures under coherent illumination. It was discovered in 1836 by Henry Fox Talbot [158] and subsequently explained by Lord Rayleigh [159] to be a manifestation of Fresnel diffraction, and it has been demonstrated for hard X-rays by Cloetens *et al.* [160]. When a coherent wave impinges on a periodic object, *e.g.* a diffraction grid, images of the object are formed at periodic distances from the object itself. The periodic distance is called the Talbot distance D and is given by:

$$D_T = \frac{2a^2}{\lambda} \quad (4.9)$$

where a is the (lateral) period of the object and λ the wavelength of the light. For distances D equal to integer multiples of half the Talbot distance (also called D_R , replication distance), an image of the object may be registered, with a translation equal to $a/2$ in the detector plane for the odd integers and no translation for even integers, see fig.4.28.

In the case of a phase gratings, the results are different: no image is recorded at a distance equal to the replication distance (and its integer multiple) but images of the grid (with a contrast that depends on the phase shift created by the grating) are recorded at a distance equal to $D_T/4$ (and odd integer multiples of this).

For a perfectly coherent illumination the pattern reproduces itself at each replication distance. In the case of a partial coherent beam, the contrast of the image at every distance becomes weaker and weaker at every repetition distance. It is possible to model this by introducing a damping factor $\tilde{S}(zf)$, [160]:

$$I_m = \tilde{S}(zf)I_m^{coh} \quad (4.10)$$

where I_m and I_m^{coh} are the Fourier coefficients of the intensity distribution for a partially and a totally coherent beam, respectively. $\tilde{S}(zf)$ is the Fourier transform of the angular source size $S(\alpha)$ at a frequency f . By assuming a Gaussian distribution for the source

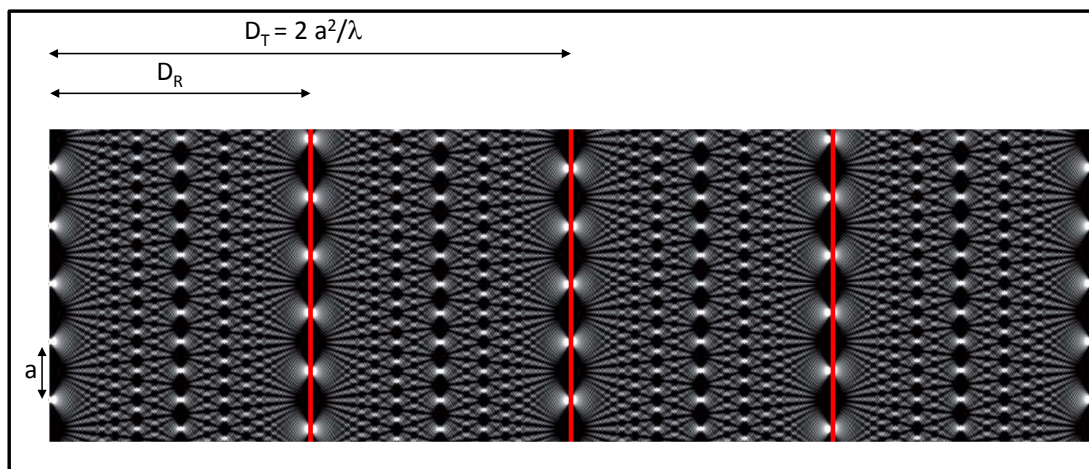


Figure 4.28: The Talbot effect for an absorbing gratings of period a , duty cycle 0.1 (90% is opaque, 10% is transparent). Indicated are the positions of the screen where the maximum contrast with the same period as the grid are collected. The image is a re-elaboration of the one in [161].

size, it is possible to obtain an estimate of the angular source size α_0 for the partially coherent beam as:

$$\alpha_0 = \frac{a}{\pi \sqrt{2(z_k^2 - z_0^2)}} \sqrt{\left[\ln \left| \frac{I_1(z_0)}{I_1(z_k)} \right| \right]} \quad (4.11)$$

where z_k and z_0 are distances from the screen with $z_k = z_0 + D_r$ and the $I_1(z)$ are the Fourier coefficients for the frequency $1/a$ of the image collected at the position z .

Experimental results

The experiments were performed at the long beamline ID19. The source size is $30 \times 120 \mu\text{m}^2$ (V×H) and the distance from the source is 150 m, resulting in an angular source size of $\approx 0.2 \times 0.8 \mu\text{rad}^2$ and a transversal coherence length of $\approx 290 \times 70 \mu\text{m}^2$ at 0.6 \AA . The choice of ID19 was taken especially considering the high degree of spatial coherence at the sample position. The grating we used was a two-dimensional grid, of period $\approx 6 \mu\text{m}$, made of silicon. Fig.4.29 shows an SEM image of the grid, taken using the secondary electrons with the in-lens detector. It shows that the differences of thickness in the grid are about $1.8 \mu\text{m}$. At the energy we performed the experiment, 20.5 keV, the difference in absorption is negligible, $\approx 0.1\%$.

4. CHARACTERIZATION OF SINGLE CRYSTAL DIAMONDS

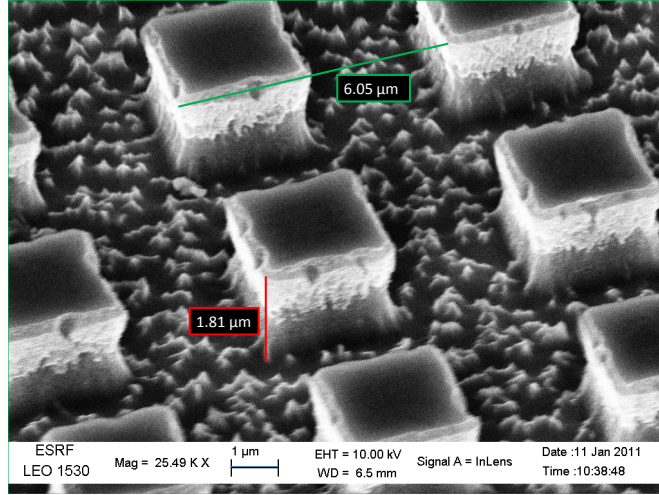


Figure 4.29: SEM picture of the Talbot grid.

Therefore the grid can be considered as a pure phase grid. The beam was produced by a U32 undulator with a gap of 17 mm, using the third harmonic. From the beam energy and the period of the grid is possible to calculate the Talbot distance, using equation 4.9. The results is $D_T \approx 1.2$ m. The detector was a FReLoN camera [139]. The pixel size after the optics was $0.7 \mu\text{m}$ resulting in a field of view of $1.4 \times 1.4 \text{ mm}^2$. Images were collected at distances of 300 mm and 900 mm from the sample, being respectively $D_T/4$ and $3D_T/4$, the positions where the contrast is maximum. Possible contributions from higher harmonics (mostly 333 reflection of the ninth undulator harmonics at 61.5 keV) were reduced (*e.g.* by a factor ≈ 70 for the third harmonic) by detuning the second crystal of the monochromator $\approx 0.5''$ ($\approx 20\%$ of the Si 111 Darwin width).

Fig.4.30 shows the configurations used to measure the transverse coherence of the beam. From equation 4.11 it is possible to see that it is possible to obtain the angular source size (in the approximation of a Gaussian distribution for beam) by using the coefficients of the Fourier transform of the image of the grid (at the spatial frequency corresponding to the inverse of the period) for two distances, in our case $D_T/4$ and $3D_T/4$. We collected a dataset of three images for each position: a *darkfield* image without the beam, a *flatfield* image with the beam but without the grid and finally a *fullfield* image, with the beam and the grid. In order to correct for “hot” pixels in the camera, which give fixed white spots, the darkfield was subtracted from both the other images.

4.2 Characterization of synthetic diamonds. Experimental results.

Afterwards, to correct for the presence of inhomogeneities in the beam, the resulting images are divided, fullfield/flatfield.

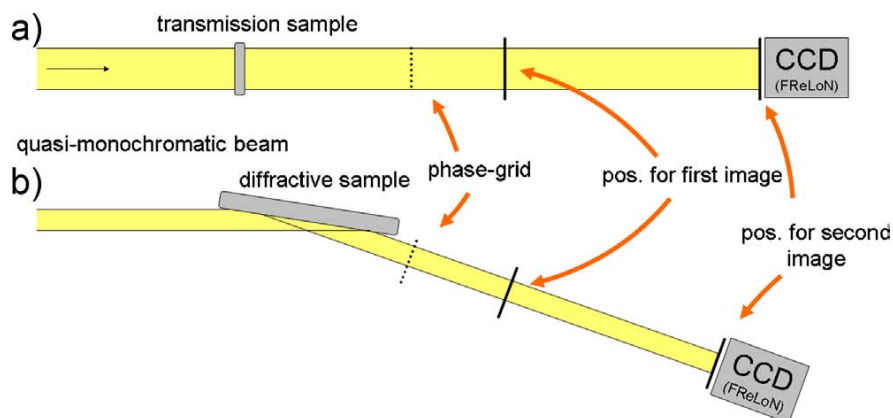


Figure 4.30: Talbot configurations used to measure the transverse coherence after optical elements: a) in transmission (filters, windows) b) in diffraction (monochromators, beam splitter). From [162].

In order to measure the increase in angular source size (resulting in a smaller transverse coherence length) arising from imperfections in the diffracting crystals, it is necessary to measure the angular source size of the beam impinging on the sample. This was done simply by collecting the two images in transmission without any sample. The values obtained were $0.3 \times 1.2 \mu\text{rad}$, slightly larger than the theoretical value ($0.2 \times 0.8 \mu\text{rad}$). This is related to the presence of optical elements (monochromator, beryllium windows and diamond filter) that disturb the wavefront.

To analyze the data I used a program written by Rafael Klünder (which is an improved version of a previous one by Peter Cloetens and Pierre Bluet). One of the improvements was the possibility of correct small misalignments of the grid with respect to the camera. Also, the two corrected images can be slightly misaligned, and a translation correction was made in order to have them overlapping exactly. Another point in the analysis that was improved compared to the previous versions was the leakage correction. Leakage is a problem that arises when using a Fast Fourier Transform of a signal which is not periodic in the sample window. This results in a smearing out of the amplitude of the real frequency into adjacent frequencies. In order to correct for this effect, two processes are effectuated on the data. First, the window is automatically cut pixel

4. CHARACTERIZATION OF SINGLE CRYSTAL DIAMONDS

sample	reflection	α_0 [μrad]	S [μm]
reference	-	0.32 ± 0.05	48 ± 8
diamond Ib (100)	022	1.7 ± 0.2	255 ± 30
diamond Ib (111)	111	0.91 ± 0.13	137 ± 20
diamond IIa (100)(top plate)	400	0.65 ± 0.12	98 ± 18
diamond IIa (100)(middle plate)	400	1.4 ± 0.2	210 ± 30
diamond IIa (100)(top plate)	022	1.3 ± 0.15	195 ± 23
diamond IIa (111)	0 $\bar{2}2$	1.4 ± 0.3	210 ± 45
diamond IIa (111)	111	0.85 ± 0.15	128 ± 23

Table 4.2: Angular source size for the reference beam and for different diffracting diamonds.

by pixel until the amplitude of the coefficient of the Fourier transform at the spatial frequency $1/a$ is maximised. Second, the signal is multiplied by a function, called the *Hanning truncation function* defined as

$$H(x) = \cos^2\left(\frac{\pi x}{2w}\right) \quad (4.12)$$

Where w is the width of the as-cut window. The user defines a Region of Interest (ROI) in the image. After the corrections described previously, a Fourier transform of the data in both the vertical and the horizontal direction is performed. The angular source size is obtained by inserting in equation 4.11 the intensities of the Fourier-transformed coefficient at the frequency $\frac{1}{a}$ for each propagation distance.

With the configuration shown in fig.4.30, it is possible to measure the coherence of the beam either in transmission or in diffraction. A summary of the results in diffraction is shown in tab.4.2, since in transmission the coherence appears to be always preserved. All the data were collected using horizontal geometry, *i.e.* the diffraction vector was horizontal. Moreover, the beam was monochromatized by a double silicon monochromator, diffracting in the vertical plane. Therefore, the geometry was a dispersive in both the horizontal and vertical direction, resulting in a diagonal band diffracting at each angular position of the sample.

For all the samples there is a considerable increase of the source size, from a factor of two to a factor of more than 4. The biggest values are for the type Ib diamonds and

4.2 Characterization of synthetic diamonds. Experimental results.

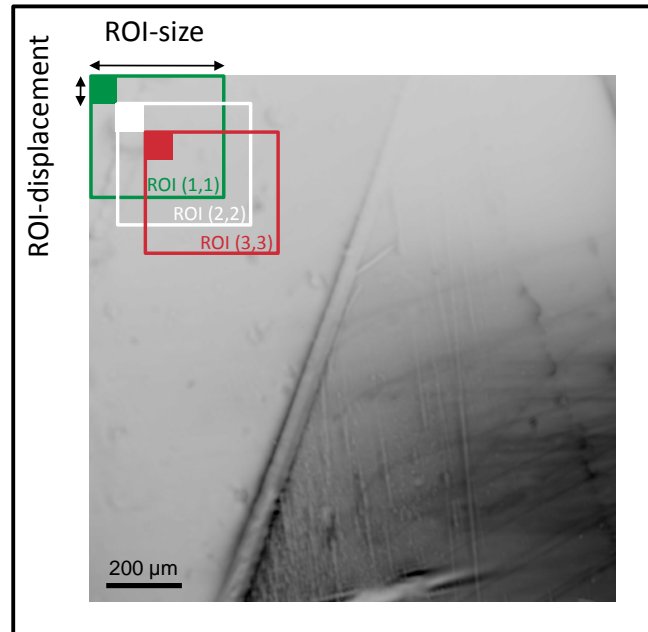


Figure 4.31: Example of ROIs and ROI displacement, shown on top of a diffraction image recorded at 300 mm from the sample. The coherence is calculated using all the pixels inside the ROI and the value is recorded in the top-left region of size equal to the displacement. Sample: 100 oriented, HPHT IIa crystal, reflection 400, and horizontal diffraction.

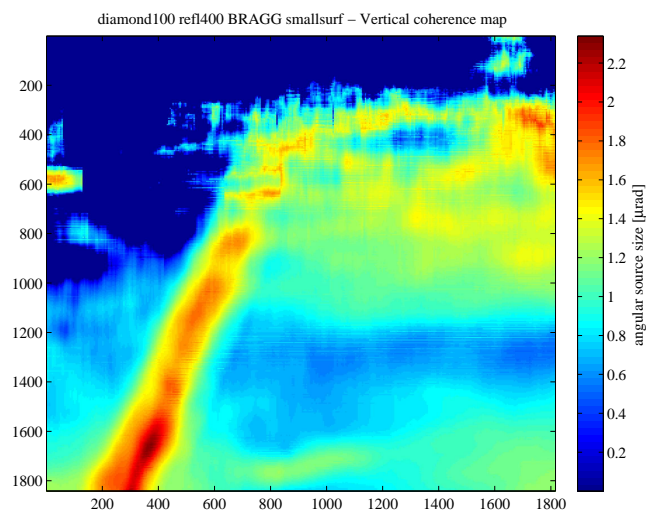


Figure 4.32: Example of the local coherence map of the sample shown in fig.4.31. ROI size 200×200 pixels, ROI-displacement 5 pixels.

4. CHARACTERIZATION OF SINGLE CRYSTAL DIAMONDS

for the symmetric Laue reflections, whilst the smaller values are obtained compared to the symmetric Bragg (for the same plate).

Recently, I've extended the main program, in collaboration with Rafael Klünder. By inserting two parameters, ROI size and displacement (fig.4.31), the software calculates the coherence over the entire image and produces a map of vertical and horizontal angular source sizes. In order for the program to analyze the data correctly, a lower limit on the ROI size of $\approx 150 \times 150$ pixels ($100 \times 100 \mu\text{m}^2$) has been used. There is no theoretical lower limit for the smaller displacement, but the time of calculation increases quadratically; in practice a displacement of 25 pixels gives a good compromise between calculation time and the resolution obtained on the coherence map.

The idea behind this extension to the original program is to try to measure the local effect of crystalline defects on the coherence properties of the diffracted beam. Moreover, by simply making a histogram of results "pixel by pixel", it is possible to obtain statistically valid values, such as the mean angular source size and standard deviation. The results obtained are comparable with the previous version of the software.

The advantage of the local mapping of the coherence is shown in fig.4.32 using the data obtained for the 100-oriented sample in fig.4.31. It is clear that the dislocations in the bottom-left part of the image increase the angular source size dramatically. The rest of the crystal seems better, but on average an increase of the angular source of approximately three times is obtained even in the more perfect region.

All the diamonds tested increased the angular source size, partially spoiling the coherence of the beam. Since the quality of the synthetic diamond bulk has been shown in the previous sections to be in some cases very good, we think that the problem still resides mainly in an imperfect finishing of the diamond surface or could be related to a small bending of the sample (some samples are rather thin, varying from 200 to 700 μm). Efforts for the future are concentrated in this direction: to improve the polishing process, in some cases by finding alternative methods, and to characterize not only the surface profile but also the damaged sub-surface layer.

4.2.4 Surface sensitive techniques.

Polishing diamonds is not an easy task, since diamond is among the hardest of materials. Nevertheless, diamonds for jewellery have been polished for centuries, and are still, using the so-called *scaife technique*. In this technique, a cast iron wheel (called a scaife)

4.2 Characterization of synthetic diamonds. Experimental results.

hkl	F_{hkl}	integr. refl.	t_{ex} [μm]	t_{abs} [μm]
111	17.67	1	2.21	630
220	16.00	0.60	3.99	1029
400	12.45	0.36	7.25	1456
333	7.52	0.21	15.58	1890

Table 4.3: Structure factor, integrated reflectivity, extinction and absorption depth values for 1 mm thick diamond at 300 K calculated using the XCRYSTAL tool in XOP, $E = 12$ keV.

charged with diamond powder is used. The polishing process is strongly anisotropic: the wear rate strongly depends on the crystallographic orientation of the surface being polished and on the direction of the polishing [163]. This is well known by gem polishers, who categorize diamond surfaces in “hard” and “soft” directions. The softer directions are the $\langle 100 \rangle$ on $\{110\}$ and $\{100\}$ surfaces (with the former being the softest) whilst the hardest are all directions on a $\{111\}$ surface. It has been recently shown using molecular dynamics simulations that during mechanical polishing of diamonds the crystal undergoes an sp^3 to sp^2 order-disorder transition resulting in the formation of an amorphous layer [164]. The growth rate of this layer depends on orientation and the difference originates in the way the crystal bonds are broken. At the same time, the $\{111\}$ surfaces are the most interesting if the crystal is to be used as Bragg monochromator, due to the largest structure factor and consequently largest integrated intensity of the 111 reflection, see tab.4.3 where the different integrated intensities have been calculated for a diamond sample 1 mm thick and at an energy of 12 keV. The structure factors are expressed in units of Thomson scattering length ($r_e = 2.82 \times 10^{-15}$ m). The integrated reflectivities are obtained multiplying the reflectivity curve by itself and they have been normalized to the integrated intensity obtained for the 111 reflection. Moreover, a large structure factor results also in a small extinction depth, making the 111 reflection more sensitive to sub-surface distortion than any other symmetric reflection. Therefore, alternative methods to the mechanical polishing need to be considered in order to obtain well-polished $\{111\}$ surfaces. One method that avoids polishing is by cleaving the crystal. Cleavage is the tendency of a crystal to split along some definite crystallographic orientations. Diamond cleaves preferentially on the $\{111\}$

4. CHARACTERIZATION OF SINGLE CRYSTAL DIAMONDS

surfaces. A theoretical explanation has been recently given [165] relating it to a much lower strength and energy for fracture on the $\{111\}$ planes compared to other planes. Unfortunately, the cleaved surfaces normally appear not to be atomically smooth, but to present terraces, [166, 167]. Other alternative methods of polishing diamonds, such as chemo-mechanical, electrical discharge or thermo-chemical polishing, are presented in the reviews by Malshe, *et al.* [168] and by Chen and Zhang [169].

The thermo-chemical polishing was investigated by our group at the ESRF, in collaboration with the University of Johannesburg. The results obtained have been submitted to the proceedings of the XTOP 2010 conference [170]. Polishing using a hot-metal plate was introduced by Grodzinsky in 1953 [171] and has been recently developed by Yoshikawa [172]. Different metals have been tested for the polishing wheel but the highest polishing rate is obtained using very pure iron. By pressing a diamond on a heated metal plate, carbon atoms are diffused from the diamond to the plate itself. This process will remove atoms from the diamond surface and leaves it flatter. The system implemented at the iThemba Labs in Johannesburg uses an iron wheel heated to around 810-850°C, 4.33. The load on the samples (pressing them onto the hot metal plate) was 0.1 N and the polishing time was 4 hours.



Figure 4.33: The Hot-metal polishing apparatus.

In this study, three diamond samples were characterized, both at the University of Johannesburg and at the ESRF. The characteristics of the three samples are shown in table 4.4. The miscut angle (the angle between the lattice planes and the surface of the crystal) of the samples discussed here was determined during the experiment at ID01

4.2 Characterization of synthetic diamonds. Experimental results.

	Sample 1	Sample 2	Sample 3
dimensions [mm ³]	4.5×5.8×0.69	6.0×7.6×0.69	4.9×5.9×0.78
first surface	as-grown + HMP	HMP	lapped + HMP
miscut ()	0.23°	0.02°	5.20°
miscut (⊥)	0.04°	0.02°	5.20°
second surface	cleaved	cleaved	lapped
miscut ()	≈ 0°	not measured	not measured
miscut (⊥)	0.40°	not measured	not measured

Table 4.4: Samples parameters. The miscuts were measured in two orthogonal directions, indicated with || and ⊥.

by measuring angular positions of the symmetric 111 reflection, after having carefully adjusted the surface for the XRR data collection.

In our experiments we wanted to study both the roughness of the surface and the depth of the deformed layer created (if any) during the polishing process, using respectively X-ray reflectivity and Grazing Incidence X-ray Diffraction (in-plane). It needs to be pointed out that our understanding of the technical requirements to perform the experiments increased after each experimental session. For example, the requirements on the crystal plates are very stringent: the miscut angle needs to be smaller than the critical angle in order to be able to perform GID studies. For this reason, we decided to work at lower energy (7 keV for XRR, 8.5 keV for GID) in order to maximize the critical angle. To work at even lower energies would have required the beam path to be under vacuum to minimize absorption. We decided to avoid this since it would limit the number of samples that is possible to analyze due to the long time to switch from atmospheric to low pressures.

4.2.4.1 Optical surface profile and AFM results

Fig.4.34 shows the optical surface profiles for both surfaces of two diamonds (sample 1 and sample 3, sample 2 being very similar to sample 1).

These maps are obtained by Vertical Scanning Interferometry (VSI) using a WYKO NT9300, working with filtered white light at ≈550 nm. The vertical resolution is ≈0.5 nm rms (root mean square) for a highly rough surface. The lateral resolution

4. CHARACTERIZATION OF SINGLE CRYSTAL DIAMONDS

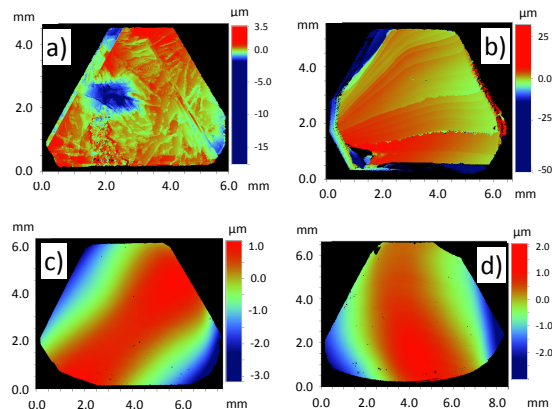


Figure 4.34: Surface morphology of diamond samples measured with the Vertical Scanning Interferometer at the ESRF Metrology Lab. a) sample 1, Hot Metal Polished b) sample 1, cleaved, c) sample 3 lapped with a 5° miscut + Hot Metal polished, d) lapped 5° miscut.

depends on the objective; it can be $4\ \mu\text{m}$, $2.2\ \mu\text{m}$ and $0.5\ \mu\text{m}$ for the magnifications of 2.5x, 5x, 50x, respectively. In order to cover the whole surface of each diamond, since they are larger than the field of view of the objective, a microstitching interferometry technique is used. This consists of taking sub-apertures but overlapping them, and reconstructing the topography through the computational assemblage of the image fields obtained by VSI. The Hot Metal polished faces have deformed profiles, with a rms roughness of almost $1\ \mu\text{m}$. The cleaved surface shows a deeply terraced profile, with height differences of several μm . Sample 3 surfaces are curved, and have height differences across the face of $\approx 1\ \mu\text{m}$. This is due probably to small instabilities of the goniometer head during the polishing process; improvements in this direction are already being made by our collaborators in South Africa.

Micro roughness analyses have also been performed, over four regions of approximately $100 \times 130\ \mu\text{m}^2$. On the polished side the roughness is $\approx 20\ \text{nm}$ for sample 1, $\approx 100\ \text{nm}$ for sample 2, and $\approx 5\ \text{nm}$ for sample 3. The polished side of sample 3 is locally smoother than sample 1 and 2, and has some characteristic grooves, due to the lapping process. The roughness on the cleaved surface is almost the same for all samples, the value being close to $\approx 6\ \text{nm}$ locally. AFM results confirm VSI analysis. In samples 1 and 2, several μm of roughness characterize the Hot Metal polished face, and the cleaved face appears locally smooth on a single terrace. Sample 3 was lapped on both faces, and

4.2 Characterization of synthetic diamonds. Experimental results.

some characteristic grooves are visible on the unpolished face. The opposite face was analyzed before and after the Hot Metal polishing process 4.35. Polishing appears to smooth out the grooves a little.

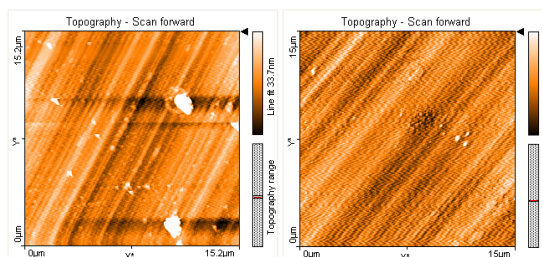


Figure 4.35: AFM analysis of sample 3. Surface before (on the left) and after (on the right) the Hot Metal polishing process. In the image on the right the roughness is ≈ 5 nm over a $15 \times 15 \mu\text{m}^2$ area.

4.2.4.2 Sample preparation

The original carbon surface of diamonds can be rapidly polluted by airborne contaminants, or by contact with other material surfaces. Metal traces derived from the polishing process, and particulates in the atmosphere could be responsible for the presence of thin layers on the diamond surfaces which are then evidenced in the common surface investigation methods. In order to minimise surface contamination, before the XRR and GID analysis, the diamonds were cleaned in a boiling ($\approx 90^\circ\text{C}$) acid mixture of ($\text{HCl}:\text{HNO}_3$) in a molar ratio 1:1 for ten minutes and an acid preparation ($\text{H}_2\text{SO}_4:\text{HNO}_3$) with a 3:1 molar ratio at boiling temperature ($\approx 250^\circ\text{C}$), and subsequently stored in deionised water-filled hermetic ampoules. The acid etch applied is a modified process based on [173] and leaves an oxygen terminated surface [174]. During the experiment, the samples were exposed to normal atmosphere for several minutes, before the X-ray data collection which was carried out in a helium atmosphere. The contamination in air to a level significant for the sensitivity of the techniques used cannot be discounted.

4. CHARACTERIZATION OF SINGLE CRYSTAL DIAMONDS

4.2.5 Grazing Incidence Diffraction

For the GID measurements an energy of 8.5 keV was used (the reason for this was that at 7 keV, $2\theta_B$ for the 220 reflection is close to 90° , resulting in an impossibility of the detector, attached to the ν rotation of a six circle diffractometer, to move out of the plane of incidence). The incident beam was limited to $0.5 \times 0.7 \text{ mm}^2$ (V \times H). The scattering geometry was vertical, *i.e.* sample mounted vertically, in order to exploit the smaller vertical divergence of the beam. Detector slits were $0.4 \times 5 \text{ mm}^2$. The data were collected using a NaI scintillator counter (Cyberstar). In order to study the depth of the distorted region due to the polishing, we collected GID scans at different incidence angles. Two types of scans have been recorded, namely radial and transverse scans together with reciprocal space maps. The radial scans are sensitive to the d-spacing changes whilst the transversal scans measure the mosaic spread.

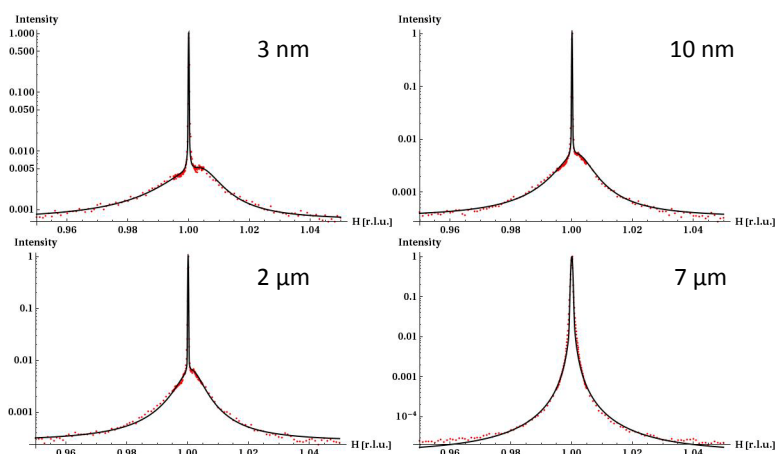


Figure 4.36: Example of radial scans for the sample 1, reflection -202, $E = 8.5 \text{ keV}$. It is possible to notice, at small penetration depth a broad peak related to a layer under compressive strain.

Fig.4.36 shows an example of radial scans collected for sample 1, reflection -202. The penetration depths are estimated from the angle of incidence using eq.3.9. The experimental data are a combination of bulk, surface and background contributions to intensity. A higher, narrow peak originates from the bulk, while a low, broad peak originates from the sample surface. The curve has been modelled as the sum of a Pseudo Voigt function (for the contribution from the bulk), a split-Lorentzian function

4.2 Characterization of synthetic diamonds. Experimental results.

¹ (surface contribution) and a constant value (background). In addition the normalized areas under each curve were calculated and compared to assess the contributions arising from bulk and surface. The analysis of these data was performed by Genziana Bussone as part of her Master's thesis.

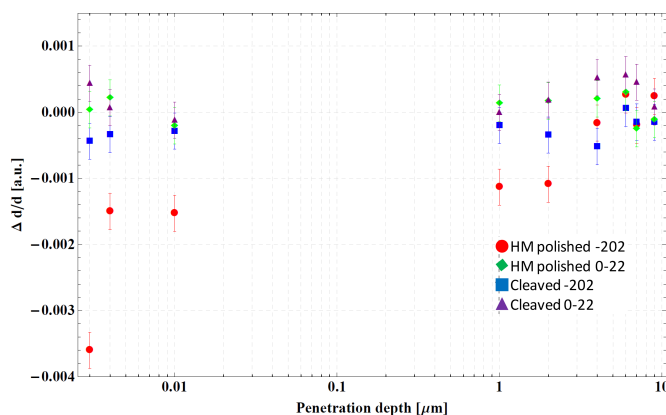


Figure 4.37: Comparison of the strain estimations for the cleaved and Hot Metal polished face of sample 1 as a function of the penetration depth.

The in-plane grazing incidence diffraction analysis shows clearly the difference between the two faces of sample 1. The cleaved face is locally smooth; in fitting the curves, the contribution of the background intensity is insignificant compared to that of the bulk. At greater penetration depths an increase of the background, attributed to defects in the bulk, is observed. On the Hot Metal polished surface, the polishing process produces a deformed surface layer which gives high background and surface contributions at small penetration depths. Both background and surface contributions decrease as penetration depth increases, as the higher quality bulk starts to dominate the measurement. In reflection -202 radial scans, a strong asymmetry of the surface peak can be observed for depths less than 4 μm , the diffraction from the surface layer being displaced from that of the contribution from the bulk. It is possible to obtain the strain directly from the displacement of the surface peak. The strain calculation indicates a compressively-strained, near-surface region a few μm deep. The strain calculation for the cleaved face, considering the same reflection, shows a region a few micrometers deep (4 to 7

¹a split function consists of two functions with different FWHMs but same height, allowing asymmetric peaks to be treated [175]

4. CHARACTERIZATION OF SINGLE CRYSTAL DIAMONDS

μm) under a smaller compressive stress. At greater penetration depths, more than 7 μm , all data tend toward bulk behaviour. In contrast, the 0-22 reflection of both faces shows approximately bulk behaviour for all penetration depths. Thus it appears that the surface strain is anisotropic, as shown in fig.4.37.

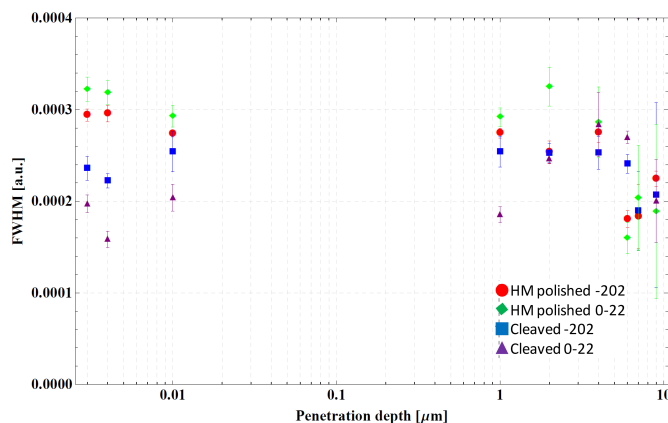


Figure 4.38: Comparison of the FWHM of the peak for the transversal scans, for the Hot Metal polished and cleaved faces of sample 1 for two directions (-202 and 0-22) as a function of the penetration depth.

The transverse scans can be interpreted by considering the variation of the FWHM of the fitted curves. The broader the FWHM, the more the variation in misorientation of the mosaic elements in plane. The results are shown in fig.4.38. In the top few microns of the Hot Metal polished face, the FWHM values are higher than those at greater depths (tending to bulk), consistent with a deformed surface region. For the cleaved face, the FWHM values vary less with penetration depth, that is, the mosaic spread at the surface is no greater than in the bulk.

4.2.6 X-ray Reflectivity

Measurements of specular and transverse diffuse reflectivity curves have been performed in order to obtain information about the roughness, density, thickness and the interfaces of thin layered structures apparent in the samples. The true specular reflectivity was obtained by subtracting the average forward-diffuse scatter $\pm 0.12^\circ$ either side of the specular peak, from the specular XRR data. The fitting was performed by Tamzin Lafford using the Bede REFS software [176].

4.2 Characterization of synthetic diamonds. Experimental results.

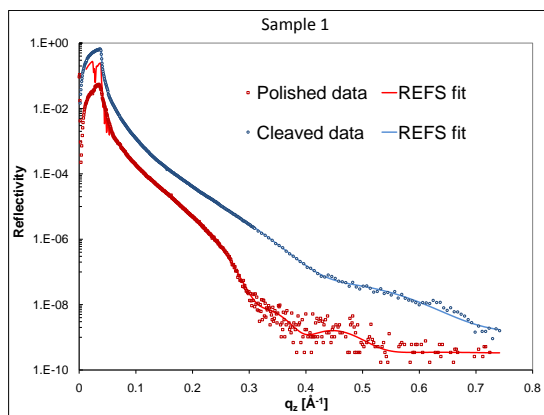


Figure 4.39: True specular reflectivity of sample 1, Hot Metal polished and cleaved surfaces.

The XRR data do not show Kiessig fringes from the thick ($\approx 4 \mu\text{m}$) deformed layer, detected through GID, but the effects of a modified density and effective interface width are present. The thickness of this layer was therefore fixed in the fitting process in accordance with the VSI results. The true specular reflectivity data for sample 1 could be fitted only by including thin low density layers near the surface fig.4.39, which could derive from surface contamination. No repeatable, unique fit was obtained for the data from sample 2.

The differences in roughness for the opposite faces of the samples are clear from a comparison of profilometry and transverse diffuse XRR data, fig.4.40.

However, the roughness indicated by XRR fitting is much less than that indicated by the profilometer. With roughness (damage) a few microns deep, this is more likely to be reflected in XRR in reduced density values of the thick layer than in the roughness parameter, which is valid only up to $\approx 35\text{-}50 \text{ \AA}$. Fitting the specular reflectivity of sample 1 required layers of 40-55% of bulk density, with two thin surface contamination layers totalling 45 \AA . Fitting data for the cleaved face, the thick layer density was very similar to bulk density, while the surface contamination layers (totalling 116 \AA) ranged from 94% to 105% of bulk density, with some uncertainty.

The absence of a clear specular peak in the transverse diffuse reflectivity data for the polished side of sample 3 fig.4.41 clearly shows that the surface is either very rough or very curved. The VSI data (fig.4.34.c-d) show that the surface is curved.

4. CHARACTERIZATION OF SINGLE CRYSTAL DIAMONDS

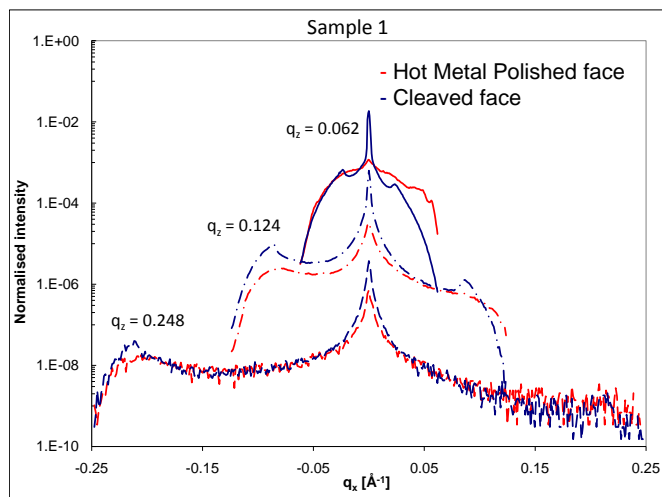


Figure 4.40: Transverse diffuse scattering of sample 1, Hot Metal polished and cleaved surfaces.

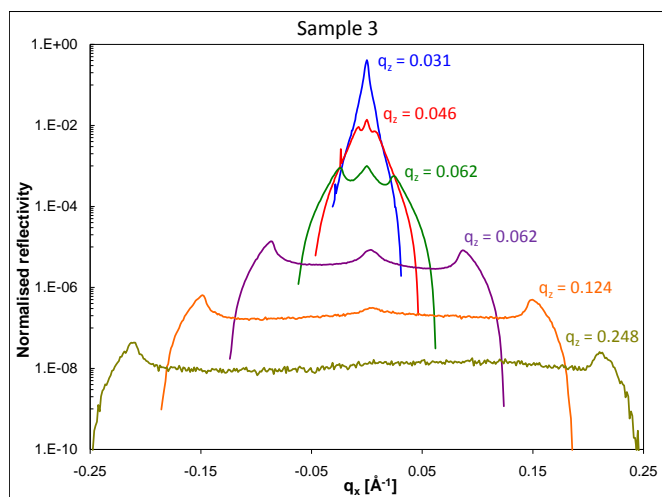


Figure 4.41: Transverse diffuse scattering of sample 3, Hot Metal polished surface. There is very little specular reflectivity, indicating either a very rough or a highly curved surface.

Chapter 5

Improvements to polishing of silicon crystals and beryllium windows

In this chapter I will present results obtained in the characterization of materials, mainly high quality single crystal silicon and ultra high purity beryllium foils, used as optical elements that should not disturb the wavefront, spoiling the coherence properties of the synchrotron beam.

5.1 Improvements and quantification of silicon crystals processing at the ESRF Crystal Laboratory

Thanks to the huge investment made in the last decades by the electronic industry, [177], it is possible to obtain silicon crystals with a very high quality and a residual strain of the order of 10^{-8} , [157].

In order to be used as optical element, the crystal needs to be cut into the foreseen shape and the surfaces need to be polished with high quality. This is done in different steps that, for what concerns the ESRF, are often made at the Crystal Laboratory:

- cutting the plates from the silicon float zone wafer with diamond saw (76 μm grain);
- rough lapping using silicon carbide (SiC) powder (37 μm) mixed with water;

5. IMPROVEMENTS TO POLISHING OF SILICON CRYSTALS AND BERYLLIUM WINDOWS

- chemical etching for 3 to 5 minutes in a bath made of a mixture of nitric acid (HNO_3) and hydrofluoric acid (HF) in a ratio 1:4 and soft lapping with SiC of 17 μm ;
- mechanical polishing (also called optical polishing since it results in mirror-like surfaces), using a slurry of diamond powder with 1 μm grain size and alcohol. For this process the polishing plate is covered by a silk cloth.

It is known that processing of crystals induces lattice deformations in the crystal, [178, 179], in the form of a cold deformed layer. This layer creates an elastic strain in the crystal underneath whose strength decreases with depth. The thickness of the deformed layer is proportional to the dimension of the grain used. Therefore, each step is required to remove the deformed layer from the previous step but at the same time, it creates a new thinner deformed layer. One way of removing a deformed layer is to chemically etch it away; however, as it will be shown in the results, etching results in a modulation of the surface, called “orange peel”. Depending on the applications, this modulation may be tolerated or not, *e.g.* for small angle scattering it needs to be minimised or avoided.

Another way of removing a deformed layer is to use a mechano-chemical polishing, which uses very small grains and leaves a flatter surface compared to the etching. At the ESRF Crystal Laboratory this consists of two steps. In the first step it is used a slurry of colloidal silica (Grace Davison LUDOX[®] P-W30) with grain size dispersed around an average value of 30 nm and a pH of 9. The second step is done by replacing the pad used in the previous step with a polyurethane embossed pad named ÅKERS SUPRA5 and using the same slurry as before.

The removal rate of this technique is rather low (typically of the order of 1 μm per hour) and therefore it can be used only crystals which have a very small (few μm thick) deformed layer.

In order to find the critical points of the actual procedure, we performed different polishing tests.

5.1.1 First test - Localization of the main problem.

Normally at the Crystal Laboratory, the way to inquire whether a crystal is well polished or not is by inspection via optical microscopy. Fig.5.1 shows three images, each showing

5.1 Improvements and quantification of silicon crystals processing at the ESRF Crystal Laboratory

the state of the surface after a removal of respectively 9 μm , 13 μm and 19 μm . Many spot-like features are visible on the first image; these are indentations related to the lapping step. In the second image, most of the indentations appear to be removed. Finally in the last picture, no more indentations are visible. At this stage, the crystal was considered as ready for the following final step, the mechano-chemical polishing.



Figure 5.1: Optical microscopy of silicon crystals after different polishing times and consequently different thicknesses removed, measured using an infrared interferometer.

In order to verify whether this procedure was accurate enough we made a series of 111 oriented silicon samples. The reason to work with 111 oriented samples is twofold: first, as shown previously in section 4.2.4, this is the preferred direction for Bragg monochromator. Second, it allows for the collection of non-dispersive X-ray topographs with the standard double Si111 monochromator of BM05. The description of the different samples is shown in tab.5.1.

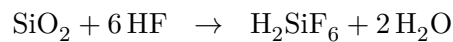
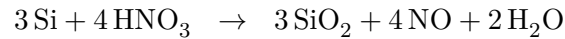
Step/Sample	Description	Samples	Removed
1	Surface Lapping	All	
2	Optical Polishing	2 to 6	$\approx 20 \mu\text{m}$
3	1st etching	3-4-5	$\approx 10 \mu\text{m}$
4	2nd etching	4-5	$\approx 10 \mu\text{m}$
5	3rd etching	5	$\approx 10 \mu\text{m}$

Table 5.1: Series of samples for the calibration of the optical polishing process

The three etching steps were done in order to obtain a rough idea of how thick is the deformed layer due to the lapping and mechanical polishing. The etching reaction is

5. IMPROVEMENTS TO POLISHING OF SILICON CRYSTALS AND BERYLLIUM WINDOWS

composed of two steps [180, 181]:



the first step is oxidation of silicon by nitric acid followed by dissolution of SiO_2 by the hydrofluoric acid. The samples have been characterized using different methods, namely High Resolution X-ray Diffraction, X-Ray Topography, Optical Profilometer and AFM. The HRXRD measurements have been carried out initially with a laboratory source first and then again afterwards at ID18.

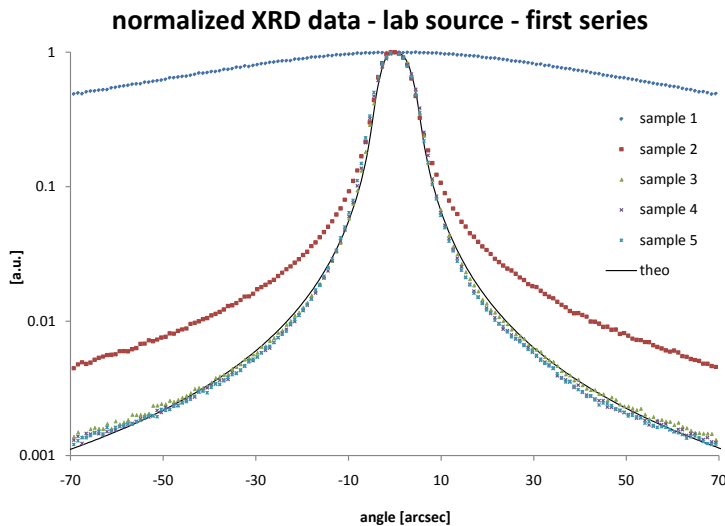


Figure 5.2: Normalized rocking curves of the different samples from the first polishing series. $\text{Cu} - K_{\alpha 1}$ radiation, 111 reflection.

For the laboratory source setup, a crystal with an asymmetry angle of 9.5° from the 111 direction has been prepared by the crystal lab. This crystal used in grazing incidence geometry (with asymmetry factor $b=-0.2$ for $\text{Cu}-K_{\alpha 1}$ radiation) act as a monochromator and as a collimator, producing a radiation with a divergence 5 times smaller than the acceptance of the sample. In order to avoid contaminations of the $\text{Cu}-K_{\alpha 2}$ radiation, a double set of slits has been used at the exit of the X-ray tube.

An example of the normalized recorded rocking curves of the 111 reflection for the series of samples is shown in fig.5.2. It is obvious (and expected) the large difference

5.1 Improvements and quantification of silicon crystals processing at the ESRF Crystal Laboratory

between the rocking curve for the lapped (sample 1) and optical polished (sample 2) samples, due to the bad surface status. But already after the first etching (sample 3), the different rocking curves become indistinguishable and they agree perfectly with the theoretical values.

A slight difference is recorded if the rocking curves are measured with higher order reflection (444) using the highly monochromatized beam produced at ID18, $E=21.541$ keV (corresponding to the ^{151}Eu nuclear resonance transition) with $\frac{\Delta\lambda}{\lambda} \approx 10^{-7}$, see fig.5.3. In this case it is possible to discern a small difference in the tails between samples 3 - 4 and sample 5.

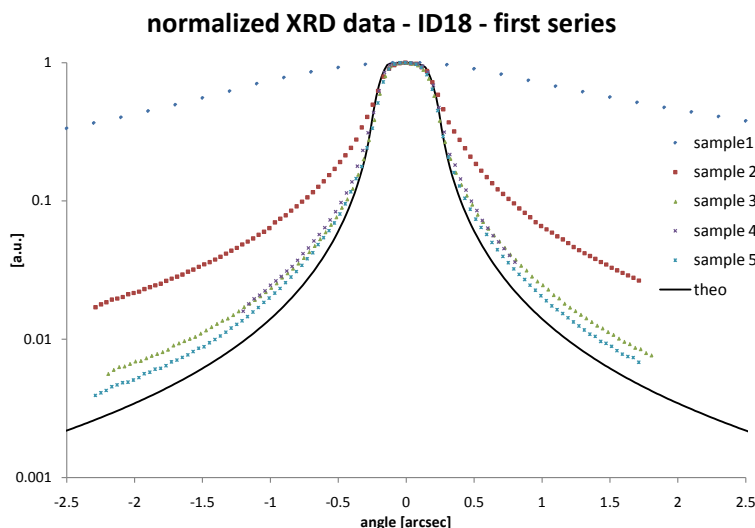


Figure 5.3: Normalized rocking curves of the different samples from the first polishing series. $E = 23.871$ keV, 444 reflection.

The difference between the samples appears to be even clearer when comparing X-ray topographs of the different samples, fig.5.4. The topographs are collected at BM05 on the flanks of the rocking curve, non-dispersive configuration at 20 keV. The strain detection limit for these conditions is $\approx 1.4 \times 10^{-7}$, obtained from the slope of the rocking curve, which is $0.35''^{-1}$ and by considering that it is possible to detect intensity variation of the order of 1%. In the lapped sample 1, the deformed layer creates a grainy structure of deformations. In sample 2 scratches coming from the optical polishing are clearly visible, together with strong indentations, black spot-like contrasts, coming from the lapping.

5. IMPROVEMENTS TO POLISHING OF SILICON CRYSTALS AND BERYLLIUM WINDOWS

After the first etching (removal of $\approx 10 \mu\text{m}$), there are still scratches and indentations visible. After the second etching (total removal of $\approx 20 \mu\text{m}$), all the scratches are removed, implying that they are located in the upper part of the deformed layer. Nevertheless, indentations are still visible, *i.e.* they are located deep in the layer. Finally, with the third etching (total removal of $\approx 30 \mu\text{m}$), no defects are visible in the topographs. This implies that the thickness of the deformed layer is between $20\mu\text{m}$ and $30 \mu\text{m}$.

The roughness measurement obtained using the optical profilometer and the AFM at the Metrology Laboratory are shown in fig.5.5. The data labelled 5X and 50X are obtained using a Micromap Promap 512 optical profiler, each representing the possible magnifications. The field of view for the 5X is $1.64 \times 0.83 \text{ mm}^2$ with a spatial resolution of $2.5 \mu\text{m}$; for the 50X, field of view is $163 \times 83 \mu\text{m}^2$ and a spatial resolution of $0.5 \mu\text{m}$. The AFM measurements, have a field of view of $15 \times 15 \mu\text{m}^2$ with a spatial resolution of 30 nm . It is clear that the samples which have been etched for a long time present a rough surface with strong low frequency modulations (“orange peel”), visible especially in the values of the rms-roughness measured at low magnification (5X).

From this first polishing test we started to doubt whether the removal of material done by the optical polishing was too small, leaving the crystal with a thick deformed layer and with the indentations produced during the lapping. Therefore we decided to make a second test in order to calibrate the removal of the deformed layer by the optical polishing.

5.1.2 Second test - Calibration of the optical polishing.

In the second polishing test, we try to define how much material is necessary to remove in order to completely eliminate the indentations after the optical polishing.

We decided to procede in two different ways, producing two different series of sample. In the first series (samples 21 to 24) we increased the time of optical polishing for each crystal, starting with all the crystals, then removing sample 21 and continuing with the rest and so on. We obtained therefore four samples with a different thickness of material removed, namely $19 \mu\text{m}$, $31 \mu\text{m}$, $66 \mu\text{m}$ and $80 \mu\text{m}$. The removed thicknesses were measured using a Fogale Low Coherence Interferometric Sensor, which accuracy is of $\pm 1 \mu\text{m}$.

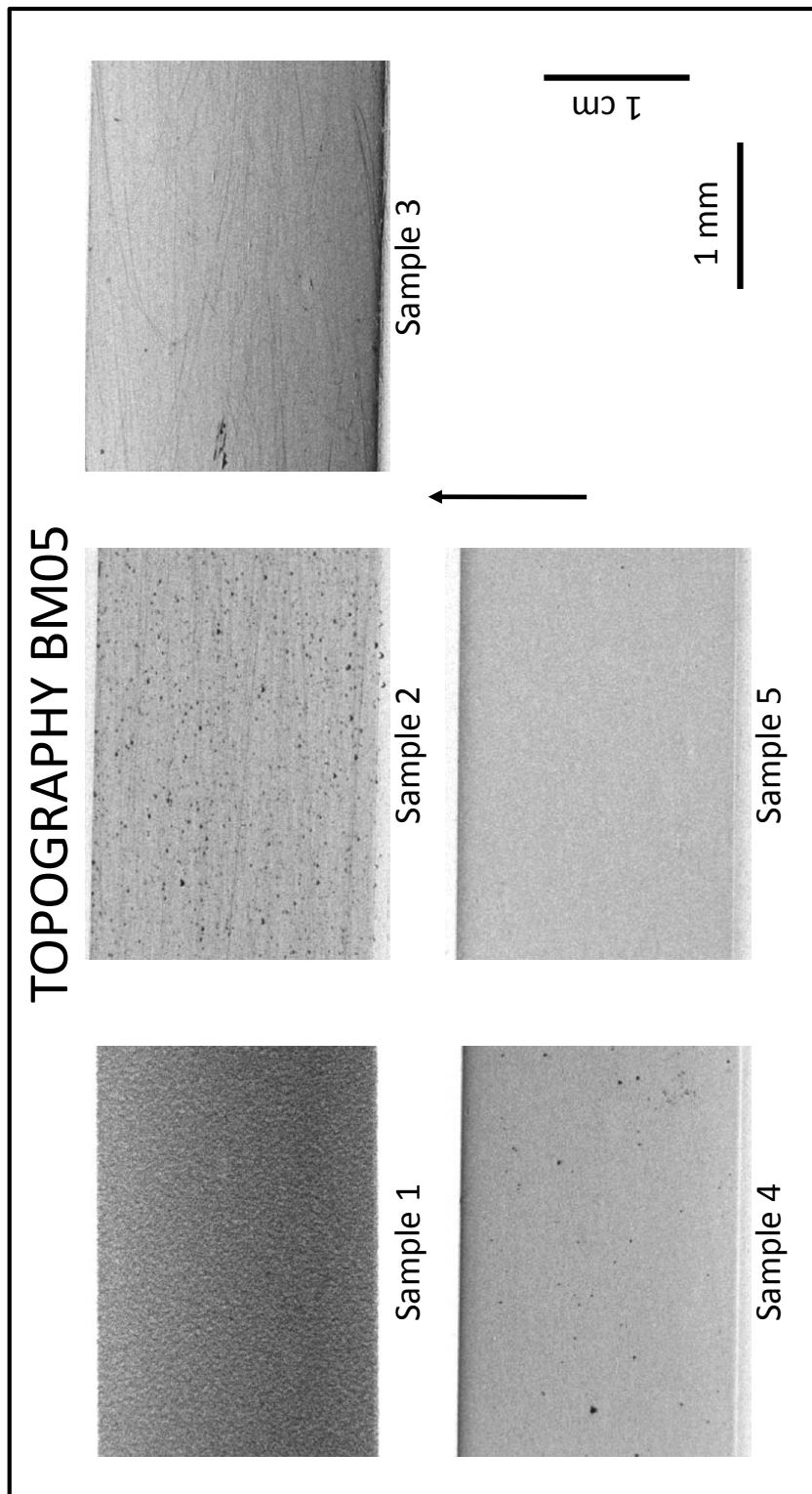


Figure 5.4: Double crystal topographs of the different samples from the first polishing series. $E = 20$ keV, 111 reflection. For geometrical reasons, the image appears compressed in the vertical direction by a factor 10.12 ($=1/\sin(\theta_B)$). The arrow represent the projection of the incoming and diffracted wavevectors.

5. IMPROVEMENTS TO POLISHING OF SILICON CRYSTALS AND BERYLLIUM WINDOWS

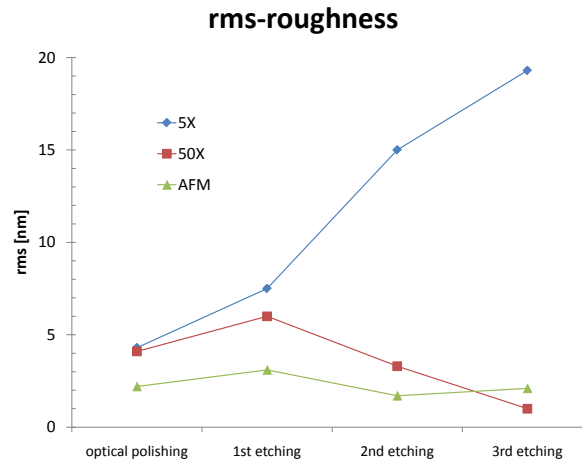


Figure 5.5: Roughness root mean squared values of the different samples from the first series. The increase in roughness at low spatial frequency (5X) is clear for the etched samples.

For the second series, we decided to add one extra polishing step with a granularity between the lapping at $17\ \mu\text{m}$ grain size and the optical polishing at $1\ \mu\text{m}$, using an intermediate slurry with silicon carbide of $9\ \mu\text{m}$. After this extra step, the four samples have been polished like for the previous series, obtaining an estimate thickness removal of $14\ \mu\text{m}$, $29\ \mu\text{m}$, $56\ \mu\text{m}$ and $73\ \mu\text{m}$.

The two series of samples have been characterized using Rocking Curve Imaging, [102]. We collected 101 images along the rocking curve with a step size of 0.2° , using the symmetric 111 reflection at $E=20\ \text{keV}$. The images have been analyzed using the *Visrock* software, [143]. The FWHM maps appear to show all the deformations in the crystal and we decided to use them.

Some of the results obtained are presented in fig.5.6. For both series it is clear the complete disappearance of indentations spots in the topographs for removal of the order of $30\ \mu\text{m}$ and above. No particular difference was noticed between the series of samples with the intermediate lapping with $9\ \mu\text{m}$ grain and the one without this step. Since the extra step brings technical complications (related to the limited number of polishing machines available at the Crystal Lab) we decided to not pursue this solution any longer.

These results confirmed what was obtained with the previous rough estimation made

5.1 Improvements and quantification of silicon crystals processing at the ESRF Crystal Laboratory

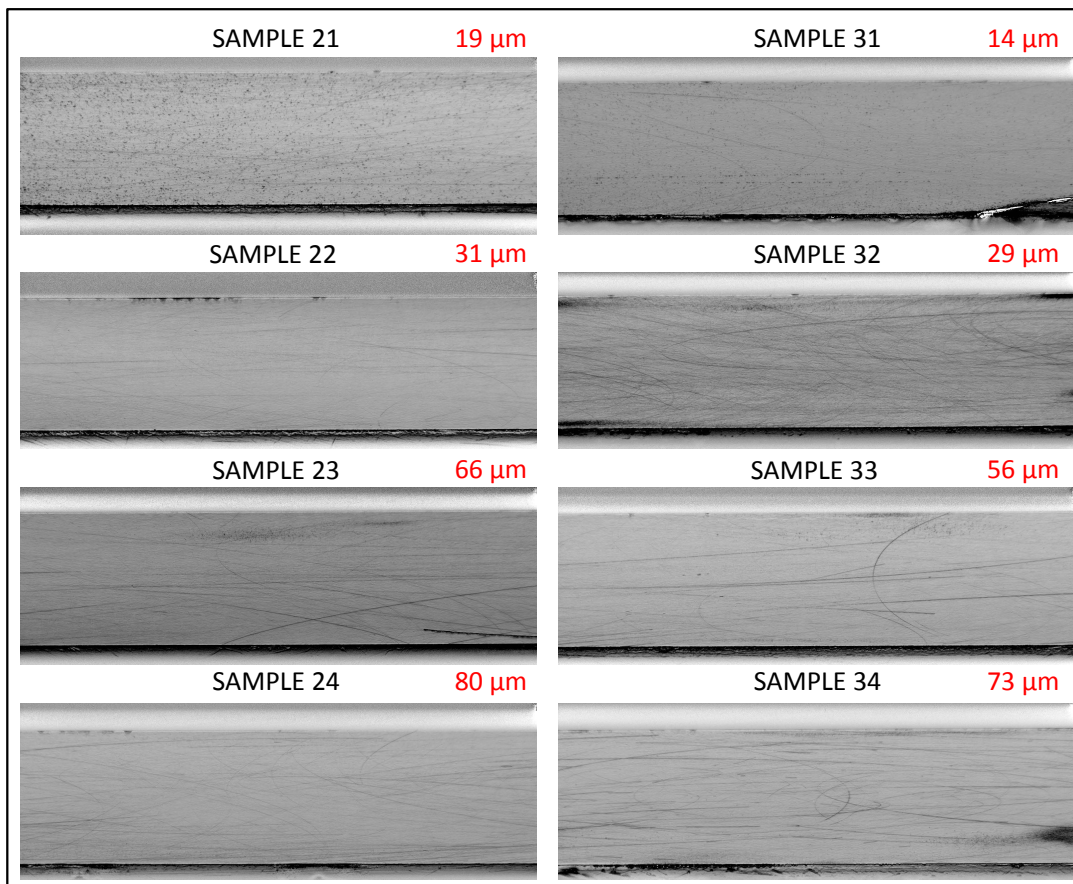


Figure 5.6: Rocking Curve Imaging - FWHM maps of the samples from the second polishing test; in red are indicated the estimated removed thicknesses.

via etching. It is necessary to remove at least 30 μm of material during the optical polishing. In order to be on the safe side, we decided that for all the future crystals polished at the Crystal Laboratory at least 40 μm needs to be removed.

Finally, we decided to also optimize the next polishing step, the mechano-chemical polishing.

5.1.3 Third test - Optimization of the MCP.

An important parameter for the Mechano Chemical Polishing step is the pH of the slurry used. Using the same philosophy as before a series of samples were prepared in an identical way (lapping, optical polishing with removal thickness of at least 40 μm).

5. IMPROVEMENTS TO POLISHING OF SILICON CRYSTALS AND BERYLLIUM WINDOWS

Sample 41 was put aside, as witness of the optical polishing. The other samples were mechano-chemical polished in three different ways:

- samples 42 and 43 using pure Grace Davison LUDOX[®] P-W30, pH 9, for respectively 12 and 24 hours;
- samples 44 and 45 using a mixture of LUDOX[®] P-W30 and GIGAPUR detergent, with a final pH of 12, for respectively 12 and 24 hours;
- samples 46 and 47 using a mixture of LUDOX[®] P-W30 and KOH, final pH 10.2¹, for respectively 12 and 24 hours.

The layer removed was measured using the Fogale Low Coherence Interferometric Sensor. The values obtained vary between 2 μm and 20 μm , but they are not directly correlated with the polishing time or the pH used. It seems that other factors may influence the removal speed, *e.g.* the quality of the pad or of the slurry may change with time. The samples were characterized using Rocking Curve Imaging at BM05 and using optical profilometer and AFM at the Metrology Lab. From the X-ray topographs collected, we established that in the case the removal is below 3 μm , scratches are still visible. For removal above 10 μm , the scratches disappeared, but “clouds” of little dots appear in the topographs. We conclude that a removal between 3 μm and 10 μm seems optimal, but further tests to obtain a better quantification are necessary. The influence of the pH value on the quality of the crystals was not very clear. For what concerns the roughness, better values (between 3 \AA at 50X and 9 \AA at 2.5X) were obtained with higher pH (10.2 and 12) compared to the pH 9 (rms-roughness between 4-5 \AA at 50X and 17 \AA at 2.5X).

5.2 Coherence measurements of the polished samples

The set of samples was also used to measure the transversal coherence of the X-ray beam after diffraction. In this way it is possible to verify the influence of the surface quality on the coherence. Two different experiments have been performed: the first one at ID19, using the Talbot effect already discussed in 4.2.3 for the diamond samples and the second at ID06 using an interferometer based on bi-lens [15].

¹The value of pH 10.2 has been obtained after private discussion with colleagues from Max Planck Institute for solid state research in Stuttgart and with prof. Yasunaga from Tokai University

5.2.1 Talbot effect measurements

As in the previous case for the diamond samples 4.2.3, the beam energy was 20.5 keV, the grid period 6 μm and the Talbot distances 300 and 900 mm. An example of the results obtained for the sample 21 (optical polished with a removal of 19 μm is shown in fig.5.7.

All the deformations that are visible in the topograph (on the left) are visible also in the calculated coherence maps. It is clear that the indentations, seen here as elongated deformations in the vertical direction, disturb considerably the coherence, increasing the vertical angular source size from 0.3-0.5 μrad to 1-2 μrad .

It is important to notice that the scratches appear as dark lines in the coherence map, *i.e.* as if they improve the coherence. In reality, the calculated values of source size on the scratches are zero, which has no physical meaning. The program fails to correctly calculate the coherence locally in the neighbourhood of the scratches, and returns a null value.

In order to have an estimation of the angular source size after diffraction from each silicon crystal a statistical analysis was performed on the obtained 2D maps. In fig.5.8 is shown an example of histogram corresponding to sample 21 and a ROI of 100x100 pixels.

The null values are automatically removed. The mean values and standard deviations of every map for some of the samples are compared in fig.5.9.

The general behaviour of the angular source sizes measured with the different samples is in good agreement with the previous X-ray Topography characterization, *i.e.* less deformations visible on the topographs implies a smaller angular source size.

5. IMPROVEMENTS TO POLISHING OF SILICON CRYSTALS AND BERYLLIUM WINDOWS

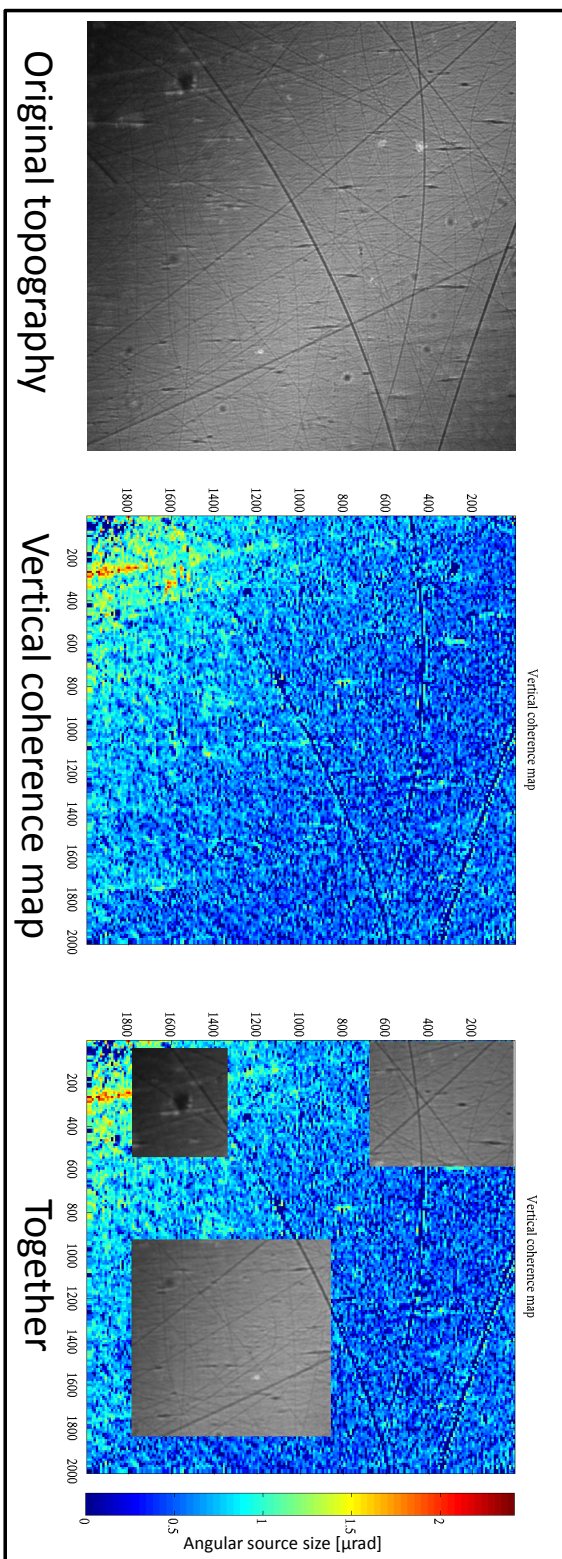


Figure 5.7: Example of results obtained with one of the samples from the silicon polishing test - sample 21. The coherence map was calculated using a ROI of 20 x 20 pixels and a ROI's displacement of 10 pixels, see fig.4.31 for the meaning of ROI and ROI's displacement.

5.2 Coherence measurements of the polished samples

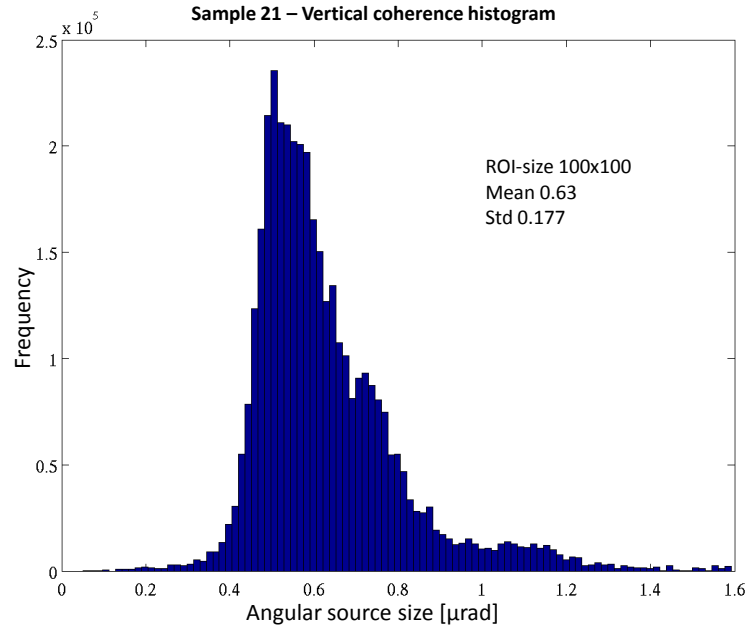


Figure 5.8: Histogram of the vertical coherence angular source size map of sample 21, ROI 100x100 points.

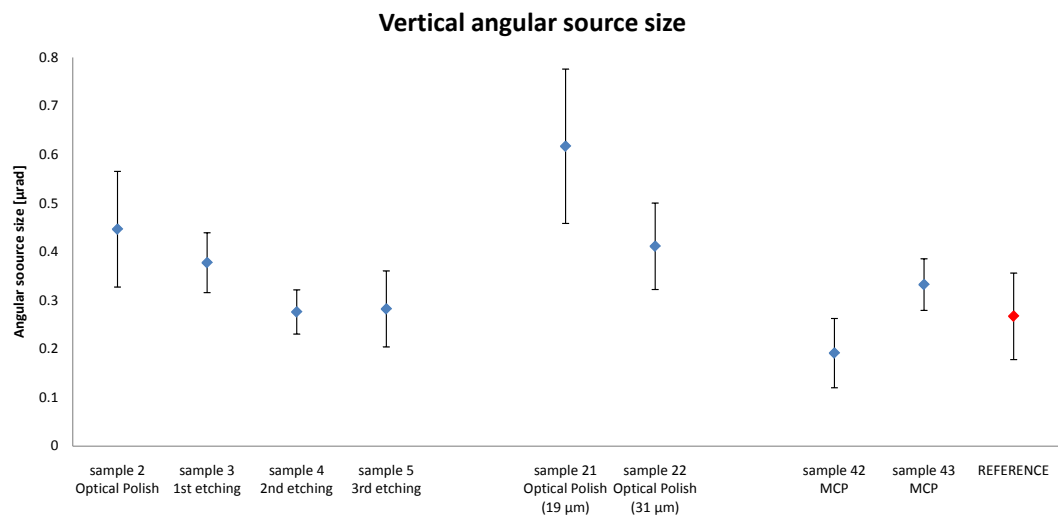


Figure 5.9: Mean angular source size for some of the polished silicon samples. The last point, in red, represents the angular source size measured on the direct beam.

5. IMPROVEMENTS TO POLISHING OF SILICON CRYSTALS AND BERYLLIUM WINDOWS

5.2.2 Coherence measurements using bi-lens-based interferometer

Recently, Snigirev and co-workers [15] presented a novel type of X-ray interferometer employing a bi-lens system consisting of two parallel Compound Refractive Lenses (CRL).

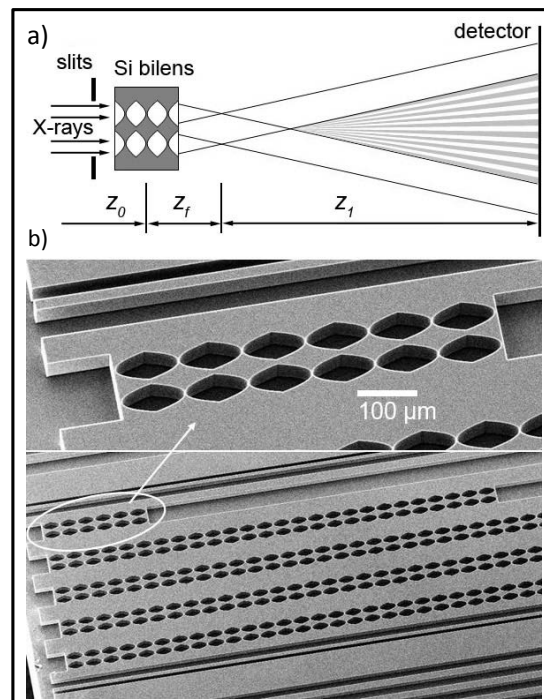


Figure 5.10: a) schematic view of the bi-lens system, b) scanning electron microscope images of a set of bi-lenses, used for different beam energies (from [15]).

Fig.5.10a) shows the operating principle of the interferometer. Two identical parallel planar CRLs are transversally separated by a distance d . Each CRL focuses the incoming beam at a distance $z_f = F/(1 - F/z_0)$, where z_0 is the distance from the source to the lenses and $F = R/2N\delta$ is the focal length of the CRL, R being the radius of curvature of one parabolic surface, N the number of lenses and δ the decrement of refraction index, see eq.3.6. If the distance between the lenses d is smaller than than the transverse coherence length l_t , see eq.2.28, then each lens is illuminated coherently and will generate two waves which will interfere at a distance $z_1 > z_f d/A_{\text{eff}}$, with A_{eff} the absorption limited effective aperture of the lens. The authors demonstrated that

5.2 Coherence measurements of the polished samples

it is possible to measure the value of the source size from the visibility of the fringes using the following formula:

$$S = \frac{\Lambda z_0}{z_f + z_1} \left(-\frac{\ln V}{3.56} \right)^{\frac{1}{2}} \quad (5.1)$$

where Λ is the fringe spacing defined as $\Lambda = \lambda z_1/d$ and V is the visibility, defined as $V = (I_{\max} - I_{\min})/(I_{\max} + I_{\min})$ where I_{\max} and I_{\min} are the intensities on a peak in a valley of the fringes. The experimental configuration used for the experiment is shown in fig.5.11. The energy used was $E=18$ keV, and the different distances were: $z_0 = 54$ m, $z_f = 0.02$ m, $z_1 = 2.98$ m, $d = 30$ μm .

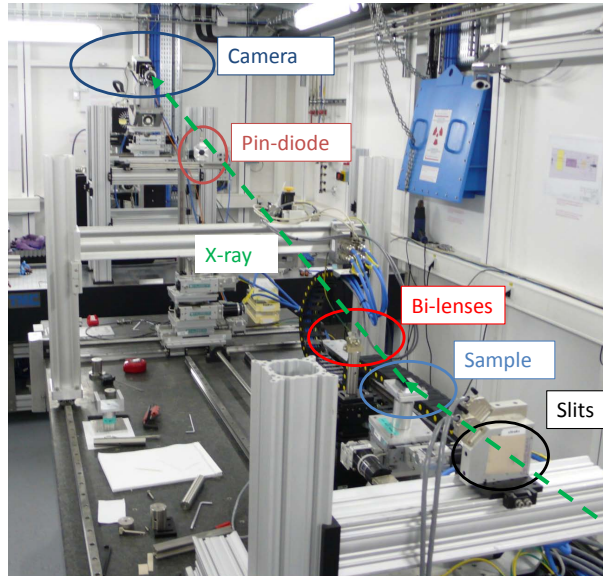


Figure 5.11: The experimental configuration used for the experiment at ID06.

Fig.5.12 shows an example of recorded interference fringes. The different coloured regions represent the different ROI that have been analyzed. I wrote a code in Matlab to analyze these data and to obtain the value of the source size. The program analyzes the data inside the ROI and calculates the visibility of each fringe. The final visibility for each ROI is then calculated as the average of the single fringe visibility, using the standard deviation as the error.

The results obtained for the same samples at ID19 using the Talbot effect and at ID06 are shown in fig.5.13. It is important to notice the big angular source size measured

5. IMPROVEMENTS TO POLISHING OF SILICON CRYSTALS AND BERYLLIUM WINDOWS

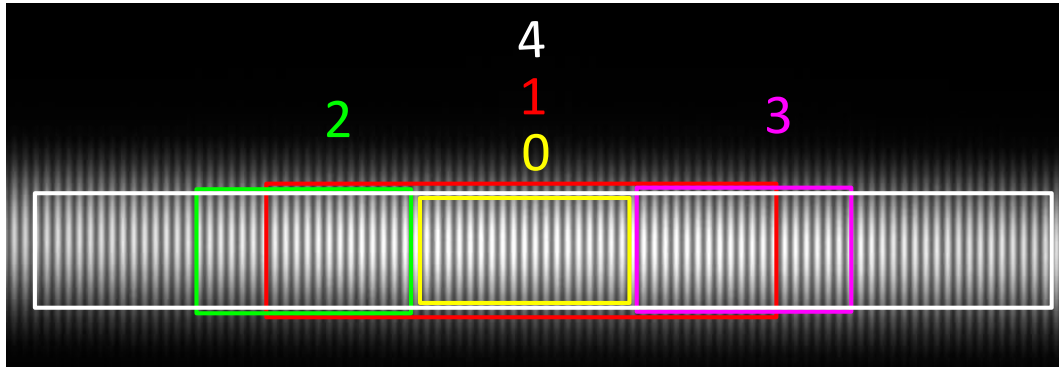


Figure 5.12: An example of the fringes produced by the bi-lenses at ID06. The analysis of the visibility was performed on the different ROI indicated with the different colours. The image is rotate 90° from the original view.

at ID06 without any sample, which corresponds to a source size of $67 \mu\text{m}$, which is much bigger than the expected value. A possible explanation is vibrations of the monochromator. Nevertheless, by comparing the relative increases in angular source size with respect to the reference values for both ID19 and ID06, we see that the behaviour is similar.

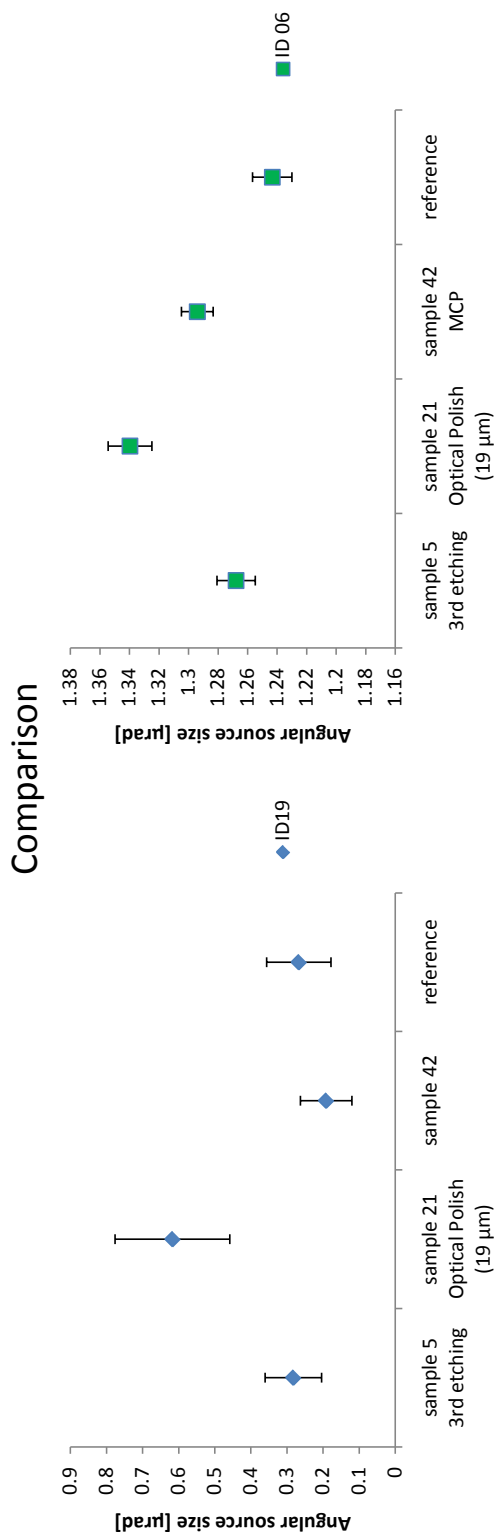


Figure 5.13: Angular source size measured at ID19 and ID06 using the Talbot effect and an interferometer based on bi-lenses.

5. IMPROVEMENTS TO POLISHING OF SILICON CRYSTALS AND BERYLLIUM WINDOWS

5.3 Improvements on the polishing of beryllium windows

Most beamlines at synchrotron radiation sources use beryllium for windows separating regions with high-vacuum and normal air pressure. For a good performance it is important that the window does not deform the wavefront. In order to obtain this, it is essential to minimise fluctuation in the bulk material density (no pores or voids, no density fluctuations) as well as to guarantee geometrically smooth surfaces.

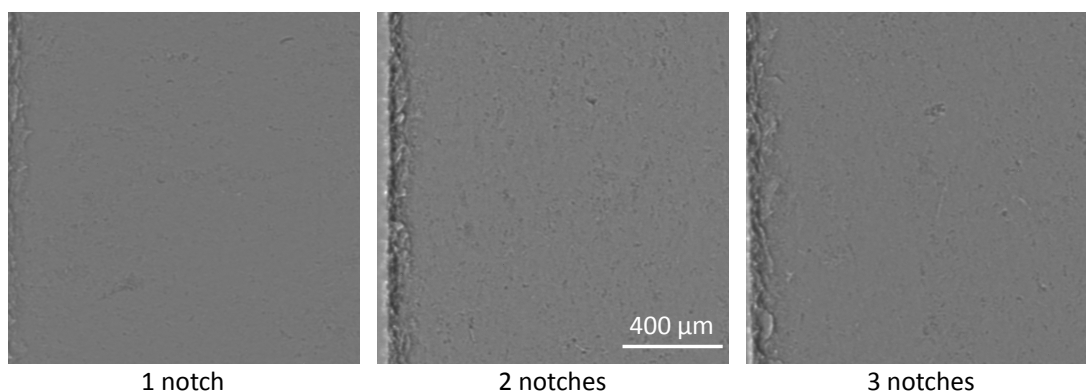


Figure 5.14: X-ray radiographs of three beryllium plates, flat field corrected. It is possible to see large inhomogeneities distributed on most of the plates. The straight feature on the left of the images is one of the edges of the samples. The number of notches was used to identify the samples.

In collaboration with P. Theveneau from ESRF and the company Brush Wellmann we performed a study of the quality of the material and of the polishing of Be plates of the ultra high purity class IF-1[®] produced by eletrofusion.

The tests were performed at ID19 and BM05 collecting phase sensitive X-ray radiographs of the three Be plates ($\approx 500 \mu\text{m}$ thick) by using a large sample to camera distance after different polishing steps. Moreover, the geometrical surfaces were characterized by using a Micromap Promap 512 optical profiler at the Metrology Laboratory. In order to classify the three samples, each one had a different number of notches on the corner, respectively one, two and three notches. The results of the first test are shown in fig.5.14. This test was performed at ID19, using a FReLoN camera with $0.7 \mu\text{m}$ resolution and a field of view of $1.4 \times 1.4 \text{ mm}^2$. The energy of the beam was 20.5 keV and the sample-to-detector distance 0.9 m.

5.3 Improvements on the polishing of beryllium windows

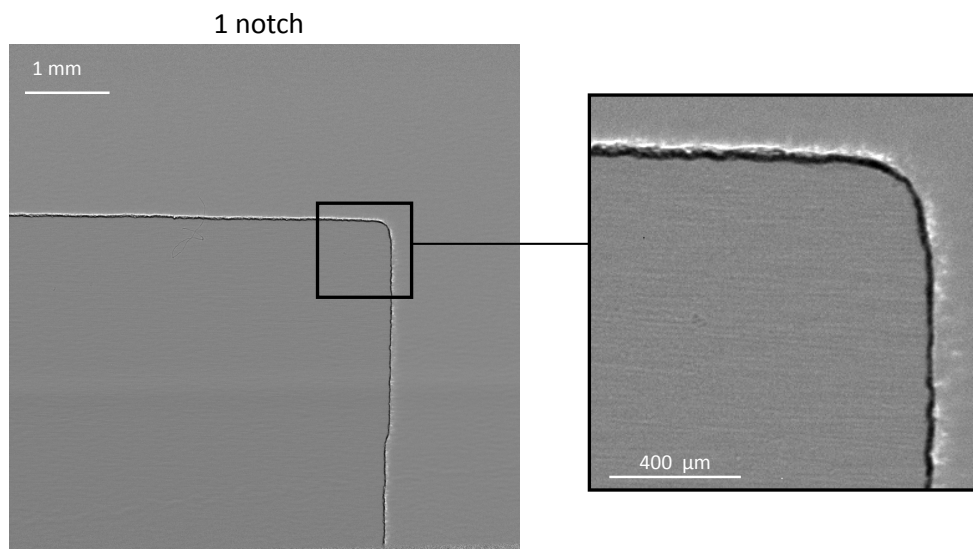


Figure 5.15: X-ray radiographs of one beryllium plate after the first polishing. The corner of the sample is visible in the image. In the zoom on the right it is possible to clearly see polishing grooves.

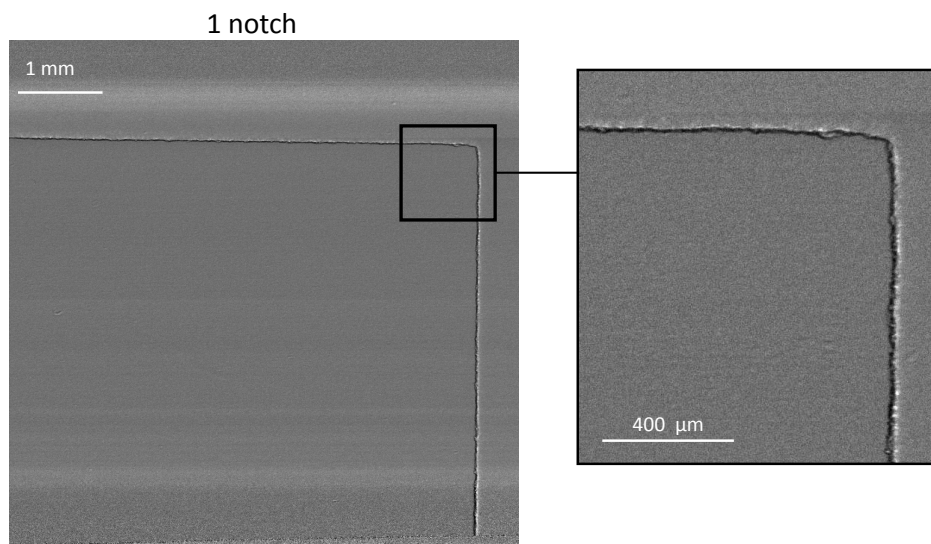


Figure 5.16: X-ray radiographs of one beryllium plate after the second polishing. In the zoom on the right it is now impossible to distinguish any features related to the Be window.

5. IMPROVEMENTS TO POLISHING OF SILICON CRYSTALS AND BERYLLIUM WINDOWS

It is clear from these images that the samples present a high number of inhomogeneities and it is not of the necessary quality to be used as window for synchrotrons.

The situation improved after the first polishing process, as shown in fig.5.15, which show the phase sensitive radiograph of one of the three plates (the other two being very similar to this one). This test was performed at BM05 using the PCO camera with a resolution of 3 μm and a field of view of $6 \times 6 \text{ mm}^2$ and a sample to detector distance of 125 cm. The large inhomogeneities are not visible any longer but strongly anisotropic polishing grooves are visible.

Finally, after a second polishing, no more features are visible on the radiographs, see fig.5.16 (same conditions as for the previous test).

The values of the rms-roughness (expressed in μm) measured with the optical profilometer at the Metrology Laboratory for the three beryllium samples and for the first and second polishing are shown in tab.5.2.

The roughness appears almost constant for the three magnifications after the first polishing and is slightly smaller after the second polishing, especially at the high frequency (magnification 50X). Also from the profilometer maps it is possible to see that the polishing process is anisotropic, with straight parallel lines which are visible at all magnifications, see fig.5.17.

sample	1st polishing			2nd polishing		
	2.5X	5X	50X	2.5X	5X	50X
1 notch	0.35	0.33	0.32	0.26	0.25	0.18
2 notch	0.36	0.33	0.25	0.27	0.15	0.19
3 notch	0.32	0.34	0.32	0.20	0.21	0.18

Table 5.2: Roughness - rms values, in μm for the three Be plates after the first and second polishing

By comparing the X-ray radiographs and the data obtained with the optical profiler it is possible to conclude that a clear improvement of the surface is visible between the first and the second polishing. No beam inhomogeneities have been recorded with the X-ray radiographs; nevertheless it is important to highlight the fact that the detector to sample distance used is still very small compared to the window to detector distance at the beamlines. Some inhomogeneities at much larger distance can still appear. To

5.3 Improvements on the polishing of beryllium windows

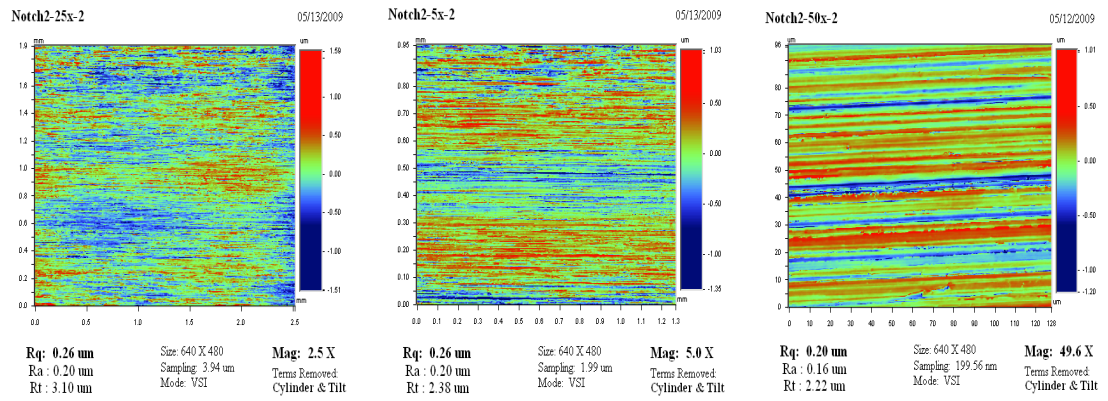


Figure 5.17: Profilometer maps of one of Be plates after the second polishing process, obtained at three different magnifications.

conclude, the sample processing should still be improved, in order to have surface modulations of less than 0.1 µm and rms roughness smaller than about 20 nm.

5. IMPROVEMENTS TO POLISHING OF SILICON CRYSTALS AND BERYLLIUM WINDOWS

Chapter 6

X-ray coherence exploited in imaging of ferroelectric domains

In this chapter, I will present an example of applications exploiting the transversal coherence of the X-ray beam: the investigation by coherent X-ray section topography of ferroelectric domain behaviour as a function of temperature in periodically-poled rubidium-doped potassium titanyl phosphate (Rb:KTP).

Before entering into the details of the experiment, I will introduce briefly some concepts about ferroelectricity, together with the main applications of periodically-poled ferroelectric crystals. Afterwards, I will describe the furnace that we developed and characterized at the ESRF and that allowed the investigation. Finally I will present the results obtained, together with simulations and a model proposed to describe the behaviour of the domains at high temperature.

6.1 Ferroelectricity

Ferroelectricity is the property of some dielectrics to have a permanent polarization in the absence of an external electric field. The discovery of ferroelectric crystals by J. Vasalek dates back to 1920 [182]. By modifying the electric field on a plate of Rochelle salt (potassium sodium tartrate) he recorded a hysteresis loop in the polarization, with the presence of a residual polarization at zero electric field. The name ferroelectricity comes by analogy with the properties of ferromagnetic materials, although the physical natures of the phenomena are very different. By analogy with ferromagnetic crystals,

6. X-RAY COHERENCE EXPLOITED IN IMAGING OF FERROELECTRIC DOMAINS

ferroelectric crystals possess a temperature, the Curie temperature T_c , where a phase transition from the ferroelectric to the paraelectric state occurs.

All ferroelectric crystals are non-centrosymmetric and they have one polar axis. They belong to a larger class of crystals, called pyroelectrics, which are polarized if the temperature is changed.

Barium titanate (BaTiO_3) is an example of a ferroelectric crystal. This crystal undergoes different phase transitions with temperature. Above 393 K, it has a perovskite structure: this is a centrosymmetric cubic structure. Therefore the crystal is paraelectric, since all the charges in the lattice are compensated. At lower temperatures, the crystal is subject to different structural changes, becoming tetragonal at 393 K, orthorhombic at 278 K and finally rhombohedral below 183 K. In all these structures, the crystal lattice is no longer centrosymmetric, and the charges are not compensated due to a displacement of the cations Ba^{2+} and Ti^{4+} with respect to the O^{2-} . This displacement is in three different crystallographic directions: $[100]$ for the tetragonal, $[110]$ for the orthorhombic and $[111]$ for the rhombohedral structure.

In fig.6.1 are shown the cubic and tetragonal structures. In the tetragonal structure, the Ti^{4+} and the Ba^{2+} cations are displaced slightly, by 0.1 \AA , producing a net polarization pointing, in this diagram, upwards and elongating the lattice parameter c . If an external electric field is applied to a ferroelectric crystal it is possible to permanently switch the polarization from one direction to the opposite, *i.e.* having the cations displaced downwards.

In fig.6.2 is shown a schematic hysteresis loop of a ferroelectric crystal. Under normal conditions, *i.e.* zero field and unprepared sample, the crystal will have different regions, called *domains*, within which the polarization is uniformly oriented. The polarization is differently oriented from one domain to another, which are separated by the so-called *domain walls*. In this configuration, the total polarization is close to zero under a zero applied field corresponding to the origin of the graph, O. As an external field is applied, the different domains start to orient in the direction of the field, until the applied field is sufficient for the crystal to become single-domain. In this condition, the polarization reaches a “saturation” value, indicated by P_s . If the field is now decreased to zero, a residual polarization, P_r , remains. This is due to the fact that some of the domains remain aligned in the same direction. It is necessary to invert the polarity of the electric field until a value called the *coercive field*, E_c to obtain again zero polarization. In order

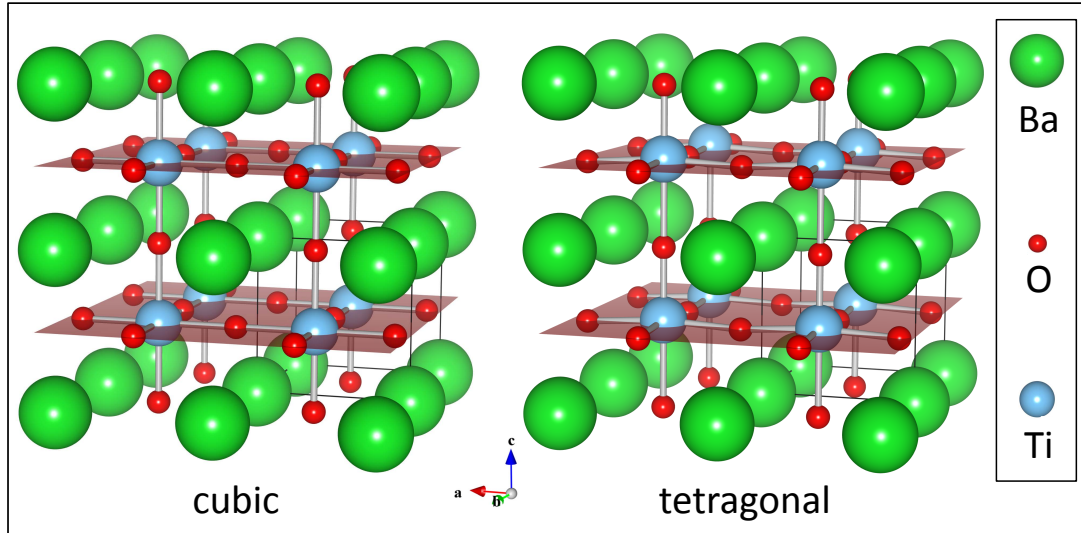


Figure 6.1: Cubic and tetragonal structures of BaTiO_3 . The pictures of the structures were generated using structural data from [183] and the software *Vesta*. The difference between the two structures is very small, and the best way to see it is to focus on the slight bending of the Ti-O bonds upwards in the tetragonal structure.

to depolarize the crystal, it is necessary either to increase its temperature above T_c or to repeat the hysteresis cycle with smaller and smaller electric field strengths until the original position O is reached.

The applications of ferroelectric crystals are very wide-ranging: among others, they can be used as tunable capacitors, non-volatile memory, sensors, *e.g.* in ultrasound machines, or in infrared cameras. Moreover, some ferroelectrics present very high non-linear optical properties that make them very useful as optical devices, for example in laser optics as frequency converters via quasi-phase matching (QPM). This particular application was foreseen for the crystal we have been studying, therefore the basis of the theory will be introduced here.

6.2 Ferroelectric crystals used for non-linear optics applications.

When electromagnetic radiation propagates in a medium, the electric field produces a polarization density inside the medium. This polarization can be expressed as a Taylor

6. X-RAY COHERENCE EXPLOITED IN IMAGING OF FERROELECTRIC DOMAINS

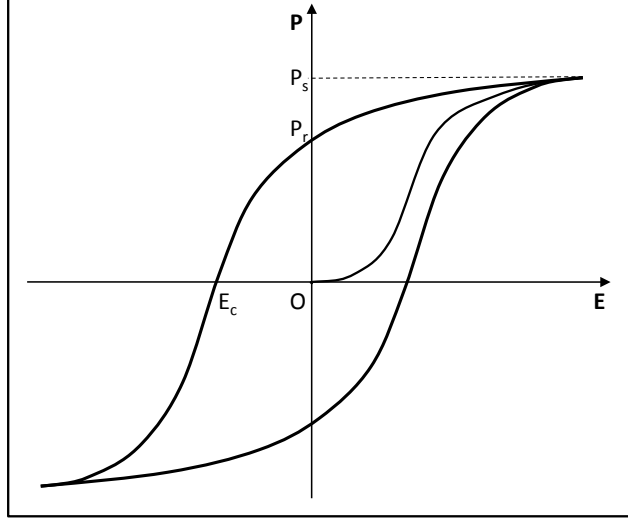


Figure 6.2: Hysteresis cycle of a ferroelectric crystal. P_S and P_r are the saturation and residual polarizations, E_c is the coercive field.

series expansion [184]

$$P_i(t) = \sum_j \epsilon_0 \chi_j E_j(t) + \sum_{j,k} \epsilon_0 \chi_{j,k}^{(2)} E_j(t) E_k(t) + \sum_{j,k,l} \epsilon_0 \chi_{j,k,l}^{(3)} E_j(t) E_k(t) E_l(t) + \dots \quad (6.1)$$

where the subscript indicates the Cartesian component of $P(t)$, the instantaneous polarization; $E(t)$, the instantaneous electric field; χ the linear susceptibility; and $\chi^{(n)}$ are the non-linear susceptibility of order n .

When the intensity of the electric field is weak, the non-linear terms may be neglected but in the case of high intensities, *e.g.* lasers, they cannot, resulting in non-linear optical effects.

One of the non-linear effects widely used in laser technology is the so-called *Second Harmonic Generation* (SHG), also known as *frequency doubling*. This phenomenon was observed for the first time by Franken and co-workers in 1961 [185]. In fig.6.3 is shown a diagram of SHG. An intense incident beam is passed through a non-linear crystal. Inside the crystal, there will be two polarization waves, corresponding to linear and quadratic susceptibilities. Therefore, at the exit of the crystal there will be a wave composed of two wavelengths: the fundamental, which has the same wavelength

6.2 Ferroelectric crystals used for non-linear optics applications.

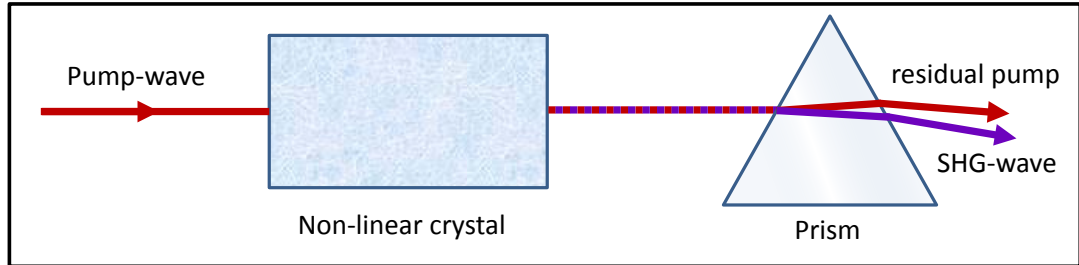


Figure 6.3: Second Harmonic Generation (SHG) scheme. A monochromatic wave of frequency ω impinges a non-linear optical crystal. At the exit of the crystal, a combination of the pump-wave and the frequency-doubled wave is obtained (symbolically separated by a prism).

as the pump-wave; and the SHG wave, with a wavelength that is half of the incident wavelength. In the picture, the two waves are ideally separated by a prism.

SHG is extremely sensitive to the phase of the waves. If the phase of the two waves is not matched, the intensity of the frequency-doubled radiation produced is very small. In order to be phase matched, the phase velocities of the pumping and the frequency-doubled radiations need to be equal. This implies that $n(\omega) = n(2\omega)$. The waves are said to be *perfectly matched* and the intensity of the SHG-radiation will increase inside the medium, at the same time reducing intensity from the pump wave, in so-called (*pump depletion*). Nevertheless, in the normal dispersion region, $n(\omega) < n(2\omega)$, resulting in different phase velocities. The result of having different phase velocities for the two waves is depicted in fig.6.4.

The graph represents the value of the second harmonic electric field, E_{SH} as a function of the distance travelled, z , by the wave in the crystal. The black dash-dotted line indicates the case of perfect phase matching, whilst the green dashed line shows the case of zero phase matching. In the small inset are plotted the photon momenta for the different cases. In the case of zero phase matching, the strength of the electric field increases until the radiation has travelled a distance called the coherence length¹, defined as $l_c = \pi/\Delta\mathbf{k}$ where \mathbf{k} is the photon momentum. This point corresponds to the first half of the polygon plotted in green in the inset. Starting from this point, E_{SH} decreases since the energy is flowing back from the frequency-doubled wave to

¹not to be confused with the coherence length defined in 2.3

6. X-RAY COHERENCE EXPLOITED IN IMAGING OF FERROELECTRIC DOMAINS

the pump wave. After a distance $z = 2l_c$ the SHG wave disappears, with all the energy reconverted into the pump wave. This phenomenon repeats periodically, with small maxima for odd multiples of l_c and minima for even multiples.

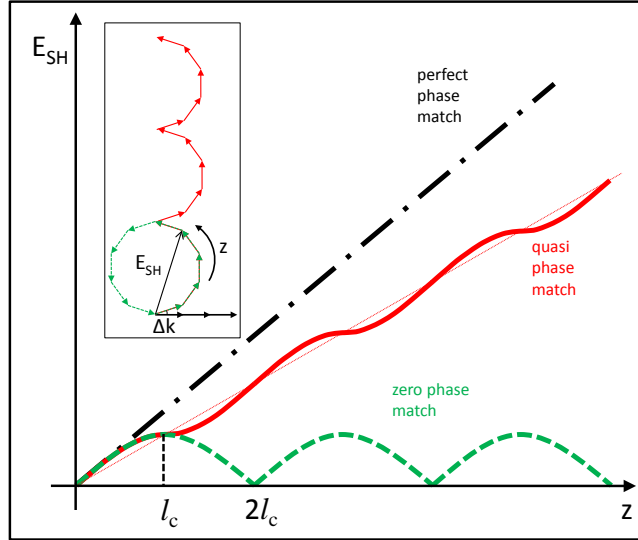


Figure 6.4: Plot of the strength of the electric field of the SHG radiation as a function of the distance travelled inside the crystal. In the inset is presented a geometrical approach to the phenomenon. In the case of perfect phase match, the arrows are all aligned, producing a linear increase of E_{SH} with the distance. If there is a phase shift of Δk , represented with a rotation of the photon momentum, the intensity increases until it reaches a maximum and decreases to zero, green curves. Finally, if quasi-phase match is implemented, it is possible to achieve an increase in the SHG radiation.

One way to match the phases is the so-called *quasi phase matching*. This method was proposed in theoretical work by Armstrong and co-workers, [186] and consists of alternating slabs of crystals with each slab being a symmetric inversion of the previous one with respect to the polar direction. If the length of the slabs is matched to the coherence length, it is possible to obtain the red curve in 6.4. Among the different methods used to achieve this, we are interested in the periodic poling of ferroelectric crystals.

Periodic poling is a method to obtain inversed domains in a crystal with widths which match the coherence length. The method was proposed by Yamada and co-workers, [187]. It consists in applying to a single-domain ferroelectric crystal an external electric

6.3 Visualization of ferroelectric domains using X-ray

field higher than the coercive field. The field is applied to periodic electrodes which are deposited using lithographic techniques on the $c+$ polar face of the crystal. In this way, it is possible to obtain a periodic structure of inverted domains. The width of the period is matched to the coherence length, which is calculated via the dispersion relation. When the two domains have the same width, *i.e.* duty-cycle 50:50, the quasi-phase matching is the highest and is said to be of first order. Domain widths are typically of the order of 3 μm to 40 μm .

6.3 Visualization of ferroelectric domains using X-ray

There are several methods of visualizing inverted ferroelectric domains, among others polarization microscopy, surface etching, powder or liquid crystal decorations, atomic force microscopy and X-ray topography techniques [188]. I will concentrate only on the last. First of all, we need to consider that for the 180° inverted domains, there is no lattice mismatch between the domains at the domain walls, unlike for e.g the 90° ones. Nevertheless, since the polarity is inversed, the same diffraction spot will be hkl for one domain type and $\bar{h}\bar{k}\bar{l}$ for the other, composing a *Friedel pair*. In a Friedel pair, the moduli of the structure factors are the same whilst the phases are inverted, therefore no intensity variation between domains is expected within the diffracted beam under normal conditions.

One way to visualize the inverted domains is to work in anomalous scattering conditions, *i.e.* at an energy close to an absorption edge of one of the elements. If one of the atoms in the lattice is scattering anomalously, then the amplitude of the factor structure is different for each component of the Friedel pair. This method has been used by Nizeki and Hasegawa [189]. They visualized inverted domains in a BaTiO_3 crystal using $\text{CrK}\alpha$ radiation and the 00 ± 3 Friedel pair.

Another method of visualizing inverted ferroelectric domains is by a combination of Bragg and Fresnel diffraction [190], and it is the method we used for our experiments. This method requires a large transverse coherence length of the incident X-ray beam, and can therefore be performed only at third generation synchrotron sources. As previously stated, the phase of the inverted domains is different from each reflection of the Friedel pair. A phase jump $\Delta\phi = \phi_{hkl} - \phi_{\bar{h}\bar{k}\bar{l}}$ is present. Therefore a periodically poled ferroelectric crystal can be seen as a phase grating by the incoming X-ray beam if set in

6. X-RAY COHERENCE EXPLOITED IN IMAGING OF FERROELECTRIC DOMAINS

Bragg condition for a given reflection. As it has been shown in 4.2.3, a periodic object illuminated with a coherent beam will produce a periodic pattern in both the direction of the periodicity and in the direction of propagation of the beam.

This method has been successfully used to solve the structural matching between inverted domains in potassium titanyl arsenate (KTA) and potassium titanyl phosphate (KTP), [191, 192]. It has also been successfully applied to *in situ* studies of the behavior of rubidium titanyl arsenate (RTA) under an electric field [193]. In the experiments we performed, we wanted to study the behaviour of domains at temperatures close to and above the Curie temperature of KTA and rubidium doped KTP (Rb:KTP) crystals. In fact, the process of transition from one stable polarization state to another with opposite direction of the macroscopic electrical dipole remains poorly understood and related studies on KTP and isomorphic crystal are limited. However, its understanding is crucial for obtaining highly efficient QPM devices.

In order to perform the experiment, we developed a furnace whose main characteristic is to preserve the coherence of the incoming X-ray beam.

6.4 Coherence preserving furnace

The furnace was developed in the Sample Environment Laboratory of the ESRF by B. Gorges and H. Vitoux. The results of the characterization of the furnace that I report here have been also published in an article, [194], of which I am a co-author. The challenge in the design of the furnace concerns the facts that the crystals we want to study are, in general, optically transparent and thermal insulators, and the experiments needs to be performed in transmission geometry. If the sample is heated only from below, a very large thermal gradient would be produced, provoking distortions that would conceal the effects we are looking for. Therefore, an alternative way of heating the sample was proposed, consisting of two black-body radiator plates located near the sample. The radiators need to have low absorption for X-ray in the 15-50 keV range, be chemically homogenous, with very small thickness variation, *i.e.* very well polished, with good heat conductivity and high irradiation power. By considering all these requirements, a good solution seemed to be to use single silicon crystal plates of 150 μm thickness.

6.4 Coherence preserving furnace

Another problem is the fixing of the sample in order to keep it free of strain when heated. The use of glue or a clamp can introduce distortion when the sample is heated due to the different thermal expansion coefficients of different materials. In order to avoid this, the sample is simply rested on a boron nitride support between the silicon plates. A thermocouple is in contact with the lower part of the sample through a hole in the boron nitride support. Moreover, to avoid deleterious contact between the heater, made out of nickel, and the silicon, a boron nitride framework was also fabricated. In fig.6.5 are shown the different parts of the furnace, together with a photograph of it.

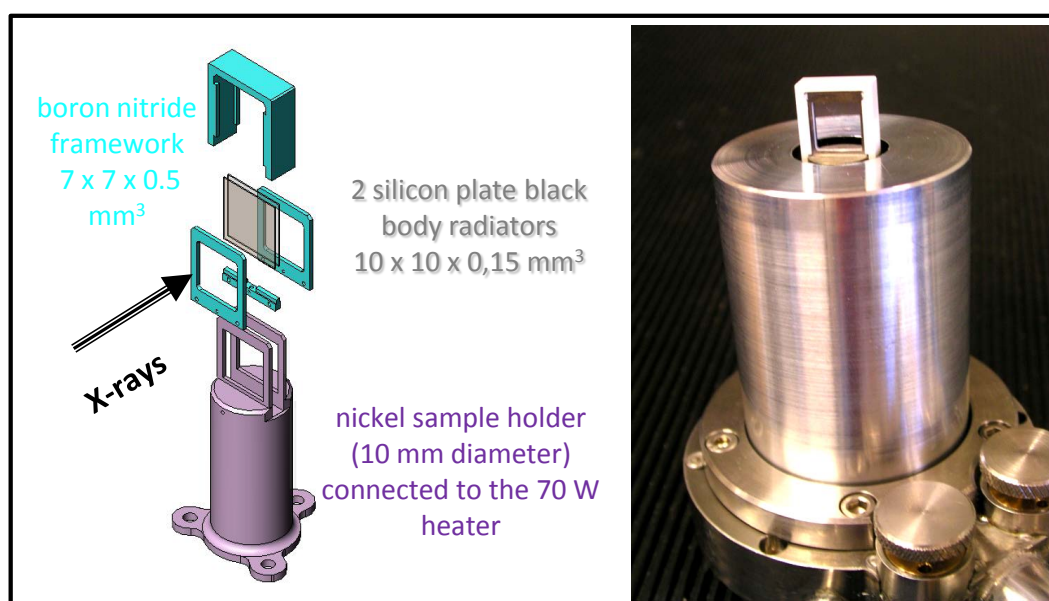


Figure 6.5: Left, scheme of the furnace's sample holder. In purple, the nickel sample holder which is connected to the resistance heater; in cyan, the boron nitride pieces; and in grey, the silicon plates. Right, a photograph of the furnace, with an aluminium cover to minimize heat losses.

The furnace was tested at the BM05 beamline using different crystal samples. The first test was made to check the efficiency of the heating and the reliability of the indication provided by the thermocouple. In order to do so, we studied the phase transition between α and β phases in a $5 \times 5 \text{ mm}^2$ quartz crystal which exhibits Dauphiné twins. α and β are two of the nine possible crystalline phases of silica SiO_2 with the former being the stable phase at low temperature and the latter being stable between 573°C

6. X-RAY COHERENCE EXPLOITED IN IMAGING OF FERROELECTRIC DOMAINS

and 870°C. Dauphiné twins are one of the three types of twinning commonly found in natural quartz, together with Brazil and Japan twins, and is composed of two quartz crystals with the same chirality (either two right-handed or two left-handed crystals) combined. Fig.6.6.a) shows a white beam topograph of the sample at 50°C where the two twins are clearly visible. The sample was then heated to 600°C, which is above the phase transition temperature $T=573^\circ\text{C}$, fig.6.6.b). At this temperature, the quartz is completely transformed into the β form, and the twins are reorganized into a single crystal. In fig.6.6.c) is shown the situation after the sample has been cooled again to room temperature, showing that the Dauphiné twins have reappeared, but in a completely different arrangement. By this first test, we determined that the difference between the temperature read by the thermocouple and the real temperature at the sample was about 10°C.

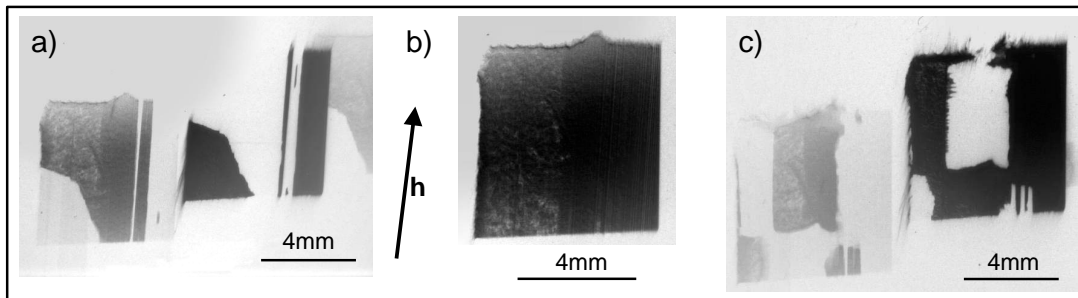


Figure 6.6: a) the quartz at 50°C, presenting clearly visible twins. b) the crystal at 600°C, completely in the β phase and without any twinning visible. c) the crystal cooled down to room temperature, presenting twins again, but differently organized. Projection of the diffraction vector represented by h .

A second test was performed in order to estimate the temperature gradient inside the furnace, by studying the ferro-paraelectric phase transition of a $5 \times 5 \text{mm}^2$ BaTiO_3 crystal, which has a Curie temperature $T_c \approx 121^\circ\text{C}$. Fig.6.7.a) shows a white beam topograph of the sample at room temperature. The crystal is ferroelectric and it is strongly distorted by the presence of 90° domains. At 120°C, the different domains start to disappear together with the strain fields related to them, fig.6.7.b). In the lower part of the image, closer to the heater, the phase transition is practically complete (the strain field related to the different domains tends to disappear), while the middle and top parts of the crystal are still in the ferroelectric state (still strongly distorted).

Finally, in fig.6.7.c) is shown the topograph of the sample above the Curie temperature. The crystal is almost completely in the paraelectric state, except a small part on the upper right corner which is still ferroelectric and distorted. This gives us an estimation of the thermal gradient, being of the order of $1^{\circ}\text{C}/\text{mm}$.

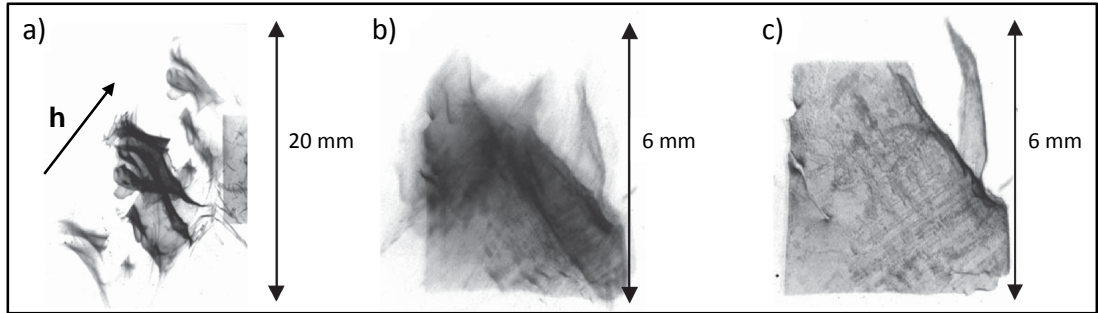


Figure 6.7: a) BaTiO_3 crystal at room temperature; the crystal appears strongly distorted due to the presence of 90° ferroelectric domains. b) $T=120^{\circ}\text{C}$, the crystal is undergoing phase transition. The bottom part of the crystal, which is closer to the heater, is slightly warmer and is already in the paraelectric phase. The middle and the top parts are still ferroelectric and therefore deformed. c) $T=125^{\circ}\text{C}$, the crystal is almost completely paraelectric, except at the top right corner. The arrow represents the projection of the diffraction vector.

Finally, the last test was intended to check whether the furnace preserved the coherence of the beam. In order to do so, we measured the coherence of the beam using the Talbot effect as explained in 4.2.3. We measured the value of the angular source size: (i) without the furnace; (ii) in transmission with the furnace at room temperature; (iii) in transmission with the furnace at 800°C . We obtained the following results: (i) 0.80 ± 0.02 , (ii) 0.98 ± 0.02 , (iii) 0.99 ± 0.02 . A slight increase in the value of the angular source size was measured. Nevertheless, the transversal coherence length of the beam with the furnace is $\approx 40 \mu\text{m}$ and does not depend on the temperature. This value is enough for the visualization of inverted ferroelectric domains through the coupling of Bragg and Fresnel diffraction.

6. X-RAY COHERENCE EXPLOITED IN IMAGING OF FERROELECTRIC DOMAINS

6.5 Visualization of inverted domains in KTA and Rb:KTP crystals.

We performed two separated experiments, both at the ESRF beamline BM05. In the first experiment we studied a KTA crystal whilst in the second one we studied a Rb:KTP crystal.

The KTA sample was about $3 \times 3 \times 0.4 \text{ mm}^3$ with a poling period of $39 \mu\text{m}$. The Curie temperature for KTA is 880°C [195]. In order to index the diffraction spots I used a software called Orient Express¹, see fig.6.8.

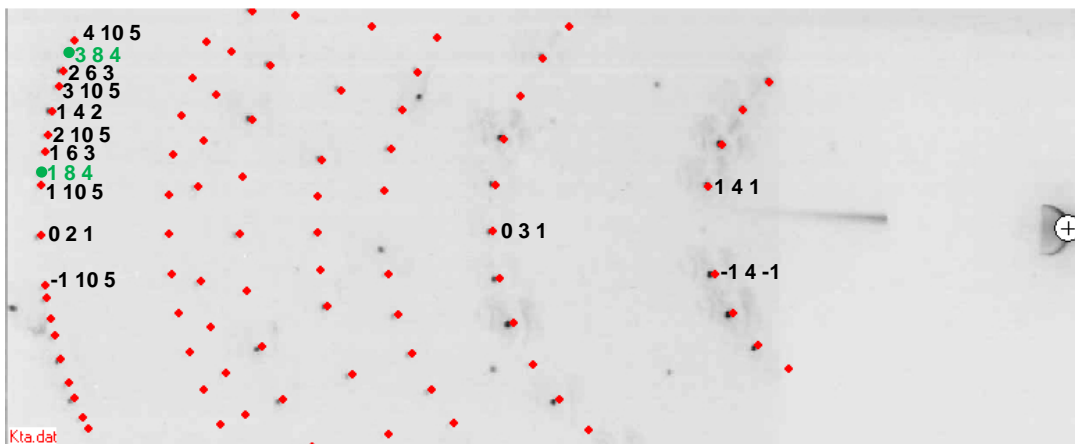


Figure 6.8: Indexation of the KTA crystal using the software Orient Express. In green, the reflections which were analyzed because they showed a maximum contrast of the periodic pattern. Some spots are due to the silicon crystal plates and therefore are not taken into account in the indexation process.

Unfortunately, the experiment was not very successful, due to a severe distortion of the crystal under heating, fig6.9. We understood that the calibration made for the thermal gradient was not correct at higher temperatures (above 700°C) and that we needed to improve the design of the furnace if we wanted to study samples at such high temperatures.

¹available from <http://www.ccp14.ac.uk/ccp/web-mirrors/lmgp-laugier-bochu/>

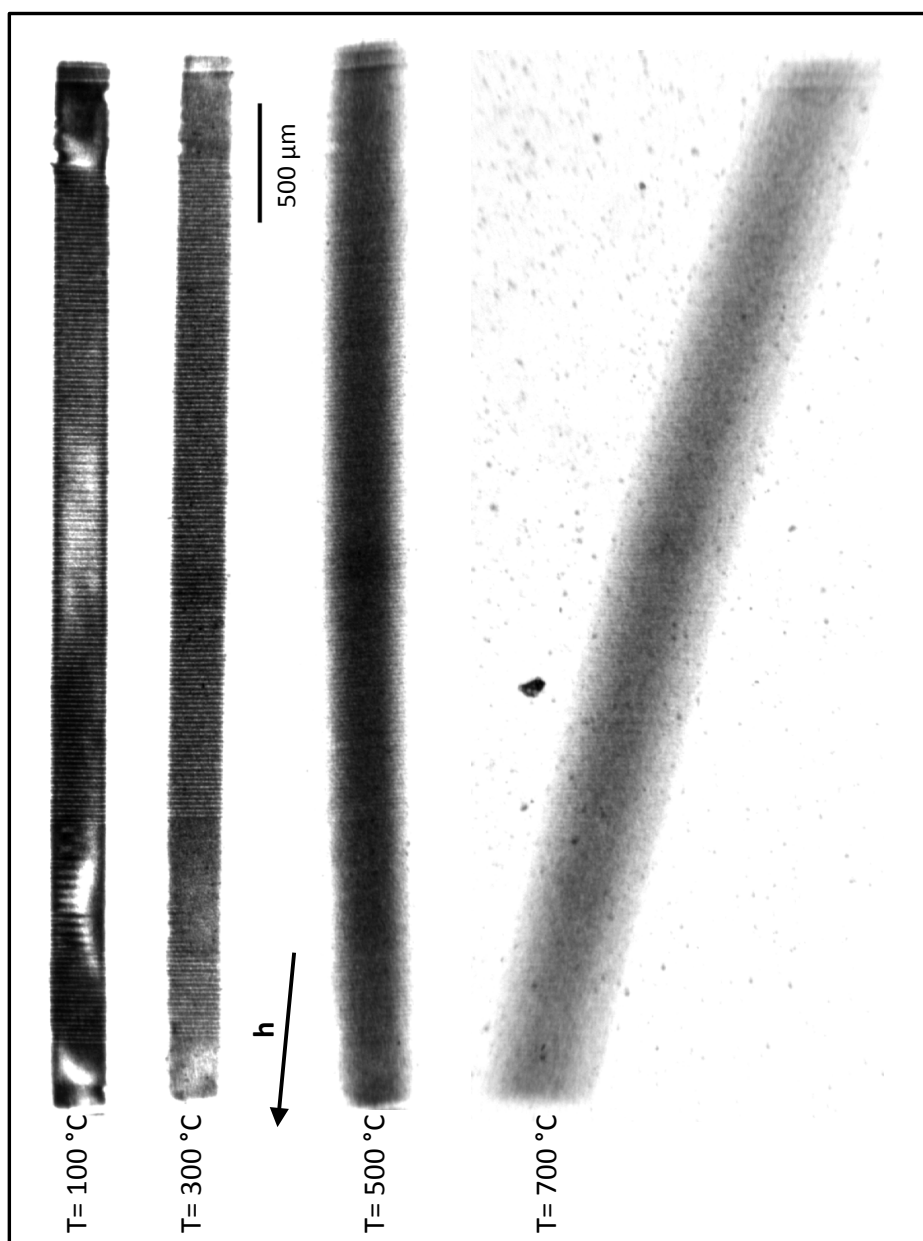


Figure 6.9: White beam topographs of the 184 reflection of the KTA sample, $\lambda \approx 0.29\text{\AA}$, film-to-sample distance 120 cm. The image at 700 °C appears very blurred, due most probably to strong distortion and vibrations of the crystal

6. X-RAY COHERENCE EXPLOITED IN IMAGING OF FERROELECTRIC DOMAINS

Thanks to the technical help of colleagues from the Sample Environment Lab, we made two improvements. First, we added a small aluminium cylinder with two holes (one for the incoming and one for the diffracted beam) to be used as an additional infrared mirror. Second, we enclosed the whole furnace inside a larger dome, again with entrance and exit holes for the beam, closed with Kapton[®] foils, 6.10. By using a primary pump, we evacuated the air inside the dome, then we replaced the air with nitrogen (in order to avoid oxidation of the nickel components of the furnace) and finally we evacuated the nitrogen again. The experiments were then performed under a low vacuum of approximately 10^{-2} mbar.

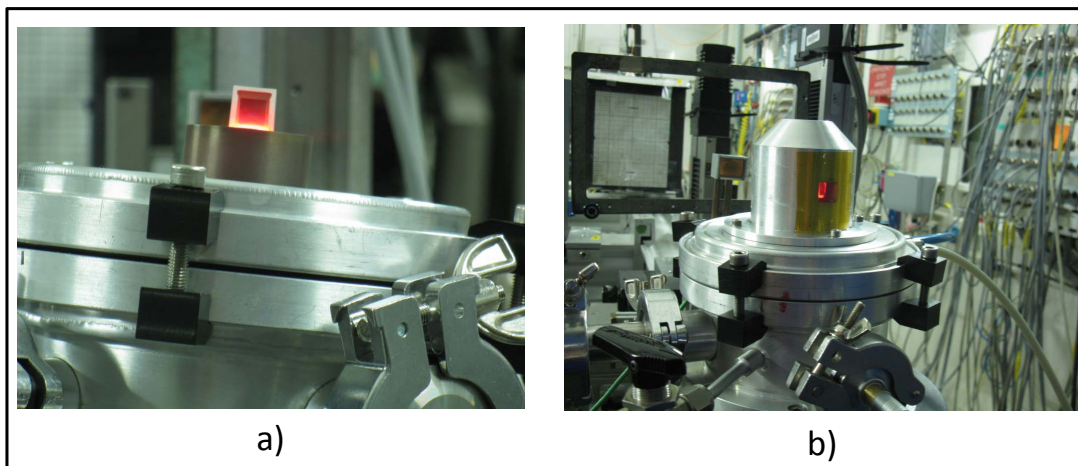


Figure 6.10: a) furnace for the experiment with the KTA crystal; b) improved furnace, with an internal infrared mirror (not visible in the picture) and the external dome.

These improvements allowed us to perform the experiment on a Rb-doped KTP crystal. The results of this experiment have been published in the Journal of Applied Crystallography, [196].

6.6 Investigation by coherent X-ray section topography of ferroelectric domain behaviour as a function of temperature in periodically-poled Rb:KTP.

Rb-doped KTP is one of the most attractive ferroelectric non-linear optical materials for quasi-phase matched devices due to its limited domain broadening, which grants

6.6 Ferroelectric domain behaviour with temperature in Rb:KTP

high pattern fidelity, and to its high resistance to optical damage, especially in the blue-green region [54, 197]. The sample was obtained from a 3mm thick single domain c-cut flux-grown Rb:KTP crystal. The poling was done using an aluminium grating with period $\Lambda = 38.83 \mu\text{m}$ with a duty cycle of 25%:75% (Al:insulator). The thickness of the sample was then reduced to $500 \mu\text{m}$ by mechano-chemical polishing. The structure of the Rb:KTP crystal used is shown in fig.6.11. The structural data were obtained from a small section of the crystal ($210 \times 80 \times 120 \mu\text{m}^3$) using a Gemini kappa-geometry CCD Diffractometer (Oxford Diffraction Ltd., UK) with Mo-K α radiation (0.707 \AA). The refinement of these data confirmed the structure as that accepted for pure KTP, namely orthorhombic in space-group $Pna21$. The refined percentage of Rb replacing K was $0.3\% \pm 0.1\%$. The Curie temperature was estimated to be approximately the same as for KTP, $T_c (\approx 935 \text{ }^\circ\text{C}, [198])$ given the very low content of Rb and the linear relationship between T_c and the amount of Rb suggested by Thomas *et al.*, [199].

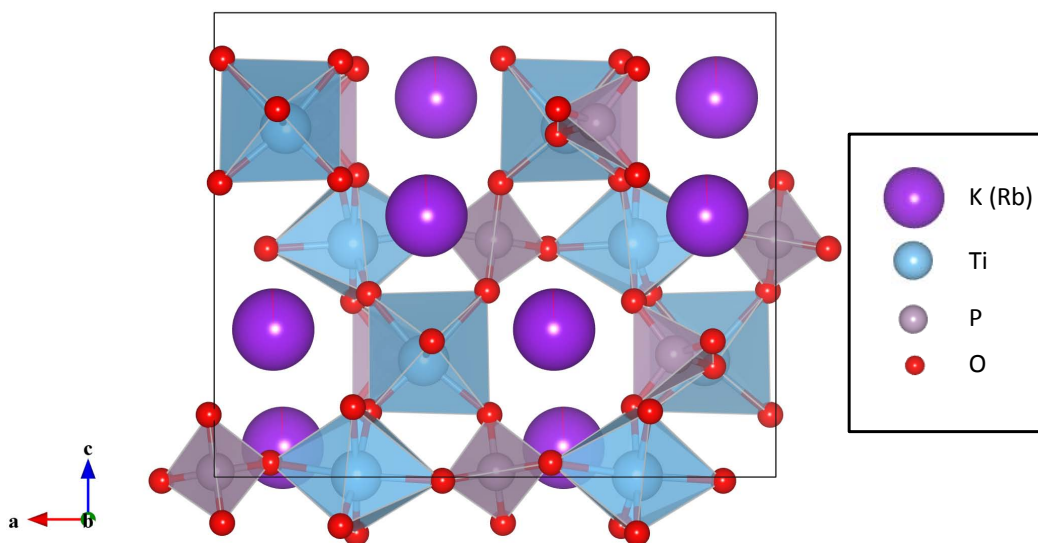


Figure 6.11: Structure of the Rb:KTP crystal. Due to the very low level of doping, there are no Rb atoms displayed, even though from the structure we know that 0.3% of the K is replaced by Rb.

The fundamental harmonic of reflection used in the experiment was the 162 as obtained by using the software Orient Express. By knowing the d-spacing of the 162 reflection

6. X-RAY COHERENCE EXPLOITED IN IMAGING OF FERROELECTRIC DOMAINS

together with the distances from the sample to the film and from the topograph to the direct beam spot, it is possible to obtain the wavelength of the fundamental harmonic by simply applying Bragg's law. We obtained a value of 0.62 Å for the first harmonic. Nevertheless, considering the sample thickness and absorption, we estimated that most of the fundamental harmonic was absorbed. Therefore the spot recorded corresponds to the 12 2 4 reflection with a wavelength of 0.31 Å. The phase shift between adjacent domains was calculated using the structural data and the software DABAX included in the package XOP, [200]. We obtained a phase shift $\Delta\phi$ of 25.77°. The phase shift was calculated assuming ([192]) that the atom P1 is the pivot atom for the inversion of the adjacent domain. Due to this phase shift, the crystal acts as a phase grating for the diffracted beam, therefore producing, via the Talbot effect, a periodic pattern in both the propagation distance and the detector plane. The simulation of the topographs was made using the same software used by Rejmankova *et al.*, [190]. The Fourier coefficients of the intensity profile recorded at a distance D from a sample can be expressed as:

$$I_m(D) = I_{m,\text{coh}}(D) \gamma(\lambda Dm/a) R(m/a) \quad (6.2)$$

where $I_{m,\text{coh}}(D)$ are the Fourier coefficients corresponding to the illumination by a transversal fully coherent beam, $\gamma(\lambda Dm/a)$ is the degree of coherence between two points separated by $(\lambda Dm/a)$, $R(m/a)$ is the resolution of the detector for the spatial frequency m/a , and a is the period of the grating. D is the defocusing distance, defined as

$$D = \frac{(d_1 d_2)}{(d_1 + d_2)} \quad (6.3)$$

where d_1 is the distance from the source to the sample and d_2 from the sample to the film. Using the Zernike-Van Cittert theorem [51], it is possible to express the degree of coherence as a function of the angular source size as

$$\gamma(\lambda Dm/a) = e^{-(\alpha\pi Dm/2a)^2/\ln 2} \quad (6.4)$$

for an angular Gaussian beam profile of width α .

In fig.6.12 are shown the experimental topographs together with the simulations obtained at room temperature and at different defocusing distances. The agreement

6.6 Ferroelectric domain behaviour with temperature in Rb:KTP

between the data and the simulations is very good, and confirms the validity of the theory used.

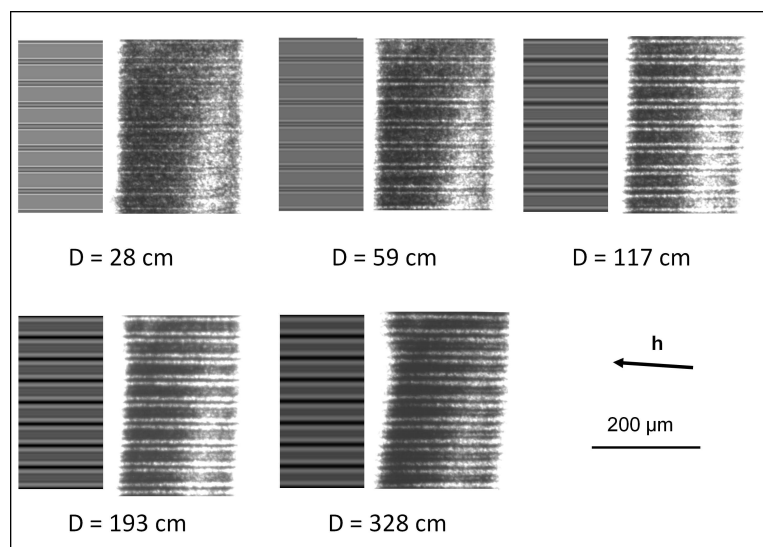


Figure 6.12: Part of the section topographs of 2 12 4 reflection, recorded at different defocusing distances, compared with the simulations made over 8 periods. $\lambda = 0.31 \text{ \AA}$, point spread function of the film being $2 \mu\text{m}$. Small absorption ($\mu_0 t \approx 0.7$). \mathbf{h} is the projection of the diffraction vector onto the film.

The sample was then heated and a series of topographs at different temperatures and distances was collected. In fig.6.13 are shown the experimental topographs at a defocusing distance of 117 cm, together with the simulations obtained using the domain models shown on the right of the simulations. In order to simulate the behaviour of the domains with temperature it has been necessary to use a non-constant domain profile in the bulk of the crystal, changing from one surface to the other. The ratios of the widths of inverted domains compared to the width of the period are represented in black, as well as its percentage. At temperatures below 800°C , the ratio is the nominal obtained during the poling, *i.e.* 25% of the period is composed of inverted domains. At a temperature recorded by the thermocouples of 800°C , the simulation requires 30% of the period to be inverted at the predominately c^+ face, linearly graded to 25% in the bulk and linearly graded again towards lower values, $\approx 10\%$, at the opposite face. This tendency is increased at higher temperature, with the c^+ face becoming 60% inverted at 930°C , and with the c^- face becoming mono-domain above $\approx 875^\circ\text{C}$. Unfortunately,

6. X-RAY COHERENCE EXPLOITED IN IMAGING OF FERROELECTRIC DOMAINS

at higher temperatures, physical distortions of the crystal prevented the observation to a completely mono-domain state or the ferro-paraelectric phase transition. It is important to highlight the fact that the temperature recorded is that at the thermocouple, and could be overestimated with respect to the real temperature at the sample, due to a thermal gradient along the sample that, at high temperatures, appears to be bigger than the calibrated value for the BaTiO₃ sample of 1°C/mm, and is most probably of the order of 25°C/mm.

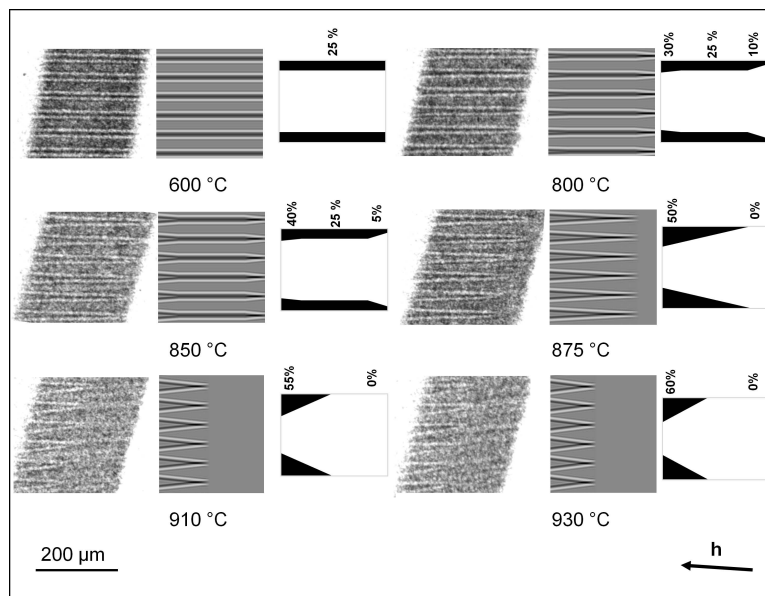


Figure 6.13: Parts of the section topographs of the 2 12 4 reflection showing six periods, recorded at defocusing distance of 117 cm and at different temperatures (as read by the thermocouple), together with the simulations obtained using the domain models shown on the right of the corresponding simulations. The model profiles are drawn over one period, where black represents the inverted domain part of the period, and white the non-inverted one.

The observed behaviour can be explained by assuming the presence of an internal electric field, E_{bi} , built in during the thermal treatment of the crystal. This field is due to concentration gradients of ionized defects created mainly by out-diffusion of potassium and oxygen atoms when heated, as shown by Kugel and Rosenman [201] for another ferroelectric crystal, LiNbO₃ (in that case, only the diffusion of oxygen has been considered) and by Angert *et al.* for KTP, [202]. The depth into which the built-in

6.6 Ferroelectric domain behaviour with temperature in Rb:KTP

electric field penetrates increases with the heat treatment time and temperature, though the magnitude of the field is reduced. At the same time, the coercive field, E_c necessary to switch the domains becomes weaker as the temperature is increased, [203]. This results in $E_{bi} > E_c$ in near surface regions and the domains are switched consecutively. Fig.6.14 shows the model used to interpret the results obtained. Fig.6.14.a) presents the situation at low temperature. The inverted domains are represented in blue while the non-inverted ones are in white. The arrows represent the polarization, and the left surface corresponds to the predominately c^+ face. In fig.6.14.b) the built-in electric field is created, in light blue, near the c^+ faces. Under the condition $E_{bi} > E_c$, the domains are switched near the surfaces. This would produce head-to-head domain walls which are energetically unfavourable. A compromise between electrostatic and elastic energies is necessary, and the system relaxes into the “saw tooth” domain structure, as shown in fig.6.14.c). By increasing the temperature, the inverted domains disappear from the initially c^- -dominated face of the sample, and become wider at the opposite face 6.14.d).

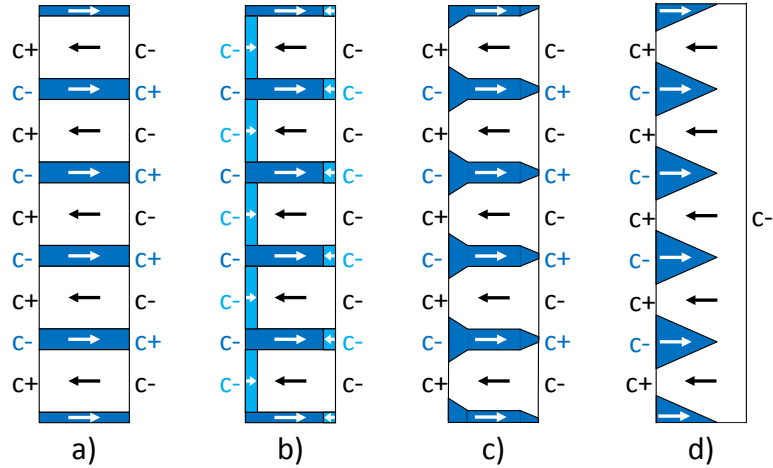


Figure 6.14: Model of the behaviour of the periodic domains as a function of temperature. a) low temperature, showing the domains as poled; b) at high temperature a built-in electric field is created, represented in cyan. This field attempts to switch the polarity in the areas near the sample surfaces corresponding to a c^+ face as-poled. This results in the “saw tooth” domains represented in c). At higher temperature, the inverted domains disappear on the originally c^- -dominated surface, while they increase on the opposite surface (d).

6.7 Conclusions

The study of the high temperature behaviour of ferroelectric domains in a periodically-poled Rb:KTP crystal from room temperature to around the Curie temperature has been performed *in situ* using synchrotron radiation. This has been possible thanks to the transversal coherence of the beam and is an example of the studies which are possible to perform only at a third generation synchrotron source.

The simulations confirm the validity of the atomic model presented by Pernot *et al* [192] that consider the atom P(1) as the pivotal atom between inverted domains. The obtained data have been successfully modelled in terms of the spontaneous polarization inversion due to ionized defect gradients created by out-diffusion of potassium and oxygen ions when the sample is heated close to T_c in a low vacuum.

The results obtained are in agreement with *ex situ* work published by Kugel and Rosenman [201] and Angert *et al.* [202].

Chapter 7

Further diamond related studies

In this chapter I will introduce three studies which resulted in three different published papers that I have co-authored. These studies are not directly related with the main topic of my thesis but they all have in common the used material (diamond) and the characterization techniques used (X-ray Topography).

7.1 Bending diamonds by femtosecond laser ablation

The subject of the first paper, [92], is the possibility of producing statically bent diamonds by using femtosecond laser ablation; such a bent crystal could be used as an extraction device for high energy beam, *e.g.* at the Large Hadron Collider (LHC) in Geneva. It was proven that charged particles incident on a single-crystal with small angles respect to crystallographic directions and having low transverse momentum with respect to the axis of the crystal are channelled inside the lattice. This effect persists even if the crystal is slightly bent, such that the particles may be deviated from their original direction of motion as in a dipole magnet. Since the fields are very strong, this results in bending power equivalent to a magnetic field of several thousand Tesla. Diamond has proven to be resistant to the harsh environment close to the particle beam, but being rigid and brittle, mechanical bending has been proven to be almost impossible. Laser ablation seems a promising technique to bend the crystals. Two high quality HPHT type IIa diamond samples were characterized before and after laser ablation by white beam X-ray topography in order to verify whether the ablation destroys the quality of the crystal. One sample presented trenches only on one surface while the

7. FURTHER DIAMOND RELATED STUDIES

other on both surfaces. A bent crystal in Laue geometry focuses a polychromatic beam. If the crystal is cylindrically bent, the radius of curvature for meridional focusing and in the case of a large source to sample distance is $R \approx 2q/\cos(\theta_B)$, where q is the focusing distance, [204]. By collecting topographs at different sample to film distances and by comparing the dimension of the topographs, we obtained an estimation of the bending radius of the crystals. For the crystal with trenches on both sides, no difference in the size of the topographs was recorded at the different distances, meaning that the sample was flat. For the other sample instead, focusing of the beam (in both vertical and horizontal direction) was obtained if the trenches were upstream, and defocusing for downstream trenches, see fig.7.1.

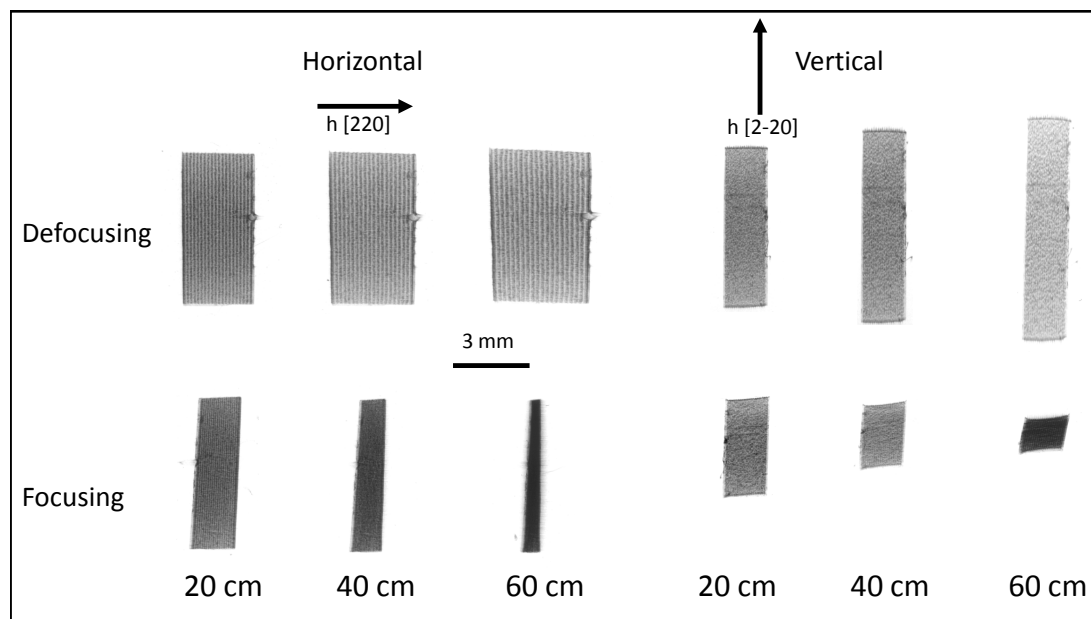


Figure 7.1: White beam topographs of a laser ablated diamond at different sample to film distances. Focussing of the beam is obtained for trenches upstream. Projection of the diffraction vectors are represented by the arrows.

From the widths and heights of the topographs at the different positions it was possible to obtain the focal lengths in the two directions, (84.0 ± 0.8) cm and (97.2 ± 0.5) cm respectively. This results radii of curvatures of (171 ± 2) cm in the horizontal direction and (200 ± 2) in the vertical. Furthermore, by converting the distance between adjacent trenches in each picture to local curvature, it is found that the maximum possible non-

7.2 X-ray topography of diamond using forbidden reflections: which defects do we really see?

uniformity in relative curvature across the crystal is about 3%.

7.2 X-ray topography of diamond using forbidden reflections: which defects do we really see?

The second paper, [205], was written in collaboration with A. Shiryaev and colleagues from Russia. The subject of the paper was to compare the contrast obtained on synthetic diamond in allowed and forbidden reflections. In the diamond structure (space group $Fd\bar{3}m$), the X-ray reflections from the 222 planes are forbidden because of symmetry restrictions. However, the thermal anharmonicity of atomic vibrations, and the covalent character of bonding in crystals like diamond, Si and Ge, lead to distortion of the shape of the electron cloud which, in contrast with an ideal crystal, deviates from spherical. These reflections are sometimes called quasi-forbidden.

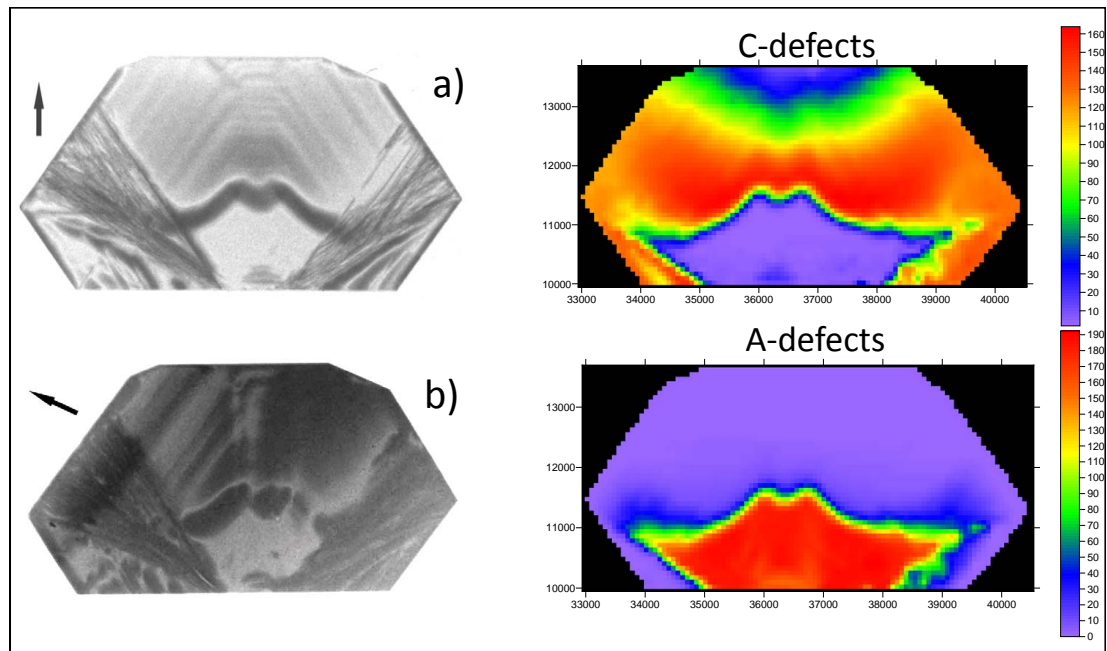


Figure 7.2: On the left, X-ray topograph in transmission geometry, obtained by rocking the crystal and integrating the diffracted intensity, $E = 20\text{keV}$. a) 400 reflection, b) 222 reflection. On the right, IR maps showing the concentrations of C and A defects.

The study of quasi-forbidden reflections can give information on lattice deformations, such clusters of impurity atoms but the influence of points defect on the intensities of

7. FURTHER DIAMOND RELATED STUDIES

forbidden reflections remains an open question. We studied two synthetic and three natural diamonds plates by X-ray topography in monochromatic beam, at 20 keV. Due to dispersion and in order to obtain the entire image of the plates the topographs were obtained by rocking the crystal and integrating the diffracted intensity. The synthetic diamonds were a type IIa HPHT diamond grown from Element Six and a Ib diamond grown by the split sphere (BARS) method by colleagues in Novosibirsk.

The latter sample was very interesting since it presents two regions with different types of nitrogen impurities, as it is possible to see from fig.7.2 in the central part of the plate, the N is single substitutional (C defects) while in the bottom part, close to the seed it form nitrogen pairs (A defects). We collected X-ray topographs of this sample at room temperature and also, using a furnace, at temperature of about 1000 K, using a FReLoN camera with 3 μm resolution. We measured the ratio of the diffracted intensity between two regions with different nitrogen defects. For the allowed 111 reflections, this ratio is constant with temperature, but for the 222 reflections we see that above 873 K it decreases, therefore suggesting that point defects can influence the intensity of a forbidden reflection.

7.3 Crystal growth and perfection of large octahedral synthetic diamonds

The third and last paper, [206] was written in collaboration with F. Khokhryakov, I. Kupriyanov and other Russian colleagues. In this work we characterized octahedral diamond crystals grown by the temperature gradient method at $T=1550\pm 20$ °C and at a pressure $P=5.7\pm 0.1$ GPa, using a split-sphere (BARS) apparatus, using $\text{Ni}_0.7\text{Fe}_0.3$ alloy as solvent catalyst.

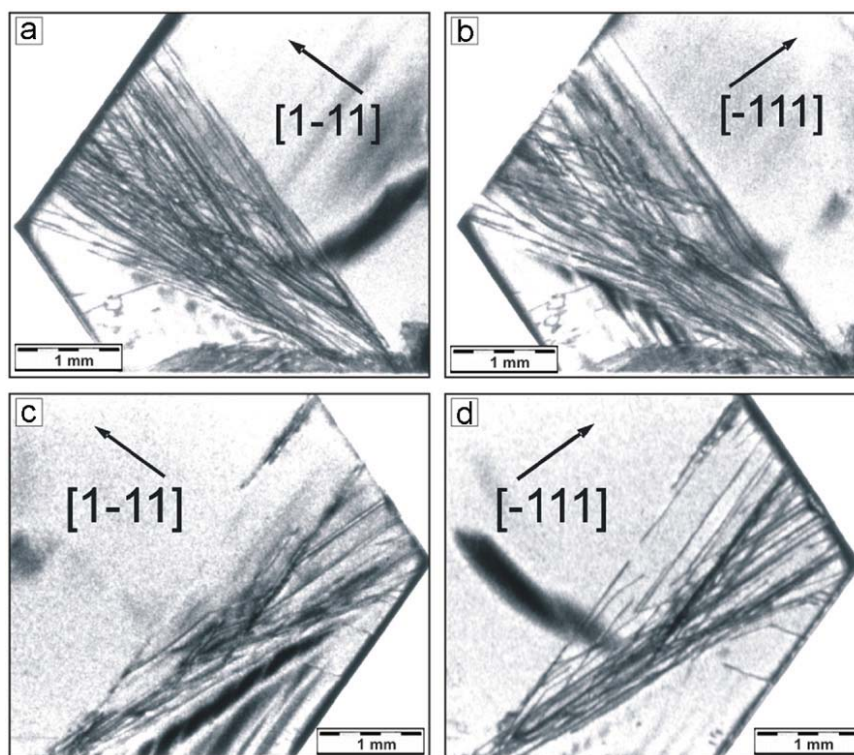


Figure 7.3: Zoom of the white beam topography of a Ib synthetic diamond. The projection of the diffraction vector is represented by the arrows.

The characterization was performed by selective etching, X-ray topography, IR spectroscopy, photoluminescence topography and cathodoluminescence topography. One of the plates characterized was the same Ib synthetic diamond used for the previous paper on forbidden reflections, see fig.7.2. Fig.7.3 shows a set of sub-images of a white beam topographs collected at BM05. It is possible to see bunches of defects. It is difficult

7. FURTHER DIAMOND RELATED STUDIES

to determine exactly the types of most defects due to their high density. The majority of these defects are $\langle 111 \rangle$ oriented dislocations, generated within the seed crystal area, together with $\langle 112 \rangle$ oriented planar defects (stacking faults or microtwins).

The fact that the source of most of the defects is in the region close to the seed is a result which is common to most of the plates studied. This could be related to a low quality of the seed crystal or of its surface finishing.

Chapter 8

Conclusions

The main goal of this PhD was twofold.

On the one hand the task of characterizing different materials of interest to be used as X-ray optical elements (diamond, silicon and beryllium). This was done in collaboration with the producers and/or with the people involved in the finishing processes. The main purpose was to improve the bulk and/or surface quality in order to meet the stringent requirements for the materials to be used as X-ray optical elements which preserve the transverse coherence of the beam.

On the other hand, the purpose was to use this extraordinary property of coherence in a synchrotron beam to investigate, for the first time with *in situ* visualization methods, the behaviour of ferroelectric domains in a periodically-poled rubidium-doped potassium titanyl phosphate (Rb:KTP) single crystal as the Curie temperature T_c is approached.

Characterization of high quality crystals was performed with a set of different X-ray based methods (and supplemented by other methods, *e.g.* optical) on many different beamlines and in collaboration with many scientists and technical staff. Here a main task was not only to use the complementary methods, but to push their limits and to obtain semi-quantitative and, above all, quantitative results concerning crystal defects and crystal quality.

One of the main results regarding the diamonds is the considerable improvement of the bulk quality (and to some degree also of the crystals dimension) of the synthetic diamonds. This was only possible thanks to the longstanding collaboration between the ESRF, Element Six in South Africa and on the Isle of Man and the University of

8. CONCLUSIONS

Johannesburg. An idea of the quality jump between the “old” (produced in the last decade of the last century) and “new” material is given by the comparison of phase plates shown in fig.4.27. An impressive example of the increased efficiency of the new material used in an application as X-ray optical elements may be that of beam-splitter monochromator at the ESRF beamline ID14. Recently, just by replacing an old type Ib plate by a new type IIa one, a tenfold increase of the flux at the sample position was obtained.

We pushed the possibilities of HRXRD to quantify sub-arcsecond broadening of rocking curves of high quality crystals (in particular of diamond) that is due to the presence of residual strains in the bulk and the subsurface region. This was performed in two different steps. First, by implementing different numerical methods either to calculate the instrumental function or to determine it from measurements. The final result was compared with a direct measurement of the instrumental function by using high order *e.g.* 999 and forbidden 222 reflections. Second, once we could determine the apparatus function with sufficient reliability, we were able to determine the broadening of the rocking curves due to the presence of defects. The results obtained show that, in the case of high quality type IIa diamonds, this broadening is practically negligible. For lower quality crystals (bulk and/or surface quality), a broadening varying from 0.4” to 0.9” at the FWHM level was measured.

Several X-ray topography techniques were extensively used to characterize a big variety of diamond plates. As a first, but very important step, this characterization was simply qualitative in order to assess the presence and distribution of extended defects in the crystal plates. This is of great importance for the crystal growers to be able to optimise the growth parameters and to reduce or even avoid the creation of defects. At the same time, we showed the possibility of obtaining semi-quantitative estimates of the stronger strain fields, *e.g.* related to metallic inclusions in the crystal.

A special effort was undertaken in order to measure the local effective misorientation in high quality type IIa diamonds. This was achieved by analysing topographs with selected non-dispersive and quasi non-dispersive double-crystal setups, but mainly by using an instrument with bendable monochromators. We showed that in regions up to $0.5 \times 0.5 \text{ mm}^2$ the effective misorientation in a crystal is 4×10^{-8} . This value is comparable to those routinely obtained for float-zone silicon crystals.

We studied the influence of the quality of the diamond crystal on the transverse coherence of the beam and we found that the coherence of the diffracted beam is never preserved, with increases of the angular source size of the order of two to five times the values obtained for the reference beam. This influence was attributed to the presence of remaining residual strains in the bulk of the plates, small local bendings (samples were rather thin) and of a deformed sub-surface layer due to the polishing of the crystal. Therefore, a quantification of the deformation due to the polishing was attempted using surface-sensitive X-ray techniques. This is, to our knowledge, the first time that results on the crystalline quality of diamonds in this deformed layer have been reported. We found that, in the case of a 111 diamond polished by the Hot Metal Polishing method, a layer $\approx 4 \mu\text{m}$ thick is compressively strained and that this strain is anisotropic. Moreover, the “mosaic spread” measured in the deformed layer is larger than in the bulk. In the case of a cleaved sample, terraces are present on the surface of the diamond and neither strain nor “mosaicity” of the sub-surface layer is recorded. Some improvements to the polishing apparatus are now being completed by our colleagues in South Africa and new experiments to study further the subsurface damage with X-ray techniques are planned for the near future.

An important task for the ESRF Crystal Laboratory was (and still is) the improvement, and in particular the quantification of the different steps of the polishing technology. In collaboration with the Crystal and the Metrology Laboratories of the ESRF, the surface quality of silicon crystals was studied using different X-ray-based and complementary (optical, AFM) characterization techniques. The main results obtained are, firstly, that the thickness of the deformed layer due to the lapping procedure is of the order of $30 \mu\text{m}$. Therefore, the removal of at least $40 \mu\text{m}$ by optical polishing is necessary. Secondly, the layer thickness necessary to be removed by mechano-chemical polishing seems to be between $3 \mu\text{m}$ and $10 \mu\text{m}$. Further tests are necessary and will be done in future. In this way a crystal surface with an undetectable (by our double crystal topography methods) deformed sub-surface layer is obtained. Moreover, the coherence preservation properties of various silicon crystals with different surface qualities were tested using two independent methods: using the Talbot effect and by bi-lens-based interferometry. The results obtained are similar and are consistent with those of the X-ray topography.

8. CONCLUSIONS

The quality of ultra-high-purity beryllium foils was studied in cooperation with the producer to check and help optimise the bulk quality and the polishing procedure. After some polishing steps no phase contrast was visible on the radiograph recorded at 125 cm from the sample. Already this is a very promising result. In future it could be necessary to make tests with much larger propagation distances, or to make ultimate tests directly at the beamlines where those plates will be used.

In order to exploit the coherence of the beam in the study of ferroelectric domains as a function of temperature, we developed, in collaboration with the Sample Environment Laboratory, a special furnace. This furnace allows the performance of experiments in transmission geometry while preserving the coherence of the beam. Moreover, it allows the heating of optically transparent and thermally insulating samples without creating a large thermal gradient across the crystals. The furnace was tested with different crystals and the coherence properties were established using the Talbot effect.

The main motivation of the investigation of the ferroelectric inverted domains as a function of temperature was to improve the understanding of the transition from one electrical polarization state to the opposite one. This will help in the fabrication of highly efficient QPM devices.

Imaging the domains was performed using combined Bragg-Fresnel imaging. The white beam section topographs obtained at different temperatures, from room temperature to 930°C were correctly simulated. The modelling of the results obtained at high temperature is based on the assumption that an internal electric field (built in) is created on the c^+ face during heating. The penetration depth of this field into the crystal increases with the heat treatment time and temperature, though the magnitude of the field is reduced. Moreover, the coercive field necessary to switch the polarization state decreases with temperature. This results in an inversion of the polarization on the c^+ surface, producing head-to-head domains which are energetically unfavourable. The system therefore relaxes into a “saw tooth” structure, as shown in the experimental data.

Finally, I presented three different studies which were not directly related with the main subject of the thesis but that have in common diamond as the material used and X-ray topography as one of the characterization techniques used. The first on the possibility of bending diamonds using laser ablation, the second on the investigation of the type of defects which are possible to record using forbidden reflections and the

third on the characterization of large octahedral synthetic diamonds grown with the split-sphere (BARS) method.

In conclusions, X-ray characterization techniques have been successfully applied to the study of the materials quality of interest for X-ray optical applications, resulting in improvements of the bulk quality of the diamonds and of the surface treatment processing of the silicon. Moreover, X-ray Bragg Fresnel imaging was efficaciously applied to the understanding of ferroelectric domain behaviour as a function of temperature.

8. CONCLUSIONS

References

- [1] B. LENGELER. **Coherence in X-ray physics.** *Naturwissenschaften*, **88**(6):249–260, 2004. 1
- [2] A. SNIGIREV, I. SNIGIREVA, V. KOHN, S. KUZNETSOV, AND I. SCHELOKOV. **On the possibilities of x-ray phase contrast microimaging by coherent high-energy synchrotron radiation.** *Review of Scientific Instruments*, **66**(12):5486–5492, 1995. 1
- [3] P. CLOETENS, R. BARRETT, J. BARUCHEL, J.-P. GUIGAY, AND M. SCHLENKER. **Phase objects in synchrotron radiation hard x-ray imaging.** *Journal of Physics D: Applied Physics*, **29**(1):133, 1996. 1
- [4] T. THURN-ALBRECHT, W. STEFFEN, A. PATKOWSKI, G. MEIER, E. W. FISCHER, G. GRÜBEL, AND D. L. ABERNATHY. **Photon Correlation Spectroscopy of Colloidal Palladium Using a Coherent X-Ray Beam.** *Physical Review Letters*, **77**(27):5437–5440, 1996. 1
- [5] S. G. J. MOCHRIE, A. M. MAYES, A. R. SANDY, M. SUTTON, S. BRAUER, G. B. STEPHENSON, D. L. ABERNATHY, AND G. GRÜBEL. **Dynamics of Block Copolymer Micelles Revealed by X-Ray Intensity Fluctuation Spectroscopy.** *Physical Review Letters*, **78**(7):1275–1278, 1997. 1
- [6] J. MIAO, J. CHARALAMBOUS, P. AND KIRZ, AND D. SAYRE. **Extending the methodology of X-ray crystallography to allow imaging of micrometre-sized non-crystalline specimens.** *Nature*, **400**:342–344, 1999. 1
- [7] S. MARCHESINI, H. CHAPMAN, S. HAU-RIEGE, R. LONDON, A. SZOKE, H. HE, M. HOWELLS, H. PADMORE, R. ROSEN, J. SPENCE, AND U. WEIERSTALL. **Coherent X-ray diffractive imaging: applications and limitations.** *Optics Express*, **11**(19):2344–2353, 2003. 1
- [8] T. ISHIKAWA. **Measurement of the coherence length of highly collimated X-rays from the visibility of equal-thickness fringes.** *Acta Crystallographica Section A*, **44**(4):496–499, 1988. 1

REFERENCES

- [9] A. R. LANG AND A. P. W. MAKEPEACE. **Production of synchrotron X-ray biprism interference patterns with control of fringe spacing.** *Journal of Synchrotron Radiation*, **6**(2):59–61, 1999. 1
- [10] V. KOHN, I. SNIGIREVA, AND A. SNIGIREV. **Direct Measurement of Transverse Coherence Length of Hard X Rays from Interference Fringes.** *Physical Review Letters*, **85**(13):2745–2748, 2000. 1
- [11] W. LEITENBERGER, S. M. KUZNETSOV, AND A. SNIGIREV. **Interferometric measurements with hard X-rays using a double slit.** *Optics Communications*, **191**(1-2):91–96, 2001. 1
- [12] W. LEITENBERGER, H. WENDROCK, L. BISCHOFF, AND T. WEITKAMP. **Pinhole interferometry with coherent hard X-rays.** *Journal of Synchrotron Radiation*, **11**(2):190–197, 2004. 1
- [13] A. DIAZ, C. MOCUTA, J. STANGL, M. KEPLINGER, T. WEITKAMP, F. PFEIFFER, C. DAVID, T. H. METZGER, AND G. BAUER. **Coherence and wavefront characterization of Si-111 monochromators using double-grating interferometry.** *Journal of Synchrotron Radiation*, **17**(3):299–307, 2010. 2, 30
- [14] J. P. GUIGAY, S. ZABLER, P. CLOETENS, C. DAVID, R. MOKSO, AND M. SCHLENKER. **The partial Talbot effect and its use in measuring the coherence of synchrotron X-rays.** *Journal of Synchrotron Rad.*, **11**(6):476–482, 2004. 2, 29
- [15] A. SNIGIREV, I. SNIGIREVA, V. KOHN, V. YUNKIN, S. KUZNETSOV, M. B. GRIGORIEV, T. ROTH, G. VAUGHAN, AND C. DETLEFS. **X-Ray Nanointerferometer Based on Si Refractive Bilenses.** *Physical Review Letters*, **103**(6):064801, 2009. 2, 29, 120, 124
- [16] G. GELONI, E. SALDIN, L. SAMOYLOVA, E. SCHNEIDMILLER, H. SINN, T. TSCHENTSCHER, AND M. YURKOV. **Coherence properties of the European XFEL.** *New Journal of Physics*, **12**(3):035021, 2010. 2
- [17] A. K. FREUND. **Synchrotron X-Ray beam optics.** In K. FURRER AND A, editors, *Proceedings of the 6th Summer School on "Complementarity between Neutron and Synchrotron X-Ray Scattering"*, pages 329 – 349. World Scientific, 1998. 2
- [18] Y. V. SHVYD'KO, S. STOUPIN, A. CUNSOLO, A. H. SAID, AND X. HUANG. **High-reflectivity high-resolution X-ray crystal optics with diamonds.** *Nature Physics*, **6**(3):196–199, 2010. 3
- [19] G. GELONI, V. KOCHARYAN, AND E. SALDIN. **A simple method for controlling the line width of SASE X-ray FELs.** *Arxiv preprint arXiv:1004.4067*, 2010. 3
- [20] J. P. BLEWETT. **Synchrotron Radiation - Early History.** *Journal of Synchrotron Radiation*, **5**(3):135–139, 1998. 5

-
- [21] F. R. ELDER, A. M. GUREWITSCH, R. V. LANGMUIR, AND H. C. POLLOCK. **Radiation from Electrons in a Synchrotron**. *Physical Review*, **71**(11):829–830, 1947. 6
- [22] H. WINICK. **Fourth generation light sources**. In *Particle Accelerator Conference, 1997. Proceedings of the 1997*, **1**, pages 37–41. IEEE, 2002. 7
- [23] R. TALMAN. *Accelerator x-ray sources*. Wiley-VCH, Weinheim, 2006. 7
- [24] A. HOFMANN AND L. RIVKIN. **Fourth generation storage ring sources**. *Synchrotron Radiation News*, **12**(6):6–15, 1999. 7
- [25] D. H. BILDERBACK, P. ELLEAUME, AND E. WECKERT. **Review of third and next generation synchrotron light sources**. *Journal of Physics B: Atomic, Molecular and Optical Physics*, **38**(9):S773, 2005. 7
- [26] D. H. BILDERBACK, J. D. BROCK, D. S. DALE, K. D. FINKELSTEIN, M. A. PFEIFER, AND S. M. GRUNER. **Energy recovery linac (ERL) coherent hard x-ray sources**. *New Journal of Physics*, **12**(3):035011, 2010. 7
- [27] J. FELDHAUS, J. ARTHUR, AND J. B. HASTINGS. **X-ray free-electron lasers**. *Journal of Physics B: Atomic, Molecular and Optical Physics*, **38**(9):S799, 2005. 8
- [28] T. I. MORRISON, BANDYOPADYHAY P., AND P. R. JEMIAN. **Potential opportunities for materials research at the advanced photon source**. *Nuclear Instruments and Methods in Physics Research Section B*, **97**(1-4):515 – 517, 1995. Synchrotron Radiation in Materials Science. 8
- [29] D. RAOUX. *Neutron and synchrotron radiation for condensed matter studies*, **1**, chapter 2, pages 38–78. Springer Verlag - Berlin and Les Editions de Physique - Les Ulis, 1993. 10
- [30] V.L. GINZBURG. **On emission of micro waves and their absorption in air**. *Izvestiya Akademii Nauk SSSR - Seriya Fizicheskaya*, **11**:165–181, 1947. 10
- [31] H. MOTZ. **Applications of the Radiation from Fast Electron Beams**. *Journal of Applied Physics*, **22**(5):527–535, 1951. 10
- [32] E. ZOLOTUYABKO, D. SHILO, W. SAUER, E. PERNOT, AND J. BARUCHEL. **Visualization of 10 μm surface acoustic waves by stroboscopic x-ray topography**. *Applied Physics Letters*, **73**(16):2278–2280, 1998. 12
- [33] W. FRIEDRICH, P. KNIPPING, AND M. LAUE. **Interferenzerscheinungen bei Röntgenstrahlen**. *Annalen der Physik*, **346**(10):971–988, 1913. 12
- [34] M. VON LAUE. **Concerning the Detection of X-ray Interferences**. *Nobel Lectures, Physics 1901-1921*:347–355, 1914. 12

REFERENCES

- [35] A. AUTHIER AND C. MALGRANGE. **Diffraction Physics**. *Acta Crystallographica Section A*, **54**(6 Part 1):806–819, 1998. 13
- [36] W. H. ZACHARIASEN. *Theory of X-ray Diffraction in Crystal*. Wiley - Dover, 1945 (version reprinted in 1994). 13, 25
- [37] A. AUTHIER. *Dynamical Theory of X-Ray Diffraction*. Oxford University Press, 2001. 13, 14, 31
- [38] B. W. BATTERMAN AND H. COLE. **Dynamical Diffraction of X Rays by Perfect Crystals**. *Reviews of Modern Physics*, **36**(3):681–717, 1964. 13, 14, 25
- [39] C. G. DARWIN. **The theory of X-ray reflexion**. *Philosophical Magazine Series 6*, **27**(158):315–333, 1914. 14
- [40] P. P. EWALD. **Zur Begründung der Kristalloptik. III. Die Kristalloptik der Röntgenstrahlen**. *Annalen der Physik*, **54**:519–597, 1917. 14
- [41] M. VON LAUE. **Die dynamische Theorie der Röntgenstrahlinterferenzen in neuer Form**. *Ergebnisse der exakten Naturwissenschaften*, **10**:133–158, 1931. 14
- [42] H. WAGENFELD. **Ewald’s and von Laue’s dynamical theories of X-ray diffraction**. *Acta Crystallographica Section A*, **24**(1):170–174, 1968. 14
- [43] G. BORRMANN. **Über Extinktionsdiagramme der Röntgenstrahlen von Quarz**. *Physikalische Zeitschrift*, **42**:157–162, 1941. 19
- [44] M. VON LAUE. **Die Absorption der Röntgenstrahlen in Kristallen im Interferenzfall**. *Acta Crystallographica*, **2**(2):106–113, 1949. 19
- [45] G. BORRMANN. **Die Absorption von Röntgenstrahlen im Fall der Interferenz**. *Zeitschrift für Physik A Hadrons and Nuclei*, **127**(4):297–323, 1950. 19
- [46] J. KUBĚNA AND V. HOLÝ. **Investigation of the growth striations in silicon by X-ray topography**. *Czechoslovak Journal of Physics*, **33**(12):1315–1322, 1983. 21, 81
- [47] M. FATEMI. **Explanatory Notes on W. H. Zachariasen’s ”Theory of X-Ray Diffraction in Ideal Crystals”**. Technical report, NAVAL RESEARCH LAB WASHINGTON DC, 1973. 25
- [48] R. CACIUFFO, S. MELONE, F. RUSTICHELLI, AND A. BOEUF. **Monochromators for x-ray synchrotron radiation**. *Physics Reports*, **152**(1):1 – 71, 1987. 25
- [49] A. FINGERLAND. **Some properties of the single-crystal rocking curve in the Bragg case**. *Acta Crystallographica Section A*, **27**(3):280–284, 1971. 25
- [50] B. LENGELER. **Coherence**. *Applied Physics A*, **87**(3):585–592, 2007. 28

-
- [51] M. BORN AND E. WOLF. *Principles of Optics - Sixth Edition*. Pergamon Press, 1980. 29, 148
- [52] A. SNIGIREV, I. SNIGIREVA, V. KOHN, AND S. KUZNETSOV. **On the requirements to the instrumentation for the new generation of the synchrotron radiation sources. Beryllium windows.** *Nuclear Instruments and Methods in Physics Research Section A*, **370**(2-3):634 – 640, 1996. 30
- [53] I. A. VARTANYANTS AND I. K. ROBINSON. **Origins of decoherence in coherent X-ray diffraction experiments.** *Optics Communications*, **222**(1-6):29 – 50, 2003. 30
- [54] S. WANG, V. PASISKEVICIUS, AND F. LAURELL. **High-efficiency frequency converters with periodically-poled Rb-doped KTiOPO₄.** *Optical Materials*, **30**(4):594 – 599, 2007. 30, 147
- [55] H. YAMAZAKI AND T. ISHIKAWA. **Propagation of X-ray coherence for diffraction of perfect crystals.** *Journal of Applied Crystallography*, **35**(3):314–318, 2002. 30
- [56] D.K. BOWEN AND B.K. TANNER. *High Resolution X-Ray Diffractometry and Topography*. Taylor & Francis, 1998. 31
- [57] J. ALS-NIELSEN AND D. MCMORROW. *Elements of Modern X-Ray Physics*. John Wiley & Sons, New York, 2001. 31
- [58] J. DAILLANT AND A. GIBAUD. *X-Ray and Neutron Reflectivity: Principles and Applications*. Springer, 1999. 31
- [59] V. HOLÝ, U. PIETSCH, AND T. BAUMBACH. *High-Resolution X-ray Scattering from thin films and multilayers*. Springer, 1999. 31
- [60] L. TAPFER, J. R. MARTINEZ, AND K. PLOOG. **Structural investigation by X-ray diffraction of GaAs epilayers and AlAs_yGaAs superlattices grown on Si by MBE.** *Semiconductor Science and Technology*, **4**(8):617, 1989. 31
- [61] T. A. LAFFORD, P. J. PARBROOK, AND B. K. TANNER. **Influence of alloy composition and interlayer thickness on twist and tilt mosaic in Al_xGa_{1-x}N/AlN/GaN heterostructures.** *Applied Physics Letters*, **83**(26):5434–5436, 2003. 31
- [62] L. TAPFER, M. OSPELT, AND H. VON KÄNEL. **Monolayer resolution by means of x-ray interference in semiconductor heterostructures.** *Journal of Applied Physics*, **67**(3):1298–1301, 1990. 31
- [63] T. IDA, M. ANDO, AND H. TORAYA. **Extended pseudo-Voigt function for approximating the Voigt profile.** *Journal of Applied Crystallography*, **33**(6):1311–1316, 2000. 35

REFERENCES

- [64] INC. WOLFRAM RESEARCH. *Mathematica Version 7.0.1*. Wolfram Research, Inc., Champaign, Illinois, 2009. 36
- [65] A. F. JONES AND D. L. MISELL. **The problem of error in deconvolution.** *Journal of Physics A: General Physics*, **3**(5):462, 1970. 39, VI
- [66] H. C. BURGER AND P. H. VAN CITTERT. **Wahre und scheinbare Intensitätsverteilung in Spektrallinien.** *Zeitschrift für Physik A Hadrons and Nuclei*, **79**(11-12):722–730, 1932. 39, III
- [67] W. H. RICHARDSON. **Bayesian-Based Iterative Method of Image Restoration.** *Journal of the Optical Society of America*, **62**(1):55–59, 1972. 39, III
- [68] L. B. LUCY. **An iterative technique for the rectification of observed distributions.** *Astronomical Journal*, **79**:745–754, 1974. 39, III, VI
- [69] R. W. ALKIRE, W. B. YELON, AND J. R. SCHNEIDER. **Determination of the absolute structure factor for the forbidden (222) reflection in silicon using 0.12Å γ rays.** *Phys. Rev. B*, **26**(6):3097–3104, Sep 1982. 40
- [70] W. BERG. **Über eine röntgenographische Methode zur Untersuchung von Gitterstörungen an Kristallen.** *Naturwissenschaften*, **19**(19):391–396, 1931. 10.1007/BF01522358. 42
- [71] C. S. BARRETT. **A new microscopy and its potentialities.** *Transactions of the American Institute of Mining, Metallurgical and Petroleum Engineers*, **161**:15–64, 1945. 42
- [72] G. N. RAMACHANDRAN. **X-ray topographs of diamond.** *Proceedings of the Indian National Science Academy - Part A*, **19**:280–292, 1944. 42
- [73] W. L. BOND AND J. ANDRUS. **Structural imperfections in quartz crystals.** *American Mineralogist*, **37**(7-8):622–632, 1952. 42
- [74] A. R. LANG. **Direct Observation of Individual Dislocations by X-Ray Diffraction.** *Journal of Applied Physics*, **29**(3):597–598, 1958. 42
- [75] J. HÄRTWIG. **X-ray diffraction imaging (X-ray topography) - An Overview of Techniques and Applications**, 1999. 42
- [76] N. KATO AND A. R. LANG. **A study of pendellösung fringes in X-ray diffraction.** *Acta Crystallographica*, **12**(10):787–794, 1959. 43
- [77] J. R. PATEL. **X-ray anomalous transmission and topography of oxygen precipitation in silicon.** *Journal of Applied Physics*, **44**(9):3903–3906, 1973. 43

-
- [78] A. R. LANG. **The projection topograph: a new method in X-ray diffraction microradiography.** *Acta Crystallographica*, **12**(3):249–250, 1959. 43
- [79] J. BARUCHEL AND J. HÄRTWIG. *X-Ray Topography*, pages 342 – 348. Elsevier, 2005. 44
- [80] M. DUDLEY, X. R. HUANG, AND W. HUANG. **Assessment of orientation and extinction contrast contributions to the direct dislocation image.** *Journal of Physics D: Applied Physics*, **32**(10A):A139–A144, 1999. 44
- [81] B. K. TANNER AND D. K. BOWEN. **Synchrotron X-radiation topography.** *Materials Science Reports*, **8**(8):371 – 407, 1992. 46
- [82] J. BORDAS, A. M. GLAZER, AND H. HAUSER. **Use of synchrotron radiation for X-ray topography of phase-transitions.** *Philosophical Magazine*, **32**(2):471–489, 1975. 47
- [83] M. HART. **Synchrotron radiation – its application to high-speed, high-resolution X-ray diffraction topography.** *Journal of Applied Crystallography*, **8**(4):436–444, 1975. 47
- [84] J. GASTALDI, C. JOURDAN, P. MARZO, C. ALLASIA, AND J. N. JULLIEN. **Ultra-high vacuum heating camera for *in situ* synchrotron radiation X-ray topographic studies.** *Journal of Applied Crystallography*, **15**(4):391–395, 1982. 47
- [85] A. BUFFET, G. REINHART, T. SCHENK, H. NGUYEN-THI, J. GASTALDI, N. MANGELINEK-NOEEL, H. JUNG, J. HAERTWIG, J. BARUCHEL, AND B. BILLIA. **Real-time and *in situ* solidification of Al-based alloys investigated by synchrotron radiation: a unique experimental set-up combining radiography and topography techniques.** *Physica Status Solidi (a)*, **204**(8):2721–2727, 2007. 47
- [86] B. K. TANNER, M. SAFA, AND D. MIDGLEY. **Cryogenic X-ray topography using synchrotron radiation.** *Journal of Applied Crystallography*, **10**(2):91–99, 1977. 47
- [87] J. BARUCHEL, C. MEDRANO, AND M. SCHLENKER. **Synchrotron radiation topographic study of the thick ferromagnetic-fan interface in MnP.** *Journal of Physics D: Applied Physics*, **38**(10A):A67, 2005. 47
- [88] I. B. MACCORMACK AND B. K. TANNER. **Application of X-ray synchrotron topography to *in situ* studies of recrystallization.** *Journal of Applied Crystallography*, **11**(1):40–43, 1978. 47
- [89] F. ZONTONE, L. MANCINI, R. BARRETT, J. BARUCHEL, J. HÄRTWIG, AND Y. EPELBOIN. **New Features of Dislocation Images in Third-Generation Synchrotron Radiation Topographs.** *Journal of Synchrotron Radiation*, **3**(4):173–184, 1996. 47

REFERENCES

- [90] I. MATSOULI, V. KVARDAKOV, J. ESPESO, L. CHABERT, AND J. BARUCHEL. **A study of the x-ray focusing effect of a magnetoacoustically excited FeBO₃ crystal using synchrotron radiation diffraction imaging.** *Journal of Physics D: Applied Physics*, **31**(12):1478–1486, 1998. 47
- [91] J. HÄRTWIG, S. KÖHLER, W. LUDWIG, H. MORICEAU, M. OHLER, AND E. PRIEUR. **X-ray Diffraction Topography at a Synchrotron Radiation Source Applied to the Study of Bonded Silicon on Insulator Material.** *Crystal Research and Technology*, **37**(7):705–715, 2002. 47
- [92] P. BALLING, J. ESBERG, K. KIRSEBOM, D. Q. S. LE, U. I. UGGERHOJ, S. H. CONNELL, J. HAERTWIG, F. MASIELLO, AND A. ROMMEVEAUX. **Bending diamonds by femtosecond laser ablation.** *Nuclear Instruments and Methods in Physics Research Section B*, **267**(17):2952–2957, 2009. 47, 153
- [93] T. TUOMI, K. NAUKKARINEN, AND P. RABE. **Use of synchrotron radiation in x-ray diffraction topography.** *Physica Status Solidi (a)*, **25**:93 – 106, 1974. 47, 48
- [94] R. BARRETT, J. BARUCHEL, J. HARTWIG, AND F. ZONTONE. **The present status of the ESRF diffraction topography beamline: new experimental results.** *Journal of Physics D: Applied Physics*, **28**(4A):A250, 1995. 48
- [95] J. W. M. DUMOND. **Theory of the Use of More Than Two Successive X-Ray Crystal Reflections to Obtain Increased Resolving Power.** *Physical Review*, **52**(8):872–883, 1937. 48
- [96] B. JENICHEN, R. KÖHLER, AND W. MÖHLING. **Checking plane-wave approximation for Double Crystal Topography with curved samples.** *Zeitschrift für Naturforschung Section A-A Journal Of Physical Sciences*, **37**(5):405–411, 1982. 50, 75
- [97] R. KÖHLER. **High-Resolution X-ray Topography.** *Applied Physics A: Materials Science & Processing*, **58**(3):149–157, 1994. 50, 75
- [98] D. ALTIN, J. HÄRTWIG, R. KÖHLER, W. LUDWIG, M. OHLER, AND H. KLEIN. **X-ray diffraction topography using a diffractometer with a bendable monochromator at a synchrotron radiation source.** *Journal of Synchrotron Radiation*, **9**(5):282 – 286, 2002. 50, 75, 86
- [99] T. ISHIKAWA, T. KITANO, AND J. MATSUI. **Synchrotron Plane Wave X-Ray Topography of GaAs with a Separate (+, +) Monochro-Collimator.** *Japanese Journal of Applied Physics*, **24**(12):L968–L971, 1985. 50, 75
- [100] T. ISHIKAWA. **X-ray topography with highly collimated beam at photon factory.** *Review of Scientific Instruments*, **60**(7):2490–2493, 1989. 50

-
- [101] H. HASHIZUME, A. IIDA, AND K. KOHRA. **A Multiple Crystal System for High Strain-Sensitivity X-Ray Topography and Its Applications.** *Japanese Journal of Applied Physics*, **14**(10):1433–1442, 1975. 50, 75
- [102] D. LÜBBERT, T. BAUMBACH, J. HÄRTWIG, E. BOLLER, AND E. PERNOT. **μm -resolved high resolution X-ray diffraction imaging for semiconductor quality control.** *Nuclear Instruments and Methods in Physics Research Section B*, **160**(4):521 – 527, 2000. 50, 80, 118
- [103] H. DOSCH, B. W. BATTERMAN, AND D. C. WACK. **Depth-Controlled Grazing-Incidence Diffraction of Synchrotron X Radiation.** *Physical Review Letters*, **56**(11):1144–1147, 1986. 52, 55
- [104] H. KIESSIG. **Investigations into the total reflexion of roetgen rays.** *Annalen der Physik*, **10**(6):715–768, 1931. 52
- [105] L. G. PARRATT. **Surface Studies of Solids by Total Reflection of X-Rays.** *Physical Review*, **95**(2):359–369, 1954. 52
- [106] L. NÉVOT AND P. CROCE. **Sur l'étude des couches superficielles monoatomiques par réflexion 'rasante' (spéculaire ou diffuse) de rayons X, par la méthode de l'empilement 'sandwich'.** *Journal of Applied Crystallography*, **8**(2):304–314, 1975. 53
- [107] S. K. SINHA, E. B. SIROTA, S. GAROFF, AND H. B. STANLEY. **X-ray and neutron scattering from rough surfaces.** *Physical Review B*, **38**(4):2297–2311, 1988. 53
- [108] A. GIBAUD, G. VIGNAUD, AND S. K. SINHA. **The correction of geometrical factors in the analysis of X-ray reflectivity.** *Acta Crystallographica Section A*, **49**(4):642–648, 1993. 54
- [109] J. H. UNDERWOOD, A. C. THOMPSON, Y. WU, AND R. D. GIAUQUE. **X-ray microprobe using multilayer mirrors.** *Nuclear Instruments and Methods in Physics Research Section A*, **266**(1-3):296 – 302, 1988. 54
- [110] Y. YONEDA. **Anomalous Surface Reflection of X Rays.** *Physical Review*, **131**(5):2010–2013, 1963. 55
- [111] W. C. MARRA, P. EISENBERGER, AND A. Y. CHO. **X-ray total-external-reflection–Bragg diffraction: A structural study of the GaAs–Al interface.** *Journal of Applied Physics*, **50**(11):6927–6933, 1979. 55
- [112] S. A. STEPANOV, E. A. KONDRASHKINA, R. KÖHLER, D. V. NOVIKOV, G. MATERLIK, AND S. M. DURBIN. **Dynamical x-ray diffraction of multilayers and superlattices: Recursion matrix extension to grazing angles.** *Physical Review B*, **57**(8):4829–4841, 1998. 56

REFERENCES

- [113] R. C. BURNS, A. CHUMAKOV, G. CARBONE, S. H. CONNELL, D. DUBE, H. P. GODFRIED, J. O. HANSEN, J. HÄRTWIG, F. MASIELLO, M. REBAK, A. ROMMEVEAUX, R. SETSHEDI, P. VAN VAERENBERGH, AND A. GIBAUD. **Diamonds for X-ray optical applications at 3rd and 4th generation X-ray sources - art. no. 67050K**. In *ADVANCES IN X-RAY/EUV OPTICS AND COMPONENTS II*, **6705** of *PROCEEDINGS OF SPIE*, page K7050, 2007. 57, 83
- [114] R. C. BURNS, A. I. CHUMAKOV, S. H. CONNELL, D. DUBE, H. P. GODFRIED, J. O. HANSEN, J. HÄRTWIG, J. HOSZOWSKA, F. MASIELLO, L. MKHONZA, M. REBAK, A. ROMMEVEAUX, R. SETSHEDI, AND P. VAN VAERENBERGH. **HPHT growth and x-ray characterization of high-quality type IIa diamond**. *Journal of Physics: Condensed Matter*, **21**(36):364224, 2009. 57, 63, 64, 71
- [115] P. VAN VAERENBERGH, C. DETLEFS, J. HÄRTWIG, T. A. LAFFORD, F. MASIELLO, T. ROTH, W. SCHMID, P. WATTECAMPS, AND L. ZHANG. **High Heat Load Diamond Monochromator Project at ESRF**. *AIP CConference Proceedings*, **1234**(1):229–232, 2010. 57, 74
- [116] P. JOHN, N. POLWART, C. E. TROUPE, AND J. I. B. WILSON. **The oxidation of (100) textured diamond**. *Diamond and Related Materials*, **11**(3-6):861 – 866, 2002. 57
- [117] G. DAVIES AND T. EVANS. **Graphitization of Diamond at Zero Pressure and at a High Pressure**. *Proceedings of the Royal Society of London. A. Mathematical and Physical Sciences*, **328**(1574):413–427, 1972. 57
- [118] J. E. FIELD, editor. *Properties of Natural and Synthetic Diamond*. Academic Press, 1992. 58, 63
- [119] F. MOMMA, K. IZUMI. **VESTA: a three-dimensional visualization system for electronic and structural analysis**. *Journal of Applied Crystallography*, **41**(3):653–658, 2008. 58
- [120] N. DUBROVINSKAIA, L. DUBROVINSKY, W. CRICHTON, F. LANGENHORST, AND A. RICHTER. **Aggregated diamond nanorods, the densest and least compressible form of carbon**. *Applied Physics Letters*, **87**(8):083106, 2005. 58
- [121] V. BLANK, M. POPOV, G. PIVOVAROV, N. LVOVA, K. GOGOLINSKY, AND V. RESHETOV. **Ultrahard and superhard phases of fullerite C60: Comparison with diamond on hardness and wear**. *Diamond and Related Materials*, **7**(2-5):427 – 431, 1998. 58
- [122] L. G. LUNDBLAD. **High pressure synthesis of diamond in Sweden in 1953**. In S. C. SCHMIDT, J. W. SHANER, G. A. SAMARA, AND M. ROSS, editors, *High-pressure science and technology–1993*, **309**, pages 503–506. AIP, 1994. 58

REFERENCES

- [123] F. P. BUNDY, H. T. HALL, H. M. STRONG, AND R. H. WENTORF. **Man-made Diamonds.** *Nature*, **176**:51–55, 1955. 58
- [124] R. H. WENTORF, JR. **Some Studies of Diamond Growth Rates.** *The Journal of Physical Chemistry*, **75**(12):1833 – 1837, 1971. 59
- [125] Y. N. PAL'YANOV, Y. M. BORZDOV, A. G. SOKOL, A. F. KHOKHRYAKOV, V. A. GUSEV, G. M. RYLOV, AND N. V. SOBOLEV. **High-pressure synthesis of high-quality diamond single crystals.** *Diamond and Related Materials*, **7**(6):916 – 918, 1998. 59, 66
- [126] S. T. LEE, Z. LIN, AND X. JIANG. **CVD diamond films: nucleation and growth.** *Materials Science and Engineering*, **25**:123 – 154, 1999. 59
- [127] S. FERRO. **Synthesis of diamond.** *Journal of Materials Chemistry*, **12**(10):2843 – 2855, 2002. 59
- [128] P. M. MARTINEAU, M. P. GAUKROGER, K. B. GUY, S. C. LAWSON, D. J. TWITCHEN, I. FRIEL, J. O. HANSEN, G. C. SUMMERTON, T. P. G. ADDISON, AND R. BURNS. **High crystalline quality single crystal chemical vapour deposition diamond.** *Journal of Physics: Condensed Matter*, **21**(36):364205, 2009. 59
- [129] F. P. BUNDY. **The P, T Phase and Reaction Diagram for Elemental Carbon.** *Journal of Geophysical Research*, **85**(B12):6930–6936, 1980. 60
- [130] F. P. BUNDY. **Direct Conversion of Graphite to Diamond in Static Pressure Apparatus.** *The Journal of Chemical Physics*, **38**(3):631–643, 1963. 60
- [131] J. SUNG. **Graphite diamond transition under high pressure: A kinetics approach.** *Journal of Materials Science*, **35**:6041–6054(14), 2000. 60
- [132] R. C. BURNS AND G. J. DAVIES. *The Properties of Natural and Synthetic Diamond*, chapter 10, pages 395 – 422. Academic New York, 1992. 61
- [133] H. SUMIYA, N. TODA, AND S. SATOH. **Sumitomo Electric Technical Review.** Technical report, Sumitomo, 2005. 61
- [134] R. C. BURNS, J. O. HANSEN, R. A. SPITS, M. SIBANDA, C. M. WELBOURN, AND D. L. WELCH. **Growth of high purity large synthetic diamond crystals.** *Diamond and Related Materials*, **8**(8-9):1433 – 1437 – 5, 1999. 61, 62
- [135] H. KANDA. **Large diamonds grown at high pressure conditions.** *Brazilian Journal of Physics*, **30**(3):482 – 489, 2000. 62
- [136] G. S. WOODS AND A. R. LANG. **Cathodoluminescence, optical absorption and x-ray topographic studies of synthetic diamonds.** *Journal of Crystal Growth*, **28**(2):215 – 226, 1975. 63

REFERENCES

- [137] Y. N. PAL'YANOV, Y. M. BORZDOV, V. A. GUSEV, A. G. SOKOL, A. F. KHOKHRYAKOV, G. M. RYLOV, V. A. CHERNOV, AND I. N. KUPRIYANOV. **High-quality synthetic diamonds for SR application.** *Nuclear Instruments and Methods in Physics Research Section A*, **448**(1-2):179 – 183, 2000. 66
- [138] H. SUMIYA. **Crystalline perfection of high purity synthetic diamond crystal.** *Journal of Crystal Growth*, **178**:485 – 493 – 9, 1997. 66
- [139] J. C. LABICHE, J. SEGURA-PUCHADES, D. VAN BRUSSEL, AND J. P. MOY. **FRELON camera: Fast REadout LOW Noise.** *ESRF Newsletter*, **25**:41–43, 1996. 68, 96
- [140] K. WATANABE, S. C. LAWSON, J. ISOYA, H. KANDA, AND Y. SATO. **Phosphorescence in high-pressure synthetic diamond.** *Diamond and Related Materials*, **6**(1):99 – 106, 1997. 71
- [141] J. HÄRTWIG, V. HOLÝ, R. KITNER, J. KUBĚNA, AND V. LERCHE. **Investigation of quartz crystals with non-homogeneous distributions of impurity atoms by X-ray methods.** *Physica Status Solidi (a)*, **105**(1):61 – 75, 1988. 74
- [142] J. F. PETROFF, M. SAUVAGE, P. RIGLET, AND H. HASHIZUME. **Synchrotron-radiation plane-wave topography .1. Application to misfit dislocation imaging in III-V heterojunctions.** *PHILOSOPHICAL MAGAZINE A*, **42**(3):319–338, 1980. 75
- [143] D. LÜBBERT AND T. BAUMBACH. **Visrock: a program for digital topography and X-ray microdiffraction imaging.** *Journal of Applied Crystallography*, **40**(3):595–597, 2007. 80, 118
- [144] A. R. LANG, M. MOORE, A. P. W. MAKEPEACE, W. WIERZCHOWSKI, AND C. M. WELBOURN. **On the dilatation of synthetic type Ib diamond by substitutional nitrogen impurity.** *Philosophical Transactions: Physical Sciences and Engineering*, **337**(1648):497–520, 1991. 81, 89
- [145] V. LERCHE, P. DÖRNFELDER, AND J. HÄRTWIG. **Direct backward calculation from x-ray double crystal topographs.** *physica status solidi (a)*, **128**(2):269–283, 1991. 81
- [146] J. HÄRTWIG. **Hierarchy of dynamical theories of x-ray diffraction for deformed and perfect crystals.** *Journal of Physics D: Applied Physics*, **34**(10A):A70, 2001. 81
- [147] U. BONSE. **Zur Röntgenographischen Bestimmung Des Typs Einzelner Versetzungen In Einkristallen.** *Zeitschrift für Physik A Hadrons and Nuclei*, **153**(3):278–296, 1958. 81
- [148] I. USCHMANN, E. FÖRSTER, K. GÄBEL, G. HÖLZER, AND M. ENSSLEN. **X-ray reflection properties of elastically bent perfect crystals in Bragg geometry.** *Journal of Applied Crystallography*, **26**(3):405–412, 1993. 85

-
- [149] S. TAKAGI. **Dynamical theory of diffraction applicable to crystals with any kind of small distortion.** *Acta Crystallographica*, **15**(12):1311–1312, 1962. 85
- [150] D. TAUPIN. **Dynamic theory of x-ray diffraction in crystals.** *Bulletin de la Societe Francaise de Mineralogie et de Cristallographie*, **87**(4):469–511, 1964. 85
- [151] F. N. CHUKHOVSKII, M. KRISCH, AND A. K. FREUND. **Nondispersive Bragg diffraction in the general case of two cylindrically bent crystals.** *Review of Scientific Instruments*, **63**(1):920–923, 1992. 85
- [152] I. USCHMANN, C. MALGRANGE, AND E. FÖRSTER. **Measurement of a bent-crystal rocking curve with oscillations.** *Journal of Applied Crystallography*, **30**(6):1150–1151, 1997. 86
- [153] U. BONSE. **Elastic strain and coloration pattern in natural quartz crystals.** *Zeitschrift für Physik A Hadrons and Nuclei*, **184**(1):71–84, 1965. 10.1007/BF01380669. 88
- [154] S. KIKUTA, K. KOHRA, AND Y. SUGITA. **Measurements on Local Variations in Spacing and Orientation of the Lattice Plane of Silicon Single Crystals by X-Ray Double-Crystal Topography.** *Japanese Journal of Applied Physics*, **5**(11):1047–1055, 1966. 89
- [155] J. YOSHIMURA, T. MIYAZAKI, T. WADA, K. KOHRA, M. HOSAKA, T. OGAWA, AND S. TAKI. **Measurement of local variations in spacing and orientation of lattice plane of synthetic quartz.** *Journal of Crystal Growth*, **46**(5):691 – 700, 1979. 89
- [156] A. T. MACRANDER, S. KRASNICKI, Y. ZHONG, J. MAJ, AND S. CHU. **Strain mapping with parts-per-million resolution in synthetic type-Ib diamond plates.** *Applied Physics Letters*, **87**(19):194113, 2005. 89
- [157] U. BONSE AND I. HARTMANN. **X-ray measurement of minute lattice strain in perfect silicon crystals.** *Zeitschrift für Kristallographie*, **156**(3-4):265–279, 1981. 91, 111
- [158] H. F. TALBOT. **Facts relating to optical science.** *Philosophical Magazine*, **9**:401–407, 1836. 94
- [159] LORD RAYLEIGH. **On copying diffraction-gratings, and on some phenomena connected therewith.** *Philosophical Magazine*, **11**:196 – 205, 1881. 94
- [160] P. CLOETENS, J.-P. GUIGAY, C. DE MARTINO, J. BARUCHEL, AND M. SCHLENKER. **Fractional Talbot imaging of phase gratings with hard x rays.** *Optics Letters*, **22**(14):1059–1061, 1997. 94

REFERENCES

- [161] W. B. CASE, M. TOMANDL, S. DEACHAPUNYA, AND M. ARNDT. **Realization of optical carpets in the Talbot and Talbot-Lau configurations.** *Optics Express*, **17**(23):20966–20974, 2009. 95
- [162] R. KLUENDER, F. MASIELLO, P. VAN VAERENBERGH, AND J. HÄRTWIG. **Measurement of the spatial coherence of synchrotron beams using the Talbot effect.** *Physica Status Solidi (a)*, **206**(8):1842–1845, 2009. 9th Biennial Conference on High Resolution X-Ray Diffraction and Imaging, Linz, AUSTRIA, SEP 15, 2008-SEP 19, 2009. 97
- [163] S. E. GRILLO AND J. E. FIELD. **The polishing of diamond.** *Journal of Physics D: Applied Physics*, **30**(2):202, 1997. 101
- [164] L. PASTEWKA, S. MOSER, P. GUMBSCH, AND M. MOSELER. **Anisotropic mechanical amorphization drives wear in diamond.** *Nature Materials*, Advance online publication doi:10.1038/nmat2902:., 2010. 101
- [165] R. H. TELLING, C. J. PICKARD, M. C. PAYNE, AND J. E. FIELD. **Theoretical Strength and Cleavage of Diamond.** *Physical Review Letters*, **84**(22):5160–5163, 2000. 102
- [166] F. M. VAN BOUWELEN, A. L. BLELOCH, J. E. FIELD, AND L. M. BROWN. **Wear by friction between diamonds studied by electron microscopical techniques.** *Diamond and Related Materials*, **5**(6-8):654 – 657, 1996. Proceedings of the 6th European Conference on Diamond, Diamond-like and Related Materials Part 2. 102
- [167] F. K. DE THEIJE, E. VAN VEENENDAAL, W. J. P. VAN ENCKEVORT, AND E. Vlieg. **Oxidative etching of cleaved synthetic diamond 111 surfaces.** *Surface Science*, **492**(1-2):91 – 105, 2001. 102
- [168] A. P. MALSHE, B. S. PARK, W. D. BROWN, AND H. A. NASEEM. **A review of techniques for polishing and planarizing chemically vapor-deposited (CVD) diamond films and substrates.** *Diamond and Related Materials*, **8**(7):1198 – 1213, 1999. 102
- [169] Y. CHEN AND L. C. ZHANG. **On the polishing techniques of diamond and diamond composites.** *Key Engineering Materials*, **404**:85–96, 2009. 102
- [170] G. BUSSONE, T. A. LAFFORD, F. MASIELLO, A. GIBAUD, G. CARBONE, T. U. SCHÜLLI, CONNELL S. H., VIVO-ROMMEVEAUX A., AND M. WORMINGTON. **Investigation of surface and sub-surface damage in high quality synthetic diamonds by X-ray reflectivity and grazing incidence diffraction.** submitted to *physica status solidi (a)*. 102
- [171] P. GRODZINSKI. *Diamond technology production methods for diamond and gem stones.* N.A.G. Press, 1953. 102

-
- [172] M. YOSHIKAWA. **Development and performance of a diamond-film polishing apparatus with hot metals.** In A. FELDMAN AND S. S. HOLLY, editors, *Diamond Optics III*, **1325**, pages 210–221. SPIE, 1990. 102
- [173] H. G. MAGUIRE. **Investigation of the Band Structure of Diamond Using Low-Energy Electrons.** *Physica Status Solidi (b)*, **76(2)**:715–726, 1976. 105
- [174] B. D. THOMS, M. S. OWENS, J. E. BUTLER, AND C. SPIRO. **Production and characterization of smooth, hydrogen-terminated diamond C(100).** *Applied Physics Letters*, **65(23)**:2957–2959, 1994. 105
- [175] S. A. HOWARD AND R. L. SNYDER. **An Evaluation of Some Profile Models and the Optimization Procedures used in Profile Fitting.** *Advances in X-Ray Analysis*, **26**:73–80, 1983. 107
- [176] M. WORMINGTON, C. PANACCIONE, K. M. MATNEY, AND D. K. BOWEN. **Characterization of structures from X-ray scattering data using genetic algorithms.** *Philosophical Transactions of the Royal Society of London. Series A*, **357(1761)**:2827–2848, 1999. 108
- [177] W. ZULEHNER. **Historical overview of silicon crystal pulling development.** *Materials Science and Engineering B*, **73(1-3)**:7 – 15, 2000. 111
- [178] T. N. BUCK AND R. L. MEEK. **Crystallographic damage to silicon by typical slicing, lapping and polishing operations.** *National Bureau of Standards special publication*, **337**:419–430, 1970. 112
- [179] L. ZHANG AND I. ZARUDI. **Towards a deeper understanding of plastic deformation in mono-crystalline silicon.** *International Journal of Mechanical Sciences*, **43(9)**:1985 – 1996, 2001. 112
- [180] H. ROBBINS AND B. SCHWARTZ. **Chemical Etching of Silicon.** *Journal of the Electrochemical Society*, **106(6)**:505–508, 1959. 114
- [181] M. STEINERT, J. ACKER, S. OSWALD, AND K. WETZIG. **Study on the Mechanism of Silicon Etching in HNO₃-Rich HF/HNO₃ Mixtures.** *The Journal of Physical Chemistry C*, **111(5)**:2133–2140, 2007. 114
- [182] J. VALASEK. **Piezo-Electric and Allied Phenomena in Rochelle Salt.** *Physical Review*, **17(4)**:475–481, 1921. 133
- [183] R. H. BUTTNER AND E. N. MASLEN. **Structural parameters and electron difference density in BaTiO₃.** *Acta Crystallographica Section B*, **48(6)**:764–769, 1992. 135

REFERENCES

- [184] Y. XU. *Ferroelectric materials and their applications*. North-Holland - Amsterdam, 1991. 136
- [185] P. A. FRANKEN, A. E. HILL, C. W. PETERS, AND G. WEINREICH. **Generation of Optical Harmonics**. *Physical Review Letters*, **7**(4):118–119, 1961. 136
- [186] J. A. ARMSTRONG, N. BLOEMBERGEN, J. DUCUING, AND P. S. PERSHAN. **Interactions between Light Waves in a Nonlinear Dielectric**. *Physical Review*, **127**(6):1918–1939, 1962. 138
- [187] M. YAMADA, N. NADA, M. SAITOH, AND K. WATANABE. **First-order quasi-phase matched LiNbO₃ waveguide periodically poled by applying an external field for efficient blue second-harmonic generation**. *Applied Physics Letters*, **62**(5):435–436, 1993. 138
- [188] E. SOERGEL. **Visualization of ferroelectric domains in bulk single crystals**. *Applied Physics B: Lasers and Optics*, **81**:729–751, 2005. 10.1007/s00340-005-1989-9. 139
- [189] N. NIIZEKI AND M. HASEGAWA. **Direct Observation of Antiparallel 180° Domains in BaTiO₃ by X-Ray Anomalous Dispersion Method**. *Journal of the Physical Society of Japan*, **19**(4):550–554, 1964. 139
- [190] P. REJMÁNKOVÁ-PERNOT, P. CLOETENS, J. BARUCHEL, J.-P. GUIGAY, AND P. MORETTI. **Phase Retrieval by Combined Bragg and Fresnel X-Ray Diffraction Imaging**. *Physical Review Letters*, **81**(16):3435–3438, 1998. 139, 148
- [191] P. PERNOT-REJMÁNKOVÁ, P. A. THOMAS, P. CLOETENS, F. LORUT, J. BARUCHEL, Z. W. HU, P. URENSKI, AND G. ROSENMAN. **Periodically poled KTA crystal investigated using coherent X-ray beams**. *Journal of Applied Crystallography*, **33**(4):1149–1153, 2000. 140
- [192] P. PERNOT-REJMÁNKOVÁ, P. A. THOMAS, P. CLOETENS, T. LYFORD, AND J. BARUCHEL. **Structural matching of ferroelectric domains and associated distortion in potassium titanyl phosphate crystals**. *Journal of Physics: Condensed Matter*, **15**(10):1613, 2003. 140, 148, 152
- [193] D. WALKER, P. A. THOMAS, Q. JIANG, P. PERNOT-REJMÁNKOVÁ, J. BARUCHEL, AND T. AYGUAVIVES. **X-ray imaging investigation of periodically electroded rubidium titanyl arsenate, RbTiOAsO₄, under an applied electric field**. *Journal of Physics D: Applied Physics*, **38**(10A):A55, 2005. 140
- [194] P. PERNOT, B. GORGES, H. VITOUX, R. KLUENDER, F. MASIELLO, AND J. BARUCHEL. **A furnace for coherent beam transmission topography applied to ferroelectric crystals**. *Physica Status Solidi (a)*, **206**(8):1880–1883, 2009. 9th Biennial

- Conference on High Resolution X-Ray Diffraction and Imaging, Linz, AUSTRIA, SEP 15, 2008-SEP 19, 2009. 140
- [195] J. D. BIERLEIN, H.N VANHERZEELE, AND A. A. BALLMAN. **Linear and nonlinear optical properties of flux-grown KTiOAsO_4** . *Applied Physics Letters*, **54**(9):783–785, 1989. 144
- [196] F. MASIELLO, T. A. LAFFORD, P. PERNOT, J. BARUCHEL, D. S. KEEBLE, P. A. THOMAS, A. ZUKAUSKAS, G. STRÖMQVIST, F. LAURELL, AND C. CANALIAS. **Investigation by Coherent X-Ray Section Topography of Ferroelectric Domain Behaviour as a Function of Temperature in Periodically- Poled Rb:KTP**. *Journal of Applied Crystallography*, **44**:462 – 466, 2011. submitted to Journal of Applied Crystallography. 146
- [197] Q. JIANG, P. A. THOMAS, K. B. HUTTON, AND R. C. C. WARD. **Rb-doped potassium titanyl phosphate for periodic ferroelectric domain inversion**. *Journal of Applied Physics*, **92**(5):2717–2723, 2002. 147
- [198] V. K. YANOVSKII AND V. I. VORONKOVA. **Ferroelectric phase transitions and properties of crystals of the KTiOPO_4 family**. *Physica Status Solidi (a)*, **93**(2):665–668, 1986. 147
- [199] P. A. THOMAS, S. C. MAYO, AND B. E. WATTS. **Crystal structures of RbTiOAsO_4 , $\text{KTiO}(\text{P}_{0.58},\text{As}_{0.42})\text{O}_4$, RbTiOPO_4 and $(\text{Rb}_{0.465},\text{K}_{0.535})\text{TiOPO}_4$, and analysis of pseudosymmetry in crystals of the KTiOPO_4 family**. *Acta Crystallographica Section B*, **48**(4):401–407, 1992. 147
- [200] M. SÁNCHEZ DEL RÍO AND R. J. DEJUS. **XOP 2.1: A new version of the X-ray optics software toolkit**. In T. WARWICK, editor, *XOP 2.1: A new version of the X-ray optics software toolkit*, pages 784–787, 2004. 148
- [201] V. D. KUGEL AND G. ROSENMAN. **Domain inversion in heat-treated LiNbO_3 crystals**. *Applied Physics Letters*, **62**(23):2902–2904, 1993. 150, 152
- [202] N. ANGERT, M. TSEITLIN, L. KAPLUN, E. YASHCHIN, AND M. ROTH. **Ferroelectric domain reversal in KTP crystals by high-temperature treatment**. *Ferroelectrics*, **157**(1):117–122, 1994. 150, 152
- [203] P. URENSKI, G. ROSENMAN, AND M. MOLOTSKII. **Polarisation reversal and domain anisotropy in flux-grown KTiOPO_4 and isomorphous crystals**. *Journal of Materials Research*, **16**(5):1493–1499, 2001. 151
- [204] V. MOCELLA, J. P. GUIGAY, J. HRDÝ, C. FERRERO, AND J. HOSZOWSKA. **Bent crystals in Laue geometry: dynamical focusing of a polychromatic incident beam**. *Journal of Applied Crystallography*, **37**(6):941–946, Dec 2004. 154

REFERENCES

- [205] A. A. SHIRYAEV, F. MASIELLO, I. N. HÄRTWIG, J. AND KUPRIYANOV, T. A. LAF-
FORD, S. V. TITKOV, AND Y. N. PALYANOV. **X-ray topography of diamond using
forbidden reflections: which defects do we really see?** *Journal of Applied Crys-
tallography*, **44**(1):65–72, Feb 2011. 155
- [206] A. F. KHOKHRYAKOV, Y. N. PALYANOV, I. N. KUPRIYANOV, Y. M. BORZDOV, A. G
. SOKOL, AND F. HÄRTWIG, J. AND MASIELLO. **Crystal growth and perfection of
large octahedral synthetic diamonds.** *Journal of Crystal Growth*, **317**:32 – 38, 2011.
157
- [207] N. R. HILL AND G. E. IOUP. **Convergence of the van Cittert iterative method
of deconvolution.** *Journal of the Optical Society of America*, **66**(5):487–489, 1976. IV

REFERENCES

Appendix A

Apparatus function determination - Direct deconvolution methods

In order to deconvolve the apparatus function, I wrote a code in Mathematica that uses two different deconvolution algorithms: the Burger-Van Cittert algorithm [66] and the Richardson-Lucy algorithm [67, 68].

A.1 Burger - Van Cittert

By using the commutative property of the convolution, it is possible to write the convolution integral 3.1 as

$$e(t) = \int_{-\infty}^{\infty} i(\tau) f(t - \tau) d\tau \quad (\text{A.1})$$

since now the unknown is the instrument broadening function that is broadened by the known reflectivity curves of decreasing widths. It is possible to write A.1 as a Fredholm integral equation of the second kind

$$e(t) = i(t) + \int_{-\infty}^{\infty} i(\tau) [f(t - \tau) - \delta(t - \tau)] d\tau \quad (\text{A.2})$$

An approximate solution of A.2 is given by the following iterative algorithm:

$$i_n = n e - \frac{n(n-1)}{2!} e_1 + \frac{n(n-1)(n-2)}{3!} e_2 + \frac{n(n-1)(n-3)}{3!} e_3 - \dots \pm e_{n-1} \quad (\text{A.3})$$

A. APPARATUS FUNCTION DETERMINATION - DIRECT DECONVOLUTION METHODS

where

$$e_1 = e * f; \quad e_2 = e_1 * f = (e * f) * f \quad \dots \quad e_n = e_{n-1} * f \quad (\text{A.4})$$

It is possible to write A.3 by using the binomial coefficient, defined in the multiplicative form as

$$\binom{n}{k} = \frac{n^k}{k!} = \frac{n(n-1)(n-2)\dots(n-k+1)}{k(k-1)(k-2)\dots 1} \quad (\text{A.5})$$

obtaining

$$i_n = n e + \sum_{i=1}^{n-1} (-1)^i \binom{n}{i+1} e_i \quad (\text{A.6})$$

Let's clarify the ideas behind this deconvolution algorithm: in the first iteration, the experimental data e is taken as the first approximation to the instrumental broadening function i_1 . Convolution of i_1 with the reflectivity curve f yields e_1 , the first approximation of e . The second approximation i_2 is then obtained by adding a correction to i_1 which is the difference between e and the e_1 and so on and so forth.

Hill and Ioup, [207] studied the necessary convergence conditions for the Van Cittert iterative method. Among others, it is required that the used function is even, with a maximum on the origin and, with continuous derivatives everywhere if the derivatives are continuous at the origin. All these requirements are fulfilled in our case. There is one peculiarity considering the requirements that the maximum has to be in the origin; the origin is not always, as one could think, the position of the maximum of the experimental data. In fact, in some cases, the theoretical curve and the experimental data have been shifted in order to obtain a more stable solution.

Nevertheless, the algorithm fails to converge to a good solution in many cases. Fig.A.1 shows an example of the Van Cittert code failing for Si 555 reflection and slits open 0.7 mm whilst in fig.A.2 an example of a converging result for Si 555 and slits 0.04 mm.

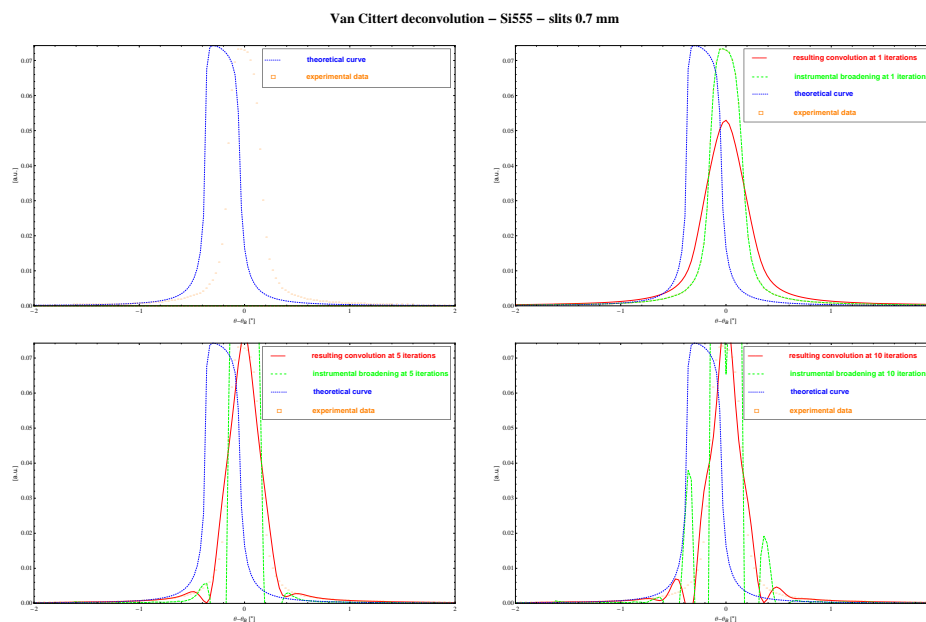


Figure A.1: The deconvolution results at different iterations in a case where a good final result is not obtained. Notice the shift between experimental data and reflectivity curve needed to have a better convergence.

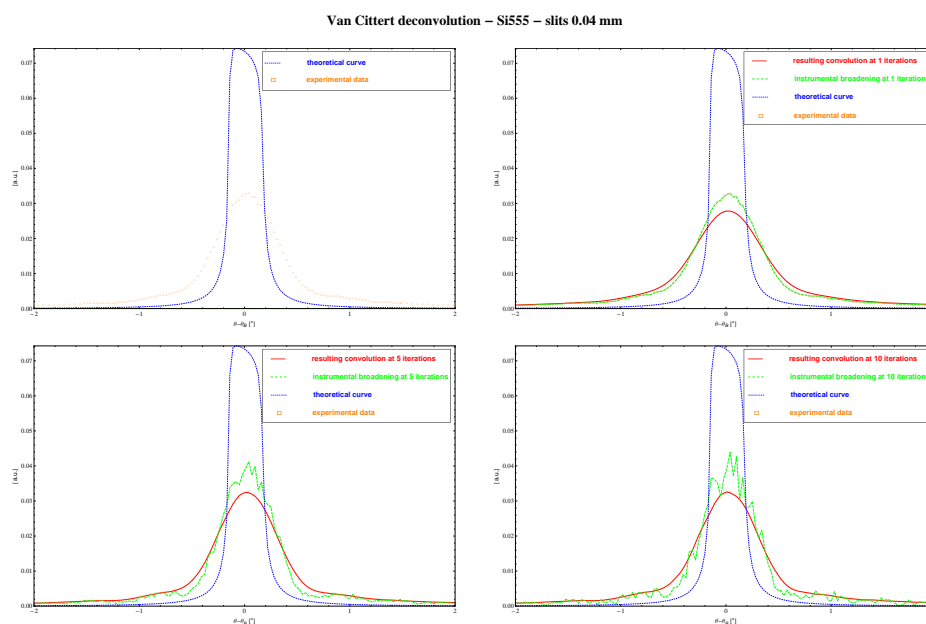


Figure A.2: The deconvolution results at different iterations, this time where a good result is obtained in less than 6 iterations.

A. APPARATUS FUNCTION DETERMINATION - DIRECT DECONVOLUTION METHODS

The main problem with the Van Cittert is the fact that the first approximation of the instrumental broadening is the experimental curve itself. This can work for curves where the broadening is considerable (e.g. when the slits are closed to a value smaller than 100 μm , the Fraunhofer diffraction from the slits become important). In fact, the results obtained for example in fig.A.2 are in good agreement with the Fraunhofer diffraction calculated from 32 μm slits, very close to the nominal value of 40 μm . This is a systematic nuisance in deconvolution problems, and it is well stated in [65]: it is difficult to deconvolute a narrow curve from a broader one. Nevertheless, this has been possible by using the Richardson-Lucy algorithm.

A.2 Richardson - Lucy

In [68] the convolution is seen as a particular type of a more general probabilistic theory. Following the notation used by Lucy:

$$\phi(x) = \int \psi(\xi)P(x|\xi)d\xi \quad (\text{A.7})$$

where $P(x|\xi)$ is the probability that x' will fall in $(x, x + \Delta x)$ if $\xi' = \xi$. In our case, the probability function is the theoretical reflectivity, while ϕ and ψ are respectively the experimental data and the instrumental broadening function.

Bayes' theorem for conditional probabilities states that:

$$P(A|B) = \frac{P(B|A)P(A)}{P(B)}$$

where $P(A), P(B)$ are the probabilities a priori of A and B , while $P(A|B)$ is the conditional probability of realizing A given B .

By using this theorem and by imposing the normalization of $P(x|\xi)$ we obtain:

$$\psi(\xi) = \int \phi(x)Q(\xi|x)dx \quad \text{with} \quad Q(\xi|x) = \frac{\psi(\xi)P(x|\xi)}{\int \psi(\xi)P(x|\xi)d\xi} \quad (\text{A.8})$$

By guessing a first value for ψ , we can obtain an estimation of $Q(\xi|x)$, that we can use in the first part of A.8 to obtain an improved estimation of ψ by using $\hat{\phi}$, an estimation of ϕ (in our case the experimental data).

We obtain the following recursive algorithm:

$$\psi^{r+1}(\xi) = \psi^r(\xi) \int \frac{\hat{\phi}(x)}{\phi^r(x)} P(x|\xi) d\xi \quad (\text{A.9})$$

with

$$\phi^r(x) = \int \psi^r(\xi) P(x|\xi) d\xi. \quad (\text{A.10})$$

One of the main differences between the Van Cittert and the Richardson-Lucy algorithms is the fact that in the latter an initial guess for the instrumental broadening function is made. This gives more freedom to the algorithm, and it has been possible to deconvolute an instrumental broadening for the cases where the Van Cittert failed. The problem in having the freedom for the initial guess is to find a correct way to choose the best one. I have decided to use as a guess the same function I have used for the fitting procedure, the sum of a Gaussian and Lorentzian with normalized area. In order to choose the best value for the ω and σ parameters I have made a test by using different values and by checking the results of the iteration algorithm.

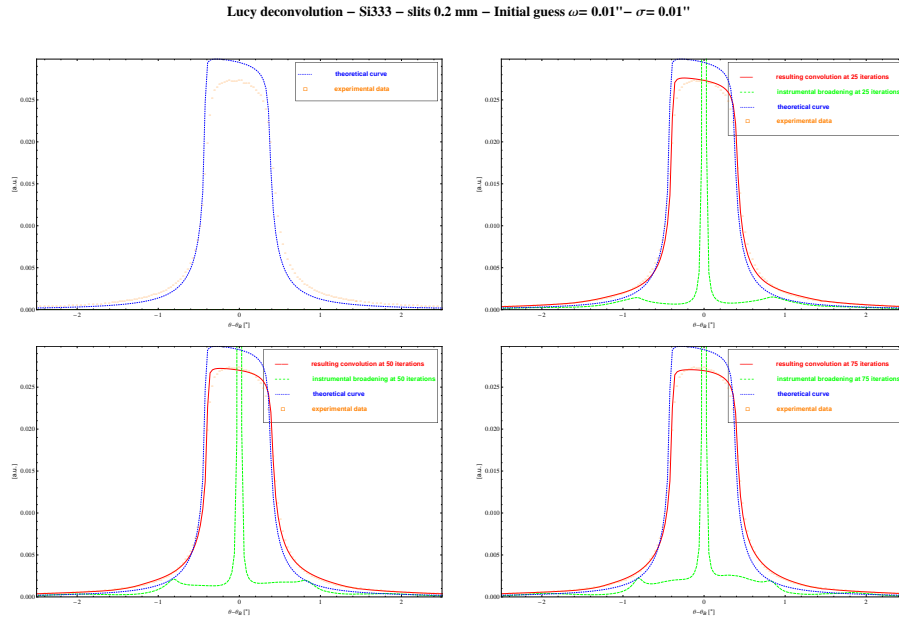


Figure A.3: Richardson-Lucy deconvolution test, with narrow initial guess, $\sigma = \omega = 0.01''$.

A. APPARATUS FUNCTION DETERMINATION - DIRECT DECONVOLUTION METHODS

Lucy deconvolution – Si333 – slits 0.2 mm – Initial guess $\omega = 0.05''$ – $\sigma = 0.05''$

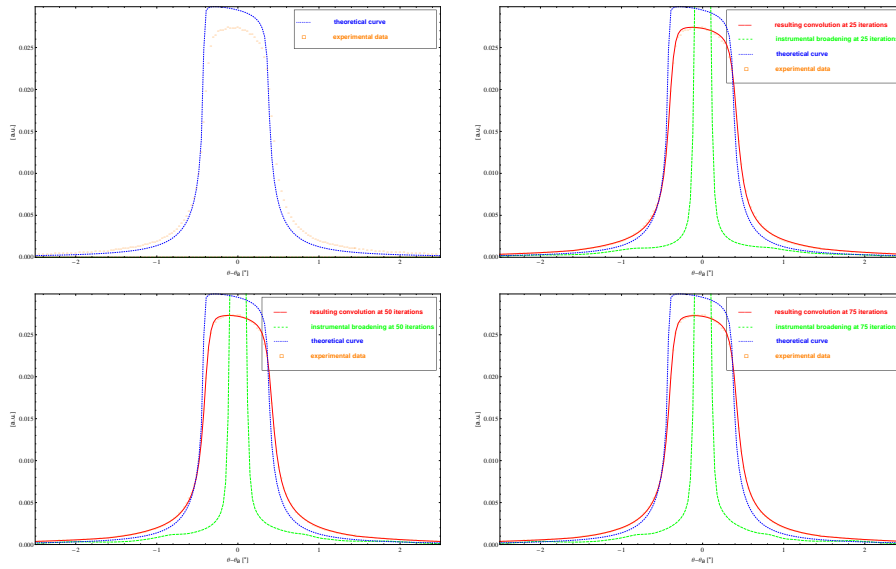


Figure A.4: Richardson-Lucy deconvolution test, with intermediate initial guess, $\sigma = \omega = 0.05''$.

Lucy deconvolution – Si333 – slits 0.2 mm – Initial guess $\omega = 0.1''$ – $\sigma = 0.1''$

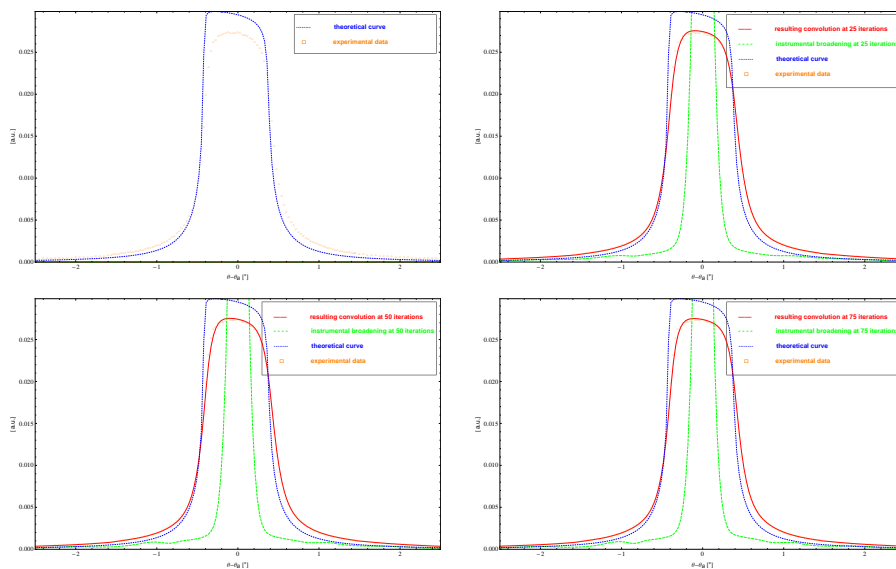


Figure A.5: Richardson-Lucy deconvolution test, with broad initial guess, $\sigma = \omega = 0.1''$.

The results obtained by the test are shown in fig.A.3,A.4,A.5. If the initial guess is too narrow, *e.g.* 0.01" (fig.A.3) the obtained results is not good even after a big number (100) iterations, especially for what concerns the top part of the rocking curve. If the initial guess is too broad, *e.g.* 0.1" (fig.A.5), the convergence is slower but at around 75 iterations a good results is obtained. In this case, a good guess is for example 0.05" (fig.A.4), giving a good results already after only 25 iterations. In order to be able to compare the apparatus functions obtained for different reflection I have therefore decided to keep the value of 0.05" as initial guess.

Finally, in the case where both Van Cittert and Richardson-Lucy algorithms converged to a solution this appear to be the comparable for both methods. This is visible in figure fig.A.6, where the two methods are compared together with the Fraunhofer diffraction profile for the experiemental slits size.

Van Cittert deconvolution – Si555 – slits 0.04 mm

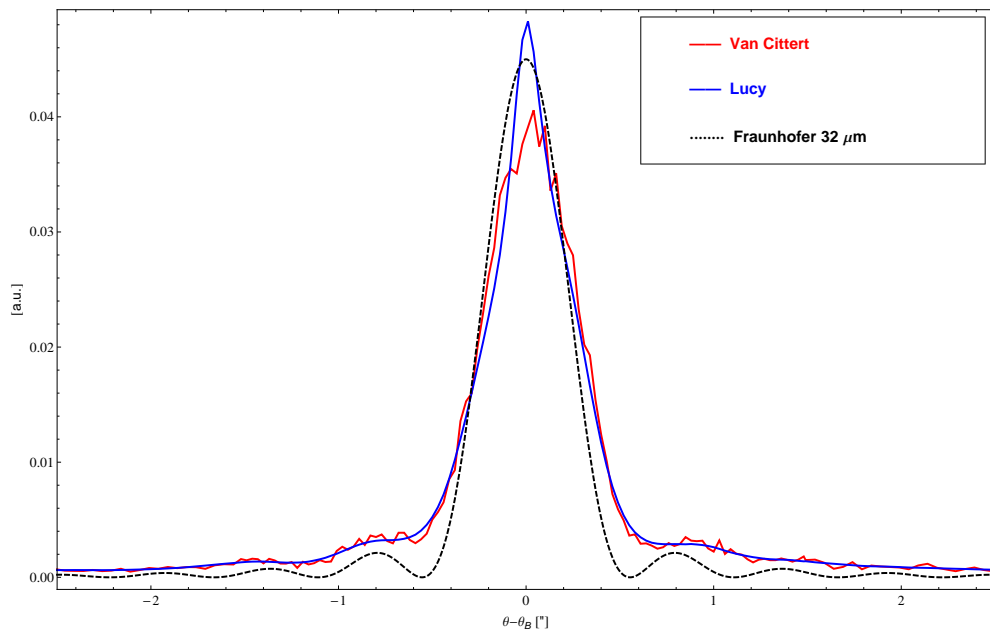


Figure A.6: Comparison between the deconvolved functions from the 555 reflection, nominal slits size 40 μm with both methods and the Fraunhofer diffraction from 32 μm slits.

Riassunto.

Le proprietà eccezionali delle sorgenti di radiazione di sincrotrone sono state e sono tuttora utilizzate in maniera sempre più frequente in discipline molto diverse, che spaziano dall'archeologia alla chimica, dalla scienza dei materiali alla biologia, dalla medicina alla fisica. Tra queste proprietà, è importante sottolineare la brillantezza della radiazione, lo spettro continuo, l'alto grado di polarizzazione, la struttura temporale e la ridotta dimensione della sorgente e della divergenza del fascio. Quest'ultime proprietà risultano in una grande coerenza trasversale della radiazione prodotta.

La coerenza della luce di sincrotrone ha permesso lo sviluppo di nuove tecniche, ad esempio l'imaging basato sul contrasto di fase, la spettroscopia a correlazione di fotoni e la diffrazione X coerente. È dunque di primaria importanza che le ottiche possano preservare questa proprietà, perturbando il meno possibile il fronte d'onda.

La tesi è costituita da tre parti.

Nella prima parte, viene presentato il lavoro effettuato all'interno del gruppo ottico dell'ESRF relativo alla caratterizzazione di cristalli di diamante sintetico di alta qualità previsti per applicazioni nelle ottiche a raggi X. Questa caratterizzazione è stata effettuata utilizzando diverse tecniche complementari basate sui raggi X, quali la diffrattometria ad alta risoluzione, la topografia, la diffrazione ad incidenza rasante, la riflettometria e misure di preservazione della coerenza utilizzando l'effetto Talbot.

Nella seconda parte, vengono esposti i risultati ottenuti nello studio del comportamento di domini ferroelettrici ad alta temperatura in un cristallo periodicamente polarizzato. In questo tipo di misure, basato sulla diffrazione di Bragg-Fresnel, è necessario un'alta coerenza della luce di sincrotrone.

Nella terza parte vengono illustrati i risultati ottenuti nella caratterizzazione di diamanti per applicazioni differenti dalle ottiche a raggi X.

Rèsumè.

Les propriétés exceptionnelles des sources de rayonnement synchrotron ont été et sont de plus en plus exploitées dans des disciplines très différentes, allant de l'archéologie à la chimie, de la science des matériaux à la biologie, de la médecine à la physique. Parmi ces propriétés, il est important de mentionner la haute brillance, le spectre continu, le haut degré de polarisation, la structure temporelle, la petite taille de la source et la petite divergence du faisceau. Ces dernières propriétés entraînant une forte cohérence transversale du rayonnement produit.

La cohérence du faisceau a permis le développement des nouvelles techniques comme par exemple, l'imagerie à contraste de phase, la spectroscopie à corrélation des photons et l'imagerie par diffraction des photons cohérents. Par conséquent, il est de première importance que les éléments optiques puissent préserver cette propriété, perturbant le moins possible la front d'onde.

Ce travail de thèse se constitue de trois parties.

Dans la première partie, je vais présenter le travail effectué au sein du groupe optique de l'ESRF dans la caractérisation des cristaux de diamant synthétique de haute qualité prévus pour des applications aux optiques pour les rayons X. Cette caractérisation a été effectuée en utilisant différentes techniques rayons X complémentaires, telles que la diffractométrie à haute résolution, la topographie, la diffraction en incidence rasante, la réflectométrie et des mesures de préservation de cohérence en utilisant l'effet Talbot.

Dans la deuxième partie, je expose les résultats obtenus dans l'étude du comportement à haute température des domaines ferroélectriques dans un cristal périodiquement polarisé. Dans ce type d'étude, basé sur la diffraction de Bragg-Fresnel, est nécessaire une haute cohérence du faisceau.

Dans la troisième partie, je présente des résultats obtenus dans la caractérisation des diamants prévus pour des applications autres que les optiques rayons X.